Data Reconstruction and Analysis for the GERDA Experiment

Dissertation
zur
Erlangung der naturwissenschaftlichen Doktorwürde
(Dr. sc. nat.)

vorgelegt der
Mathematisch-naturwissenschaftlichen Fakultät
der
Universität Zürich

von
Giovanni Benato
aus
Italien

Promotionskomitee

Prof. Dr. Laura Baudis (Vorsitz)
Prof. Dr. Ulrich Straumann
Dr. Alexander Kish

Zürich, 2015

ZUSAMMENFASSUNG

Der neutrinolose Doppelbetazerfall ($0\nu\beta\beta$) ist ein nuklearer Prozess, der durch verschiedene Erweiterungen des Standardmodells der Teilchenphysik vorhergesagt wird. Die Beobachtung dieses Prozesses würde beweisen, dass die Leptonzahl nicht erhalten ist und dass ein nichtverschwindender Majorana-Massenterm für Neutrinos existiert. Im Fall, dass ein leichtes Neutrino ausgetauscht wird, würde diese Beobachtung es ermöglichen, die effektive Neutrinomasse zu bestimmen und letztendlich zwischen normaler und invertierter Massenhierarchie zu unterscheiden.

Das "Germanium Detector Array" (GERDA) ist ein Experiment, das nach dem $0\nu\beta\beta$-Zerfall in ^{76}Ge sucht. Es befindet sich im Laboratori Nazionali del Gran Sasso (LNGS) in Italien. In GERDA fungieren 18 kg auf 86% ^{76}Ge angereicherte high-purity Germaniumdetektoren (HPGe) gleichzeitig als Quelle, als auch als Detektor für diesen Prozess. Diese hängen innerhalb von flüssigem Argon (LAr), das sowohl für die Kühlung der Detektoren verwendet wird, als auch eine Abschirmung gegen externe Strahlung darstellt. Phase I wurde im Jahr 2013 abgeschlossen mit einem Produkt aus Detektormasse und Messzeit von 21.6 kg·yr und einen Background-Index BI $\simeq 10^{-2}$ counts/(keV·kg·yr) bei 2039 keV, dem Q-Wert dieser Reaktion ($Q_{\beta\beta}$). Sie führten zu einem Limit von $T^{0\nu}_{1/2} > 2.1 \cdot 10^{25}$ yr, bei 90% confidence level. Für Phase II des GERDA-Experimentes wurden weitere 20 kg Broad Energy Germanium Detektoren (BEGes) hergestellt und charakterisiert. Zusätzlich wurde das LAr-Volumen mit Lichtsensoren ausgestattet, die das Szintillationslicht von LAr detektieren sollen. Wird der angestrebte BI von 10^{-3} counts/(keV·kg·yr) erreicht, dann kann GERDA mit Phase II eine mediane Sensitivität von $1.4 \cdot 10^{26}$ yr erreichen, bei einem Produkt aus Detektormasse und Messzeit von 100 kg·yr.

In dieser Arbeit wird eine komplette Rekonstruktion der Daten von Phase I vorgestellt, sowie die darauf folgende erneute Auswertung. Es wurde ein neuer digitaler Shapingfilter für die Energiebestimmung entwickelt und optimiert. Dadurch konnte eine Verbesserung der Energieauflösung von etwa 12% bei $Q_{\beta\beta}$ erreicht werden. Ausserdem wurde eine vollautomatische Energiekalibrierung erstellt, die auf alle Daten von Phase I angewendet wurde. Das Ergebnis dieses Verfahrens wird benutzt, um die systematischen Unsicherheiten für die Energiebestimmung jedes einzelnen Events und der Energieauflösung bei $Q_{\beta\beta}$ zu bestimmen. Zusätzlich dazu wird die Analyse des $0\nu\beta\beta$-Zerfalls auf die reprozessierten Daten angewendet. Dabei wurden mögliche Verbesserungen des statistischen Ansatzes genau überprüft. Insgesamt konnte eine Verbesserung von $\gtrsim 5\%$ auf die $T^{0\nu}_{1/2}$-Sensitivität erreicht werden. Letztendlich wurde dann die Optimierung über den digitalen Filter auf die Rekonstruktion von Pulsen für die Pulse Shape Discrimination angewendet. Dabei wurden Hinweise gefunden, dass sich die $T^{0\nu}_{1/2}$-Sensitivität um $\gtrsim 10\%$ verbessert.

Für die Phase II von GERDA wurden vier ^{228}Th Kalibrierungsquellen mit reduziertem Neutronenhintergrund hergestellt. Die γ- und Neutronenaktivität wur-

de durch geeignete Messungen in einer Low-Background-Umgebung charakterisiert. Darüber hinaus wurde eine neu entwickelte Technik verwendet, um ein mögliches Entweichen radioaktiven Materials aus der Quellenummantellung aufzuspüren. Dadurch wurde die Stärke der Neutronenquelle um eine Grössenordnung unterdrückt im Vergleich zu kommerziell erhältlichen Quellen und die Existenz von Lecks konnte bis zu 10 mBq ausgeschlossen.

Gleichzeitig zu den experimentellen Arbeiten für GERDA, wird eine Studie über die Aussichten der Suche nach dem $0\nu\beta\beta$-Zerfall vorgestellt. Für die Wahrscheinlichkeitsverteilung der effektiven Majorana-Masse im Fall des Austausches leichter Neutrinos wurden Zufallsereignisse der Neutrino-Mischungswinkel und der quadrierten Massendifferenzen erzeugt unter Berücksichtigung der kosmologischen Grenzen auf der Summe der Neutrinomassen. Darauf beruhend wird die benötigte Sensitivität auf $T^{0\nu}_{1/2}$ für Experimente angegeben, die den $0\nu\beta\beta$-Zerfall mit ^{76}Ge untersuchen.

ABSTRACT

Neutrinoless double beta ($0\nu\beta\beta$) decay is a nuclear process predicted by several extensions of the Standard model of particle physics. Its observation would prove the non-conservation of total lepton number and the existence of a non-vanishing Majorana mass term for neutrinos. In case of light neutrino exchange, it would also provide a measurement of the effective Majorana mass and eventually allow to disentangle between the normal and inverted neutrino mass schemes.

The Germanium Detector Array (GERDA) is an experiment for the search of $0\nu\beta\beta$ decay in ^{76}Ge, located at the Laboratori Nazionali del Gran Sasso (LNGS), Italy. In GERDA, 18 kg of high-purity germanium crystals (HPGe) with $\sim$ 86% enrichment in ^{76}Ge are simultaneously operated as source and detector of the process. They are directly inserted in liquid argon (LAr), acting as cooling medium and shielding against external radiation. The first data collection (Phase I) was completed in 2013 with a total exposure of 21.6 kg·yr. It was characterized by a background index $BI \simeq 10^{-2}$ counts/(keV·kg·yr) at 2039 keV, the Q-value of the reaction ($Q_{\beta\beta}$). This led to a lower limit on the $0\nu\beta\beta$ decay half-life ($T^{0\nu}_{1/2}$) of $T^{0\nu}_{1/2} > 2.1 \cdot 10^{25}$ yr at 90% confidence level. In view of GERDA Phase II, additional 20 kg of Broad Energy Germanium (BEGe) detectors were successfully produced and characterized, and the LAr volume was instrumented with light sensors to detect the LAr scintillation light induced by background radiation. If the aimed BI of 10^{-3} counts/(keV·kg·yr) is achieved, GERDA Phase II will reach a median sensitivity on the $0\nu\beta\beta$ decay half-life of $1.4 \cdot 10^{26}$ yr with an exposure of 100 kg·yr.

In this work, a complete reconstruction of the Phase I data and a re-analysis of $0\nu\beta\beta$ decay are reported. A new digital shaping filter for energy reconstruction is developed and optimized, yielding a $\sim$ 12% improvement in energy resolution at $Q_{\beta\beta}$. Moreover, an automatic procedure for the energy calibration is developed and applied to all Phase I data. The output of this procedure is used for computing the systematic uncertainty on the energy reconstruction of each single event, as well as the energy resolution at $Q_{\beta\beta}$. In addition, the $0\nu\beta\beta$ decay analysis is applied on the reprocessed data, and possible improvements of the statistical approach, which can yield a $\gtrsim$ 5% improvement in $T^{0\nu}_{1/2}$ sensitivity, are scrutinized. Finally, the optimization of digital filters is applied to the reconstruction of current pulses for pulse shape discrimination, and an indication for a $\gtrsim$ 10% improvement in $T^{0\nu}_{1/2}$ sensitivity is found.

In view of GERDA Phase II, four ^{228}Th calibration sources with reduced neutron emission rate were produced. Their γ and neutron activities were characterized with dedicated measurements performed in low background environments, and a newly developed technique was employed to detect possible leaks of radioactive material from the source encapsulation. As a result, the neutron source strength is suppressed by one order of magnitude with respect to commercially available sources, and the presence of leaks is excluded down to a 10 mBq level.

In parallel to the experimental work for GERDA, a study of the perspectives for $0\nu\beta\beta$ decay searches is described. The probability distribution for the effective Majorana mass in case of light neutrino exchange is extracted through a random sampling of the involved neutrino mixing angles and squared mass differences, with the inclusion of the cosmological bound on the sum of neutrino masses. Based on this study, the required discovery sensitivity on $T^{0\nu}_{1/2}$ for experiments investigating $0\nu\beta\beta$ decay in ^{76}Ge is reported.

CONTENTS

LIST OF TABLES

LIST OF FIGURES

ABBREVIATIONS

BEGe	Broad energy germanium
BI	Background index
BSM	Beyond the standard model
C.I.	Credibility interval
C.L	Confidence level
FWHM	Full width at half maximum
GERDA	Germanium detector array
HdM	Heidelberg-Moskow
HPGe	High-purity germanium
IH	Inverted neutrino mass hierarchy
LAr	Liquid argon
mwe	Meter of water equivalent
MC	Monte Carlo
NH	Normal neutrino mass hierarchy
NME	Nuclear matrix element
PMT	Photo-multiplier tube
PSD	Pulse shape discrimination
RMS	Root mean square
ROI	Region of interest
SiPM	Silicon photo-multiplier
SM	Standard model of particle physics
$0\nu\beta\beta$ decay	Neutrinoless double beta decay
$2\nu\beta\beta$ decay	Two neutrino double beta decay
$T^{0\nu}_{1/2}$	$0\nu\beta\beta$ decay half-life
$T^{2\nu}_{1/2}$	$2\nu\beta\beta$ decay half-life
$Q_{\beta\beta}$	Q-value of $0\nu\beta\beta$ decay (2039 keV for ^{76}Ge)
$\lvert m_{\beta\beta}\rvert$	Effective Majorana mass
$G_{2\nu}$	Phase space integral
$\mathcal{M}_{2\nu}$	Nuclear matrix element
m_e	Electron neutrino mass

1

INTRODUCTION

85 years after the postulation of neutrinos by W. Pauli and 62 years after the discovery of the electron neutrino by F. Reines and C. L. Cowan Jr., neutrinos are still a topic of major interest in particle physics. Despite the measurement of all mixing angles and of the squared mass differences, a list of questions remains open today: what is the absolute neutrino mass scale? Do neutrino masses follow the normal or the inverted hierarchy scheme? Are neutrinos pure Dirac particles, or do they have a Majorana mass component, as well? Is the total lepton number a conserved quantity?

An answer to all – or at least some – of these questions can be given by neutrinoless double beta ($0\nu\beta\beta$) decay. It is a nuclear process violating the total lepton number conservation predicted by several beyond the Standard Model (BSM) theories. The discovery of $0\nu\beta\beta$ decay would prove that neutrinos have a Majorana mass component, and provide information regarding the neutrino mass hierarchy and the absolute neutrino masses.

The GERDA experiment is searching for $0\nu\beta\beta$ decay in ^{76}Ge. The aim of the PhD work presented here is the enhancement of the GERDA sensitivity to a $0\nu\beta\beta$ decay signal through the optimization of the data reconstruction algorithms. In parallel, the production of ^{228}Th calibration sources with reduced neutron strength is performed, and the perspectives for the future of $0\nu\beta\beta$ decay search are investigated.

The thesis is structured as follows. In Ch. 2 an overview of the theoretical aspects of neutrino physics and $0\nu\beta\beta$ decay is given. Moreover, a phenomenological study of the future perspectives of the experimental search is reported, and its current status summarized. A description of the interaction processes which can be detected by a $0\nu\beta\beta$ decay experiment, of the working principles and of the main characteristics of germanium detectors is given in Ch. 3. The physics program, the experimental setup and the data structure of GERDA are presented in Ch. 4, together with the most important results of GERDA Phase I.

The main content of the thesis starts with Ch. 5, where the full analysis of calibration data is described, as well as the determination of the energy resolution at $Q_{\beta\beta}$ and the systematic uncertainties on the reconstructed energy of each single event. The development of a new digital shaping filter and the consequent reprocessing of all Phase I data can be found in Ch. 6. In the same chapter, a re-analysis of $0\nu\beta\beta$ decay with the reprocessed data and the sensitivity of GERDA Phase I are reported. In Ch. 7, the optimization of digital shaping filters is applied to the reconstruction of current pulses for pulse shape discrimination, with encouraging results in view of Phase II.

Finally, Ch. 8 describes the production and characterization in terms of γ and neutron activity of 4 custom ^{228}Th calibration sources for GERDA Phase II, together with a new procedure for testing the source capsule tightness after the deployment in cryogenic environment.

As it can be expected, most of the introductory parts result from the comparison between several literature sources, which are cited in the text. The original contribution of the author comprises Secs. 2.4 and 8.1–8.3, Chs. 5–7, and Apps. A–D.

Part of the material presented here is already pubished in peer-reviewed journals [1, 2, 3].

2

NEUTRINOS AND DOUBLE BETA DECAY

In this chapter, a theoretical introduction to $0\nu\beta\beta$ decay and an overview on the status of the experimental search are given. In Sec. 2.1 a historical summary of the discoveries and open questions in neutrino physics is given. Sec. 2.2 describes the possible neutrino mass term in the SM Lagrangian, while the theoretical description of $0\nu\beta\beta$ decay is given in Sec. 2.3. A phenomenological study of the perspectives of $0\nu\beta\beta$ search based on the results of oscillation experiments and of cosmological measurements is reported in Sec. 2.4. Finally, the status of the $0\nu\beta\beta$ decay search is revised in Sec. 2.5. More details on $0\nu\beta\beta$ decay search with ^{76}Ge are given in Sec. 2.6.

2.1 HISTORICAL OVERVIEW

The strong effort in the study of neutrino properties is motivated by recursive tensions between the results of neutrino experiments and the Standard Model (SM) of particle physics. In order to provide a comprehensive description of the current situation, the historical development of neutrino physics is summarized. A large fraction of the information reported here is taken from [4].

The idea of the existence of a light neutral particle dates back to the late 19th century. After the discovery of radioactivity by H. Becquerel in 1896, E. Rutherford proved that the particles emitted by uranium are not X-rays, but of other two types characterized by different penetration depths and denoted as α and β [5]. Thanks to the development of the Geiger-counters, J. Chadwick measured the β spectrum, which turned out to be a superimposition of sharp lines over a broad continuum [6]. If only β particles are emitted and energy is conserved, the β spectrum should be characterized by one (or several) sharp lines. The explanation of the presence of the continuum was introduced by W. Pauli in 1930 in a letter to the "radioactive folk" in occasion of the Gauverein meeting in Tübingen [7]. Energy and momentum conservation was restored by postulating the existence of another neutral particle emitted in β-decay. This particle, originally denoted as "neutron", must have spin 1/2, obey the exclusion principle,and have a mass of order of the electron mass. In the same letter, Pauli formulated the question regarding the possibility of measuring these neutral particles, which have a greater penetration depths than γ rays.

Ein Abdruck ihrer Forme in γ-Strahlenhintergrund. Einstürzende Neubauten, Die Explosion im Festspielhaus

In 1932, J. Chadwick discovered the neutron, and the particle postulated by Pauli was renamed the neutrino. In the same year, W. Heisenberg published an explanation of the stability of isobars [8]. Assuming that the isobars with the

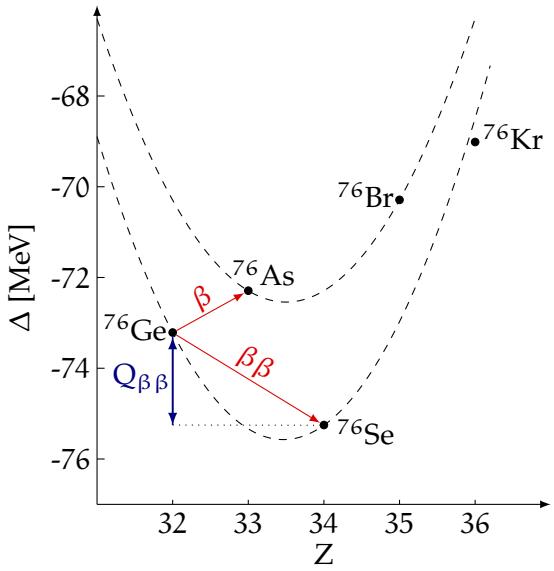

Figure 2.1.: Mass excess $\Delta = (m_A - A) \cdot u$ for isobars with mass m_A and mass number $A = 76$, where u is the atomic mass unit. Even-even nuclei are distributed on the lower curve, odd-odd nuclei on the top one.

same mass number do not have exactly the same mass, only one of them can be considered stable, and the others are expected to undergo subsequent β-decays until they are transformed into it. The isobar masses are expected to lie on a parabolic line as function of the atomic number. In truth, due to the peculiar stability of ^{4}He, the isobars with even mass and atomic number (even-even) lie on a lower curve with respect to the isobars with odd atomic number. A nucleus can go from the lower to the upper curve, or vice versa, through a β-decay. The curves and mass distribution for the nuclei with mass number 76 are shown in Fig. 2.1.

Two years later, E. Fermi provided a theoretical description of β-decay giving the first example of an effective field theory. In [9], the transition probability for β-decay was computed and the concept of forbidden transition was introduced. Moreover, Fermi pointed out that the neutrino mass can be measured by looking at the shape of β spectrum in vicinity of its end-point.

In 1935, M. Goeppert-Mayer theorized double beta decay [10]. Taking ^{76}Ge as an example and with reference to Fig. 2.1, it can happen that a nucleus on the lower curve has a smaller mass than its neighbor on the upper curve. If this is the case, the β-decay is energetically forbidden. However, the same nucleus can reach a more stable state through the simultaneous emission of two electrons and two neutrinos. This process is called two-neutrino double beta decay ($2\nu\beta\beta$). The application of the Fermi method to $2\nu\beta\beta$ decay yields a half-life estimation of $> 10^{17}$ yr.

In 1937, E. Majorana introduced a new quantization process [11] as an alternative to the Dirac formalism. Using a different variational principle, Majorana reduced the "number of hypothetical entities". The result is the absence of the states with negative energy introduced by Dirac. In the case of neutral particles, this is equivalent to the absence of the corresponding antiparticle.

In 1939, W. H. Furry merged the Majorana theory with the Goeppert-Mayer description of $\beta\beta$ decay. In [12], neutrinoless double beta decay ($0\nu\beta\beta$) was introduced, in which only two electrons are emitted. In this first treatment, a virtual neutrino is supposed to be emitted in one of the two β-decays and re-absorbed in

the other. Using the Fermi method for the calculation of the transition probability, Furry claimed shorter half-lives with respect to those for $2\nu\beta\beta$ decay.

The concept of lepton number was introduced in 1953 by E. J. Konipinski and H. M. Mahmoud for the explanation of the missing observation of them in some decays [13]. A few years later, B. Pontecorvo suggested the use of separate lepton numbers for electrons and muons in order to explain the non-observation of $\mu \rightarrow e + \gamma$ [14].

A major milestone was the discovery of the electron anti-neutrino ($\bar{\nu}_e$) by F. Reines and C. L. Cowan Jr. in 1953 [15]. The experiment consisted of a Cd-loaded scintillator in vicinity of a nuclear reactor. The measurement of inverse beta decay $\bar{\nu}_e + p \rightarrow n + \beta^+$ is possible through the detection of both the prompt positron signal and the delayed Cd de-excitation after the neutron absorption.

In 1958 the experiment of M. H. Goldhaber, L. Grodzins and A. W. Sunyar [16] proved that the helicity of the electron neutrino ν_e is negative, exploiting the reaction $e^- + {}^{152}\mathrm{Eu} \rightarrow {}^{152}\mathrm{Sm}^* + \nu_e$ and the decay ${}^{152}\mathrm{Sm}^* \rightarrow {}^{152}\mathrm{Sm} + \gamma$. The same was confirmed later for ν_μ [17, 18] and ν_τ [19, 20, 21].

The first successful accelerator neutrino experiment, performed in 1962 at the Brookhaven National Laboratory (BNL) by L. M. Lederman, M. Schwartz, J. Steinberger and others, lead to the confirmation of Pontecorvo's theory thanks to the detection of the muon neutrino (ν_μ) [22]. The measurement of the charged pion decay $\pi^\pm \rightarrow \mu^\pm + \nu(\bar{\nu})$, together with the non-observation of the alternative channel $\pi^\pm \rightarrow e^\pm + \nu(\bar{\nu})$, can only be interpreted with the existence of two types of neutrinos, denoted as ν_e and ν_μ.

A complete description of all the known particles and interactions is given in the formulation of the SM by S. Weinberg [23] and A. Salam [24] in 1967. In the first version of the SM, the neutrinos were considered massless, and therefore no mixing was contemplated.

Already in 1957, the idea of neutrino oscillation was introduced by Pontecorvo [25, 26] to explain the oscillation $K^0 \leftrightarrows \overline{K^0}$ and the claimed observation of $\bar{\nu} + {}^{37}\mathrm{Cl} \rightarrow {}^{37}\mathrm{Ar} + e^-$ via the $\nu \leftrightarrows \bar{\nu}$ oscillation of Majorana neutrinos. This is in contrast with the conservation of helicity. A solution is given by the parametrization of the neutrino flavor eigenstates as a mixing of the neutrino mass eigenstates [27, 28, 29].

The existence of neutrino oscillation has been proven by dozens of experiments involving solar, atmospheric, reactor and accelerator neutrinos. The first anomaly was the disappearance of solar ν_e detected by the Homestake experiment [30, 31] and further confirmed by Kamiokande [32, 33], SAGE [34, 35], GALLEX/GNO [36, 37], Super-Kamiokande [38, 39], SNO [40, 41], Borexino [42, 43] and KamLAND [44]. Neutrino oscillations have also been measured with atmospheric neutrinos experiments, e.g. IBM [45], Kamiokande [46, 47], MACRO [48, 49], MINOS [50, 51], Soudan 2 [52, 53], Super-Kamiokande [54, 55], ANTARES [56] and IceCube [57]. A further confirmation is provided by the reactor experiments KamLAND [58, 59], Daya Bay [60, 61], Double Chooz [62, 63] and RENO [64], and by the accelerator experiments K2K [65, 66], MINOS [67, 68], T2K [69, 70] and OPERA [71, 72].

2.2 DIRAC AND MAJORANA NEUTRINOS

In order to motivate the search for $0\nu\beta\beta$ decay, a short review of the current knowledge of neutrino physics is necessary. As for the previous section, the material presented here is taken from elsewhere, mostly from [73].

The discovery of neutrino oscillations can only be explained if neutrinos have non-zero mass, and if the neutrino flavor eigenstates ν_e, ν_μ and ν_τ are a superimposition of the neutrino mass eigenstates ν_i (with $i = 1, 2, 3$) [74, 4]. Moreover, there is an established experimental evidence that only left-handed neutrinos (ν_L) participate in weak interaction processes. The two experimental facts are taken into consideration writing:

$$\nu_{lL} = \sum_{i=1}^{3} U_{li}\nu_{iL} \quad , \tag{2.1}$$

where l denotes the lepton family (e, μ, τ), and the subscript L indicates the left-handed component of the neutrino field. The matrix U is the Pontecorvo, Maki, Nagakawa, Sakata (PMNS) mixing matrix:

$$U = \begin{pmatrix} c_{12}c_{13} & s_{12}c_{13} & s_{13}e^{-i\delta} \\ -s_{12}c_{23} - c_{12}s_{23}s_{13}e^{i\delta} & c_{12}c_{23} - s_{12}s_{23}s_{13}e^{i\delta} & s_{23}c_{13} \\ s_{12}s_{23} - c_{12}c_{23}s_{13}e^{i\delta} & -c_{12}s_{23} - s_{12}c_{23}s_{13}e^{i\delta} & c_{23}c_{13} \end{pmatrix} \quad . \tag{2.2}$$

The symbols $c_{jk}(s_{jk})$ stand for $\cos\theta_{jk}(\sin\theta_{jk})$. The transition probability for the oscillation $\nu_l \to \nu_{l'}$ is:

$$P(\nu_l \to \nu_{l'}) = \delta_{ll'} - 4\sum_{i>k} \Re\left[U^*_{li}U_{l'i}U_{lk}U^*_{l'k}\right] \sin^2\left(\frac{\Delta m^2_{ki}B}{4E}\right) + 2\sum_{i>k} \Im\left[U^*_{li}U_{l'i}U_{lk}U^*_{l'k}\right] \sin\left(\frac{\Delta m^2_{ki}B}{2E}\right) \quad , \tag{2.3}$$

where $\Delta m^2_{ki} = m^2_i - m^2_k$, E is the neutrino energy, and B is the baseline of the experiment, i.e. the distance between the neutrino source and the detector. If the PMNS matrix is complex ($U \neq U^*$), the imaginary part of Eq 2.3 changes under the substitution $U \leftrightarrow U^*$. This means that $P(\nu_l \to \nu_{l'}) \neq P(\bar{\nu}_l \to \bar{\nu}_{l'})$. In other words, if $\delta \neq \{0, \pi\}$ CP is violated. For this reason, δ is denoted as the CP-violating phase.

If right-handed neutrinos (ν_R) are SM particles, the standard Higgs mechanism can generate the neutrino masses with a Yukawa interaction. Denoting the dimensionless Yukawa coupling constants with $Y_{l'l}$, the neutrino mass term in the extended SM Lagrangian is:

$$\mathcal{L}^Y_I = -\sqrt{2}\sum_{l'l} \overline{L_{l'L}} Y_{l'l} \nu_{lR} \tilde{\phi} + \text{h.c.}, \tag{2.4}$$

where L is the lepton doublet, and ϕ is the Higgs doublet:

$$L_{lL} = \begin{pmatrix} \nu_{lL} \\ l_L \end{pmatrix} \quad , \qquad \phi = \begin{pmatrix} \phi^{(+)} \\ \phi^{(-)} \end{pmatrix} \quad , \tag{2.5}$$

with $\tilde{\phi} = i\sigma_2\phi^*$, where σ_2 is the second Pauli matrix. After spontaneous symmetry breaking:

$$\tilde{\phi} = \frac{1}{\sqrt{2}}\begin{pmatrix} v + H \\ 0 \end{pmatrix} \quad , \tag{2.6}$$

Here H is the physical Higgs boson field and $v \sim 246$ GeV its vacuum expectation value. Plugging Eq. 2.6 in Eq. 2.4 we obtain the Dirac mass term:

$$\mathcal{L}^D = -\sum_{l'l} \overline{\nu_{l'L}} M^D_{l'l} \nu_{lR} + \text{h.c.}, \tag{2.7}$$

where $M^D_{l'l} = vY_{l'l}$. The Dirac neutrino masses can be obtained by diagonalizing the matrix Y, which yields:

$$m_i = v y_i \quad . \tag{2.8}$$

From oscillation experiments we know that the mass of the heaviest neutrino is $\lesssim 10^{-1}$ eV [75], hence $y_i \lesssim 4 \cdot 10^{-13}$. This value is at least 10 order of magnitude smaller than the corresponding Yukawa couplings for charged leptons.

At this point the neutrino masses are included in the SM and the neutrino oscillations explained. What is not explained is the presence of right-handed particles which are sterile, i.e. they do not participate in SM interactions, and the smallness of the Yukawa coupling constant for neutrinos.

In realtà questo materiale era ben poco: radiazioni fotoelettriche, limatura di campi magnetici, qualche neutrino perduto per via; ma a furia d'appallottolare e umettare di saliva riuscivo a far stare tutto insieme.
I. Calvino, Le Cosmicomiche

In the Majorana framework [11] the right-handed neutrinos are parametrized as a function of the left-handed. We can require the the right-handed neutrino field to be equal to the charge conjugated of the left-handed (Majorana condition):

$$\nu_{lR} = C\overline{\nu_{lL}}^T = \nu^C_{lL} \quad , \tag{2.9}$$

where C is the charge conjugation operator:

$$C\gamma^T_\alpha C^{-1} = -\gamma_\alpha, \qquad C^T = -C \quad , \tag{2.10}$$

and $\gamma_\alpha (\alpha = 0, \cdots, 3)$ are the Dirac matrices. The Majorana neutrino field is:

$$\nu_l = \nu_{lL} + \nu_{lR} = \nu_{lL} + \nu^C_{lL} \quad , \tag{2.11}$$

and its charge conjugate is:

$$\nu^C_l = \left(\nu_{lL} + \nu^C_{lL}\right)^C = \nu^C_{lL} + \nu_{lL} = \nu_l \quad , \tag{2.12}$$

This means that the Majorana neutrino is its own anti-particle, with no electric charge and no lepton number.

Using Eq. 2.9, a lepton number violating Majorana mass term can be written as:

$$\mathcal{L}^M = -\frac{1}{2}\sum_{l'l} \overline{\nu_{l'L}} M_{l'l} \nu^C_{lL} + \text{h.c.}, \tag{2.13}$$

in which the matrix M can be diagonalized with the unitary PMNS matrix U:

$$M = UmU^T \quad , \tag{2.14}$$

This leads to:

$$\mathcal{L}^M = -\frac{1}{2}\sum_{i=1}^{3} m_i \bar{\nu}_i \nu_i \quad , \tag{2.15}$$

where ν_i are the neutrino mass eigenstates mentioned above. The question emerging at this point is which mechanism can generate the Majorana mass term of Eq. 2.13.

2.2.1 *Seesaw Mechanism*

In the SM the renormalizability requires that all terms in the Lagrangian have dimension 4. Under this condition, it is not possible to write a term which violates the total lepton number. A possible trick is to write a non-renormalizable term with higher dimensionality which is suppressed at low energy. This term must be BSM. A possibility is to use an effective Lagrangian:

$$\mathcal{L}^{eff} = -\frac{1}{\Lambda}\sum_{l'l}\overline{L_{l'L}}\tilde{\phi}\tilde{Y}_{l'l}\tilde{\phi}^{t}L^{C}_{lL} + \text{h.c.}, \tag{2.16}$$

where $\Lambda \gg v$ is the energy scale at which the total lepton number is violated. Proceeding as for the Higgs-generated neutrino mass (Eqs. 2.4, 2.6 and 2.8), after spontaneous symmetry breaking the neutrino masses are given by:

$$m_i = \frac{v^2}{\Lambda}\bar{y}_i \quad . \tag{2.17}$$

Assuming $m_i = 10^{-1}$ eV, $\bar{y}_i \sim 1$ and with $g \sim 246$ GeV, the high energy scale is $\Lambda \sim 10^{15}$ GeV. This means that the electron masses are suppressed by the ratio between the electroweak scale g and the BSM scale Λ. Such a suppression is called the "seesaw mechanism".

Several implementations of a mechanism for the generation of the neutrino masses are given in literature. In the "Type I" seesaw [76, 77, 78], the existence of right-handed Majorana neutrino fields is postulated in the framework of grand unification theories (GUT) additionally to the three light neutrino masses, which are also of Majorana type. The model is based on the assumptions that the Dirac mass term is generated by the usual Higgs mechanism, that no left-handed Majorana mass term enters the Lagrangian, and that the right-handed Majorana mass is much larger than the Dirac mass term, such that the lepton number violation takes place only at high energy. In the "Type II" seesaw [78, 79], a small but non-zero left-handed Majorana mass is present, generated by a scalar Higgs triplet. A further possibility is the "Type III" seesaw mechanism [80, 81], in which two fermion triplets are introduced.

2.3 NEUTRINOLESS DOUBLE BETA DECAY

The Feynman diagrams for $2\nu\beta\beta$ and $0\nu\beta\beta$ decays are depicted in Fig:2.2. In $2\nu\beta\beta$ decay, the final state consists of two electrons and two anti-neutrinos. The derivation of the decay rate of the processes from the interaction Lagrangian is out of the scope of the present document. For $2\nu\beta\beta$ decay, the calculation is given in [82], while for $0\nu\beta\beta$ decay it is available in [73].

The $2\nu\beta\beta$ decay is a SM process of second order in the Fermi constant G_F [82, 83]. Its half-life can be expressed as [83]:

$$\frac{1}{T^{2\nu}_{1/2}} = G_{2\nu}g_A^4|m_e c^2 \mathcal{M}_{2\nu}|^2 \quad , \tag{2.18}$$

where $G_{2\nu}$ is the phase space integral, g_A is the axial vector coupling constant, m_e is the electron mass, and $\mathcal{M}_{2\nu}$ is the nuclear matrix element.

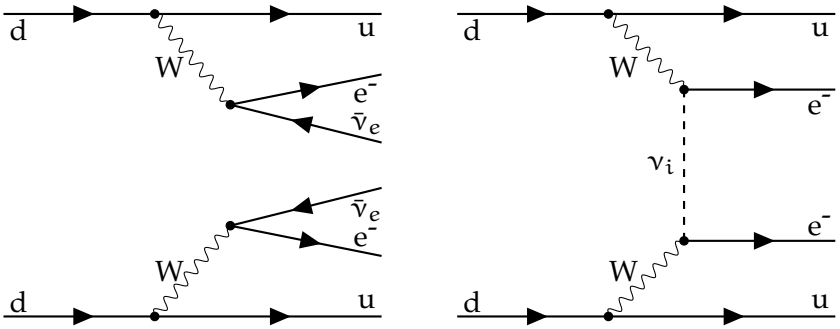

Figure 2.2.: Feynman diagrams for $2\nu\beta\beta$ decay (left) and $0\nu\beta\beta$ decay (right)

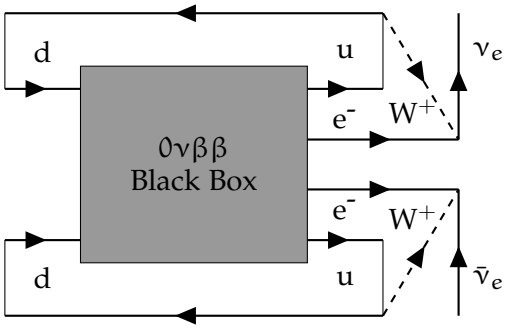

Figure 2.3.: Schechter-Valle theorem.

On the contrary, $0\nu\beta\beta$ decay is a non SM process which involves total lepton number violation by two units. The final state in this case consists of only two electrons. Independent from the mechanism inducing it, the observation of $0\nu\beta\beta$ decay would prove the existence of BSM physics, the non-conservation of total lepton number at high energy scale, and that neutrinos have a Majorana mass component. While the first two points have already been discussed, the third needs some further explanation. So far it was only shown how the presence of massive Majorana neutrinos would involve the existence of $0\nu\beta\beta$ decay[1]. On the other hand, we can ask whether the experimental observation of $0\nu\beta\beta$ decay proves the existence of massive Majorana neutrinos. A possible answer comes from the Schechter-Valle theorem [84]. As depicted in Fig. 2.3, the external lines of the quarks and electrons involved in $0\nu\beta\beta$ decay can be connected via SM weak interaction, yielding a $\bar{\nu}_e \to \nu_e$ transition. The black box represents radiative corrections at four-loop level. It can be proven [4] that no global symmetry is possible which forbids a Majorana mass term for the electron neutrino. Hence, a cancellation of this black box contribution is possible only with a fine tuning of all involved masses and mixing angles at all orders, which is very unlikely. For a long time the Schechter-Valle theorem was exploited to justify the search for $0\nu\beta\beta$ decay. Recently, a detailed calculation [85] proved that the contribution to the Majorana mass term of the electron neutrino mass provided by these radiative corrections is of $O(10^{-24})$ eV. This is many orders of magnitude smaller than the value of the electron neutrino mass expected from the combination of the measured mass splittings and mixing

1 In truth a very small or even vanishing decay rate is possible in case of fine tuning of the involved parameters (see Sec. 2.4).

angles. This implies that other Majorana and/or Dirac mass terms must exist in order to explain the known mass splittings and mixing angles.

The simplest mechanism for the generation of $0\nu\beta\beta$ decay is light neutrino exchange. Other possible mechanisms would involve the existence of new particles or interactions not described by the SM, and are not considered here. For $0\nu\beta\beta$ decay and with light neutrino exchange only the half-life is:

$$\frac{1}{T^{0\nu}_{1/2}} = G^{0\nu}(Q_{\beta\beta}, Z) g_A^4 \left|M^{0\nu}\right|^2 \frac{|m_{\beta\beta}|^2}{m_e^2} \quad , \tag{2.19}$$

where the dependence of the phase space integral on the Q-value of $0\nu\beta\beta$ decay ($Q_{\beta\beta}$) and on the atomic number Z is highlighted. The quantity $|m_{\beta\beta}|$ is the effective Majorana mass, and contains BSM physics. For a fixed effective mass, greater values of the phase space integral and NME correspond to a shorter $0\nu\beta\beta$ decay half-life and, consequently, to a greater specific activity.

If a higher $Q_{\beta\beta}$ would in principle allow for a greater phase space integral, the Coulomb potential of the daughter nucleus would play a strong role in the calculation [83]. The value of $G^{0\nu}(Q_{\beta\beta}, Z)$ is around 10^{-15}-10^{-14} yr^{-1}, depending on the isotope.

The calculation of $\left|M^{0\nu}\right|$ is usually the bottleneck for the extraction of $|m_{\beta\beta}|$ from Eq. 2.19. Despite a strong effort, different nuclear models yield $\left|M^{0\nu}\right|$ values which can vary by more than a factor two. A compilation of possible estimations for the most investigated $\beta\beta$ emitting isotopes is given in [86].

The phase space integrals and NMEs for light neutrino exchange of the isotopes most commonly employed for $0\nu\beta\beta$ decay search are reported in Tab. 2.3.

The estimation of g_A is an even more delicate topic. As pointed out in [87], typically the value of g_A for the free neutron is used. In literature, this ranges between 1.25 and 1.27. A problem arises from the comparison between the predicted and measured $2\nu\beta\beta$ decay half-lives of several isotopes, which is given by:

$$\frac{1}{T^{2\nu}_{1/2}} = G^{2\nu} g_A^4 \left|M^{2\nu}\right|^2 \quad . \tag{2.20}$$

The experimental values of $T^{2\nu}_{1/2}$ are systematically smaller than the estimated ones. A possible explanation is the "quenching" of g_A induced by either some limitation in the calculation, or by the omission of non-nucleonic degrees of freedom [87]. The quenching of g_A is related to the mass number A via the formula:

$$g_{A,eff} = g_A \cdot A^{\gamma} \quad , \tag{2.21}$$

where γ depends on the model used for the NME calculation and varies between -0.12 and -0.18. For a free neutron ($A = 1$), the effective coupling constant equals g_A. Going back to the case of $0\nu\beta\beta$ decay, we can ask if the value of g_A is quenched in the same way as for $2\nu\beta\beta$ decay or not. So far, no commonly shared answer exists, and the question is a matter of debate. Given this ambiguity, the effect of the quenching of g_A is not considered here, and only unquenched values are used.

2.4 EFFECTIVE MAJORANA MASS

The parameter of interest in $0\nu\beta\beta$ decay search is the effective Majorana mass. It is a combination of the neutrino mass eigenstates and the neutrino mixing matrix terms. Under the hypothesis that only the known three light neutrinos participate in the process, the effective mass is given by:

$$|m_{\beta\beta}| = \left| \sum_{i=1}^{3} U_{ei}^2 m_i \right| \quad , \tag{2.22}$$

where U is the PMNS mixing matrix multiplied by the matrix containing the two Majorana phases α and β:

$$U = \begin{pmatrix} c_{12}c_{13} & s_{12}c_{13} & s_{13}e^{-i\delta} \\ -s_{12}c_{23} - c_{12}s_{23}s_{13}e^{i\delta} & c_{12}c_{23} - s_{12}s_{23}s_{13}e^{i\delta} & s_{23}c_{13} \\ s_{12}s_{23} - c_{12}c_{23}s_{13}e^{i\delta} & -c_{12}s_{23} - s_{12}c_{23}s_{13}e^{i\delta} & c_{23}c_{13} \end{pmatrix} \times \begin{pmatrix} 1 & 0 & 0 \\ 0 & e^{i\alpha} & 0 \\ 0 & 0 & e^{i\beta} \end{pmatrix} \quad . \tag{2.23}$$

The symbols $c_{jk}(s_{jk})$ stand for $\cos\theta_{jk}(\sin\theta_{jk})$. While all the mixing angles θ_{12}, θ_{13} and θ_{23} are known with good precision, only hints are available for the Dirac CP-violating phase δ. No knowledge at all is available for the Majorana phases α and β. Expanding Eq. 2.22, we obtain:

$$\begin{aligned} |m_{\beta\beta}| =& \left| c_{12}^2 c_{13}^2 m_1 + s_{12}^2 c_{13}^2 m_2 e^{i\alpha} + s_{13}^2 m_3 e^{i\beta} \right| = \\ =& \left| \left(c_{12}^2 c_{13}^2 m_1 + s_{12}^2 c_{13}^2 m_2 \cos\alpha + s_{13}^2 m_3 \cos\beta \right) + \right. \\ & \left. + i\left(s_{12}^2 c_{13}^2 m_2 \sin\alpha + s_{13}^2 m_3 \sin\beta \right) \right| \quad , \end{aligned} \tag{2.24}$$

where the substitutions $2\alpha(\beta) \rightarrow \alpha(\beta)$ and $(-\delta + \beta) \rightarrow \beta$ are applied, exploiting our complete ignorance on the values of α and β. Following the definition of the absolute value for complex numbers:

$$|m_{\beta\beta}| = \sqrt{\left(c_{12}^2 c_{13}^2 m_1 + s_{12}^2 c_{13}^2 m_2 \cos\alpha + s_{13}^2 m_3 \cos\beta \right)^2 + \left(s_{12}^2 c_{13}^2 m_2 \sin\alpha + s_{13}^2 m_3 \sin\beta \right)^2} \quad . \tag{2.25}$$

The parameters involved are:

- the angles θ_{12} and θ_{13}, measured with good precision by the solar and short-baseline reactor neutrino experiments, respectively;
- the neutrino mass eigenstates m_1, m_2 and m_3, which are related to the solar and atmospheric squared mass differences $\delta m_{\odot}^2$ and Δm_{atm}^2:

$$\begin{aligned} \delta m_{\odot}^2 &= \Delta m_{12}^2 \quad , \\ \Delta m_{atm}^2 &= \frac{1}{2} \left| \Delta m_{31}^2 + \Delta m_{32}^2 \right| \quad . \end{aligned} \tag{2.26}$$

These are known with $\sim$ 3% uncertainty thanks to the oscillation experiments [75]. The mass eigenstates are also related to the total neutrino mass:

$$\Sigma = \sum_{i=1}^{3} m_i \quad , \tag{2.27}$$

for which several upper limits of about 0.1–0.2 eV are set by cosmological observations [88, 89, 90];

– the two Majorana phases α and β, for which no experimental information is available.

The relation between the mass eigenstates and the squared mass differences given in Eq. 2.26 allows two possible orderings of the neutrino masses. A first scheme, denoted as Normal Hierarchy (NH), corresponds to:

$$\begin{aligned} m_1 &= m_{min} \quad , \\ m_2 &= \sqrt{m_{min}^2 + \delta m_{\odot}^2} \quad , \\ m_3 &= \sqrt{m_{min}^2 + \Delta m_{atm}^2 + \frac{\delta m_{\odot}^2}{2}} \quad , \end{aligned} \tag{2.28}$$

where m_{min} is the mass of the lightest neutrino. The so-called Inverted Hierarchy (IH) is given by:

$$\begin{aligned} m_1 &= \sqrt{m_{min}^2 + \Delta m_{atm}^2 - \frac{\delta m_{\odot}^2}{2}} \quad , \\ m_2 &= \sqrt{m_{min}^2 + \Delta m_{atm}^2 + \frac{\delta m_{\odot}^2}{2}} \quad , \\ m_3 &= m_{min} \quad . \end{aligned} \tag{2.29}$$

Present data show no clear preference for either of the two schemes.

The effective mass can be expressed as a function of the lightest neutrino mass, as first introduced in [92]. This is normally done via a χ^2 analysis [91], where the uncertainties on the oscillation angles θ_{12} and θ_{13}, and on the squared mass differences $\delta m_{\odot}^2$ and Δm_{atm}^2 are propagated, while the values of the Majorana phases leading to the largest and smallest $|m_{\beta\beta}|$ are considered. As a result, the 1σ, 2σ and 3σ allowed regions are shown (Fig. 2.4), but no clear information about the relative probability of different $|m_{\beta\beta}|$ values for a fixed m_{min} is provided. This can become of dramatic importance in case near-term experiments prove that nature chose the NH regime. With reference to Fig. 2.4, in NH the effective mass is distributed within a flat area between $\sim 10^{-3}$ eV and $\sim 5 \cdot 10^{-3}$ eV if $m_{min} < 10^{-3}$ eV, while it can vanish for $m_{min} \in [10^{-3}; 10^{-2}]$ eV due to the combination of the Majorana phases. The case of a vanishing $|m_{\beta\beta}|$ is possible only for a smaller subset of values of the Majorana phases than the entire $[0; 2\pi]$ range. This does not necessarily mean that a vanishing effective mass implies that the theory suffers from a dangerous fine-tuning. Namely, in some models the effective mass can assume a naturally small value that remains small after renormalization due to the chiral symmetry of fermions [93, 94].

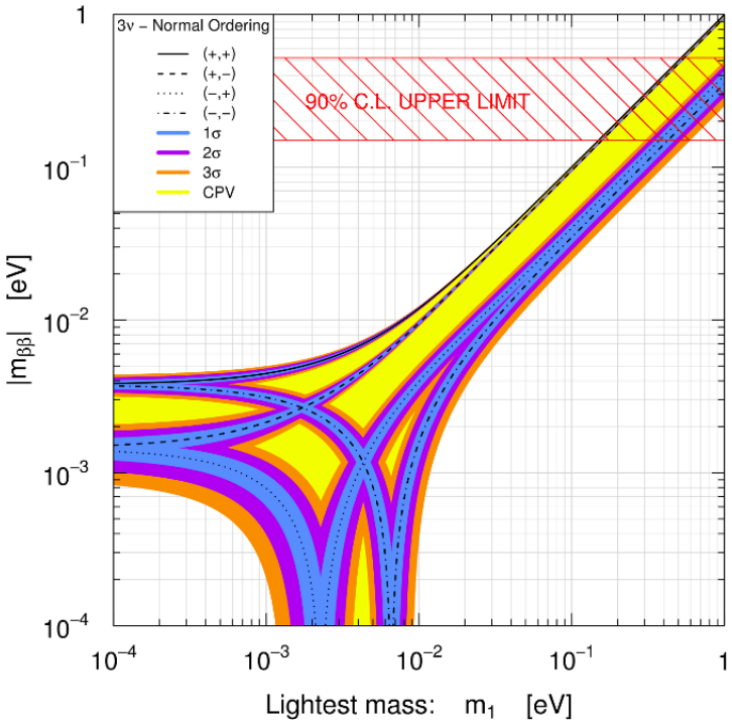

Figure 2.4.: Effective mass $|m_{\beta\beta}|$ as a function of the lightest neutrino mass for the NH case. The figure is taken from [91].

Without giving a preference to any model, we can ask what is the distribution probability for $|m_{\beta\beta}|$ given a fixed value of m_{min}. Moreover, we can ask which is the probability for the NH case of having $|m_{\beta\beta}| < 10^{-3}$ eV given the present knowledge (or ignorance) of the various parameters involved. An answer is obtained using a toy Monte Carlo (MC) approach, where a random number is sampled for each parameter according to its (un)known measured value, and $|m_{\beta\beta}|$ is computed for each trial.

The values for the experimentally measured parameters are taken from Tab. 3 of [75]. In case the upper and lower uncertainties on some parameter are different, the random sampling is performed using a Gaussian distribution with the mean given by the best fit of [75] and σ taken as the greater among the upper and lower uncertainties. These values are reported in Tab. 2.1. The effect of this conservative choice on the estimated allowed regions for $|m_{\beta\beta}|$ vs m_{min} is small, and the message of this study is not changed. Similarly, the use of a more recent and precise value for θ_{13} does not significantly affect the result.

The choice not to prefer any model is reflected on the distribution assigned to the Majorana phases. Assuming a complete ignorance on α and β, their values are sampled from a flat distribution in the $[0; 2\pi]$ range.

In order to keep the bi-logarithmic scale normally used in literature but with the aim of maintaining the same normalization over all the considered area, a two-dimensional histogram with increasing bin size is exploited. In particular, the bin width Δ_i is given by $\Delta_i = k\Delta_{i-1}$ with $k > 1$, for both the x and the y directions. For each bin of the x-axis, 10^6 random parameter combinations are used to calculate the probability distribution for $|m_{\beta\beta}|$, leading to the plot shown in Fig. 2.5. The different color levels correspond to the $1, 2, \ldots, 5\sigma$ coverage regions. The sensitivity of current experiments, at the 10^{-1} eV level, is reported, together with the

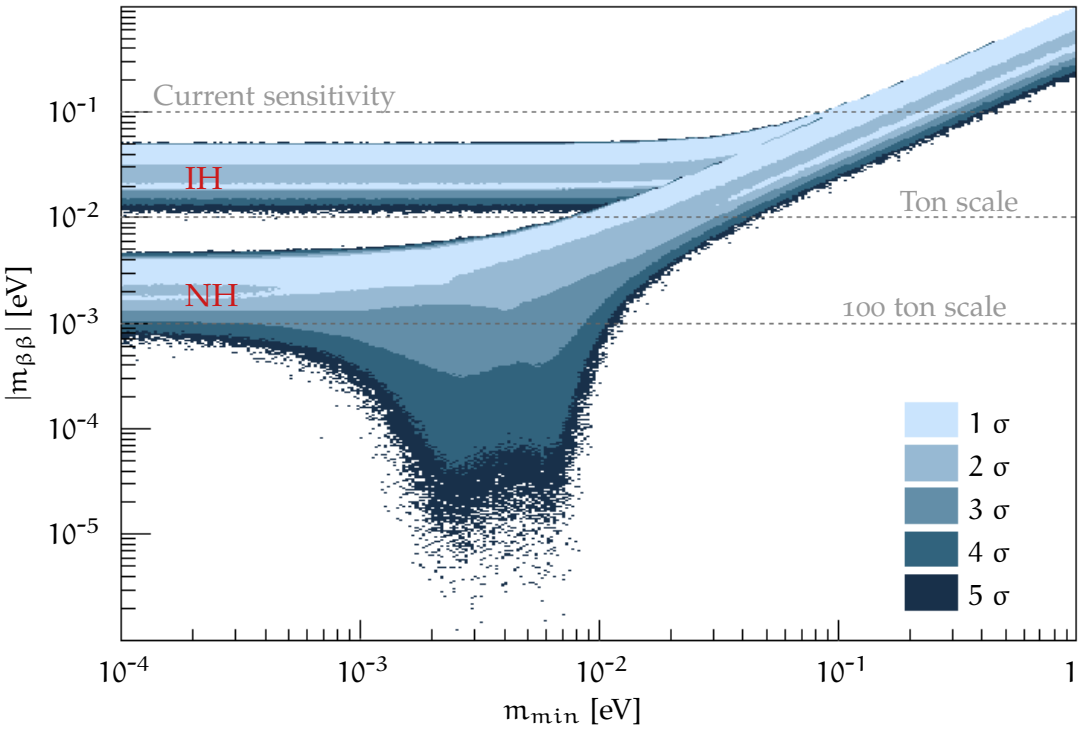

Figure 2.5.: Effective Majorana mass as a function of the lightest neutrino mass. The top band corresponds to the IH regime, the bottom to NH. The different colors correspond to the $1, \ldots, 5$ σ coverage regions.

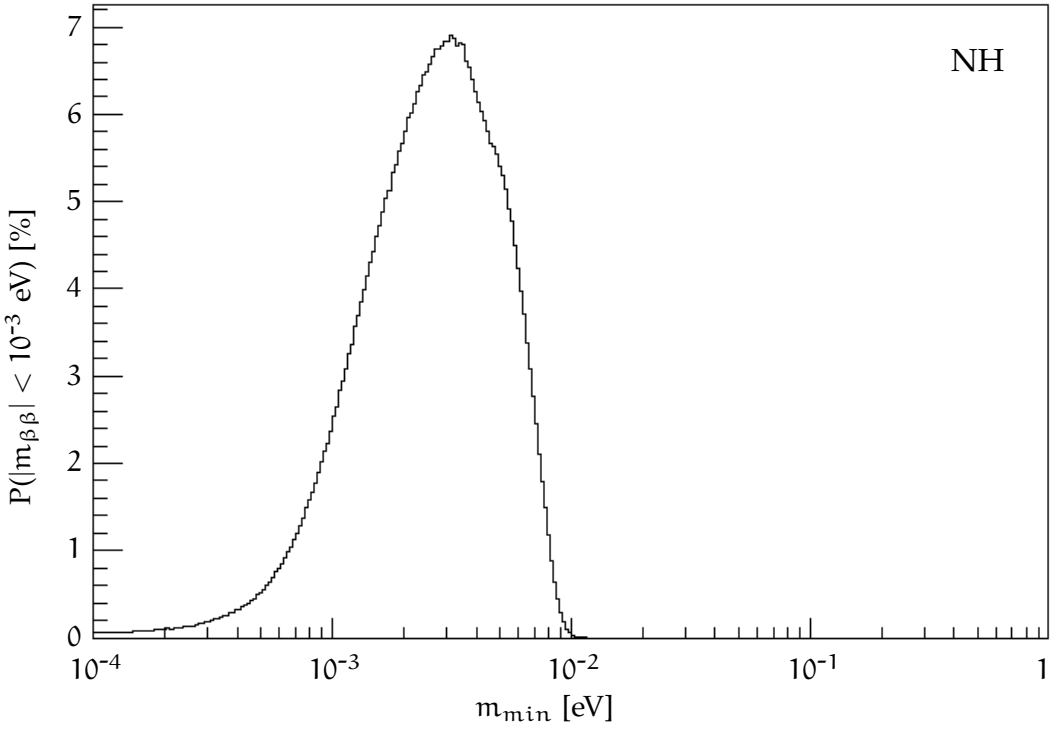

Figure 2.6.: Probability for $|m_{\beta\beta}| < 10^{-3}$ eV in the NH regime.

Table 2.1.: Parameters for the evaluation of the effective Majorana mass. The values are taken from [75].

Parameter	Value
δm^2_{sol}	$(7.54 \pm 0.26) \cdot 10^{-5}$ eV^2
Δm^2_{atm} (NH)	$(2.43 \pm 0.06) \cdot 10^{-3}$ eV^2
Δm^2_{atm} (IH)	$(2.38 \pm 0.06) \cdot 10^{-3}$ eV^2
s^2_{12}	$(3.08 \pm 0.17) \cdot 10^{-1}$
s^2_{13} (NH)	$(2.34 \pm 0.20) \cdot 10^{-2}$
s^2_{13} (NH)	$(2.40 \pm 0.22) \cdot 10^{-2}$

sensitivity of an hypothetical ton-scale experiment and the ultimate sensitivity of a 100 ton-scale setup with the assumption of zero background.

Looking at the $|m_{\beta\beta}|$ population for both the IH and NH, high values of $|m_{\beta\beta}|$ are favored for all values of m_{min}. This can have a strong impact on the perspectives of $0\nu\beta\beta$ decay search in the next decades. For the NH case, the probability of having $|m_{\beta\beta}| < 10^{-3}$ eV is reported in Fig. 2.6. Even for the most unfortunate case of $m_{min} \sim 3$–$4 \cdot 10^{-3}$ eV, given the present knowledge of the oscillation parameters, we have at least 93% probability of detecting a $0\nu\beta\beta$ decay signal if an experiment with 10^{-3} eV discovery sensitivity on $|m_{\beta\beta}|$ is available. Such a sensitivity would involve the realization of an experiment with $\sim$ 100 ton active mass operating in zero-background condition (see Sec. 2.5). If this is presently hard to imagine, some case studies are already published on the topic. On the other hand, an experiment with 10^{-5} eV sensitivity would most probably be out of reach because it would involve the deployment of $\gtrsim 10^6$ ton of active material.

One can ask which values of the Majorana phases are needed in order to obtain $|m_{\beta\beta}| < 10^{-3}$ eV. This is shown in Fig. 2.7: small values of the effective mass are only possible if α and β differ by a value $\sim \pi$. With reference to Eq. 2.25, neglecting for the moment the term $c^2_{12}c^2_{13}m_1$ and supposing all other terms have the same amplitude, $|m_{\beta\beta}|$ approaches zero only if both the pairs $(\sin\alpha, \sin\beta)$ and $(\cos\alpha, \cos\beta)$ have opposite signs. The condition is satisfied only if α and β belong to opposite quadrants. In the real case, the major difference is that $|m_{\beta\beta}|$ can become small for $m_{min} \in [10^{-3}; 10^{-2}]$ eV, instead of at zero, but the required correlation between the Majorana phases is unchanged. Hence, our result shows that in the type of models mentioned above [93, 94], the Majorana phases are closely correlated.

One remark has to be made regarding the sparsely populated region for $\alpha \in [\pi/2; 3\pi/2]$ and $\beta \sim \pi$ of Fig. 2.7. These points correspond to those in the region with $m_{min} < 10^{-3}$ eV and $|m_{\beta\beta}| < 10^{-3}$ eV of Fig. 2.5, or in other words to the bottom left part of the horizontal NH band. Hence, they can be considered a spurious contamination coming from the choice of selecting the events with $m_{min} < 10^{-3}$ eV.

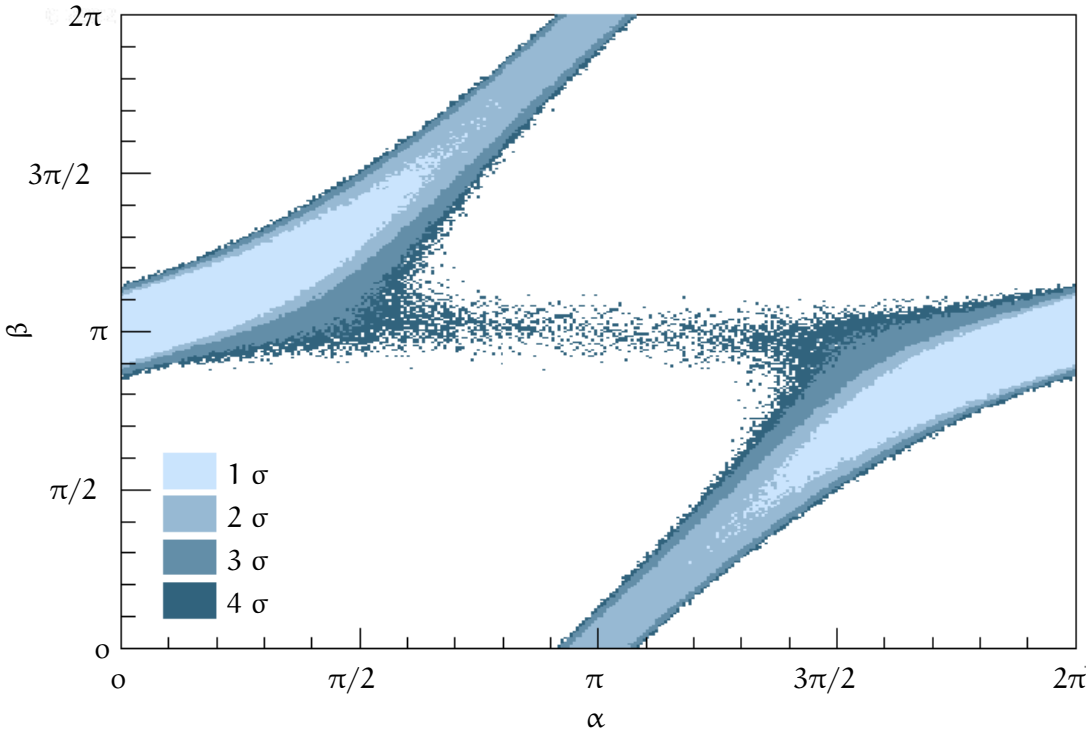

Figure 2.7.: Majorana phases α and β for $|m_{\beta\beta}| < 10^{-3}$ eV in the NH regime. The different colors correspond to the $1, \ldots, 4$ σ coverage regions.

2.4.1 *How Does Cosmology Affect $0\nu\beta\beta$ Decay Search?*

In the analysis presented so far the effective mass depends on the three free parameters: the mass of the lightest neutrino and the two Majorana phases. The latter are considered as nuisance parameters with uniform distribution, and the probability distribution for $|m_{\beta\beta}|$ as a function of m_{min} is obtained.

Several cosmological measurements put upper bounds on the sum of neutrino masses, Σ. These limits are typically around 0.1–0.2 eV, depending on the considered data sets. Recently, a combined analysis of the Planck 2013 data and several Lyman-α forest data sets lead to a Gaussian probability distribution with $\Sigma = (22 \pm 62) \cdot 10^{-3}$ eV [89, 90]. The corresponding 95% CL limit is $\Sigma < 0.146$ eV. The distribution was already used in [90] to extract the allowed range for $|m_{\beta\beta}|$ as a function of Σ. In that case, the allowed regions for NH and IH are weighted with the cosmological bound on Σ, and it is pointed out that the allowed region for IH is strongly reduced.

The study can be extended including the cosmological bound following a different approach than that used in [90]. Considering Eqs. 2.27, 2.28, and 2.29, the three parameters m_1, m_2 and m_3 depend on $\delta m^2_{\odot}$, Δm^2_{atm} and Σ, for all of which a measurement is available. Hence, a random sampling is performed on $\delta m^2_{\odot}$, Δm^2_{atm} and Σ, and the values of the mass eigenstates are extracted numerically after solving the system of Eqs. 2.27, 2.28 for NH, and 2.27, 2.28 for IH. If we con-

sider the NH case and given the measured values of the squared mass differences, Eq. 2.28 states that the minimum value of Σ is:

$$\Sigma_{min}^{NH} = \sqrt{\delta m^2_{\odot}} + \sqrt{\Delta m^2_{atm} + \frac{\delta m^2_{\odot}}{2}} \simeq 0.058 \text{ eV} \quad , \tag{2.30}$$

where m_{min} has been set to zero. Similarly, for NH:

$$\Sigma_{min}^{IH} = \sqrt{\Delta m^2_{atm} - \frac{\delta m^2_{\odot}}{2}} + \sqrt{\Delta m^2_{atm} + \frac{\delta m^2_{\odot}}{2}} \simeq 0.098 \text{ eV} \quad . \tag{2.31}$$

The combination of the cosmological bound with the measurements of $\delta m^2_{\odot}$ and Δm^2_{atm} will therefore induce a probability distribution for Σ with a sharp rise at about 0.058 (0.098) eV and a long high-energy tail for the NH (IH) regime.

The probability distributions for $|m_{\beta\beta}|$ as a function of Σ in the NH and IH cases are shown in Figs. 2.8 and 2.9, respectively. In total, 10^8 points are sampled. The thresholds on Σ correspond to the lower bounds mentioned above, while the shading for $\Sigma > 10^{-1}$ eV comes from the Gaussian distribution obtained from the cosmological data. In NH case, the vertical shading for $\Sigma \in [6;7] \cdot 10^{-2}$ eV and $|m_{\beta\beta}| < 10^{-3}$ eV is related to the combination of the Majorana phases, as explained in Sec. 2.4.

It is worth mentioning that the approach used here does not allow any statement regarding the overall probability of the NH with respect to the IH regime. The plots are populated by generating random numbers for $\delta m^2_{\odot}$, Δm^2_{atm} and Σ. If $\Sigma > \Sigma_{min}$, with Σ_{min} given by Eqs. 2.30 and 2.31, the three values are accepted and $|m_{\beta\beta}|$ is computed, otherwise another random number is extracted for Σ until the condition is satisfied. In this way, Figs. 2.8 and 2.9 are equally populated, and give no hint about the probability that nature chose either of the two regimes.

The plot of $|m_{\beta\beta}|$ as a function of m_{min} with the application of the cosmological bound is shown in Fig. 2.10. Differently from Fig. 2.5, it provides not only the probability distribution for $|m_{\beta\beta}|$ as a function of m_{min}, but also the 2-dimensional probability distribution for both the parameters together. The main difference with respect to Fig. 2.5 are the shadings for $m_{min} \in [5 \cdot 10^{-2}; 10^{-1}]$ eV, and for $m_{min} \lesssim 7 \cdot 10^{-3}$ eV. Both effects are due to the cosmological bound on Σ. Choosing arbitrarily different values for both the mean value and width for the Gaussian distribution of the total neutrino mass leads to different shadings on both sides, and induces the highly populated region around $m_{min} \sim 3 \cdot 10^{-2}$ eV to move. In particular, a looser bound on σ would favor the degenerate mass region, while a tighter limit would favor smaller values of m_{min}, as expected, with strong consequences for the expected $|m_{\beta\beta}|$. With the present assumptions, values of $|m_{\beta\beta}|$ close to the degenerate region are favored.

With an eye on the future experiments, the probability distribution for $|m_{\beta\beta}|$ can be obtained only by marginalizing the 2-dimensional distribution in Fig. 2.10 over m_{min}. This is performed separately for three ranges of the lightest neutrino mass: $m_{min} \in [10^{-4}; 10^{-3}]$ eV, $m_{min} \in [10^{-3}; 10^{-2}]$ eV and $m_{min} \in [10^{-2}; 10^{-1}]$ eV, as shown in Figs. 2.11, 2.12 and 2.13. In case of a small m_{min} (Fig. 2.11) the 90% coverage is obtained for $|m_{\beta\beta}| > 1.54 \cdot 10^{-3}$ eV and $|m_{\beta\beta}| > 1.96 \cdot 10^{-2}$ eV for NH and IH, respectively. In general, for IH high values of $|m_{\beta\beta}|$ are favored. The

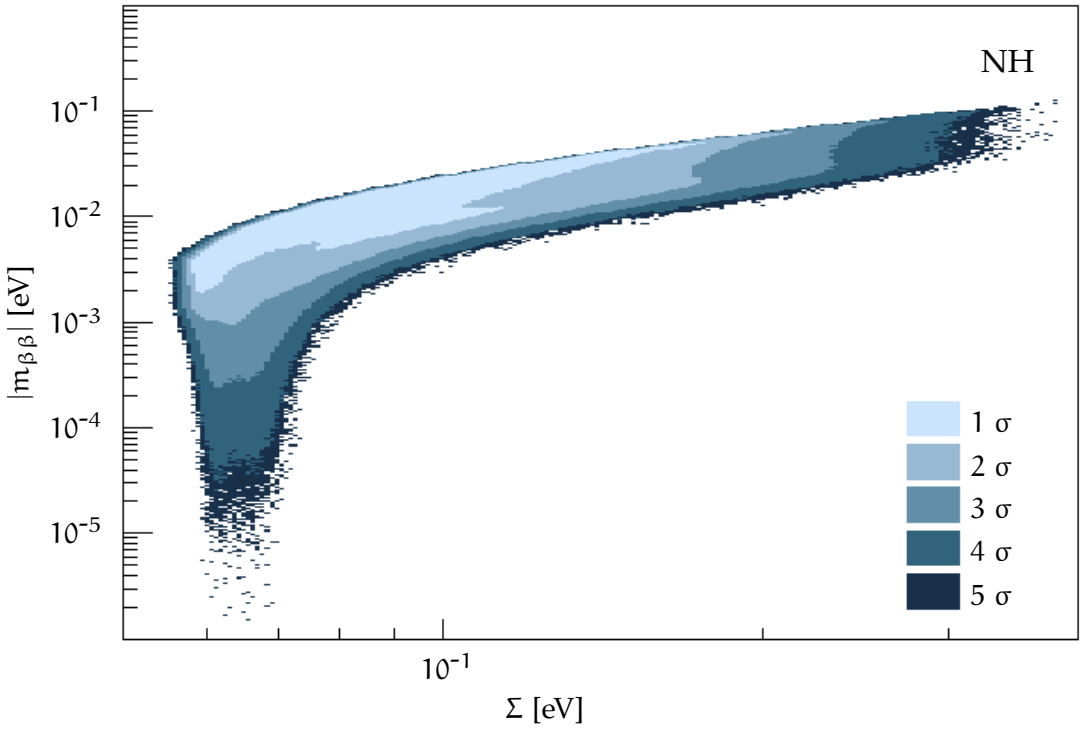

Figure 2.8.: Effective Majorana mass as a function of the sum of neutrino masses for the NH regime with the application of the cosmological bound. The different colors correspond to the $1, \ldots, 5$ σ coverage regions.

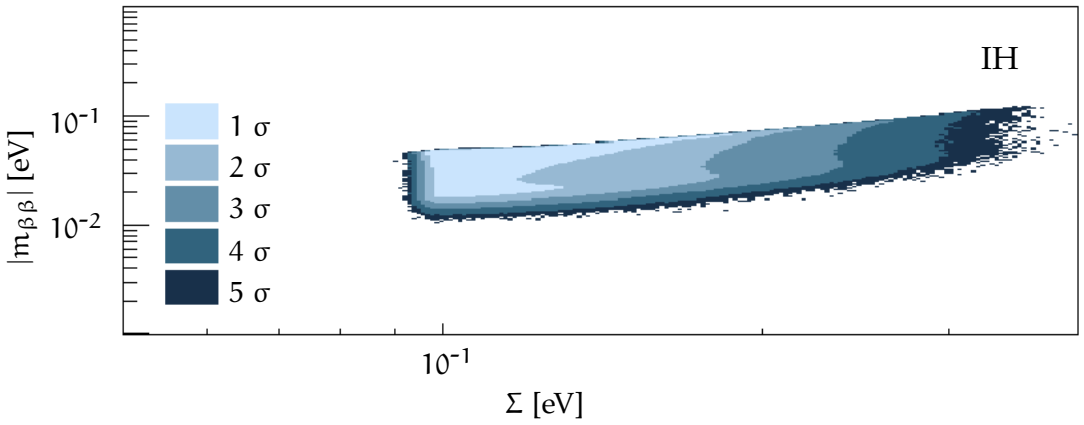

Figure 2.9.: Effective Majorana mass as a function of the sum of neutrino masses for the IH regime with the application of the cosmological bound. The different colors correspond to the $1, \ldots, 5$ σ coverage regions.

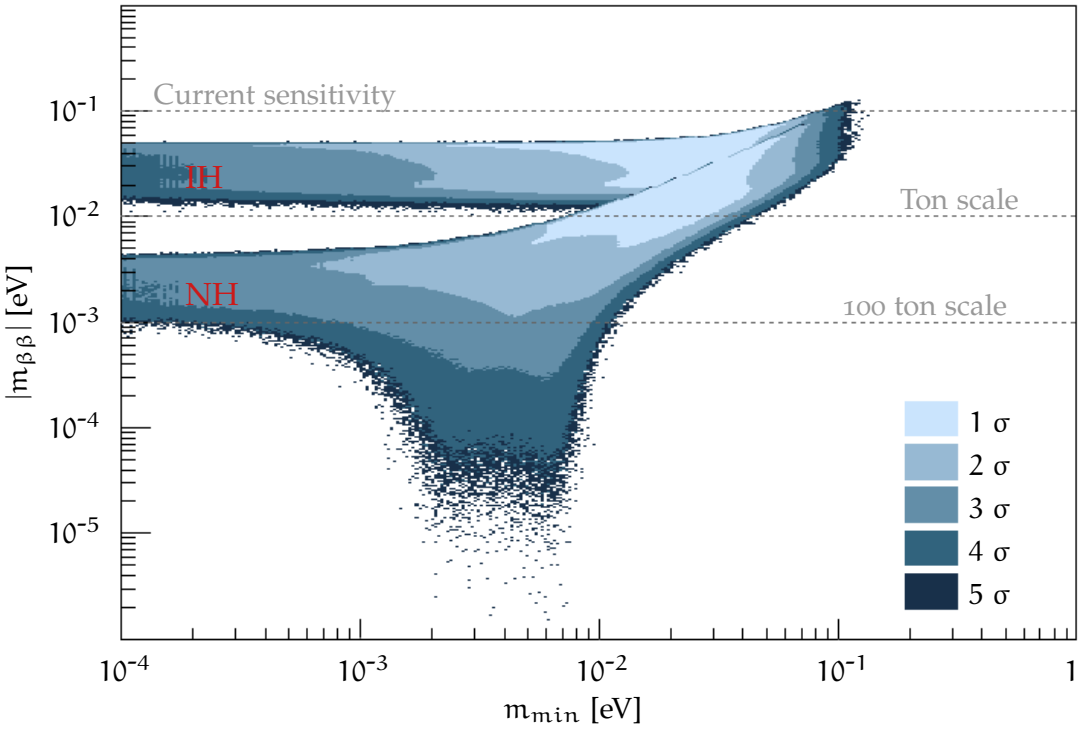

Figure 2.10.: Effective Majorana mass as a function of the lightest neutrino mass with the application of the cosmological bound. The different colors correspond to the $1, \ldots, 5$ σ coverage regions.

90% coverage on $|m_{\beta\beta}|$ for the three considered ranges are reported in Tab. 2.2, together with that of the overall range $m_{min} \in [10^{-4}; 1]$ eV. This case shows that a $3.32 \cdot 10^{-3}$ eV discovery sensitivity is required for future experiments in order to have 90% probability to measure a $0\nu\beta\beta$ decay signal in case of NH, and $2.14 \cdot 10^{-2}$ eV for IH.

The strong dependence of the result on both the choice of the Majorana phases distribution and on the cosmological bound should invoke some caution in the interpretation of Figs. 2.10–2.13 as the correct probability distributions for $|m_{\beta\beta}|$. It is rather important to highlight the fact that it is in principle possible, making some arbitrary assumption on the Majorana phases and provided a reliable cosmological limit on the total neutrino mass, to extract a probability distribution for $|m_{\beta\beta}|$. A

Table 2.2.: 90% coverage on $|m_{\beta\beta}|$ for NH and IH and different ranges of m_{min}.

	$\|m_{\beta\beta}\|$ 90% coverage [eV]	
m_{min} [eV]	NH	IH
$[10^{-4}, 10^{-3}]$	$> 1.54 \cdot 10^{-3}$	$> 1.96 \cdot 10^{-2}$
$[10^{-3}, 10^{-2}]$	$> 1.68 \cdot 10^{-3}$	$> 1.96 \cdot 10^{-2}$
$[10^{-2}, 10^{-1}]$	$> 7.16 \cdot 10^{-3}$	$> 2.20 \cdot 10^{-2}$
$[10^{-4}, 1]$	$> 3.32 \cdot 10^{-3}$	$> 2.14 \cdot 10^{-2}$

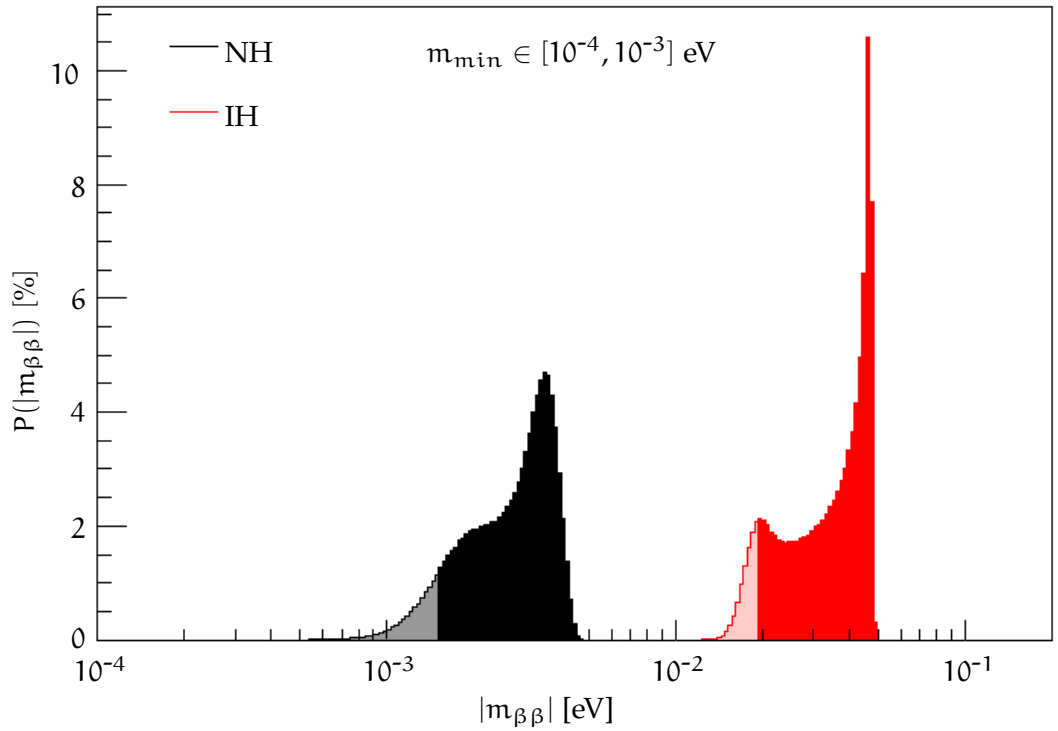

Figure 2.11.: Probability distribution for $|m_{\beta\beta}|$ with $m_{min} \in [10^{-4}, 10^{-3}]$ eV. The darker regions correspond to the 90% coverage on $|m_{\beta\beta}|$.

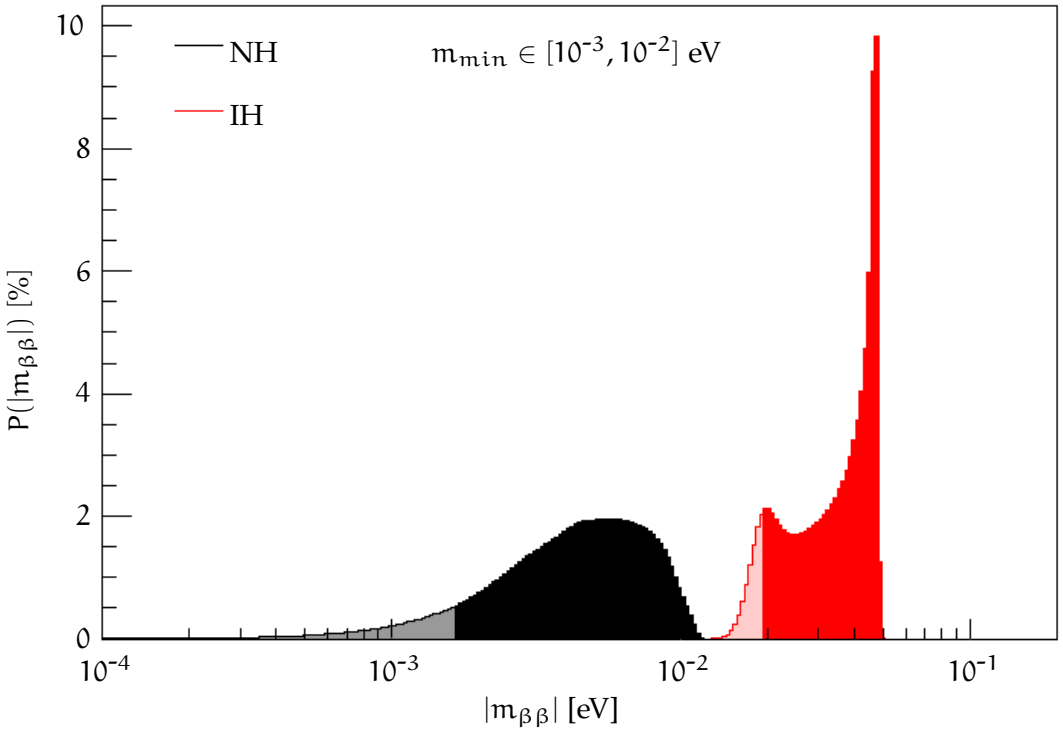

Figure 2.12.: Probability distribution for $|m_{\beta\beta}|$ with $m_{min} \in [10^{-3}, 10^{-2}]$ eV. The darker regions correspond to the 90% coverage on $|m_{\beta\beta}|$.

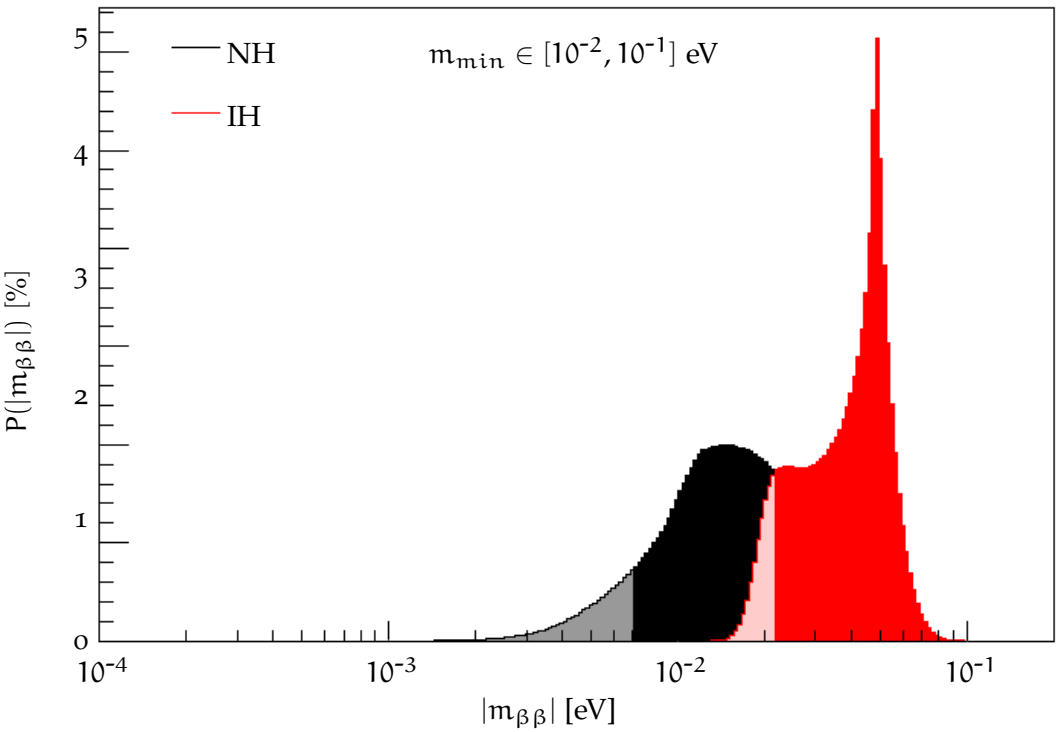

Figure 2.13.: Probability distribution for $|m_{\beta\beta}|$ with $m_{min} \in [10^{-2}, 10^{-1}]$ eV. The darker regions correspond to the 90% coverage on $|m_{\beta\beta}|$.

higher precision of the cosmological measurement, e.g. by EUCLID [95, 96], would strongly improve the reliability of a prediction on $|m_{\beta\beta}|$.

As a last step it is worth mentioning what is the required sensitivity on $T^{0\nu}_{1/2}$ in order to cover the IH or the NH region using ^{76}Ge, which is the $\beta\beta$ decaying isotope under investigation in the GERDA experiment. The probability distributions for $T^{0\nu}_{1/2}$ as a function of m_{min} with the application of the cosmological bound is shown in Fig. 2.14. The contour lines correspond to the $1, 2, \ldots, 5$ σ coverage regions. The distributions have been extracted from that of $|m_{\beta\beta}|$ with the application of Eq. 2.19. The values for the phase space integral are taken from [83], and the NME from [86], as reported in Tab. 2.3. Given the big span between different NME estimations, the largest and the smallest NME reported in [86] are used. These correspond to the blue and red distributions in Figs 2.14. The IH band for the optimal NME starts at $6\text{–}7 \cdot 10^{27}$ yr. Assuming IH and considering the worst case NME scenario, an experiment aiming to measure $0\nu\beta\beta$ decay needs a sensitivity on $T^{0\nu}_{1/2}$ of $\sim 4 \cdot 10^{28}$ yr. Assuming NH and an effective mass of 10^{-3} eV, a ^{76}Ge based experiment would need a sensitivity of $\sim 6 \cdot 10^{30}$ yr.

One remark can be made with respect to the debated Klapdor-Kleingrothaus claim of $0\nu\beta\beta$ decay observation in ^{76}Ge [97] (see Sec. 2.6). In Fig. 2.14 the 5 σ coverage region for the largest NME (blue curves) does not extend below 10^{26} yr. This is in very strong tension with the published 99.73% CL interval for the $0\nu\beta\beta$ decay half-life, $T^{0\nu}_{1/2} = (0.69 - 4.18) \cdot 10^{25}$ yr [97]. In other words, assuming that only the standard three light neutrinos participate to $0\nu\beta\beta$ decay and using the largest NME and an unquenched g_A, a > 5 σ disagreement is present between the cosmological bound and the Klapdor-Kleingrothaus claim.

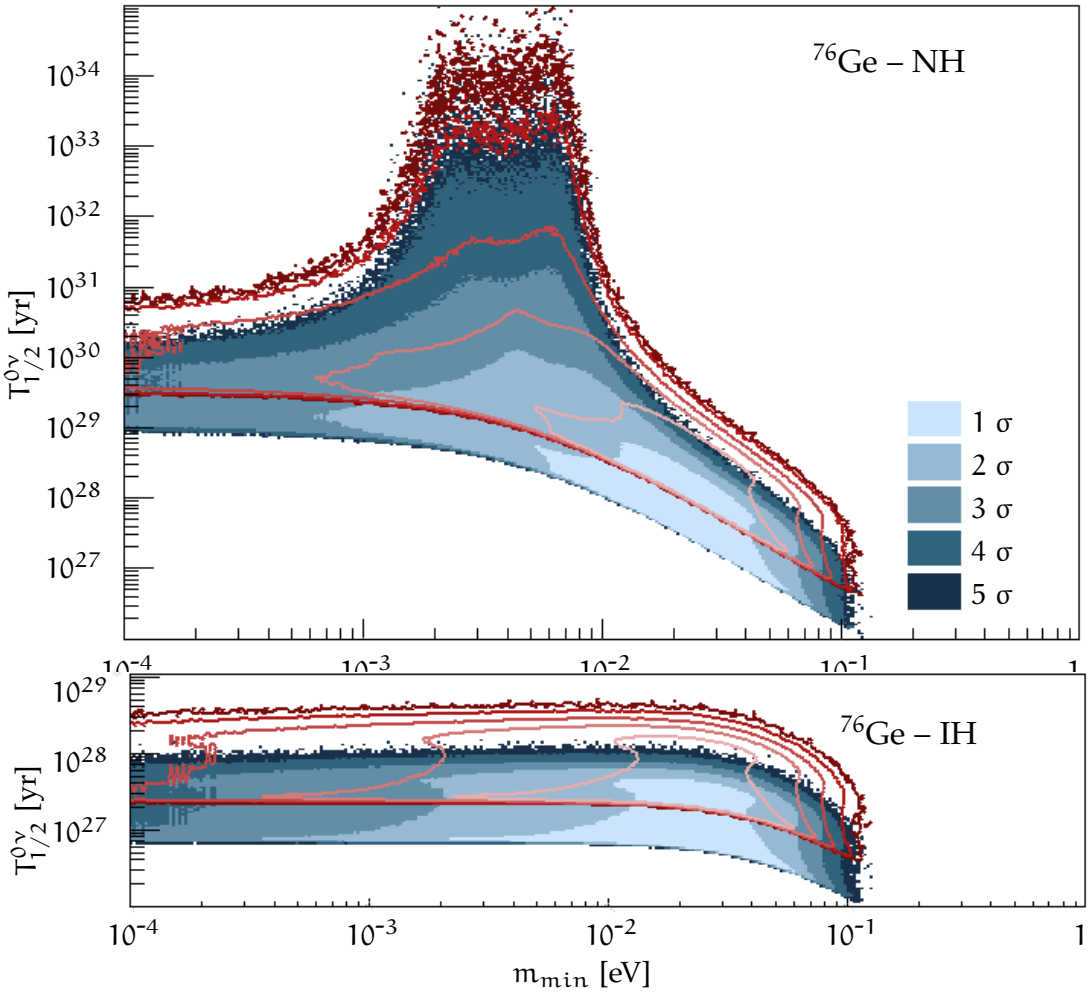

Figure 2.14.: $0\nu\beta\beta$ decay half-life for ^{76}Ge as a function of the lightest neutrino mass with the application of the cosmological bound. The blue regions are obtained with $|\mathcal{M}^{0\nu}| = 5.16$, the red curves with $|\mathcal{M}^{0\nu}| = 2.81$. The different color shadings correspond to the $1, \ldots, 5$ σ coverage regions.

All the information described in this section is available also in [1].

2.5 DOUBLE BETA DECAY SEARCH

The final state of $0\nu\beta\beta$ decay consists of the daughter nucleus and two emitted electrons. Given the $O(10^4)$ difference between the nucleus and the electron mass, the nuclear recoil can be safely neglected in all calculations. Hence, the two electrons share all the available energy, which is equal to the Q-value of the reaction ($Q_{\beta\beta}$). Most of the $\beta\beta$ emitting isotopes have a $Q_{\beta\beta}$ of $\sim$ 2–4 MeV. For high-Z elements, the range of an electron with $O(1)$ MeV kinetic energy is a few mm in liquid or solid, and some cm in gas. While gaseous detectors can distinguish the trajectories of the two emitted electrons, this is usually not possible for experiments based on liquid or solid targets. In this case the sum of the two electron energies is detected, and the $0\nu\beta\beta$ decay signature is a peak at $Q_{\beta\beta}$.

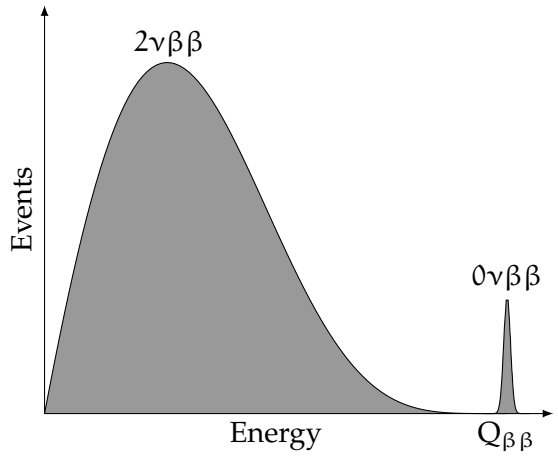

Figure 2.15.: Theoretical spectra for $2\nu\beta\beta$ and $0\nu\beta\beta$ decays with 1.5% energy resolution (FWHM), corresponding to a factor 10 worse than what is achievable with germanium detectors. The relative normalization of the two is for illustrative purpose only.

In the case of $2\nu\beta\beta$ decay the final state consists of two electrons and two antineutrinos. The summed electrons energy is therefore a continuum ranging from zero to $Q_{\beta\beta}$, described by [98]:

$$F(E) = \left(E^4 + 10E^3 + 40E^2 + 60E + 30\right) \cdot E \cdot (Q_{\beta\beta} - E)^5 \quad . \tag{2.32}$$

The experimental signatures of $0\nu\beta\beta$ and $2\nu\beta\beta$ decays are shown in Fig. 2.15.

In order to maximize the detection efficiency and the sensitivity to a potential $0\nu\beta\beta$ decay signal, the detectors are typically built with material containing the $\beta\beta$ emitting isotope. For some isotopes an enrichment is possible, leading to an increase of one order of magnitude in the fraction of the considered isotope.

The number of decays n_d taking place during a measurement time t is:

$$n_d = N_0 \left(1 - \exp\left(-\frac{\ln 2}{T^{0\nu}_{1/2}} t\right)\right) \simeq N_0 \frac{\ln 2}{T^{0\nu}_{1/2}} t \quad , \tag{2.33}$$

where N_0 is the initial number of $0\nu\beta\beta$ decay emitting isotopes. The exponential has been expanded in Taylor series due to the very small ratio $t/T^{0\nu}_{1/2} < 10^{-20}$.

The initial number of isotopes in a given mass m of material with enrichment fraction f_{enr} is:

$$N_0 = \frac{N_A}{m_a} f_{enr} m \quad , \tag{2.34}$$

where N_A is the Avogadro number and m_a is the atomic mass of the considered isotope. The number of detected signal events n_s depends on the active volume fraction of the detector, f_{AV}, and on the total detection efficiency ε:

$$n_s = n_d \cdot f_{AV} \cdot \varepsilon = \frac{1}{T^{0\nu}_{1/2}} \frac{N_A \ln 2}{m_a} f_{enr} \cdot f_{AV} \cdot \varepsilon \cdot mt \quad . \tag{2.35}$$

Hence, a higher number of signal events is obtained by maximizing the exposure mt, the enrichment and active volume fraction, and the total efficiency, which includes the detection efficiency for $0\nu\beta\beta$ decay events and that of the event selection algorithms.

Typically the $0\nu\beta\beta$ decay search is performed by counting the events or fitting the energy spectrum in a region of interest (ROI) of width ΔE around $Q_{\beta\beta}$. The

cosmic radiation and radioactive contamination of the experimental setup can induce a number of background events n_b in the ROI. n_b is proportional to ΔE and to the exposure, and can be written as:

$$n_b = BI \cdot \Delta E \cdot mt \quad , \tag{2.36}$$

where BI, the background index, represents the average background level in the ROI, expressed in counts/(keV·kg·yr).

In order to maximize the sensitivity, the BI has to be minimized. One possibility is to apply pulse shape discrimination (PSD). Neglecting the bremsstrahlung, $0\nu\beta\beta$ decay like events release energy in a limited fraction of the detector volume, and are denoted as single site events (SSE). On the other hand, γ's can undergo multiple Compton scattering within the detector volume, inducing a multi site event (MSE). For several detector technologies an event selection is possible thanks to the different properties of the signal traces recorded for SSE and MSE. If PSD is applied, the number of signal and background events will be modified into:

$$\begin{aligned} n_s &\to \varepsilon_{psd}^{SSE} n_s \quad , \\ n_b &\to \varepsilon_{psd}^{MSE} n_b \quad , \end{aligned} \tag{2.37}$$

where ε_{psd}^{SSE} and ε_{psd}^{MSE} are the survival probabilities of SSE and MSE events, respectively.

Another ingredient in the improvement of sensitivity is energy resolution. With no loss of generality, we can consider a Gaussian distribution for the potential $0\nu\beta\beta$ decay signal, and a flat background distribution around $Q_{\beta\beta}$. Both in case of events counting or spectral fitting, the choice of ΔE depends on the width of the expected signal distribution. This is normally quantified as the full width at half maximum (FWHM) of the Gaussian distribution. A higher energy resolution allows the ROI width ΔE to be reduced, increasing the signal to background ratio.

To summarize, the number of signal and background events in the ROI is:

$$\begin{aligned} n_s &= \frac{1}{T_{1/2}^{0\nu}} \frac{N_A \ln 2}{m_a} f_{enr} \cdot f_{AV} \cdot \varepsilon_\gamma \cdot \varepsilon_{psd}^{SSE} \cdot mt \quad , \\ n_b &= BI \cdot \Delta E \cdot mt \quad , \end{aligned} \tag{2.38}$$

where ε_γ is the detection efficiency of $0\nu\beta\beta$ decay events, and where the substitution $\varepsilon_{psd}^{MSE} BI \to BI$ has been applied for simplicity.

A possible expression of the sensitivity on $T_{1/2}^{0\nu}$ is obtained computing the half-life required to collect a number of signal events equal to the uncertainty on the number of background events. Given the Poisson distribution of n_b, we can set $n_s = \sqrt{n_b}$:

$$\frac{1}{T_{1/2}^{0\nu}} \frac{N_A \ln 2}{m_a} f_{enr} \cdot f_{AV} \cdot \varepsilon_\gamma \cdot \varepsilon_{psd}^{SSE} \cdot mt = \sqrt{BI \cdot \Delta E \cdot mt} \quad . \tag{2.39}$$

Hence:

$$T_{1/2}^{0\nu} = \frac{N_A \ln 2}{m_a} f_{enr} \cdot f_{AV} \cdot \varepsilon_\gamma \cdot \varepsilon_{psd}^{SSE} \sqrt{\frac{mt}{BI \cdot \Delta E}} \quad . \tag{2.40}$$

Typically, $0\nu\beta\beta$ decay experiments are operated in quasi background-free mode: the measurements are planned to last until the sensitivity curves becomes background dominated. At this point a new experiment with higher mass and lower background should then be started. It is worth mentioning how the $T^{0\nu}_{1/2}$ sensitivity is proportional to the square root of the exposure divided by the BI. Furthermore, the sensitivity on $|m_{\beta\beta}|$ is proportional to $1/\sqrt{T^{0\nu}_{1/2}}$. Therefore, a good improvement in sensitivity is achievable only in correspondence of both a mass increase and a background reduction.

2.5.1 *State of the Art in Double Beta Decay Search*

The presence of several parameters connected to the isotope and detector properties in Eqs. 2.38 allows a great field of play for $0\nu\beta\beta$ decay search. A list of the most commonly investigated isotopes is reported in Tab. 2.3. The most important criteria for the isotope choice are listed below.

- Natural abundance, possibility of enrichment at (relatively) limited cost, and good availability on the market. On this perspective, ^{76}Ge and ^{136}Xe are the favorite, given their established enrichment techniques, while ^{130}Te has already a high enough natural abundance (34%).
- A $Q_{\beta\beta}$ higher than the end-point of environmental radioactivity background is desirable. In most cases, the typical radioactive contaminants do not emit γ's above the 2615 keV line of ^{208}Tl, and the background spectrum drops by at least one order of magnitude above this energy. In this sense, ^{48}Ca, ^{82}Se, ^{96}Zr, ^{100}Mo, ^{226}Cd and ^{150}Nd are preferable. A major disadvantage of ^{48}Ca is given by the very low abundance ($\sim 0.2\%$), which makes its use very hard.
- Value of the product $G^{0\nu}|M^{0\nu}|^2$. In the worst cases (^{76}Ge, ^{48}Ca) this is $\sim 5 \cdot 10^{-14}$ yr^{-1}, while for ^{100}Mo and ^{150}Nd if goes up to $\sim 4 \cdot 10^{-13}$ yr^{-1}.
- Possibility to obtain a detector out of the isotope undergoing $\beta\beta$ decay. This is the case, e.g., of ^{76}Ge enriched diodes, TeO_2 bolometers, liquid- or high-pressure-Xe time projection chambers, and Xe-loaded liquid scintillators. The reason why the use of coinciding detector and source is pursued is because this maximizes the efficiency of $\beta\beta$ decay events detection.
- Cost and scalability of the technology to large source mass.

The choice of the isotope is strictly connected to that of the detector technology. Also in this case several criteria are followed:

- Energy resolution. This can vary from a FWHM at $Q_{\beta\beta}$ of $\sim 0.15\%$ for the newest germanium detectors, to about 15% for xenon-loaded liquid scintillators.
- Intrinsic radio-purity of the detector material. Thanks to the big effort made in the past decades, the intrinsic radioactive contamination of the detector induces a much smaller background than the surrounding material. Hence, a high detector radio-purity can be considered rather a necessary condition than an additional feature.
- Possibility of self-shielding from external background. For example, this is possible for germanium diodes thanks to the presence of a ~ 0.7 mm thick dead layer in a big fraction of the crystal surface: if an α is emitted at the

detector surface, it will be absorbed in the dead layer without inducing a signal. Similarly, the selection of a central active volume is possible with time projection chambers and liquid scintillator experiments.
- Total efficiency. The optimal value is $\sim$ 75% obtainable with germanium diodes.
- Scalability of the technology. From this perspective, a time projection chamber or a liquid scintillator experiment are preferable to a modular experiment (e.g. using germanium diodes or bolometers), however at the price of a poorer energy resolution.
- Particle identification. The capability of distinguishing between electrons and α's or γ's is a very powerful tool for background minimization. The best performances are obtained with gaseous detectors, with the disadvantage of a harder scalability due to the need of a greater volume. A partial identification is possible also with other technologies, e.g. with germanium detectors. It is anyway worth mentioning that, in case a $0\nu\beta\beta$ decay signal evidence is claimed, a clear confirmation can only come from an experiment capable of measuring the separate tracks of the two electrons.

All in all no ideal isotope and detector exist. The choice depends on which weight is assigned to each of the mentioned criteria and on the economical resources available. Thanks to the features mentioned above, of the most promising isotopes is ^{76}Ge.

2.6 DOUBLE BETA DECAY SEARCH IN ^{76}GE

^{76}Ge is being used for $0\nu\beta\beta$ decay search since half century for the several reasons. Firstly, an established detector technology is available, yielding the best energy resolution among all particle detectors, which can reach 0.15% FWHM. Secondly, germanium can be enriched at relatively low cost to $\sim$ 86% in ^{76}Ge, and germanium crystals have a very low intrinsic contamination [124]. Third, germanium detectors provide a high total efficiency, with $\varepsilon_{AV} \cdot \varepsilon_{\gamma} \sim 0.8$. Finally, for some detector types the discrimination between signal-like events releasing energy in only a small fraction of the detector volume is distinguishable from γ events undergoing multiple Compton scattering, or surface events.

Exploiting the availability of detectors with $\sim$ 2 kg mass and $\sim$ 0.2-0.3% energy resolution, a first attempt was performed in 1967 by a research group of the Milano University, leading to a 68% CL limit of $3 \cdot 10^{20}$ yr on the $0\nu\beta\beta$ decay half-life. A chronology of the limits on $T^{0\nu}_{1/2}$ is reported Tab. 2.4, and shown in Fig. 2.16. After the 1967 measurement, a strong boost in sensitivity was achieved in 1970 by the operation of the experiment in an underground laboratory, under 70 meter of water equivalent (mwe) [125]. Another major improvement was the introduction by the Russian collaboration ITEP/YePI of germanium crystals enriched to $\sim$ 85% in ^{76}Ge [126]. Thanks to this, the Heidelberg-Moskow (HdM) and the IGEX experiment operated for about a decade 5 and 3 enriched detectors, respectively.

After setting a limit of $T^{0\nu}_{1/2} > 1.9 \cdot 10^{25}$ yr [127], in 2001 H. V. Klapdor-Kleingrothaus and part of the HdM collaboration claimed the evidence for $0\nu\beta\beta$ decay [128], with a measured half-life of $\left(1.5^{+1.6}_{-0.5}\right) \cdot 10^{25}$ yr, in tension with

Table 2.3.: Isotopic abundances [99], Q-values, phase space integrals, NMEs for light neutrino exchange, $2\nu\beta\beta$ average half-lives and most recent limits on $0\nu\beta\beta$ half-lives for the most studied $\beta\beta$ isotopes. For ^{130}Te and ^{136}Xe, no clear agreement is present on the Q-value, hence all the available measurements are reported. The phase space integrals are taken from [83]. The different NMEs correspond to the extreme values reported in Tab. II of [86]; for ^{150}Nd only one value is available. For ^{82}Se, ^{100}Mo, ^{116}Cd and ^{136}Xe the average values among the most precise $2\nu\beta\beta$ half-life measurements are given.

Isotope	Isotopic Abundance [%]	$Q_{\beta\beta}$ [keV]	$G^{0\nu}$ [10^{-15} yr^{-1}]	$\lvert M^{0\nu}\rvert$	Experimental $T^{2\nu}_{1/2}$ [yr]	Lower limit on $T^{0\nu}_{1/2}$ [yr]
^{76}Ge	7.73(12)	2039.006(50) [100]	2.363	2.81-5.16	$(1.926 \pm 0.095) \cdot 10^{21}$ [101]	$2.1 \cdot 10^{25}$ (90% C.L.) [102]
^{48}Ca	0.187(21)	4267.98(32) [103]	24.81	0.54-1.75	$(4.4^{+0.5}_{-0.4} \pm 0.4) \cdot 10^{19}$ [104]	$1.3 \cdot 10^{22}$ (90% C.L.) [104]
^{82}Se	8.73(22)	2997.9(3) [105]	10.16	2.64-4.64	$(0.92 \pm 0.07) \cdot 10^{20}$ [106]	$3.6 \cdot 10^{23}$ (90% C.L.) [104]
^{96}Zr	2.80(9)	3355.85(15) [107]	20.58	2.72-2.83	$(2.35 \pm 0.14 \pm 0.16) \cdot 10^{19}$ [108]	$9.2 \cdot 10^{21}$ (90% C.L.) [104]
^{100}Mo	9.82(31)	3034.40(17) [109]	15.92	4.22-5.40	$(7.12 \pm 0.44) \cdot 10^{18}$ [110, 111]	$1.1 \cdot 10^{24}$ (90% C.L.) [112]
^{116}Cd	7.49(18)	2813.50(30) [113]	16.70	3.10-4.04	$(2.87 \pm 0.13) \cdot 10^{19}$ [106]	$1.6 \cdot 10^{22}$ (90% C.L.) [104]
^{130}Te	34.08(62)	2527.518(13) [114]	14.22	2.65-3.89	$(7.0 \pm 0.9 \pm 1.1) \cdot 10^{20}$ [115]	$4.0 \cdot 10^{24}$ (90% C.L.) [116]
		2526.97(23) [113]				
		2527.01(32) [117]				
^{136}Xe	8.85673(44)	2458.7(6) [118]	14.58	2.18-3.05	$(2.19 \pm 0.06) \cdot 10^{21}$ [119, 120]	$1.9 \cdot 10^{25}$ (90% C.L.) [121]
		2457.83(37) [122]				
^{150}Nd	5.638(28)	3371.38(20) [123]	63.03	2.67	$(9.11^{+0.25}_{-0.22} \pm 0.63) \cdot 10^{18}$ [104]	$1.8 \cdot 10^{22}$ (90% C.L.) [104]

the previously published limit. A second confirmation of the claim was published in 2004, with $T^{0\nu}_{1/2} = \left(1.19^{+0.37}_{-0.23}\right) \cdot 10^{25}$ yr [129, 130], and in 2006 with $T^{0\nu}_{1/2} = \left(2.23^{+0.44}_{-0.31}\right) \cdot 10^{25}$ yr [131]. Strong criticism resulted from the 2004 claim [132], based on the fact that the fit result is strongly dependent on the fit range and that the origin of one "peak" with the same size of the $0\nu\beta\beta$ decay peak is not explained. Regarding the 2006 claim, it was pointed out that the quoted uncertainty on the number of signal counts is smaller than that expected from Poisson statistics, and that the pulse shape discrimination efficiency is dropped from Eq. 2.38 [133]. If these effects are taken into account, a half-life similar to the one published in 2004 is obtained, and the significance of the signal is reduced.

In 2013 a new limit of $T^{0\nu}_{1/2} > 2.1 \cdot 10^{25}$ yr (90% CL) was published by the GERDA experiment [102]. A further increase by one order of magnitude in sensitivity to $T^{0\nu}_{1/2}$ is expected by GERDA Phase II, which is currently under commissioning.

Table 2.4.: Chronology of limits on $T^{0\nu}_{1/2}$ for ^{76}Ge. The claims from part of the HdM collaboration are denoted as HdM-KK.

Experiment	Date	$T^{0\nu}_{1/2}$
Milano	1967	$> 3.1 \cdot 10^{20}$ yr (68% CL) [134]
Milano	1970	$> 1.2 \cdot 10^{21}$ yr (68% CL) [125]
Milano	1973	$> 5 \cdot 10^{21}$ yr (68% CL) [135]
PNL-USC	1983	$> 1.7 \cdot 10^{22}$ yr (90% CL) [136]
Caltech	1984	$> 1.7 \cdot 10^{22}$ yr (68% CL) [137]
GDK	1984	$> 3.2 \cdot 10^{22}$ yr (68% CL) [138]
Milano	1984	$> 5 \cdot 10^{22}$ yr (68% CL) [139]
Milano	1984	$> 1.2 \cdot 10^{23}$ yr (68% CL) [140]
PNL-USC	1985	$> 7.0 \cdot 10^{22}$ yr (68% CL) [141]
PNL-USC	1985	$> 1.16 \cdot 10^{23}$ yr (68% CL) [142]
Milano	1986	$> 1.65 \cdot 10^{23}$ yr (68% CL) [143]
Gotthard	1989	$> 2.7 \cdot 10^{23}$ yr (68% CL) [144]
ITEP/YePI	1990	$> 1.3 \cdot 10^{24}$ yr (68% CL) [126]
Gotthard	1992	$> 6.0 \cdot 10^{23}$ yr (68% CL) [145]
HdM	1992	$> 1.4 \cdot 10^{24}$ yr (90% CL) [146]
HdM	1995	$> 5.6 \cdot 10^{24}$ yr (90% CL) [147]
IGEX	1996	$> 4.2 \cdot 10^{24}$ yr (90% CL) [148]
HdM	1997	$> 7.4 \cdot 10^{24}$ yr (90% CL) [149]
IGEX	1999	$> 8 \cdot 10^{24}$ yr (90% CL) [150]
IGEX	2000	$> 1.57 \cdot 10^{25}$ yr (90% CL) [151]
HdM	2001	$> 1.9 \cdot 10^{25}$ yr (90% CL) [127]
HdM-KK	2001	$\left(1.5^{+1.6}_{-0.5}\right) \cdot 10^{25}$ yr [128]
IGEX	2003	$> 1.6 \cdot 10^{25}$ yr (90% CL) [152]
HdM-KK	2004	$\left(1.19^{+0.37}_{-0.23}\right) \cdot 10^{25}$ yr [129, 130]
HdM-B	2005	$> 1.55 \cdot 10^{25}$ yr (90% CL) [153]
HdM-KK	2006	$\left(2.23^{+0.44}_{-0.31}\right) \cdot 10^{25}$ yr [131]
GERDA	2013	$> 2.1 \cdot 10^{25}$ yr (90% CL) [102]

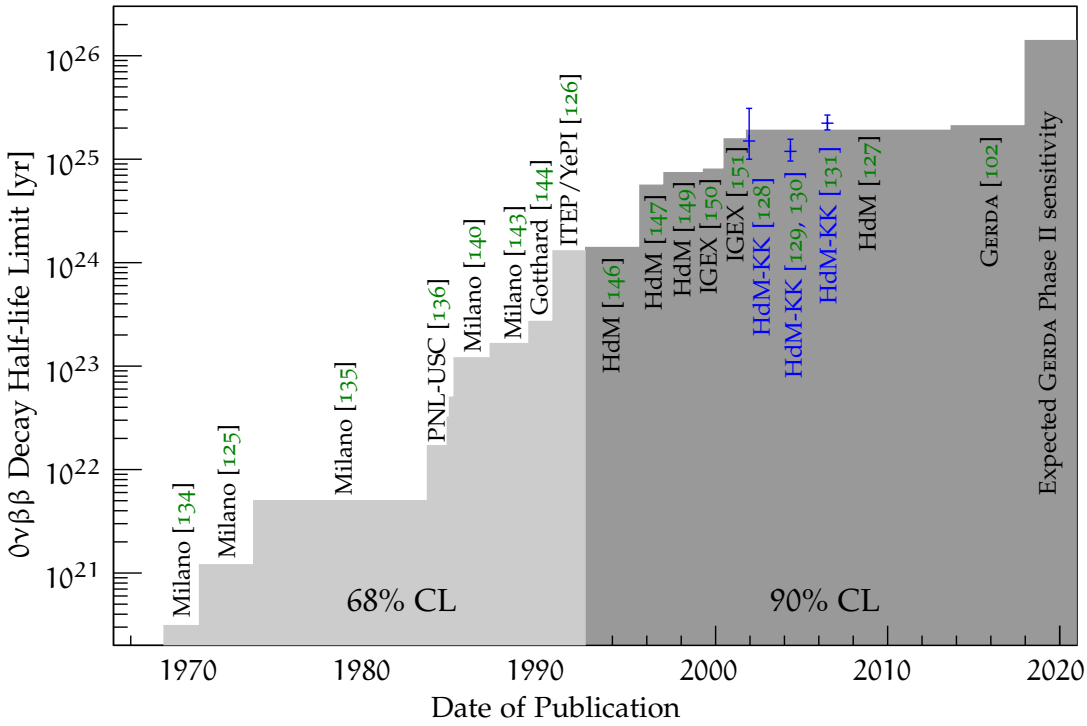

Figure 2.16.: Chronology of the strongest limits on $0\nu\beta\beta$ half-life for ^{76}Ge. Values taken from Tab. 2.4. The limits up to 1992 correspond to 68% CL, the more recent ones to 90% CL. The three HdM-KK claims are shown with blue error bars.

2.6.1 $2\nu\beta\beta$ *Decay Search in* ^{76}*Ge*

Along with $0\nu\beta\beta$ decay, the detection of $2\nu\beta\beta$ decay and the measurement of its half-life have been pursued from the beginning of $\beta\beta$ search. The major difficulty in the detection of $2\nu\beta\beta$ decay is the signal to background ratio: the continuum shape of $2\nu\beta\beta$ decay spectrum requires the background minimization in the whole range from 0 keV to $Q_{\beta\beta}$.

The chronology of $T^{2\nu}_{1/2}$ measurements is reported in Tab. 2.5 and depicted in Fig. 2.5. After the publication of some limits [143, 144], two measurements of $T^{2\nu}_{1/2}$ were performed in 1990 independently by the ITEP/YePI and the PNL-USC collaborations, with $T^{2\nu}_{1/2} \sim 10^{21}$ yr [126, 154]. These were then followed by about a dozen publications, until the most recent one reported by GERDA and based on the Phase I data, with $T^{2\nu}_{1/2} = (1.926 \pm 0.095) \cdot 10^{21}$ yr [155]. This value is a factor two higher than the first ones [143, 144]. The reason for this difference can be understood looking at Fig. 2.5: the value of $T^{2\nu}_{1/2}$ steadily increases with the publication year towards $2 \cdot 10^{21}$ yr. This trend is due to the improvement of the signal to background ratio, which reached in GERDA the unpreceeded value of 4 : 1 in the 600-1800 keV range [155].

Table 2.5.: Chronology of $T^{2\nu}_{1/2}$ limits and measurements for ^{76}Ge.

Experiment	Date	$T^{2\nu}_{1/2}$
Milano	1986	$> 2.2 \cdot 10^{19}$ yr (68% CL) [143]
Gotthard	1989	$> 1.2 \cdot 10^{20}$ yr (68% CL) [144]
ITEP/YePi	1990	$(9 \pm 1) \cdot 10^{20}$ yr [126]
PNL-USC	1990	$\left(1.1^{+0.6}_{-0.3}\right) \cdot 10^{21}$ yr (2σ) [154]
PNL-USC	1991	$\left(9.2^{+0.7}_{-0.4}\right) \cdot 10^{20}$ yr (2σ) [156]
PNL-USC	1994	$\left(1.2^{+0.2}_{-0.1}\right) \cdot 10^{21}$ yr [157]
HdM	1994	$\left(1.42 \pm 0.03 \pm 0.13\right) \cdot 10^{21}$ yr [158]
IGEX	1996	$(1.1 \pm 0.2) \cdot 10^{21}$ yr [148]
HdM	1997	$\left(1.77 \pm 0.01^{+0.13}_{-0.11}\right) \cdot 10^{21}$ yr [149]
IGEX	1999	$\left(1.45 \pm 0.30\right) \cdot 10^{21}$ yr [159]
HdM	2001	$\left(1.55 + -0.01^{+0.19}_{-0.15}\right) \cdot 10^{21}$ yr [127]
HdM-KK	2003	$\left(1.74 \pm 0.01^{+0.18}_{-0.16}\right) \cdot 10^{21}$ yr [160]
HdM-B	2005	$\left(1.78 \pm 0.01^{+0.07}_{-0.09}\right) \cdot 10^{21}$ yr [153]
GERDA	2013	$\left(1.84^{+0.14}_{-0.10}\right) \cdot 10^{21}$ yr [161]
GERDA	2015	$(1.926 \pm 0.095) \cdot 10^{21}$ yr [155]

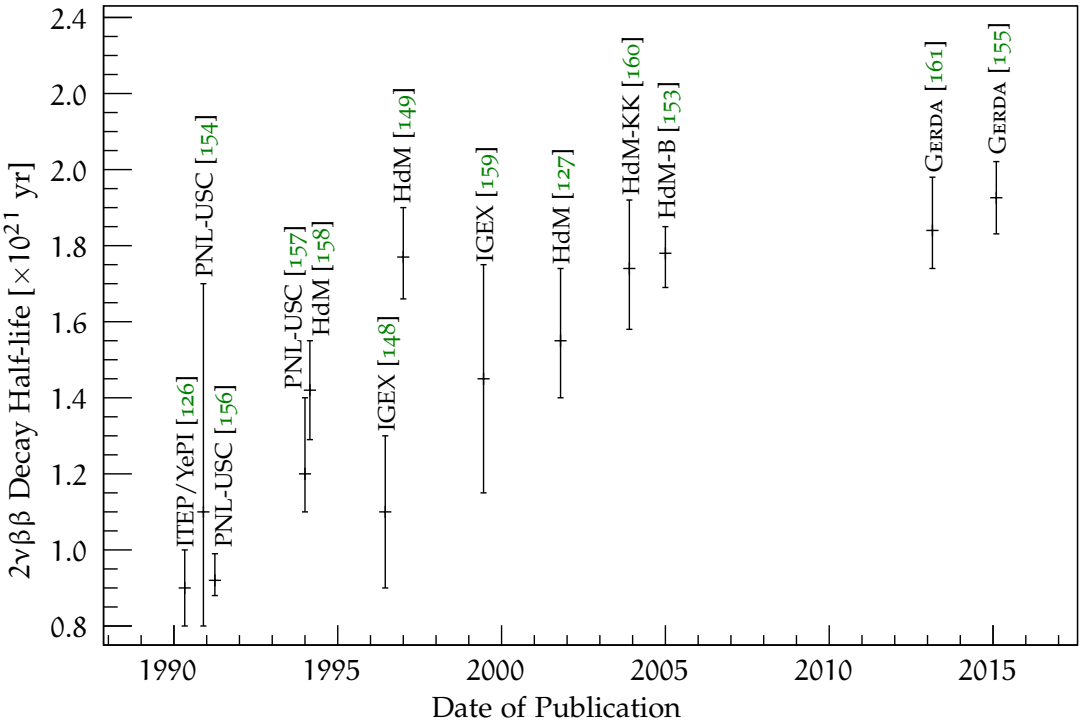

Figure 2.17.: Chronology of $T^{2\nu}_{1/2}$ limits and measurements for ^{76}Ge. Values taken from Tab. 2.5.

3

GERMANIUM DETECTORS

Germanium detectors are among the most used devices in γ spectrometry. They are characterized by a very good energy resolution of up to $O(0.1\%)$, a response proportional to the absorbed energy and a good full-energy peak efficiency.

In this chapter the working principles and main properties of germanium detectors are summarized. In Sec. 3.1 the interaction of particles in the $[0.1; 10]$ MeV range is reviewed. Secs. 3.2 and 3.3 describe the main physical characteristics of semiconductors and of germanium detectors, respectively. Finally, the signal readout and energy resolution properties of germanium detectors are presented in Secs. 3.4 and 3.5, respectively.

3.1 INTERACTION OF PARTICLES WITH MATTER

A radioactive decay is a spontaneous emission of particles by an isotope, which reaches a more stable nuclear configuration. This reaction is exothermic: the parent nucleus always has a greater mass than the daughter by some amount Δm, and an energy equal to $E = \Delta m \cdot c^2$ is shared among the daughter nucleus and the emitted particles. In most cases, radioactive decays are of type α and β. After the particle emission, the daughter nucleus can be in an excited state and further decay or de-excite, emitting γ rays to reach its ground state. The energy of α, β and γ particles emitted in radioactive decay processes is in the range of few keV to few MeV. The most frequent interactions of the three types of particles in this energy range are listed below.

3.1.1 α *Particles*

Heavy particles – with masses of $\gtrsim 1$ GeV – with up to a few MeV kinetic energy interact mainly electromagnetically and release their kinetic energy into matter via inelastic collision with atomic electrons. The rate of energy released by a heavy particle with velocity $v = \beta c$ per unit path length of traversed material with atomic number Z, atomic mass A and density ρ is given by the Bethe-Bloch formula [162, 163]:

$$-\left(\frac{dE}{dx}\right)_{col} = \left(\frac{z^2 e^2}{4\pi\varepsilon_0}\right)^2 \cdot \frac{4\pi Z \rho N_A}{A m_e v^2}\left[\ln\left(\frac{2m_e v^2}{I}\right) - \ln\left(1-\beta^2\right) - \beta^2\right] \quad , \qquad (3.1)$$

where ze is the electric charge of the incoming particle ($z = 2$ for α particles), ε_0 is the vacuum permittivity, N_A is the Avogadro number and I is the mean energy

required to ionize an atom in the considered material. This formula is based on the assumption that the mass of the incoming particle is much larger than the electron mass. Thus, the energy transferred in each single collision by the heavy particle to the electron is much smaller than the kinetic energy of the particle itself, and the heavy particle suffers negligible deflection. In particular, the rate of energy loss is proportional to the density of electrons in the material, $Z\rho N_A/A$. Hence, materials with higher density and atomic number have a higher stopping power. Moreover, a particle with higher electric charge will be stopped in a shorter range than a particle with the same mass but lower charge.

An α particle with the energy of a few MeV is characterized by a dE/dx of $O(10^3)$ MeV/cm, with a maximum energy loss around 1 MeV. Correspondingly, the range of α's rises almost linearly from few keV to several MeV. In the case of germanium, the range of an α with a few MeV kinetic energy is of $O(10)$ μm.

3.1.2 *Electrons and Positrons*

In the energy range considered here, electrons and positrons lose energy at a lower rate than heavy particles. The approximation made for the case of heavy particles are no more valid. Namely, the energy loss in this case is not necessarily much smaller than the kinetic energy of the incoming electron (positron), and the deflection angle can be large, as well. Moreover, in the case of incoming electrons, the indistinguishability between the scattering particles has to be accounted for. The energy loss by collision per unit path length is in this case more complex than for heavy particles and is not reported here. When deflected, electrons and positrons lose energy also via emission of Bremsstrahlung. Moreover, when their velocity is higher than the speed of light in the same medium, they lose energy via Cerenkov radiation. For both electrons and positrons the energy loss by collision is dominant below $\sim$ 10 MeV, while the radiation dominates for higher energies. The total energy loss for electrons of $O(1)$ MeV kinetic energy is about 10 MeV/cm, and their range in germanium is of $O(1)$ mm.

In the case of an incoming positron, most of the kinetic energy is released to the medium via the processes mentioned here. When the positron is almost at rest ($E_{e^+} \lesssim 10$ eV), an electron-positron annihilation takes place, with the corresponding emission of two γ rays of 511 keV.

3.1.3 γ *Radiation*

Charged particles like α's and electrons release energy via ionization or atomic excitation of the traversed medium. On the contrary, γ rays are electrically neutral, hence they must transfer their energy to matter through different interactions. In general, γ rays interact with the atomic electrons of the considered material, which then lose their energy as described above. Three processes dominate the interaction of γ rays with matter in the range from few keV to several MeV. These are photoelectric absorption, Compton scattering, and pair production. In all cases, the cross section depends on the energy of the γ and on the atomic number of the considered material.

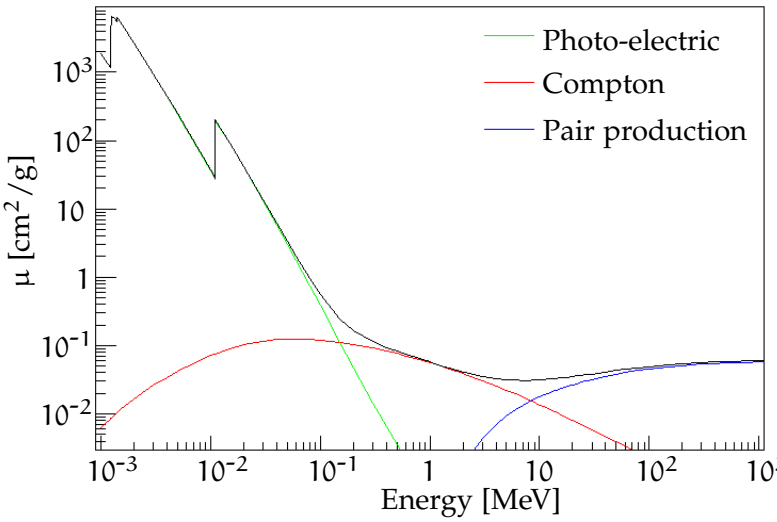

Figure 3.1.: Germanium mass attenuation coefficient for γ interactions. Values from [164].

Photoelectric absorption

In photoelectric absorption, a γ transfers all its energy to a bound electron in an atom, which is ejected from its shell. The kinetic energy of the emitted electron is:

$$E_e = E_\gamma - E_0 \quad , \tag{3.2}$$

where E_γ is the energy of the γ, and E_0 the binding energy of the electron. The atom is left in an excited state, with a vacancy in the concerned shell. The de-excitation can take place either through the transition of an other electron from a higher-energy shell to the shell with the vacancy and the corresponding emission of an X-ray, or via a recombination of the atomic electrons with the emission of Auger electrons. The cross section of Photoelectric absorption decreases exponentially with energy and is dominant below $\sim$ 200 keV, as shown in green in Fig. 3.1. The steps around few keV and 10 keV are related to the shells from which the electron is ejected. Most likely, the photoelectric absorption affects electrons from the K shell. For germanium, the binding energy of the K shell is 11.1 keV. Alternatively, the L or M electrons can be ejected, with lower probability.

The X-rays and Auger electrons produced in the atomic de-excitation have an energy lower than that of the original γ. While the electrons release their energy via collision, the X-rays undergo further photoelectric absorption, until all energy is released to the atomic electrons of the material. If the process takes place in a detector and if the entire kinetic energy of the electrons is absorbed in it, the energy spectrum will feature a full energy peak (FEP) at an energy E_γ.

3.1.4 *Compton Scattering*

Compton scattering is a process in which a γ transfers a fraction of its energy to a free electron and is deviated by an angle θ, as depicted in Fig. 3.2. The electron recoil energy is:

$$E_e = E_\gamma - E'_\gamma = E_\gamma \left[1 - \frac{1}{1 + E_\gamma \left(\frac{1-\cos\theta}{m_e c^2} \right)} \right] \quad , \tag{3.3}$$

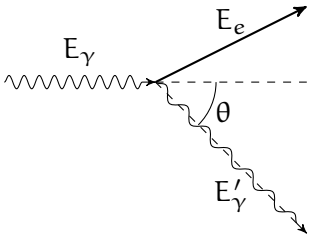

Figure 3.2.: Compton scattering.

where E_γ is the energy of the incoming γ and E'_γ is that of the scattered γ. The electron energy is a continuum from zero in case of no deflection of the γ ($\theta = 0$) to a maximum in case of total deflection ($\theta = \pi$):

$$\max(E_e) = E_\gamma \left[1 - \frac{1}{1 + 2\frac{E_\gamma}{m_e c^2}}\right] = E_\gamma \frac{2E_\gamma}{mc^2 + E_\gamma} \quad . \tag{3.4}$$

In the energy spectra recorded by γ detectors with good enough energy resolution, a shoulder is visible at energy $\max(E_e)$ in correspondence of a high intensity γ peak at energy E_γ. This feature is called Compton edge.

If the Compton scattering takes place outside the detector volume, the deflected γ can enter the detector and release all or part of its energy therein. The contribution of E'_γ to the measured energy spectrum is a continuum from a minimum

$$\min(E'_\gamma) = E_\gamma - \max(E_e) = E_\gamma \frac{m_e c^2}{m_e c^2 + E_\gamma} \tag{3.5}$$

to a maximum equal to the original γ energy, E_γ. In particular, the step at $\min(E'_\gamma)$ is called the back-scatter peak.

The Compton scattering represents the dominant fraction of γ ray interactions in the range from ~ 100 keV to ~ 10 MeV, as depicted in Fig. 3.1.

Pair Production

The third possible interaction of γ radiation with matter is pair production. This process takes place in the nuclear Coulomb field and results in the conversion of the γ into $e^- e^+$. Pair production can take place only if the energy of the incoming γ is at least as large as the rest mass of the pair, i.e. 1022 keV. The eventual excess energy is equally distributed among the two emitted particles. For the conservation of momentum, these are emitted in opposite direction in the center-of-mass frame. The cross section for pair production is dominant at energies above ~ 10 MeV (see Fig. 3.1).

If a pair production takes place outside the detector, the kinetic energy of the pair is released in the medium, as described above. Once the positron is almost at rest, it undergoes an $e^- e^+$ annihilation with an atomic electron. One of the two emitted γ's can enter and be fully absorbed in the detector volume. This is the origin of the peak at 511 keV, which is typically present in γ spectroscopy measurements. The event topology is more complicated if the pair production takes place inside the detector volume. In all cases, an energy almost equal to

$E_\gamma - 1022$ keV is absorbed in the detector. Once the two 511 keV γ's are produced, they can either be absorbed by the detector, or escape from it. If both γ's are absorbed, the total initial energy E_γ is detected, and the event will belong to the FEP in the measured energy spectrum. If one is absorbed and the other escapes, an energy equal to $E_\gamma - 511$ keV is detected. This is the origin of the so called single escape peak (SEP). If both γ's escape, only $E_\gamma - 1022$ keV are transferred to the detector. These events will belong to the double escape peak (DEP). Clearly, other possibilities exist, in which only a fraction of the energy of the 511 keV γ's is released in the detector. In such cases, an energy in the $[E_\gamma - 1022; E_\gamma - 511]$ or in the $[E_\gamma - 511; E_\gamma]$ range is detected. These types of events are responsible for high-energy steps in correspondence of the DEP and SEP.

A further remark is necessary with regard to the annihilation peak and SEP. Because of the finite momentum of the $e^- e^+$ pair, the two γ's are subject to an opposite Doppler shifting by some among $\pm\Delta E$. If only one is detected (annihilation peak, SEP), the corresponding peak is broader than a FEP of the same energy. On the contrary, if both γ'e escape, the total amount of missing energy is $(511 + \Delta E) + (511 - \Delta E) = 1022$ keV. For this reason, the DEP is not affected by the Doppler broadening.

The contributions of photoelectric absorption, Compton scattering and pair production to the total mass attenuation coefficient μ of germanium are shown in Fig. 3.1. μ is defined as:

$$\mu = \frac{N_A}{A}(\sigma_{pe} + \sigma_{Compton} + \sigma_{pp}) \quad , \tag{3.6}$$

where σ_{pe} is the cross section of the photoelectric effect, $\sigma_{Compton}$ is that of Compton scattering, and σ_{pp} that of pair production.

3.2 SEMICONDUCTOR DETECTORS

Semiconductor materials have been used for many decades as particle detectors. The detection technique consists of collecting the charge released by an ionizing particle entering the detector volume. The signal properties of a semiconductor detector strongly depend on the characteristics of the semiconductor itself. In a single atom, the electrons are only allowed to be in some defined energy levels. In a solid, the energy levels are combined to bands, which can host a fixed number of electrons. The non-empty band with highest energy is called the valence band, while the first empty band is the conduction band. The energy difference between the conduction and the valence band is called band gap, E_g. A schematic of the band structure in solids is shown in Fig. 3.3 An electron can move inside the material only passing from the valence to the conduction band.

The solids can be divided in three types, according to the amplitude of the band gap. For insulators the valence band is full and $E_g \sim 10$ eV. This value is hardly reached by an electron via thermal excitation, and the application of a however high external electric field does not induce the electrons to jump to the conduction band.

In conductors, the valence band is not full and the conduction band is superimposed with it. Electrons can move from the valence to the conduction band via

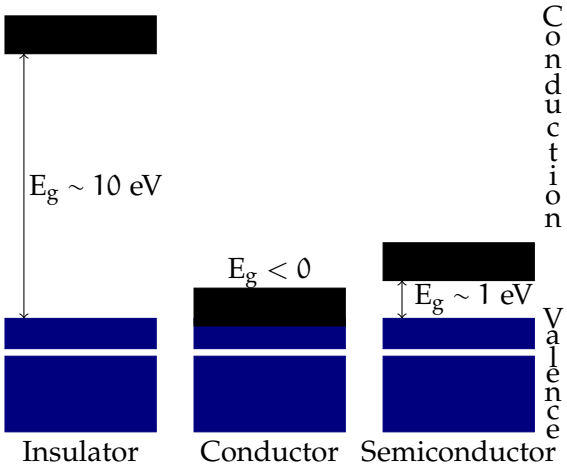

Figure 3.3.: Schematic description of the band structure for insulator, conductor and semiconductor materials.

thermal excitation, and the application of an external field induces an electrical current.

Semiconductors feature a full valence band, as for the insulators, but their band gap is of $O(1)$ eV. In this case, thermal excitation is enough to move electrons from the valence to the conduction band. The probability for an electron to jump from the valence to the conduction band is:

$$P(T) \propto T^{3/2} \cdot \exp\left(\frac{-E_g}{2kT}\right) \quad , \tag{3.7}$$

where k is the Boltzmann constant and T the temperature. Hence, the current induced by electrons moving to the conduction band due to thermal excitation increases with temperature. This quantity is called leakage current. When a semiconductor is used as particle detector, the leakage current induces a noise in the signal, which is reduced by operating the detector at low temperature.

When an electron moves to the conduction band, a vacancy is created in the valence band, which is called hole (h). A hole can be filled by another valence electron, creating a new hole. If an electric field is applied, the electrons move towards the anode, and the holes towards the cathode. On the other hand, if no electric field is applied, at some point the electron will fall back from the conduction to the valence band, in a process called charge recombination. If a γ ray or a charged particle enters the detector a number n of electron-hole pairs (e-h) is created. This is proportional to the energy absorbed in the medium, E_{abs}:

$$n = \frac{E_{abs}}{\eta} \quad , \tag{3.8}$$

where η is the average energy required for the creation of an e-h pair. If the electrons and/or holes are collected, the deposited energy can be measured. Thus, a semiconductor detector is a semiconductor material to which an electric field is applied for the collection of the charge induced by incoming ionizing radiation. Eq. 3.8 states that the number of e-h pairs is inversely proportional to η. One can expect that, for a fixed deposited energy, a higher energy resolution is achieved for a higher number of created e-h pairs. Therefore, a small value of η is desirable.

The optimal temperature for a semiconductor detector can be estimated on the base of the temperature dependence of η and E_g. So far, no theoretical model

Table 3.1.: Drift velocity for germanium and silicon. Values taken from [167]

	Mobility [$cm^4\ V^{-1}\ s^{-1}$]	
Material	Electrons	Holes
Si	1350	480
Ge	$3.6 \cdot 10^4$	$4.1 \cdot 10^4$

is available, but only parametrizations based on experimental values. A possible description of $\eta(T)$ for germanium is [165]:

$$\eta(T) = 2.2 \cdot E_g(T) + 1.99 \cdot E_g^{3/2}(T) \cdot \exp\left(4.75 \frac{E_g(T)}{T}\right) \quad , \tag{3.9}$$

while the band gap can be parametrized as [166]:

$$E_g(T) = E_g(0) - \frac{\alpha T^2}{T + \beta} = 0.7142 - \frac{4.561 \cdot 10^{-4} T^2}{T + 210} \quad , \tag{3.10}$$

where the values of $E_g(0)$, α and β are relative to germanium. If the experimental values are inserted in Eqs. 3.10 and 3.9, it results that η is decreasing with temperature. From this perspective, it would be desirable to operate the detector at high temperature. On the other hand, a high temperature would induce a high leakage current. A trade-off is therefore necessary in order to minimize the intrinsic electronic noise of the detector, and still achieve a good energy resolution. In the case of germanium, the solution is to operate the detector at liquid nitrogen (LN) temperature: at 77 K the band gap is of 0.67 eV and η is 2.96 eV [167]. As a comparison, silicon detectors are typically operated at room temperature, with $E_g = 1.106$ eV and $\eta = 3.62$ eV [167].

The performance and applicability of semiconductor detectors is also related to the drift velocity for electrons and holes. This depends on the applied voltage. The values for germanium and silicon are reported in Tab. 3.1. The drift mobility of both electron and holes for germanium is an order of magnitude higher than for silicon. Thanks to this, bigger detectors can be built with germanium. Additionally, the higher atomic number yields a higher efficiency in the absorption of γ rays of $O(1)$ MeV energy. For these two reasons germanium detectors are typically used for γ spectroscopy, while silicon detectors are employed for X-ray measurements.

So far, the assumption was made that the employed material is a pure semiconductor. In reality, impurities are always present, which can strongly affect the band levels and the band gap. As a consequence, the conductivity is modified. Germanium and silicon are tetra-valent. Each atom in the crystal lattice is surrounded by other four atoms. If an atom is present with valence five, the crystal will have an electron in excess, and the atom is called donor. Crystals with this type of impurity are called n-type, due to the presence of "negative" donor impurities. Similarly, if an atom with valence three is present, a hole is generated, and the atom is called acceptor. In this case the crystal is of p-type because of the presence of positive acceptor impurities. In general, both types of impurities are present in the crystal lattice. If the same amount of donors and acceptors is

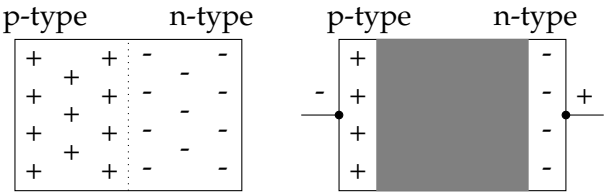

Figure 3.4.: Depletion of a semiconductor detector.

present, a pure semiconductor is obtained. The compensation of the excess impurities can be achieved inserting the same amount of opposite impurities. This process is denoted as doping. In the case of a detector with planar geometry as the one depicted in Fig. 3.4, the two types of impurities can be inserted on the two detector's surfaces. In this condition the detector has for half of p-type, and for the other half of n-type. If an electric voltage is applied, which attracts the donors and impurities to the opposite surfaces, the central part of the detector volume is depleted from the presence of impurities and behave as a pure semiconductor. In this configuration the crystal is used as a diode with a reverse bias applied. The depletion volume represents the active volume of the detector. In order to maximize the efficiency, the largest possible depletion volume is desirable. For germanium, the n-type (or n^+) junction is normally obtained via lithium drift for a thickness of about 0.5–2 mm, while the p-type junction is done via boron implantation for a thickness of few dozens nm. When a bias voltage is applied, the doped regions maintain a charge excess. If a particle interacts therein, the charge is recombined and cannot be collected. For this reason, the n- and p-type junctions are called dead layers. The depth d of the depleted volume depends on the net impurity concentration ρ_{imp} and on the applied voltage V:

$$d = \left(\frac{2\varepsilon_R \varepsilon_0 V}{e\rho_{imp}}\right)^2 \quad , \tag{3.11}$$

where $\varepsilon_R = 16$ is the dielectric constant of germanium and ε_0 is the vacuum permittivity. The voltage required to achieve a full depletion of the crystal is called depletion voltage. The applicable voltage is limited by the finite break-through voltage of the diode and by the performances of the cables and readout electronics. Moreover, the leakage current increases with the applied voltage, with strong consequences on the electronic noise. For these two reasons it is necessary to maximize the purity of the bulk material. In the case of germanium, a 12 N purity can be achieved [124]. Detectors of this type are called high purity germanium (HPGe).

A semiconductor detector with bias voltage applied (see Fig. 3.4) works as a capacitor. The detector capacitance C_D strongly affects the energy resolution, as described in Sec. 3.4. In particular, a smaller detector capacitance yields a higher energy resolution. In case of a planar geometry, as for silicon detectors, the capacitance is:

$$C_D = \frac{\varepsilon_R A}{4\pi d} \quad , \tag{3.12}$$

where A is the detector area and d are the depletion depth. Assuming that the detector is fully depleted, d can be safely approximated as the detector thickness.

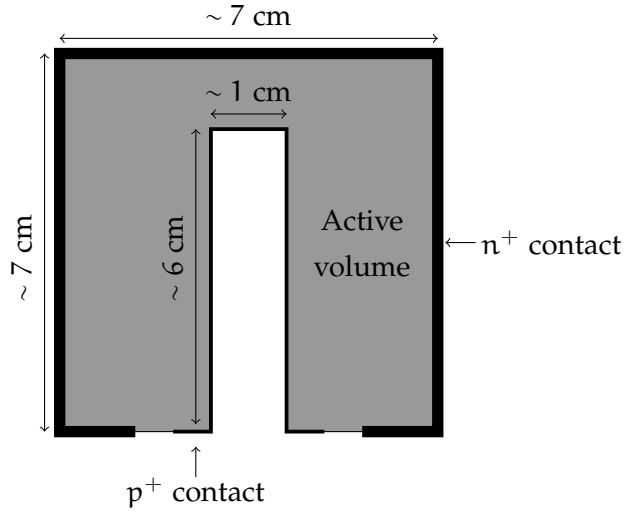

Figure 3.5.: Schematic of a semi-coaxial detector geometry.

Therefore, a planar detector features a higher energy resolution for a smaller area to thickness ratio. For a semi-coaxial detector with cylindrical shape and a central bore hole the capacitance is:

$$C_D = \frac{\varepsilon h}{2 \ln\left(\frac{r_2}{r_1}\right)} \quad , \tag{3.13}$$

where h is the detector height, r_2 the detector radius, and r_1 the bore hole radius. In this case the capacitance is minimized when the ratio r_2/r_1 is maximum. Thus, a higher energy resolution is achieved for a smaller bore hole radius. The actual shape of semiconductor detectors is typically a trade-off between the ideal shapes and the requirements connected to the manufacturing process, to the detector operation and to the signal readout.

3.3 GERMANIUM DETECTORS

Germanium detectors are typically used for γ spectrometry. The relatively high Z and the high achievable drift velocity allows the use of large size detectors featuring a high efficiency for γ detection. One of the most extensively employed types of germanium detectors is the semi-coaxial HPGe detectors. The geometry of a typical semi-coaxial detector is outlined in Fig. 3.5: it is a cylinder with a central bore hole with almost the same length as that of the detector itself. A Li-diffused $\sim$ 0.5–2 mm thick dead layer, constituting the n^+ contact, is present in all the detector surface, except than on the bore hole and its vicinity. In this region is present the p^+ contact with $O(10)$ nm thickness, obtained via boron implantation. The high voltage (HV) is applied to the n^+ contact, while the p^+ contact is used for the signal readout. The n^+ and p^+ contacts are separated by a groove, which is typically passivated. The dimensions of a semi-coaxial detector can go from $\sim$ 4 cm to $\sim$ 10 cm in both diameter and height, while the bore hole diameter is $\lesssim$ 1 cm. Under the approximation of a truly coaxial geometry, and assuming a diameter and height of 8 cm and a bore hole diameter of 1 cm, the capacitance of a semi-coaxial detector is $\sim$ 35 pF.

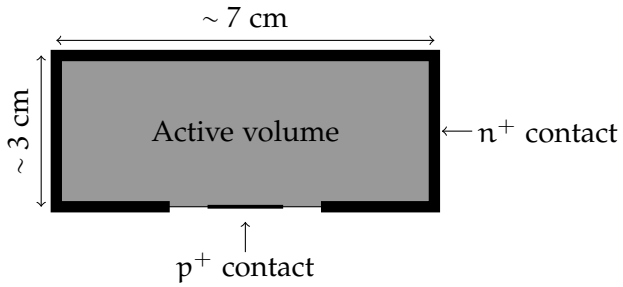

Figure 3.6.: Schematic of a BEGe detector geometry.

More recently, a new type of germanium detectors has been developed. It is characterized by a cylindrical shape with a p^+ contact limited to a $O(1)$ cm^2 spot on one of the two bases, while the n^+ contact is extended to the rest of the surface. These point-contact detectors are called broad energy germanium (BEGe). The typical geometry of a BEGe detector is depicted in Fig. 3.6. The small size of the p^+ contact yields a small detector capacitance and, therefore, a better energy resolution. Moreover, the geometrical configuration of the n^+ and p^+ contacts induces a slowly-varying electric field over a big fraction of the detector volume (see Fig. 5.2 of [168]). This results in a reduced dependence of the peak shape on the position of the energy deposition, and in a longer charge collection time of about 1 µs. This property can be exploited in the discrimination between different event topologies. More details on PSD are given in Ch. 7.

3.3.1 *Signal Formation in Germanium Detectors*

When a cloud of e-h pairs is created by an incoming particle, the electrons and holes are attracted to the opposite electrodes due to the presence of the electric field. The movement of the electrons and holes in the detector induce a mirror charge at the detector electrodes. The time development $Q(t)$ of this charge and that of the corresponding current $I(t)$ are given by the Shockley-Ramo theorem [169, 170, 171]:

$$\begin{aligned} Q(t) &= -Q \cdot [\Phi(\vec{r}_h(t)) - \Phi(\vec{r}_e(t))] \\ I(t) &= Q \cdot \left[\vec{E}(\vec{r}_h(t)) \cdot \vec{v}_h(t) - \vec{E}(\vec{r}_e(t)) \cdot \vec{v}_e(t)\right] \quad , \end{aligned} \tag{3.14}$$

where Q is the total charge generated by the incoming particle, $\vec{r}_{h(e)}(t)$ and $\vec{v}_{h(e)}(t)$ are the position and velocity of the hole (electron) cluster at time t, respectively, while $\Phi(\vec{r})$ and $\vec{E}(\vec{r})$ are the electric potential and field at position $\vec{r}$, respectively.

The weighting potential can be calculated solving the Poisson equation:

$$\Delta\Phi = 0 \tag{3.15}$$

with the boundary conditions $\Phi(\vec{r}) = 1$ for the considered electrode and $\Phi(\vec{r}) = 0$ for the other electrode. The solution of Eqs. 3.15 and 3.14 for an arbitrary detector geometry is possible only with numerical methods, and is not covered here. A calculation of the theoretical signal pulses for BEGe detectors can be found in [168].

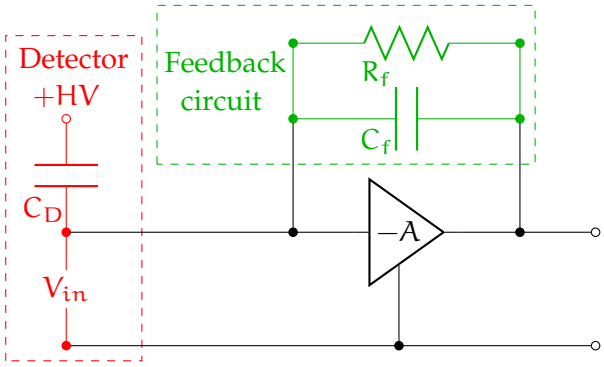

Figure 3.7.: Typical readout scheme of a germanium detector with a charge sensitive preamplifier with open loop gain A. The detector with capacitance C_D is operated with inverse bias voltage HV. The charge Q_{in} is collected on the capacitor C_f of ~ 0.3 pF which then discharges because of the presence of the feedback resistor $R_f = 500$ MΩ.

3.4 SIGNAL READOUT WITH GERMANIUM DETECTORS

The typical readout of a germanium detector, operated as a diode with inverse bias applied, consists of a charge sensitive preamplifier, whose output waveform is either shaped and then processed by an analog to digital converter or, as in GERDA, directly digitized by a flash analog to digital converter (FADC). Fig. 3.7 represents the detector and charge sensitive preamplifier system, consisting of a junction gate field-effect transistor (JFET) coupled to a feedback circuit. The capacitor C_f integrates the charge from the detector, with a step change in voltage induced at the preamplifier output. In order not to saturate the dynamic range of the digitizer, a feedback resistor R_f is connected in parallel to the capacitor, allowing to bring the voltage back to its baseline value. The shape of the preamplifier output pulse will then be characterized by a fast rise, with rise-time of about 0.5-1.5 µs, corresponding to the charge collection process, followed by an exponential decay with time constant $\tau = R_f C_f$. The values of R_f and C_f for the GERDA preamplifiers are 500 MΩ and ~ 0.3 pF, respectively, for a τ of about 150 µs. An accurate description of the GERDA readout scheme is given in [172].

The energy reconstruction through analog or digital shaping (see Ch.) is sensitive to the variability of the baseline, induced by the electronic noise. For this reason, one of the most important tasks in the design of a preamplifier is the minimization of its electronic noise, in particular the noise generated in the coupling between the detector and the preamplifier itself.

In order to understand the possible sources and characteristics of the electronic noise, the system can be modeled as in Fig. 3.8. The detector is considered as a source of a delta-like charge pulse. The fact that the pulse has a time duration can be safely neglected in the following. The charge Q is delivered to the detector capacitance C_D and to the capacitance of the detector-preamplifier coupling, or preamplifier input capacitance, C_i. The output signal read by the digitizer is the output of a noiseless preamplifier with open loop gain A connected in series to a voltage generator with spectral density $s(f)$ (green in Fig. 3.8) and in parallel to

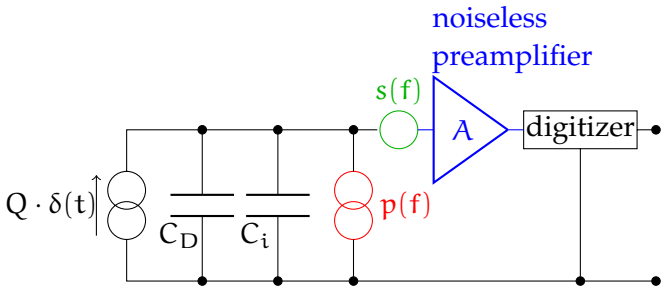

Figure 3.8.: Signal and main noise sources in the readout system of a germanium detector. The trace recorded by the digitizer can be modeled as the output of a noiseless preamplifier, connected to a noiseless detector with capacitance C_D, a series voltage generator and a parallel current generator with spectral densities $s(f)$ and $p(f)$, respectively. $Q \cdot \delta(t)$ is the original current signal and C_i is the preamplifier input capacitance.

a voltage generator with spectral density $p(f)$ (red in Fig. 3.8). The amplitude of the electronic noise can be expressed as the standard deviation in the charge measurement, i.e the standard deviation of the baseline fluctuation after the shaping process. This quantity is referred as equivalent noise charge (ENC). The ENC represents the number of electrons that would need to be collected in order to obtain a signal with an amplitude equal to the electronic noise root mean square.

The series noise can be considered to be exclusively induced by the JFET. It is characterized by a spectral power density $s(f) = s_1(f) + s_2(f)/f$, where the white noise $s_1(f)$ is given by the thermal noise and the $1/f$ term by the carrier number and mobility fluctuations. The ENC of the series noise is of the form:

$$ENC_s^2 = C_T^2 \left(\alpha \frac{2kT}{g_m \tau_s} + \beta A_f \right) \quad , \tag{3.16}$$

where C_T is the total preamplifier input capacitance:

$$C_T = C_D + C_i + C_f \quad . \tag{3.17}$$

The first term of Eq. 3.16 is related to the white noise s_1: k is the Boltzmann constant, T the JFET operational temperature (87.3 K for LAr), g_m the JFET transconductance ($\sim$ 5 mA/V in GERDA) and τ_s is the shaping time of the considered shaping filter. The second term expresses the ENC contribution of s_2, where A_f is a parameter depending on the specific JFET considered. The constants α and β are of order 1 and depend on the signal shaping filter (c.f. Ref. [173]). The white series noise can be minimized choosing a JFET with high transconductance, and operating it at low temperature. Both the white and the $1/f$ series noise are minimized choosing the smallest possible capacitances. Incidentally, Eq. 3.16 also explains why the BEGe detectors have a much better energy resolution than the semi-coaxial detectors. Namely, typical values of C_D are 30 pF for these, and 1 pF for BEGes. For a shaping time of 10 µs and setting $\alpha = 1$, the white noise contribution of the series ENC^2 is of about 170 (2700) e^2 for BEGE (coaxial) detectors. The estimation of the $1/f$ noise contribution to the ENC^2 based on the electronic components and the used shaping filter is not possible. In the optimal case of

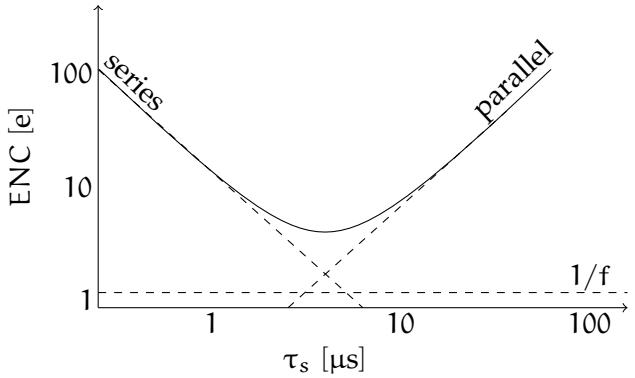

Figure 3.9.: ENC as function of the shaping time τ_s of a typical shaping filter.

negligible $1/f$ noise, the second term of Eq. 3.16 contributes with $O(10)$ e^2, while it might be of $O(10^4)$ e^2 if strong low-frequency noise or disturbance are present.

Analogously, the parallel noise can be described by a spectral density $p(f) = p_1(f) + p_2(f)$, where $p_1(f)$ is associated with the detector current and the detector and preamplifier bias circuit, while $p_2(f)$ is related to the preamplifier. The corresponding ENC is:

$$ENC_p^2 = \gamma\left(e \cdot I_L + \frac{2kT}{R_f}\right)\tau_s \quad , \tag{3.18}$$

where I_L is the detector leakage current and R_f is the feedback resistance. Neglecting I_G, whose value is typically below 1 pA, and using $I_L = 100$ pA, the parallel noise ENC^2 is ~ 8000 e^2. More detailed descriptions of the noise origin and its treatment in germanium detectors can be found in Ref. [173, 174].

The combination of the series and parallel noise components will result in a ENC having a minimum in correspondence to the optimal value of the shaping constant τ_2, as shown in Fig. 3.9. If a too short shaping time is chosen, the energy resolution will be worse due to the non optimal filtering of the series noise. If, on the other side, a too big value of τ_s is used, the parallel noise becomes dominant. For any shaping filter it is therefore mandatory to chose the value of τ_s which minimizes the electronic noise.

In the case of GERDA, an additional ENC component is induced by the microphonic disturbance related to mechanical vibrations in the long wiring (30-60 cm) connecting the detectors to the preamplifiers. The microphonic noise is a low-frequency component, independent of the detector and front-end electronics but sensitive to the environmental condition, and thus liable to time evolution. This has to be accounted for in the development of an appropriate shaping filter.

3.5 ENERGY RESOLUTION

The energy resolution of a germanium detector depends on the electronic noise, on the charge production in the crystal and on the charge collection and integration properties of the diode and the shaping filter. We can define the energy resolution ΔE as the FWHM of a given γ line in the energy spectrum.

Independently from the energy of the line, a constant contribution w_{ENC} to its width is given by the ENC:

$$w_{ENC} = 2.355 \cdot \frac{\eta}{e} ENC \quad . \tag{3.19}$$

The term w_{ENC} represents the width, in keV, of the noise pedestal in the energy spectrum. Recalling the examples given in section 3.4, the series noise contributes $> 0.1(0.4)$ keV to w_{ENC} for a BEGe (coaxial) detector, while the parallel noise contributes ~ 0.6 keV. In a realistic situation with very low electronic noise, a zero-energy FWHM of ~ 0.7 keV is expected.

A second contribution to the FWHM is given by the charge production process in the crystal. The number of electron-hole pairs created by a particle interaction in the crystal has an average value $N = E/\eta$. Assuming that the charge production follows the Poisson statistics, then $\sigma_N = \sqrt{E/\eta}$. The uncertainty on the measured energy is therefore $\sigma_E = \eta\sqrt{N} = \sqrt{\eta N}$. The corresponding contribution to the FWHM is then:

$$w_p = 2.355\sqrt{\eta \cdot E} \quad . \tag{3.20}$$

For the typical case of the ^{60}Co line at 1332.5 keV, this would correspond to 4.7 keV. In reality, an energy resolution of about 1.7 keV can easily be obtained with a BEGe at this energy. The reason for this overestimation lies on the assumption of the Poisson nature of the process. As described in [175], the correct formula for w_p contains a multiplicative term F, denoted as "Fano factor":

$$w_p = 2.355\sqrt{\eta F \cdot E} \quad . \tag{3.21}$$

For germanium, several measurements of F have been performed along the years [176, 177, 178, 179]. Although no clear consensus has been achieved yet, most publications quote for F a value ~ 0.11.

The last contribution to the width of spectral lines is given by the charge collection of the detector and electronic system, and by the charge integration properties of the shaping filter. The presence of crystal imperfections or the application of a too low HV can induce to charge recombination in the crystal lattice, inducing an incomplete charge collection. Similarly, the use of a preamplifier with a too short time constant $R_f C_f$ or of a shaping filter with too short shaping time τ_s can lead to a sub-optimal integration of the deposited charge. Given the complexity of the physics involved, the charge collection and integration term is normally expressed by the empirical formula:

$$w_c = 2.355\ c \cdot E \quad . \tag{3.22}$$

In all cases, the effect is a systematic energy underestimation by a variable amount, which induces the presence of low-energy tails in the spectral lines.

The three terms W_{ENC}, w_p and w_c have independent origins, hence they can be summed in quadrature to give the overall FWHM:

$$FWHM(E) = 2.355\sqrt{\frac{\eta^2}{e^2} ENC^2 + \eta F \cdot E + c^2 \cdot E^2} \quad , \tag{3.23}$$

which shows how the electronic noise term is dominant at low energy and the charge collection term at high energy.

4

THE GERDA EXPERIMENT

C'è mai stata al Gran Sasso? È bello, è un bel posto, se sei un lombrico per viverci è bello il Gran Sasso, stai lì quattro mesi...
M. Crozza alias A. Zichichi

The GERmanium Detector Array (GERDA) is an experiment for the search of $0\nu\beta\beta$ decay in ^{76}Ge. It is located at the Laboratori Nazionali del Gran Sasso (LNGS) of INFN, Italy. The experiment is based on the use of germanium crystals enriched to $\sim 86\%$ in ^{76}Ge and acting simultaneously as source and detector of the process. The detectors are directly immersed in liquid argon (LAr), acting as cooling medium and shielding against external background radiation. Additionally, the LAr scintillation light can be exploited as an anti-coincidence veto for events releasing energy both in germanium and in LAr itself.

The physics program of GERDA is divided in two stages, as summarized in Tab. 4.1. The first data collection, denoted as Phase I, was performed between November 2011 and June 2013 with ~ 20 kg of enriched semi-coaxial detectors. It was characterized by a background index (BI) at $Q_{\beta\beta}$ of 10^{-2} counts/(keV·kg·yr), and lead to a 90% confidence level (C.L) lower limit of $2.1 \cdot 10^{25}$ yr [102] on the half-life of the reaction, $T^{0\nu}_{1/2}$. The implementation of an active anti-coincidence veto for the readout of the LAr scintillation light and the use of additional 20 kg of enriched Broad Energy Germanium detectors (BEGe) with enhanced pulse shape discrimination capabilities are the main improvements for GERDA Phase II, which is currently in its commissioning stage. In Phase II, a BI of 10^{-3} counts/(keV·kg·yr) is expected, which will lead to a $1.4 \cdot 10^{26}$ yr sensitivity on $T^{0\nu}_{1/2}$ with three years of data collection.

Table 4.1.: Mass, BI, live time and sensitivity on $T^{0\nu}_{1/2}$ for GERDA Phase I and Phase II. The reported BI and $T^{0\nu}_{1/2}$ sensitivity for Phase II are based on MC simulations of the radioactive contamination of all involved materials and on toy-MC spectra at $Q_{\beta\beta}$, respectively.

	Mass [kg]	(Expected) BI [counts/(keV·kg·yr)]	Live time [yr]	(Expected) $T^{0\nu}_{1/2}$ sensitivity [yr]
Phase I	15	10^{-2} [102]	1.5	$2.4 \cdot 10^{25}$ [102]
Phase II	35	10^{-3}	3	$1.4 \cdot 10^{26}$

This chapter is structured as follows. In Sec. 4.1 the experimental setup is outlined, while Sec. 4.2 describes the GERDA data structure. Finally, a review of Phase I data collection and analyses is given in Sec. 4.3.

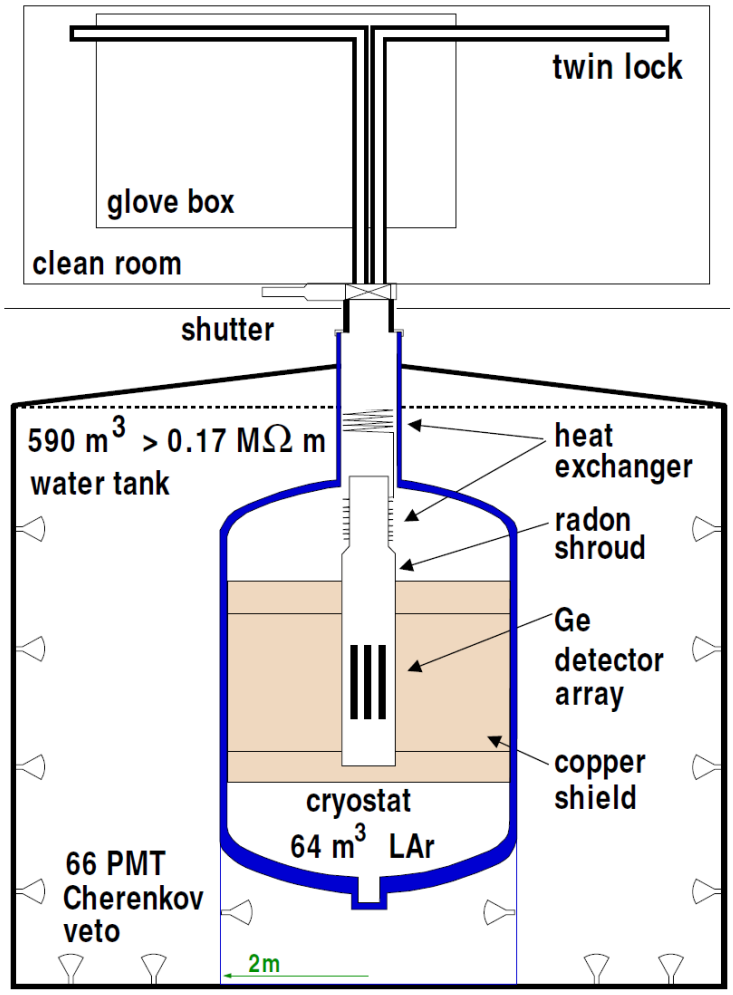

Figure 4.1.: Schematic view of the GERDA structure.

4.1 EXPERIMENTAL SETUP

A major task in the design and construction of an experiment for $0\nu\beta\beta$ decay search is the minimization of the BI at $Q_{\beta\beta}$. A first background reduction is obtained locating the experiment underground. In the case of LNGS, the residual cosmic muon flux is $\sim 1\ m^{-1}\ hr^{-1}$ [180]. This, together with the environmental γ and neutron backgrounds, is further shielded by a tank filled with 590 m^3 high-purity water instrumented with 66 photo-multiplier tubes (PMT) to read the Cerenkov light induced by muons (Fig. 4.1). A stainless steel cryostat with a 6 cm thick oxygen free radio-pure copper layer is installed in the center of the water tank and filled with 64 m^2 of LAr. A heat exchanger is installed in the top part of cryostat and reduces the LAr loss. The germanium detectors are deployed approximately in the center of the LAr volume. They are surrounded by a copper cylinder (shroud) of 75 cm diameter and 30 µm thickness, which prevents radon atoms from going in the vicinity of the detectors. A complementary muon veto system is present on the top of the experimental structure and serves to cover the cryostat area, where the water depth crossed by an incoming muon is limited to ~ 1.5 m.

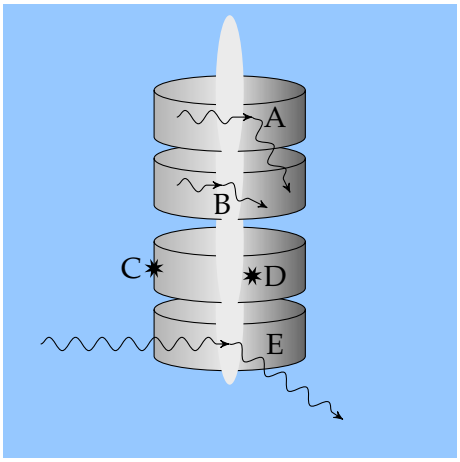

Figure 4.2.: Possible event topologies in GERDA: coincidence event (A), multi site event (B), surface event (C), single site event (D), event releasing energy both in germanium and LAr (E).

A further background reduction is possible with the use of an anti-coincidence cut between germanium detectors, between germanium and Lar, and with PSD. Fig. 4.2 depicts the different event topologies which can take place in GERDA. These can be:

- A a γ undergoing a Compton scattering in one detector, and being fully absorbed in a different detector. Two signal traces with non-zero energy are recorded, and the event can be rejected by an anti-coincidence cut;
- B a γ undergoing a Compton scattering and fully absorption in two different locations of the same detector. The event can be rejected with PSD methods (see Ch. 7);
- C an α or β particle emitted from the detector surface. Also in this case, the events can be rejected with PSD, at least for BEGe detectors (see Ch. 7).
- D a γ, α, β or $\beta\beta$ releasing energy only in one restricted fraction of the detector bulk volume. The event is identified as signal-like by the PSD;
- E a γ undergoing a Compton scattering in germanium and a full absorption in LAr, or vice versa. The energy release in LAr induces scintillation light, which can be detected by proper light sensor. Hence, the event can be rejected by a LAr anti-coincidence veto system.

The possibility of using the LAr scintillation light as a veto explains the choice of LAr instead than the more typical LN. The implementation of a veto system was planned since the beginning for the second phase of GERDA, and is currently in its final stage of commissioning.

A class 7 clean room is located on top of the water tank. Its purpose is to provide a clean environment for the detector handling, which is performed in a nitrogen flushed glove box. The deployment of the detectors in LAr is done through a lock system connected to the LAr cryostat and passing through the glove box. The detectors are connected to a cable chain fully contained in the lock system. The installation of the detectors is performed by removing a $\sim$ 1 m long part of the vertical pipe crossing the glove box. Above the glove box, the lock system features a T-shape, containing the motor for the movement of the detectors and the high-voltage (HV) and signal readout cabling. In Phase I, two independent lock systems were used for the deployment of three and one detector strings, respectively. In Phase II only one lock with 50 cm diameter is employed, which allows the simultaneous operation of 7 detector strings: 6 strings are arranged on an hexagonal

scheme, while the 7^{th} string is located at their center. A full description of the experimental setup is given in [172].

Three calibration systems, developed at the University of Zurich [181, 182, 183], are connected to the lock system and allow to lower three radioactive sources to the vicinity of the detectors. In Phase I, the source insertion systems (SISs) were located between the clean room ground and the bottom of the glove box. For Phase II, they are located on the top of the lock system. The SISs can be operated individually: this allows to optimize the detector coverage, and facilitates the repairing in case of failures. During physics runs, the sources are kept at the highest possible position to maximize their distance from the germanium detectors. A further shielding is obtained mounting each of the sources on a tantalum absorber of 60 mm height and 32 mm diameter.

4.1.1 GERDA *Detectors*

The germanium detectors used in GERDA are of two types. In Phase I, 8 semi-coaxial enriched germanium detectors with a total mass of 17.7 kg were employed. They were previously used in the HdM [149] and IGEX [148] experiments, and refurbished before the deployment in GERDA. Additionally, 6 detectors with natural isotopic abundance were available from the Genius Test Facility (GTF) [184]. All of them are p-type High Purity Germanium detectors (HPGe) from Canberra Semiconductors NV, Olen [185]. They have a diameter between 6 and 9 cm, and a height between 7 and 11 cm, with a 5–7 cm deep bore hole on one face.

For Phase II, additional 20 kg of enriched germanium are available in form of 30 BEGe detectors. The reasons why BEGe detectors have been selected are their superior energy resolution and PSD performance. The full documentation on the production and characterization of BEGe detectors for Phase II is available in [186, 187].

Most analyses presented in this work are relative to Phase I data, while only some calibration runs from the Phase II commissioning are involved. Hence, a list of all detectors employed throughout Phase I is given in Tab. 4.2. They are 5 enriched semi-coaxial detectors from HdM (ANG1, ..., ANG5), 3 enriched semi-coaxial from IGEX (RG1, RG2, RG3, 3 semi-coaxial with natural abundance from GTF (GTF112, GTF32 and GTF45), and 5 enriched BEGe detectors (with names starting with "GD"). For all detectors, the physical dimension, the mass, the operational voltage and the ^{76}Ge abundance are given.

An important part of the experimental setup is represented by the detector holders and the readout electronics. In order to achieve a competing background at $Q_{\beta\beta}$, the amount of possible radioactive contamination in vicinity of the detectors has to be minimized. This goal is obtained by reducing the amount of involved material as much as possible, and by using materials with high radio-purity.

The Phase I detector holders are shown in Fig. 4.3, left and middle. They consist of a copper structure with a threefold star on the top and bottom bases, and three lateral pillars. The crystals are separated from the copper holder by PTFE spacers. The HV contact is done by pressing a copper strip on the top of the detector (Fig. 4.3, middle), while the signal contact consists of a conical copper piece pressed against the p^+ surface on the bottom detector base. This system allowed

Table 4.2.: Detectors used in GERDA Phase I. The dimensions, masses and enrichment values for the semi-coaxial detectors are taken from [172]. Natural abundance for the GTF detector is taken from [188]. All values of BEGe detectors are from [186].

Detector Name	Origin	Diameter [mm]	Length [mm]	Mass [g]	Operational Voltage [V]	^{76}Ge abundance [%]
ANG1	HdM	58.5	68	958	3200	85.9 ± 1.3
ANG2	HdM	80	107	2833	3500	86.6 ± 2.5
ANG3	HdM	78	93	2391	3200	88.3 ± 2.6
ANG4	HdM	75	100	2372	3200	86.3 ± 1.3
ANG5	HdM	78.5	105	2746	1800	85.6 ± 1.3
RG1	IGEX	77.5	84	2110	4600	85.51 ± 0.10
RG2	IGEX	77.5	84	2166	4500	85.51 ± 0.10
RG3	IGEX	79	81	2087	3300	85.51 ± 0.10
GTF112	GTF	85	100	2965	3000	7.80 ± 0.10
GTF32	GTF	89	71	2321	3500	7.80 ± 0.10
GTF45	GTF	87	75	2312	4000	7.80 ± 0.10
GD32B	GERDA	71.8	32.2	717	4000	87.7 ± 1.3
GD32C	GERDA	72	33.2	743	4000	87.7 ± 1.3
GD32D	GERDA	72.2	32	723	4000	87.7 ± 1.3
GD35B	GERDA	76.6	32	812	4000	87.7 ± 1.3
GD35C	GERDA	74.8	26.4	635	3500	87.7 ± 1.3

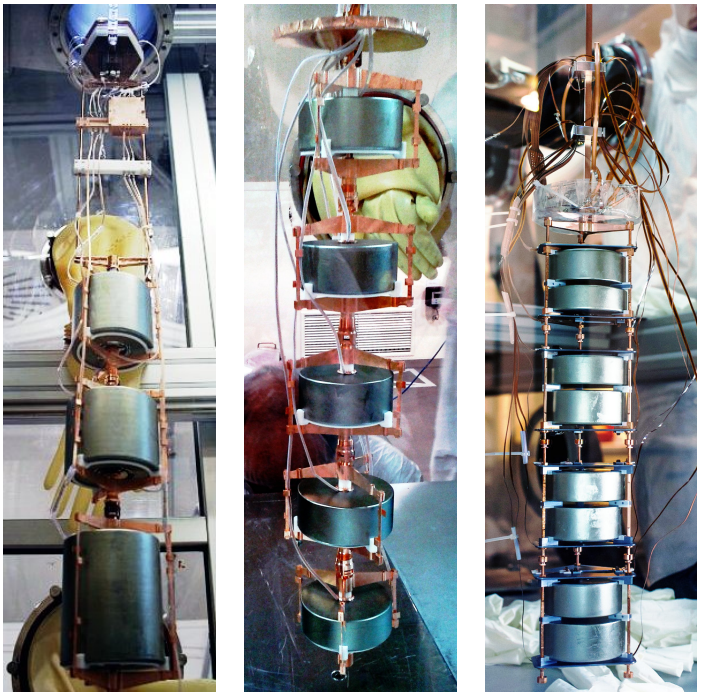

Figure 4.3.: *Left*: Phase I coaxial detector string. *Middle*: Phase I BEGe detector string. *Right*: Phase II BEGe detector string.

to deploy up to 14 detectors: three strings with three semi-coaxial detectors each were operated during all Phase I, while one string was exploited for deploying two GTF detectors in the first half of the data collection, and 5 BEGe detectors from July 2012 on.

In Phase II, about 40 detectors are going to be deployed in 7 strings. The design of the detector holder has been changed, in order to allow the installation of up to 8 BEGe detectors on one string. Special care has been taken in the further reduction of the used material quantity. In particular, given that crystalline silicon is typically more radio-pure than copper, the copper stars have been substituted by silicon plates. Fig. 4.3, right, shows 8 BEGE detectors mounted on the new holder prior to the deployment in LAr during a Phase II commissioning run. The detectors are mounted back-to-back in couples, on the top and bottom of which the crystalline silicon plates are present. The whole structure is held by three copper pillars. Moreover, the copper signal contacts are replaced by wire bonds. In this way, the total amount of copper and PTFE is reduced by one third.

4.1.2 *Readout Electronics*

The germanium detectors in GERDA are readout with custom made charge sensitive preamplifiers directly operated in LAr. The schematic of the preamplifier, called CC2 [189], is shown in Fig. 4.4. It consists of an input JFET of type BN862 from NXP Semiconductors, and a second stage is an AD8651 from Analog Devices. This is in parallel with a feedback circuit, which allows to bring back the input voltage to its baseline value. A test pulse is sent periodically to the input JFET of the CC2, allowing to monitor the stability of the whole electronics chain. The preamplifiers are integrated on a Cuflon PCB, containing the circuits of three channels. The circuitry is encased in a copper box which provides electromagnetic shielding.

The cabling between the detector and the CC2 consists of non-coaxial PTFE insulated copper strips with a cross section of 0.8 mm^2. Coaxial cables of type SM50 from Habia are used for power supply and for the preamplifier output signal. This is readout by a flash analog-to-digital converter (FADC). The FADC, the HV modules and the pulser are in an electronics cabinet located just outside of the clean room. The total cables length between the CC2 and the electronic modules is about 20 m.

4.1.3 *LAr Veto*

A major upgrade for GERDA Phase II is the implementation of a system for the detection of the scintillation light in LAr. Two arrays of 9 and 8 PMTs are installed above and below the germanium detector strings, respectively, while a cylindrical structure of optical fiber coupled to silicon photo-multipliers (SiPM) surrounds the germanium detectors and substitutes the central part of the radon shroud. This is in Phase II no more necessary, thanks to the presence of light sensors. The PMTs are the 3" R11065-10/20MOD from Hamamatsu. They were chosen due to their low radioactivity ($<$ 2mBq/PMT) and low power consumption (1.6 µA at

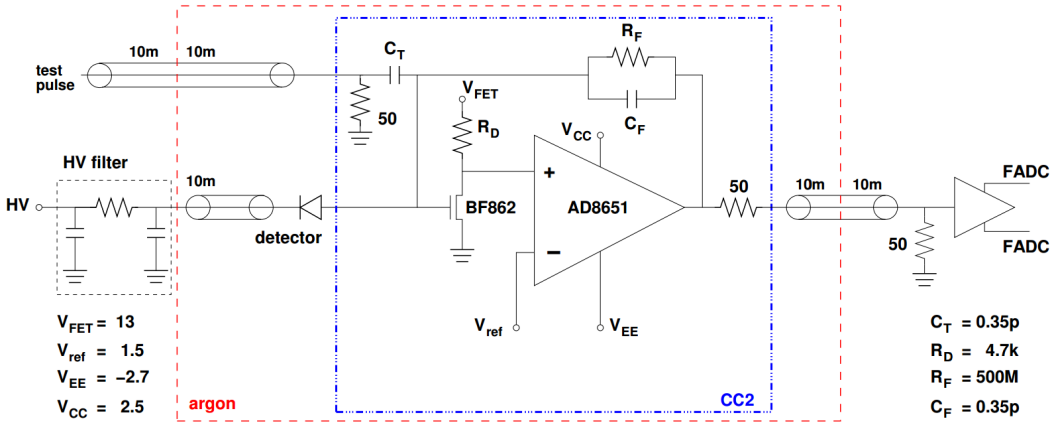

Figure 4.4.: CC2 schematic. Picture taken from [172].

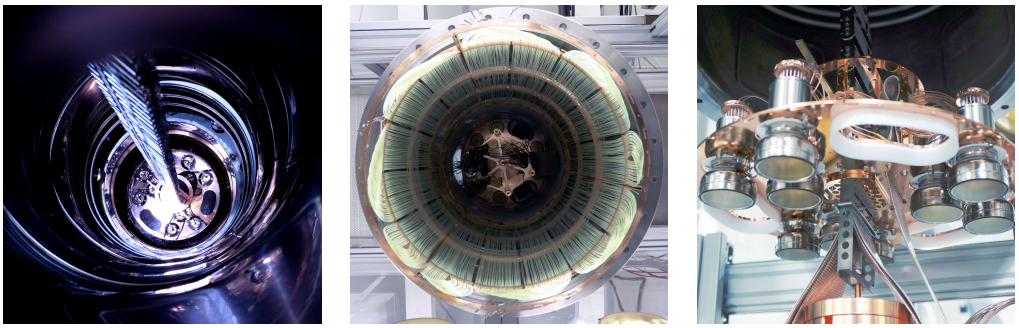

Figure 4.5.: *Left*: Phase II LAr veto system from the top of the cryostat. *Middle*: bottom view of the optical fiber system. *Right*: top PMT array.

1.5 kV) [190]. The PMTs are installed on the top and bottom of a cylinder of 49 cm diameter and 220 cm height. The lateral surface of the cylinder consists of a copper foil internally lined with a reflector foil (Tetratex coated with TPB as wavelength shifter [183]) for the upper and lower 60 cm, and of optical fiber for the central 100 cm part. The fibers are TPB-coated and have a cross section of 1×1 mm^2. They are coupled to SiPMs from Ketek, which are arranged in groups of 9. While the PMTs have a high efficiency in detecting the light inside the cylinder, the fiber structure is also capable of detecting events taking place outside it. The LAr veto system is shown in Fig. 4.5.

4.2 GERDA DATA STRUCTURE

The data collected in GERDA are organized in subsequent levels. The event reconstruction is based on the Majorana Gerda Data Object (MGDO) [191] and the GErda LAyouT for Input/Output (GELATIO) [192]. MGDO is a set of libraries containing the basic algorithms to be applied to the signal traces, and is maintained jointly by the Majorana and the GERDA collaborations. GELATIO is a C++ software package based on the MGDO libraries which provides general and flexible tools for the handling and analysis of GERDA data. Both MGDO and GELATIO depend on CLHEP [193] and FFTW3 [194] libraries for scientific computing. Moreover,

Table 4.3.: Data structure used in GERDA.

Data type	Format	Content
Tier0	Binary	Signal traces, digitizer infos
Tier1	ROOT	Signal traces, digitizer infos
Tier2	ROOT	Uncalibrated energy and A/E, trigger, rise-time, ...
Tier3	ROOT	Calibrated energy and A/E, quality cuts tags
Tier4	ROOT	Event tags for $0\nu\beta\beta$ analysis

they depend on ROOT [195] and TAM [196] for the data storage, data analysis and graphical rendering. GELATIO has a modular structure: each module is in charge of extracting information regarding one particular feature of the signal pulse, e.g. energy, baseline, rise time, amplitude of the current signal. The list of modules can be chosen by the user according to the specific need. An additional package for advanced data analysis, denoted as GERDA-ADA, is currently under development. Its completion is expected for the beginning of Phase II. More details on GERDA-ADA are given in App. C.

The standard data reconstruction procedure used in Phase I is the following:

- the whole event information (event waveform, type, time, muon veto flag, ...) is saved to disk in binary format (tier0);
- the tier0 are transformed to ROOT files (tier1) using MGDO;
- a GELATIO macro is used to extract all the needed physical quantities, e.g. energy, baseline, trigger time, rise time, ... All the computed quantities are stored in tier2 files;
- the calibration curves and the flags for the quality cuts computed. These flags regard the coincidences, muon vetoed events, pile-up events, discharges, pulser events, etc. The calibrated energy and the quality cut flags are saved in the tier3 files;
- The PSD is applied, and all event flags for $0\nu\beta\beta$ analysis are written to tier4 files.

The data reconstruction for Phase II is similar to that of Phase I, with the only difference that the PSD cut tags and the LAr veto tags are included already at the tier3 level.

A summary of the different data levels used in the GERDA Phase I is reported in Tab. 4.3.

4.3 GERDA PHASE I

The Phase I data were collected from 9 Nov. 2011 to 21 May 2013. Some additional data were collected in summer 2013. The data taking was divided in runs of variable duration. A new run was started after the configuration of the detector array was changed, in case the settings of some channel was modified, or in case of gain instabilities induced by external factors. The run numbering started during

the Phase I commissioning in 2010. The Phase I data sets comprises the runs 25–43. The channel mapping for all Phase I runs is reported in Tab. 4.4.

Table 4.4.: Detector configuration for all runs of GERDA Phase I. The detectors in gray were installed and operated for all or a fraction of their deployment time, but their data were not used for any analysis due to very poor energy resolution induced by an incomplete depletion or to strong and unexplained gain instabilities.

DAQ	Run number and data taking period			
channel	24–32	33–34	35–46	47–49
mapping	09.11.11–22.05.12	02.06.12–02.07.12	08.07.12–21.05.13	31.05.13–30.09.13
0	ANG1	ANG1	ANG1	ANG1
1	ANG2	ANG2	ANG2	ANG2
2	ANG3	ANG3	ANG3	ANG3
3	ANG4	ANG4	ANG4	ANG4
4	ANG5	ANG5	ANG5	ANG5
5	RG1	RG1	RG1	RG1
6	RG2	RG2	RG2	RG2
7	RG3	RG3	RG3	RG3
8	GTF112	GTF112	GTF112	GTF112
9	GTF45		GD32B	
10	GTF32		GD32C	
11			GD32D	
12			GD32B	
13			GD35C	

In the first part of Phase I (runs 25–32), the 8 enriched semi-coaxial detectors were deployed together with 3 semi-coaxial detectors with natural abundance. The ANG's and RG's detector were installed in the 3-string arm along with GTF112 and coupled in direct current (DC), while GTF45 and GTF32 were mounted on the 1-string arm and coupled in alternating current (AC). Already from the beginning of the data taking, RG3 was characterized by a high leakage current. Its bias voltage was progressively reduced until is was brought down to 0 V in March 2012. Similarly, the voltage of ANG1 was reduced starting from March 2012 and set to 0 V in May 2012. The data collected with these two detectors were not used for any of the physics analyses, but they were anyway exploited for the anti-coincidence cut for the periods in which they had non-zero voltage.

In May 2012 the 1-string arm detectors were extracted to prepare the installation of 5 BEGe detectors. One month of data (runs 33–34) was collected with the 3-string arm only. Most of the channels were affected by strong instabilities during run 33, which was therefore not used for any analysis.

From July 2012 to May 2013 the 5 BEGe detectors were operated in the 1-string arm, in addition to the 8 semi-coaxial in the 3-string arm. Between November 2012 and March 2013 the HV of RG2 was lowered from 4000 V down to 2000 V due to high leakage current. The data collected with RG2 up to run 43 are used for physics analyses, while those collected afterwards are only used for the anti-coincidence cut. Moreover, the data collected with GD35C are only employed for

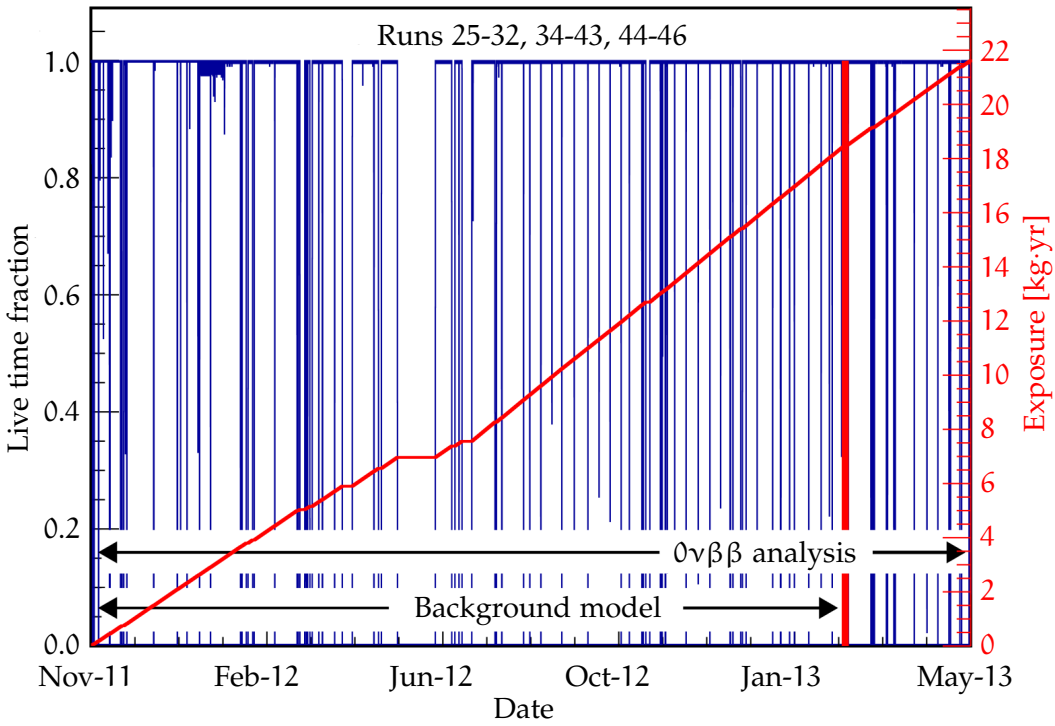

Figure 4.6.: Duty factor and exposure for GERDA Phase I.

the anti-coincidence cut due to the strong instabilities characterizing this detector over all its operation period.

After the end of Phase I, the data collection continued with the 3-string arm only until September 2013. In July 2013 the water tank was emptied to allow some maintenance operations, hence the muon veto cut could not be applied. In the same period several calibration data sets with a ^{56}Co source were acquired (see Sec. 5.9). The second part of this period was dedicated to a long background measurement with no interruptions. Its goal was to study the dependence of the gain and BI on the standard operations performed during the data taking, e.g. calibrations, and on the temperature stability in the clean room.

The data set for the $0\nu\beta\beta$ decay analysis consists of the runs 25–34 and 35–46. The measurement live time fraction f_t for this period is 88.1%. The live time is computed as the product between the number of pulser events and the time delay between them, while the live time fraction is the ratio between the live time and the total Phase I duration. The live time fraction during all Phase I is shown in blue in Fig: 4.6: during data taking, it is at a constant value of 1, with several short interruptions corresponding to the calibration runs. A longer interruption due to the operations for the substitution of GTF45 and GTF32 with the BEGe detectors is visible around June 2012. Some shorter interruptions mostly due to maintenance operations in the clean room are also present. In the same figure, the red curve shows the total exposure collected with the enriched detectors as function of time. A total of 17.9 kg·yr and 2.4 kg·yr were collected with the semi-coaxial and BEGe detectors, respectively.

During all data taken from 11 January 2012 the number, energy and waveforms of events in a 40 keV region around $Q_{\beta\beta}$ were automatically removed from the

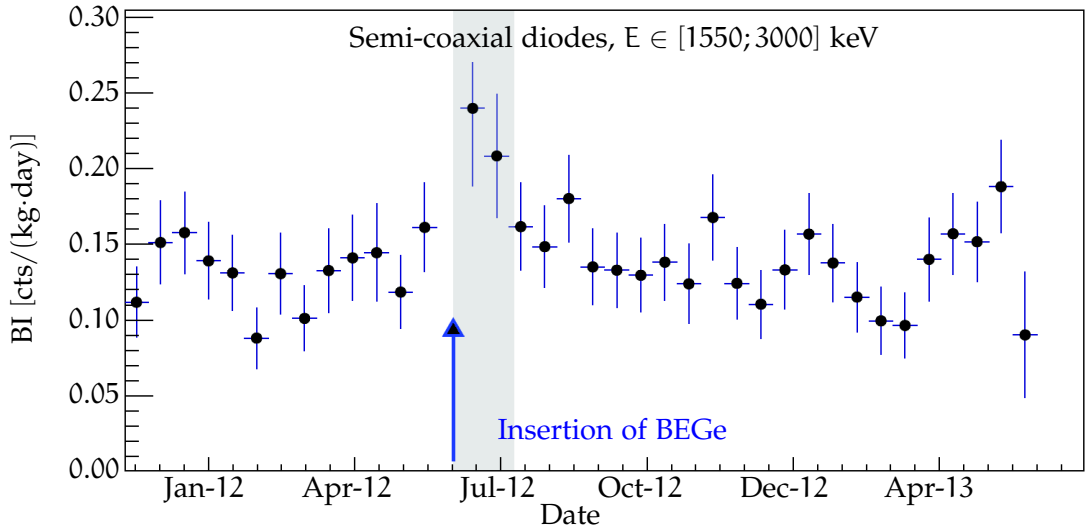

Figure 4.7.: Time development of the Phase I background index.

data flow. This blinding procedure was chosen to avoid any bias in the data selection and analysis. In particular, the availability of a reliable background model was considered a mandatory requirement to be fulfilled before the unblinding. Namely, only if the energy spectra were modeled with proper Monte Carlo (MC) simulations a prediction could be made on the background distribution and amplitude around $Q_{\beta\beta}$. The data collected up to 3 March 2013 (see Fig. 4.6) were used for the development of the background model, while the $0\nu\beta\beta$ analysis was performed on the data collected up to 21 May 2013. The unblinding was performed in June 2013, once the background model was completed and all steps for the $0\nu\beta\beta$ decay analysis were defined and frozen.

In order to maximize the sensitivity to a possible $0\nu\beta\beta$ decay signal, it is advantageous to divide the data into separate subsets according to the energy resolution and BI. This is the case for the data collected with the semi-coaxial and BEGe detectors, which are therefore divided. Moreover, the data from the semi-coaxial are further separated in two data sets according to the BI. Fig. 4.7 shows the BI in counts/(keV·kg·yr) before PSD as function of time for all the semi-coaxial detector. The [1500; 3000] keV energy range is used for the calculation, and the points correspond to 15 days time intervals. The average value over all Phase I is ~ 0.14 cts/(kg·day). Variations within $\pm 1\sigma$ are present, as it is to expect from background fluctuations. The data around July 2012 are characterized by a BI ~ 0.22 counts/(keV·kg·yr), which is $\sim 50\%$ higher than the average. This higher value is related to the operations for the removal of GTF45 and GTF32 and the subsequent insertion of the BEGe detectors. The data taken after this period are characterized by a BI close to the average. On the basis of this, the data from the semi-coaxial detectors are divided in two data sets: a "silver" data set comprising the data with higher BI and corresponding to runs 34–35, and a "golden" data set which includes all the remaining runs. The exposure of the three data sets are reported in Tab. 4.5.

Table 4.5.: Data sets parameters for the Phase I $0\nu\beta\beta$ decay analysis. The total efficiency is defined as $\varepsilon_{tot} = f_{enr} \cdot f_{AV} \cdot \varepsilon_{\gamma} \cdot \varepsilon_{psd}^{SSE}$. Values taken from [102].

Data set	$m \cdot \Delta t$ [kg·yr]	ε_{tot}	Counts in [1930; 2190] keV	BI [counts/(keV·kg·yr)]	Counts in ROI
No PSD					
Golden	17.9	0.688 ± 0.031	76	18 ± 2	5
Silver	1.3	0.688 ± 0.031	19	63^{+16}_{-14}	1
BEGe	2.4	0.720 ± 0.018	23	42^{+10}_{-8}	1
With PSD					
Golden	17.9	$0.619^{+0.044}_{-0.070}$	45	11 ± 2	2
Silver	1.3	$0.619^{+0.044}_{-0.070}$	9	30^{+1}_{-9}	1
BEGe	2.4	0.663 ± 0.022	3	5^{+4}_{-3}	0

4.3.1 *The Background in* GERDA *Phase I*

The physics spectra for the semi-coaxial and BEGe detectors relative to the period used for the development of the background model are shown in Fig. 4.8. The total number of counts is about a factor 10 higher for the semi-coaxial than for the BEGe detectors, which respects the factor 10 ratio in the exposure. The spectra are characterized by a continuum starting from the threshold at ~ 100 keV up to ~ 500 keV. This is induced by the β decay of ^{39}Ar, with a Q-value of 565 keV [197]. The continuum spectrum of $2\nu\beta\beta$ decay is dominant in the [500; 1800] keV range. Two γ lines induced by ^{40}K and ^{42}K are visible at 1461 and 1525 keV, respectively. For the semi-coaxial detectors, additional lines induced by the ^{228}Th and ^{234}U decay chains are present. As an example, two ^{214}Bi peaks at 1765 and 2204 keV and the ^{208}Tl peak at 2615 keV are labeled. The green area in the spectra corresponds to the 40 keV blinded region around $Q_{\beta\beta}$.

Ora viene fuori un isotopo del bismuto! – mi precipitavo a dire [...] – Scommettiamo! Macché: era un atomo di polonio, sano sano.
I. Calvino, Le Cosmicomiche

Above 3000 keV the spectrum is dominated by α events, induced by some contamination of the detector p^+ contacts. In principle, only α emitted in the detector volume or on the p^+ contact can be detected. If the contamination were internal, a forest of sharp peaks would be expected in correspondence to the possible energies of the emitted α's. In Phase I data, the α peaks present a pronounced low-energy tail, which can be interpreted with a incomplete collection of the deposited charge in case of an α emission in the p^+ dead layer. For the BEGe spectrum and after normalizing for the exposure, the α contamination is about one order of magnitude lower than that of semi-coaxial [198]. This is explainable with the smaller dimensions of the p^+ contact in BEGe detectors and, possibly, with a lower surface contamination. The main α peak around 5300 keV is given by ^{210}Po. This is verified by a fit of the time distribution for the events in the [3500; 5300] keV range, yielding an half-life in agreement with that of ^{210}Po [198, 199]. Additional α particles emitted by other members of the ^{234}U decay chain are visible.

Cosa diceva Madame Curie? Se il polonio è a 210, ci ritirano la patente?
M. Crozza alias A. Zichichi

Two background models have been developed [198, 199, 200] for the Golden and BEGe data sets, as well as for the spectrum taken with the GTF detectors. The same was not possible with the Silver data set due to the limited number of counts

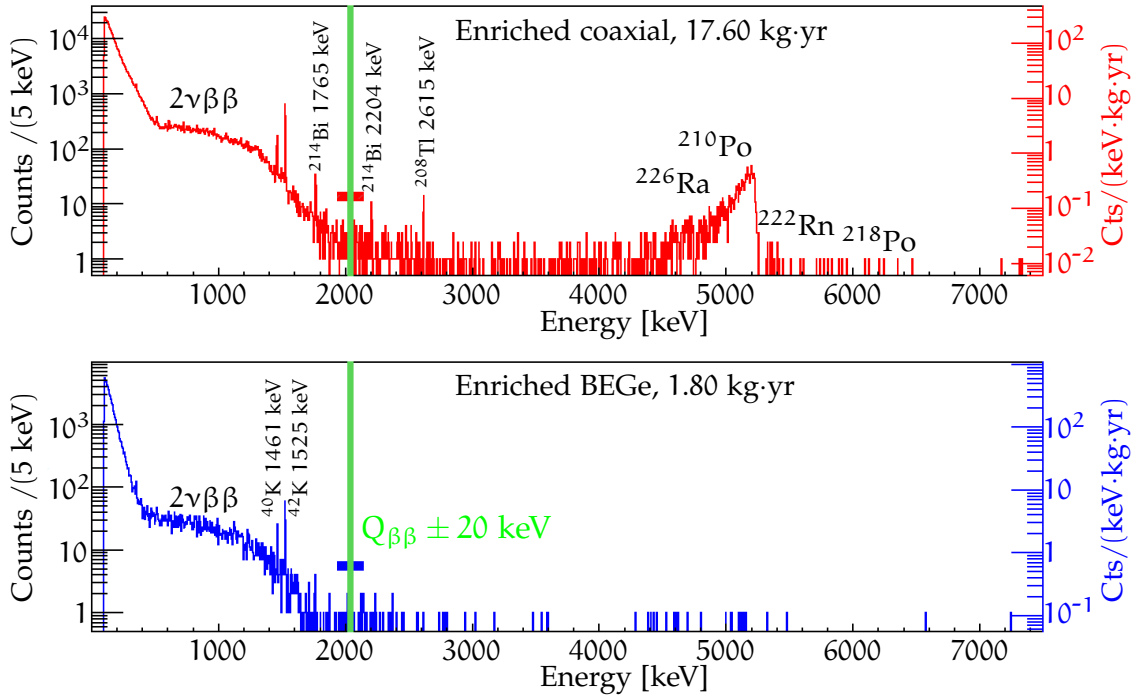

Figure 4.8.: Phase I background spectrum before the application of PSD for the semi-coaxial (top) and BEGe detectors (bottom).

present in the spectrum. The models explain all the features of the Phase I spectra in the [570; 7500] keV range.

In the first "minimum" model, the MC simulations of all visible contributions are included. In the second "maximum" model the same contributions are present, but multiple possible locations for some background contamination are considered. Given the limited statistics, the maximum model does not allow to disentangle between different possible origins of these contamination, and the p-value of the two models are comparable. The background models are then used to extract the BI at $Q_{\beta\beta}$. The two predictions are in good agreement within the uncertainties. Furthermore, an agreement is found also with the BI computed from the average number of counts in the [1930; 2190] keV region, with the exclusion of the blinded region and of a 10 keV region around the ^{208}Tl SEP at 2104 and the ^{214}Bi line at 2119 keV. This quantity is reported in Tab. 4.5 for all data sets before and after the application of PSD. Tab. 4.5 also reports the total efficiency, computed as (see Eq. 2.38): $\varepsilon_{tot} = f_{enr} \cdot f_{AV} \cdot \varepsilon_{\gamma} \cdot \varepsilon_{psd}^{SSE}$, the number of counts in the [1930; 2190] keV region (with the exclusion of the mentioned sub-regions), and the number of counts in a 10 keV wide ROI around $Q_{\beta\beta}$.

4.3.2 *Analysis of* $0\nu\beta\beta$ *Decay*

The analysis of $0\nu\beta\beta$ decay is performed with an unbinned fit in the [1930; 2190] keV region, with the exclusion of the [2099; 2109] and [2114; 2124] keV regions. The spectra of the Golden, Silver and BEGe data sets after the application of PSD are fitted separately with a Gaussian distribution over a flat background. These are parametrized as in Eq. 2.38. The fit has four parameters: $T_{1/2}^{0\nu}$, which is common

for all data sets, and one BI for each data set. All the other parameters are fixed to the value obtained from independent measurements. The systematic effect coming from the uncertainty on the additional parameters (e.g. enrichment, active volume fraction, FWHM, ...) are computed by re-running the fit n times after having varied the parameter values within according to the available distributions.

Both a profile-likelihood and a Bayesian maximum-likelihood analyses are performed. In the first case, the limit on the $0\nu\beta\beta$ decay half-life is [102]:

$$T^{0\nu}_{1/2} > 2.1 \cdot 10^{25} \text{ yr} \qquad (90\% \text{ C.L.}), \tag{4.1}$$

while in the second case [102]:

$$T^{0\nu}_{1/2} > 1.9 \cdot 10^{25} \text{ yr} \qquad (90\% \text{ C.I.}), \tag{4.2}$$

where C.I. stays for credibility interval.

The median sensitivity for a 90% C.L. (or C.I.) limit is computed generating n Toy-MC spectra according to a flat distribution with the proper BI and fitting this with the same distribution used for the signal search. In the case of profile-likelihood, the median sensitivity is:

$$T^{0\nu}_{1/2} > 2.4 \cdot 10^{25} \text{ yr} \quad , \tag{4.3}$$

while the Bayesian approach yields:

$$T^{0\nu}_{1/2} > 2.0 \cdot 10^{25} \text{ yr} \quad . \tag{4.4}$$

The slight difference on both the experimental limit and median sensitivity between the two analysis methods comes from the deep Poisson regime of the considered data. Namely, even in case a spectrum with 0 events is measured, the Bayesian 90% C.I. limit on the number of signal counts n_s is ~ 2.3, while this is not the case for the profile likelihood. In truth, a direct comparison of the two results is not possible because of their different statistical meanings.

If the GERDA Phase I limit is combined with the 2001 HdM [127] and 2002 IGEX [201] results, yielding a best fit for $n_s = 0$ and a 90% C.L. half-life limit of:

$$T^{0\nu}_{1/2} > 3.0 \cdot 10^{25} \text{ yr} \quad . \tag{4.5}$$

The GERDA limit is compared with the 2004 HdM claim [97]. The model H_1 is assumed, with a $0\nu\beta\beta$ decay half-life as reported in [97], and the probability of obtaining a best fit of 0 events (H_0) with the profile likelihood analysis for the GERDA Phase I data is $P(n_s = 0|H_1) = 0.01$. Moreover, the ratio of the two models probabilities (Bayes ratio) is $P(H_1)/P(H_0) = 0.024$. If the combined limit is taken (Eq. 4.5), the Bayes ratio is further reduced to $2 \cdot 10^{-4}$. Based on this results, the 2004 claim of evidence for a $0\nu\beta\beta$ decay signal is strongly disfavored with a NME- and model-independent measurement.

4.3.3 *Analysis of $2\nu\beta\beta$ Decay*

In addition to the $0\nu\beta\beta$ decay search, the Phase I data are used for other analyses, including the measurement of $2\nu\beta\beta$ decay half-life. A detailed description of the analysis summarized here is available in [101].

The $2\nu\beta\beta$ decay analysis is performed on the Golden data set only in order to minimize the systematic uncertainty on $T^{2\nu}_{1/2}$. The considered exposure is 17.9 kg·yr. Only unambiguously identified background components are inserted in the model, and the possible different location of the radioactive contaminants is considered as a systematic. As for the background model, the fit is performed in the [570; 7500] keV range. The measured $2\nu\beta\beta$ decay half-life is:

$$T^{2\nu}_{1/2} = \left(1.926^{+0.025}_{-0.022}(\text{stat})^{+0.091}_{-0.091}(\text{syst})\right) \cdot 10^{21} \text{ yr}, \tag{4.6}$$

where the first error is the statistical uncertainty of the fit, and the systematic error comprises the effects of the detector parameters, of the fit model, of the geometry and particle tracking limited precision in the MC simulations, and of the data acquisition and selection. Summing the two uncertainties in quadrature:

$$T^{2\nu}_{1/2} = (1.926 \pm 0.094) \cdot 10^{21} \text{ yr}. \tag{4.7}$$

The very small uncertainty of $\sim 5\%$ is achieved thanks to the unpreceeded signal-to-background ratio of 3 : 1 in the [570; 2039] keV range. The previous $T^{2\nu}_{1/2}$ determination reported by GERDA [161] was based on the first 5.04 kg·yr of Phase I data, yielding to a measured value of:

$$T^{2\nu}_{1/2} = \left(1.84^{+0.14}_{-0.10}\right) \cdot 10^{21} \text{ yr}, \tag{4.8}$$

which is in very good agreement with the latest result.

5

CALIBRATION OF THE ENERGY SCALE

This chapter describes the analysis of the GERDA calibration data. After a summary of the properties of the employed calibration sources (Sec. 5.1), the main characteristics of the calibration software are reported in Sec. 5.2. The event selection for the analysis of the calibration data is reviewed in Sec. 5.3, while Secs. 5.4 and 5.5 describe the search and fit of the gamma lines, respectively. The procedure for the extraction of the calibration and resolution curves is reported in Sec. 5.6, and the calculation of the systematic uncertainties of the energy scale is described in Sec. 5.7. The determination of the energy resolution at $Q_{\beta\beta}$ for calibration and physics data is reported in Sec. 5.8. Finally, the analysis of the data collected in GERDA with a ^{56}Co source and the study of systematic uncertainties on the energy scale based on these data are reviewed in Sec.5.9.

5.1 ^{228}TH CALIBRATION SOURCES

The choice of a calibration source is based on several requirements. Firstly, a substantial number of gamma lines has to be available for the calibration of the energy scale up to $Q_{\beta\beta}$. Secondly, the half-life has to be at least of the same order of the experiment's lifetime, i.e. a few years. Finally, the PSD methods for germanium detectors are usually tuned with double escape events, which have very similar signal properties to the expected $0\nu\beta\beta$ decay events (see Ch. 7). For this reason, a double escape peak (DEP) with sufficient statistics has to be available. The candidate which optimally fulfills these requirements is ^{228}Th, with a 1.9 yr half-life, a dozen of high statistics lines between 500 keV and 2.6 MeV, and a DEP at 1592.5 keV [182].

The decay scheme of ^{228}Th is shown in Fig. 5.1. After the decay $^{228}\text{Th} \rightarrow {}^{224}\text{Ra}$, other 6 decays take place, until the the stable ^{208}Pb nucleus is reached. The half-life of all the daughter isotopes if much shorter than that of ^{228}Th. The longest half-life is that of ^{224}Ra, with 3.6 days. Thanks to this, the decay chain is always in equilibrium. A possible break of the equilibrium is possible only in the first few weeks after the source production. Namely, ^{226}Ra might escape the source volume during the production procedure due to its high chemical reactivity. While the first five decays of the chain take place only on one channel, ^{212}Bi decays to ^{208}Tl in $\sim$ 36% of the cases, and to ^{212}Po for the remaining 64%. In all cases, 5 α particles are emitted in the chain. The energies of all α's with $> 1\%$ intensity which can be emitted in the chain are reported in Tab. 5.1. Since the GERDA sources are encapsulated in stainless steel, the α's are absorbed in the source substrate it-

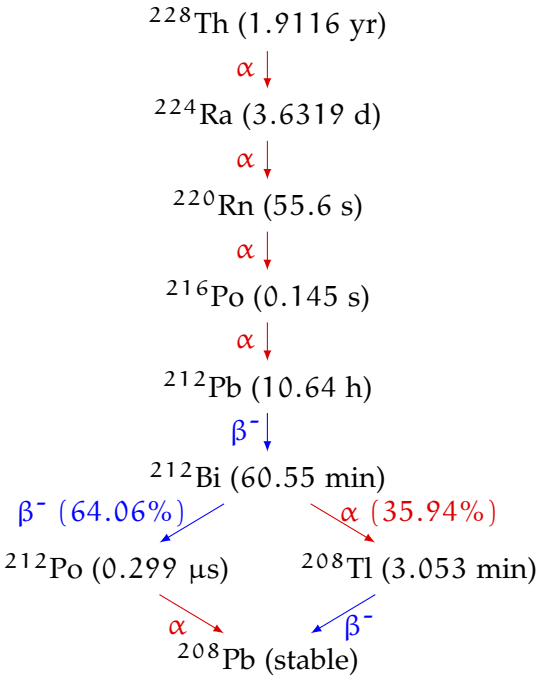

Figure 5.1.: ^{228}Th decay chain. The half-lives of all isotopes are reported in parenthesis. Values from [197].

self. This might yield (α, n) reactions, which can induce neutron activation of the germanium detectors or the material in their vicinity. The production of custom ^{228}Th sources with reduced neutron activity is described in Ch. 8.

The α or β decays of the ^{228}Th chain produce excited nuclei, which reach their ground state emitting one or more γ rays. In order to reduce the disk space usage, the energy threshold for the majority of Phase I calibration runs was set to $\sim$ 400 keV. Since $Q_{\beta\beta}$ for ^{76}Ge is at 2039 keV and the major contribution to the GERDA physics spectrum below 500 keV is the ^{39}Ar β continuum (see Sec. 4.3.1), there is no need to have a very precise calibration at low energy. In spite of this, the uncertainty of the energy scale below 500 keV is at 0.2 keV level, as described in Sec. 5.7. The list of all γ's of the ^{228}Th chain with $>$ 500 keV and with a high enough intensity is reported in Tab. 5.2. The minimum intensity for a γ to be suitable for the energy calibration depends on the collected statistic, on the intensity of the Compton continuum in vicinity of the corresponding spectral peak, and on the energy resolution, hence it cannot be defined a priori. The γ's listed in Tab. 5.2 are those which were exploited for energy calibration of GERDA Phase I data in at least 20% of the considered data sets. Most of these γ's are emitted after the decays of ^{212}Bi and ^{208}Tl. Additionally to these, a 661.7 keV gamma is listed in Tab. 5.2 due to a γ ^{137}Cs contamination of one of the Phase I sources.

Che cos'è il bismuto? Se devi fare tacere qualcuno, usi il bismuto.
M. Crozza alias A. Zichichi

A typical calibration spectrum is shown in Fig. 5.2, with the main lines labeled. In particular, a full energy peak (FEP) induced by a ^{212}Bi γ is visible at 1620.5 keV. Its intensity is comparable with that of the DEP from ^{208}Tl at 1592.5 keV. The events from these two peaks are exploited for tuning the PSD algorithms.

Isotope	Energy [keV]	Intensity [%]
^{228}Th	5340.36(15)	27.2(10)
^{228}Th	5423.15(22)	72.2(11)
^{224}Ra	5448.6(12)	5.06(5)
^{224}Ra	5685.37(15)	94.92(5)
^{220}Rn	6288.08(10)	99.886(17)
^{216}Po	6778.3(5)	99.9981(3)
^{212}Bi	6050.78(3)	25.13(7)
^{212}Bi	6089.88(3)	9.75(5)
^{212}Po	8784.12(12)	100

Table 5.1.: Alpha particles with $> 1\%$ intensity. Values from [197].

Isotope	Energy [keV]	Intensity [%]
^{212}Bi	727.330(9)	6.67(9)
^{212}Bi	785.37(8)	1.102(13)
^{212}Bi	893.408(5)	0.378(19)
^{212}Bi	1078.62(2)	0.564(19)
^{212}Bi	1512.7(3)	0.29(4)
^{212}Bi	1620.50(10)	1.47(3)
^{208}Tl	510.77(10)	22.60(20)
^{208}Tl	583.187(2)	85.0(3)
^{208}Tl	763.13(8)	1.79(3)
^{208}Tl	860.557(4)	12.50(10)
^{208}Tl	2614.511(10)	99.754(4)
^{208}Tl	2103.511(10)	SEP
^{208}Tl	1592.511(10)	DEP
^{137}Cs	661.657(3)	85.10(20)
	511	Annihilation

Table 5.2.: Gamma lines > 500 keV relevant for the energy calibration of GERDA. Values from [197].

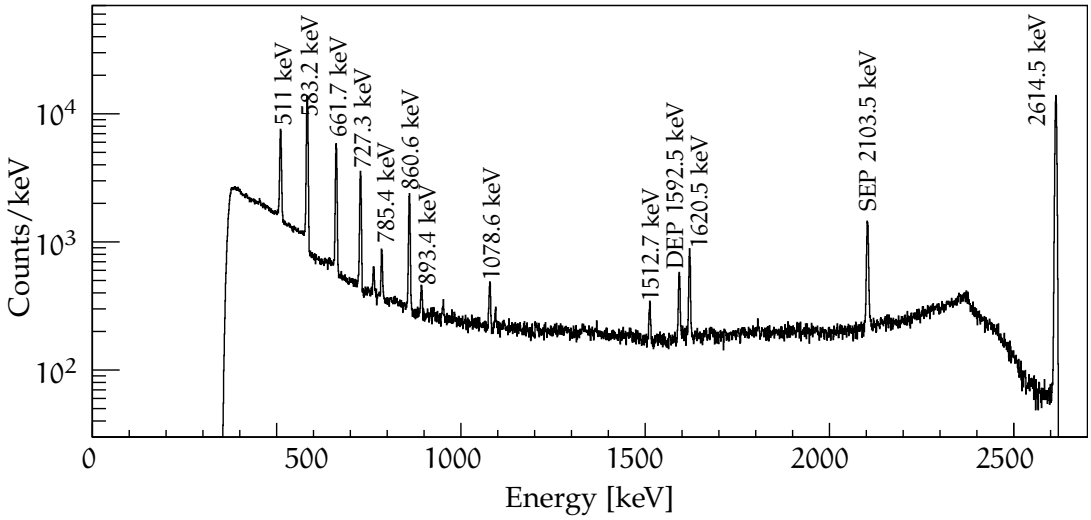

Figure 5.2.: ^{228}Th spectrum for ANG3.

5.2 THE GERDA CALIBRATION SOFTWARE

Energy calibration is a crucial part for the analysis chain because the results extracted from the physics data are strongly dependent on it. As in any spectroscopy experiment, the calibration has the aim of assigning a physical value to the reconstructed energy of an event taking place in the detector. This is done collecting data with a radioactive source, identifying the peaks in the measured spectrum and extracting their position. Once enough peaks are identified and their position obtained, a calibration curve can be calculated. Two typical problems are present in this process. Firstly, the extraction of the peak positions is done via a fit (χ^2 minimization of log-likelihood maximization). Several limitations are introduced by the used algorithm: the selected fit region, the binning used for the histogram and, last but not least, the function used for the fit. Secondly, the calibration curve is calculated via a χ^2 minimization. As for the peak fitting, the result depends on the choice of the function.

Other limitations arise from the nature of the GERDA Phase I data and the properties of the experimental setup:

- a calibration run was taken every $7-10$ days since the beginning of Phase I in November 2011. A total of 72 (45) data sets were taken with the semi-coaxial (BEGe) detectors. Given the large number of data sets involved, an automatic procedure is required for the analysis;
- several detector configurations were present during Phase I data, including the switching off of two detectors and the exchange of the crystals of the one-string arm. The software should therefore take these modifications into account;
- the energy resolution is different for each detector. The binning of the spectra has to be chosen accordingly: the bins should be small enough to fully exploit the available information, and at the same time large enough not to limit the fit algorithm performance;
- the peak shape is different for each detector, depending on the detector performance and the position of the calibration source. Moreover, the algorithm used to extract the energy from the waveforms might be more or less sensitive to the charge collection inefficiency, leading to the presence of low-energy tails. If the parameters of the energy reconstruction algorithm are different between data sets, the peak shape could be different also for the same detector. An automatic tuning of the fitting function is therefore needed.

The calibration data contain a lot of additional information which is useful for a successful analysis of the GERDA data. As an example, the resolution curves, i.e. the FWHM as a function of energy is needed for the convolution of the Monte Carlo (MC) spectra. Moreover, several other quantities, as the peak positions in the raw spectra, their resolution as well as the parameters of the calibration curves can be used to monitor the stability of the setup over time.

A calibration program has been developed in the framework of this PhD thesis with the aim of reducing as much as possible the uncertainty on the measured variables and of making the data processing as automatic as possible. The most

important features of the program, which are discussed in detail in the following sections are the following:

- the quality cuts are tuned in order to have spectra containing only clean and well-reprocessed physical events;
- the fit procedure is automatized, reducing to a very high degree the bias given by the user, e.g. the choice of the binning or of the fit range, and the initial parameters of the fitting function. Moreover an automatic check of the fit performance is included in the code, and not properly fitted peaks are skipped.

All the plots present here refer to the ANG2 detector and the calibration taken on February 15, 2013. In case a figure refers to a different detector or run, this is reported in the caption.

The calibration program for GERDA Phase I is divided in three subroutines. Firstly, a list of quality cuts is applied to the tier2 data with the aim of selecting only physical, clean and well reconstructed events. Secondly, a peak search is performed, and the recognized peaks are identified comparing their position in the uncalibrated spectrum with the literature values of Tab. 5.2. Finally, the identified peaks are fitted with a proper function, and the calibration and resolution curves are extracted.

5.3 QUALITY CUTS FOR THE ANALYSIS OF CALIBRATION SPECTRA

This section describes the procedure used to recognize the events which are either non-physical, or not properly reconstructed, or which might worsen the quality of the calibration spectrum. In general, the goal of the quality cuts is to reject the events which might induce artifacts in the energy spectrum, e.g. non-Gaussian tails in the peaks. This is done to facilitate the fit of the peaks, and to perform this on a spectrum which is as similar as possible to a physics spectrum, from which coincidence, pile-up and non-physical events are removed. The events selection consists of seven steps. Each cut is applied only to those events which survived the previous ones.

A typical calibration spectrum before the application of quality cuts is shown in Fig. 5.3. About 10 physical peaks can be exploited for the energy calibration. The peak around 6000 a.u., corresponding to about 3000 keV, is given by pulser events, while the peak at about 4800 a.u. is the ^{208}Tl FEP at 2614.5 keV. The events above the FEP are given by the summation of two coincident γ events.

For a typical one hour long calibration, 10^5 to $3 \cdot 10^5$ events are recorded for each semi-coaxial detector, and $4 \cdot 10^4$ to 10^5 for each BEGe. The explanation for this lower statistics in the BEGe's can be found in their smaller dimensions and in the fact that five detectors are on the same string. To collect more events the sources should be left in more different positions for long enough time. In any case, the better energy resolution of the BEGe's allows to identify and properly fit all the most prominent peaks regardless of the lower statistic. As a result, the uncertainty on the energy scale is comparable for the semi-coaxial and the BEGe detectors.

The first events to be rejected are the non-physical events by definition, i.e. the pulser generated events. These are responsible for a peak at energies around

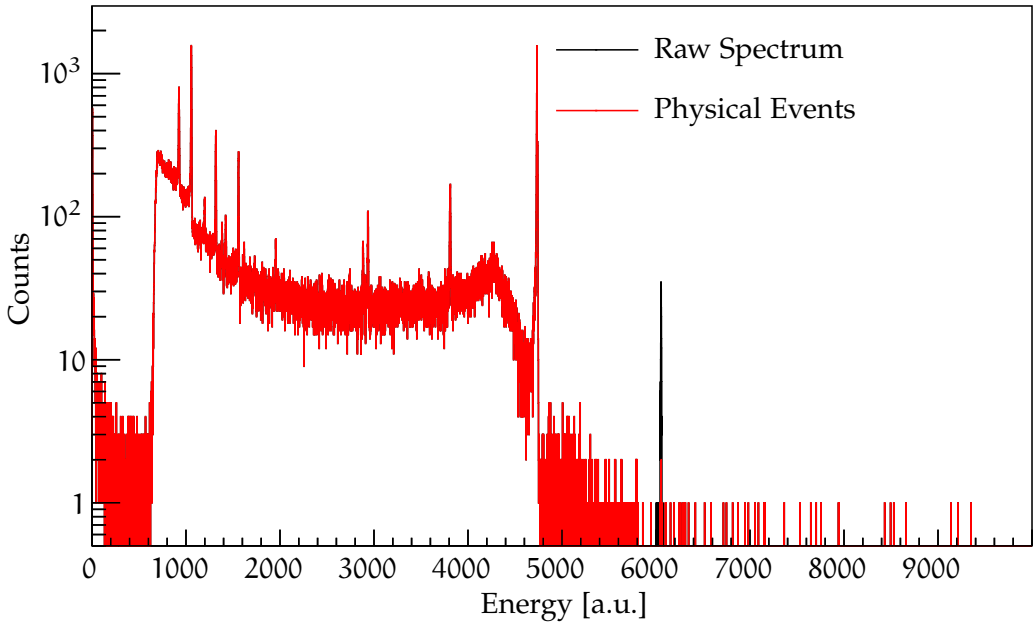

Figure 5.3.: ANG2 raw spectrum (black) and spectrum after rejecting the pulser events (red). The threshold for the main trigger is set here to about 500 keV. The events at very low energy are mostly random coincidences, while the peak around 6000 a.u. in the raw spectrum is given by the pulser events.

3000 keV. The actual position of the pulser peak with respect to the γ peaks depends on the amplitude of the original pulser signal, on the electronic components of the preamplifier, and on the charge collection properties of the detector. The physical and pulser events are identified by a tag "eventType" in the tier2 files: the first are labeled with eventType 1, the latter with 0. The raw spectrum and the spectrum after the cut of the pulser events are depicted in Figure 5.3.

The second cut regards the coincidences. In particular, events releasing energy in more than one channel are rejected. As Figures 5.4 and 5.5 show, this cut completely removes the very low-energy part of the spectrum. Namely, the events below the 400 keV region are coincidences by definition: a threshold is set at a voltage corresponding to $\sim$ 400 keV, and if the voltage of one channel overcomes that threshold, the energy and the waveform of all channels with non-zero energy are saved. Hence, the events with energy below 400 keV must be recorded in coincidence with some other event with $E > 400$ keV in a different channel.

The coincidence cut rejects 4 to 13% of the total number of physical events. The fraction of coincidence events strongly depends on the source activities, on the detector configuration, and on the distance between the sources and the crystals. The percentage of coincidence events for each channel is reported in Table 5.3. Most of the cut events are in the continuum, as it is reasonable for the case of an event undergoing a Compton scattering in a detector, and a full absorption in a different one.

The third cut is the rejection of the events for which the offline reconstruction of some parameter of interest (energy, rise time, baseline, trigger, ...) fails. Even

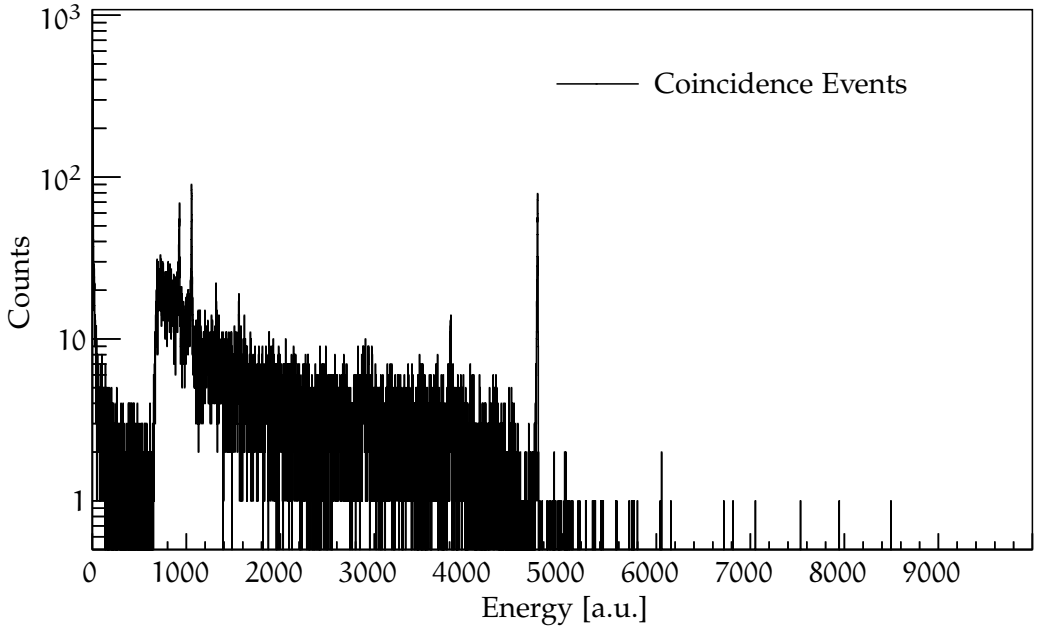

Figure 5.4.: Spectrum of the events in coincidence with some other detector. This cut mostly acts on the Compton continuum and at energies below the threshold, for which there must be a main trigger on another channel.

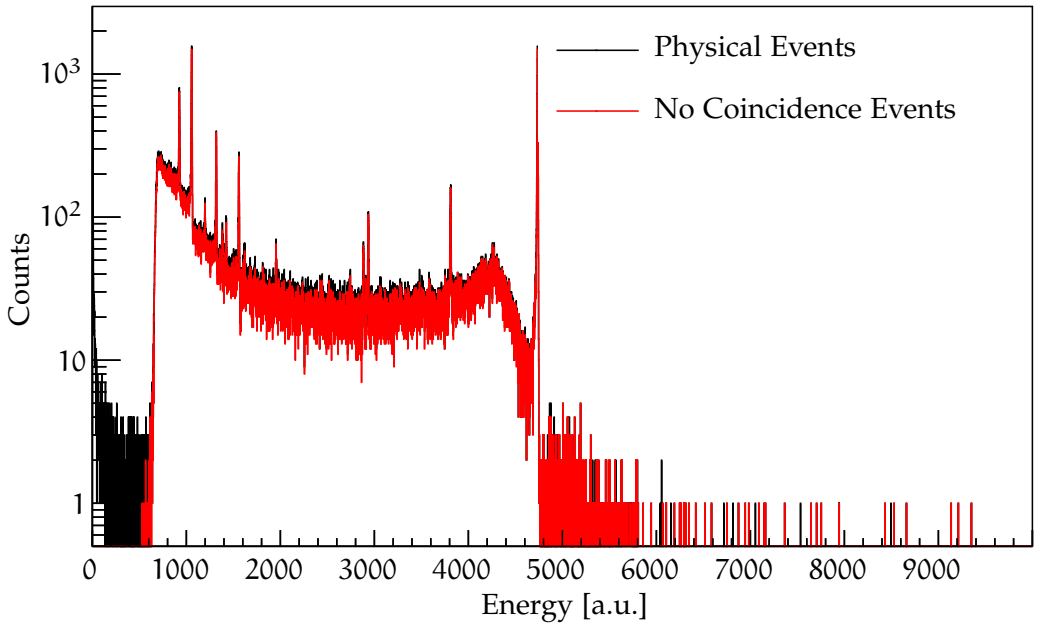

Figure 5.5.: Raw spectrum (black) and spectrum of the events surviving the coincidence cut (red). All the events below the 400 keV threshold are rejected, as well as part a $\sim 5\%$ fraction of the continuum.

Table 5.3.: Number of physical events and number of coincidences for each detector. The percentage of coincidence events is on average higher for the coaxial detectors because they were located in the 3-string arm and were therefore closer to other diodes than the BEGe's. Moreover the volume of a coaxial detector is roughly a factor three bigger than that of the BEGe's. The values refer to the calibration run taken on the 15 February 2013.

Detector	Physical Events	Coincidences
ANG2	233946	25026 (10.7%)
ANG3	166048	17683 (10.7%)
ANG4	152400	17235 (11.3%)
ANG5	230211	22471 (9.8%)
RG1	78665	9812 (12.5%)
RG2	168898	9641 (5.7%)
GTF112	149383	17346 (11.6%)
GD32B	63805	5614 (8.8%)
GD32C	85489	7404 (8.7%)
GD32D	469157	5575 (8.1%)
GD35B	40979	2814 (6.87%)
GD35C	49354	1831 (3.71%)

though there is no physical reason behind, this selection is helpful to monitor the effectiveness of the reconstruction algorithms used in GELATIO. The effect of the cut is very small for all calibration data sets, since just 0.1–0.2% of the events are rejected. A larger fraction of events rejected by this cut would be a clear symptom for the presence of either some bug in the code, or of some unexpected non-physical event. This is not the case for Phase I calibration data, for which the percentage of events with failing reconstruction is always at the mentioned level. The effect of this cut on the calibration spectrum is negligible, hence it is not shown here.

The fourth cut is the rejection of the events for which the rise of the charge pulse is not in the middle of the recorded waveform. In GERDA Phase I, the FADC was tuned such that when the voltage rose above a defined threshold, the waveform corresponding to roughly 80 µs before and after the trigger was recorded. The baseline b is computed as the average height in the first n_b bins of the trace, which typically correspond to 70 µs. Denoting with $x[i]$ the center and with $y[i]$ the amplitude of the i^{th} bin in the trace, the baseline is:

$$b = \frac{1}{n_b} \sum_{i=0}^{n_b} y[i] \quad , \tag{5.1}$$

while the baseline root mean square (RMS) is:

$$b_{RMS} = \sqrt{\frac{\sum_{i=0}^{n_b} (y[i] - b)^2}{n_b}} \quad . \tag{5.2}$$

In the signal reconstruction performed by GELATIO, a module is dedicated to the calculation of the trigger time t_t for each waveform. This is defined as the time

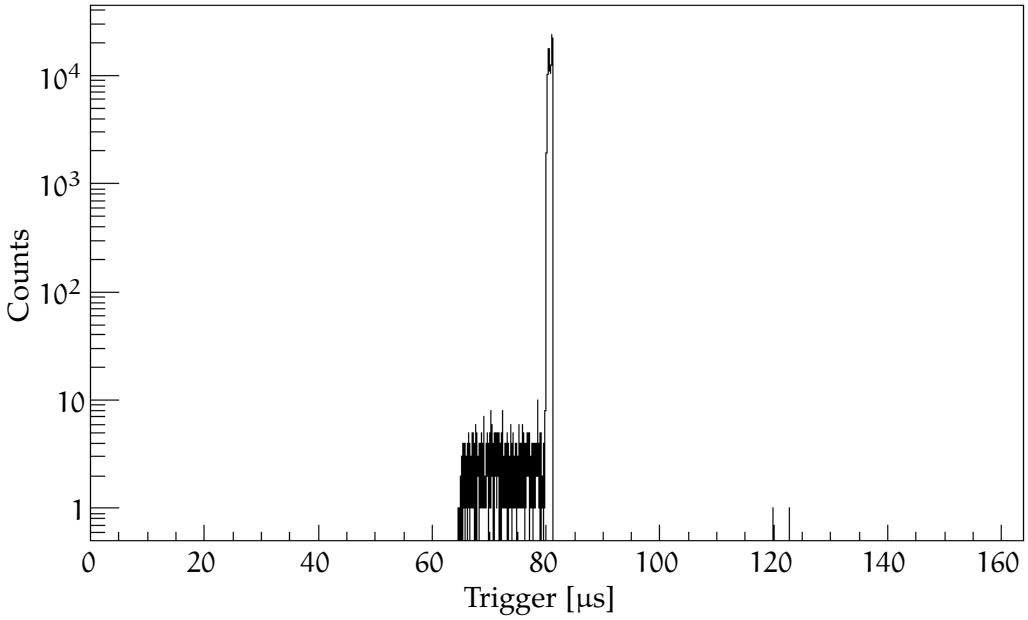

Figure 5.6.: Trigger distribution for ANG2.

at which the charge pulse overcomes a threshold equal to twice the baseline RMS and stays above this value for at least 40 μs:

$$t_t = x[i] : x[j] > (b + 2 \cdot b_{RMS}) \quad \forall \quad j \in \left[i; i + \frac{40\ \mu s}{\Delta x} \right] \quad , \tag{5.3}$$

where Δx is the bin width.

The difference between the algorithm implemented in the FADC and the one used in GELATIO causes the trigger value computed by this not to be peaked always at the same value. For most events the trigger found with GELATIO is within the $[79.5; 82]$ μs range, as shown in Fig 5.6. The events with trigger outside this range are typically coincidences which are not correctly recognized by the FADC, and are rejected. Also in this case, the effect of the cut is very small (0.1–0.2% of the events are affected). The information given by this selection is anyhow useful for monitoring the effectiveness of the offline signal reconstruction and of the FADC trigger algorithm.

The last two event selections regard the pile-up events. They are the quality cuts which mostly affect the shape of the peaks in the spectrum and, hence, the precision achievable by the peak fitting. If the time interval between the interactions is $\gtrsim 1$ μs, two signals are superimposed in the same trace, as shown in Fig. 5.7. This type of events is referred as in-trace pile-up. If the time interval between the two interactions if $O(100)$ μs, the waveform of the second signal would be superimposed to the exponential decay tail of the previous one (Fig. 5.8). These events are called pre-trace pile-ups.

In GELATIO, the identification of in-trace pile-up events is performed via a differentiation of the trace with a time delay $\delta = 2.5$ μs:

$$y_0[i] \rightarrow y_1[i] = y_0[i] - y_0 \left[i - \frac{\delta}{\Delta x} \right] \quad , \tag{5.4}$$

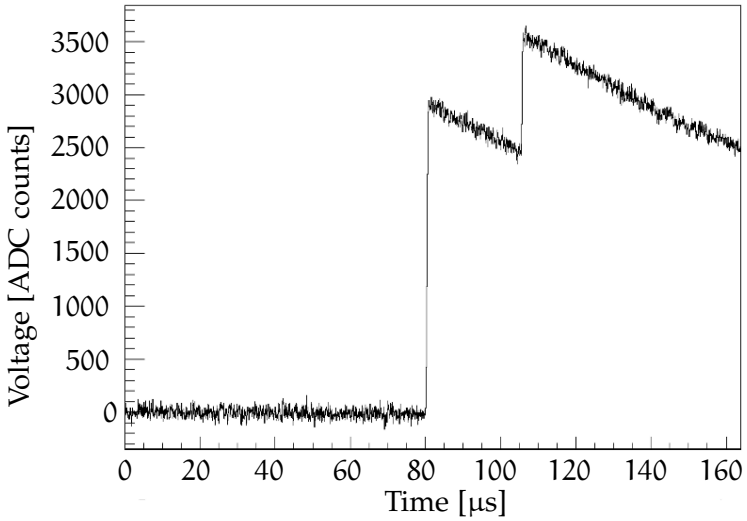

Figure 5.7.: In-trace pile-up event.

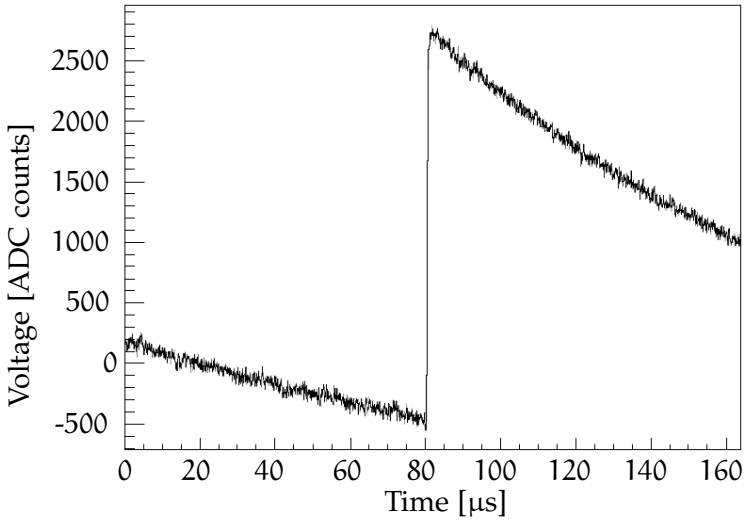

Figure 5.8.: Pre-trace pile-up event.

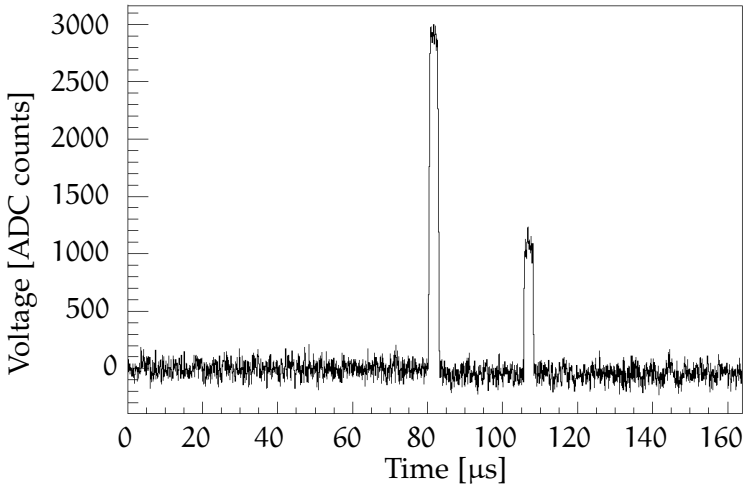

Figure 5.9.: In-trace pile-up event after filtering with the algorithm of Eqs. 5.4 and 5.5.

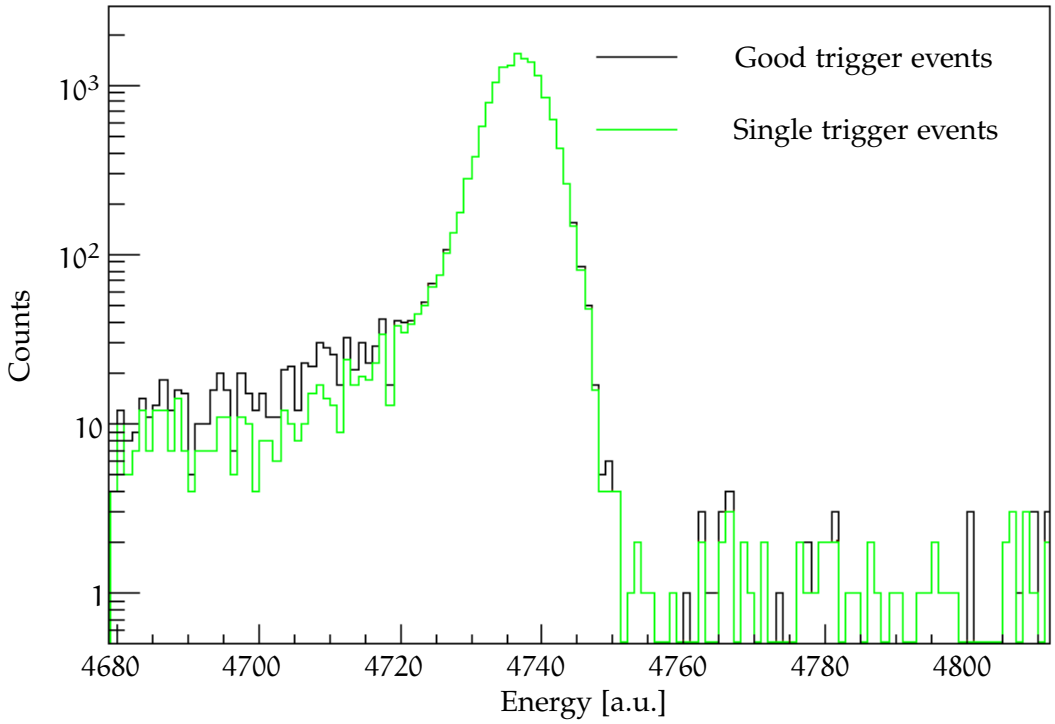

Figure 5.10.: ANG2 spectrum before (black) and after (green) the rejection of in-trace pile-up events.

where y_0 and y_1 are the original and the differentiated waveforms, respectively. The waveform is then integrated with a moving average of width $\delta' = 2$ µs:

$$y_1[i] \rightarrow y_2[i] = \frac{\Delta x}{\delta'} \sum_{j=i-\delta'}^{i} y_1[j] \quad . \tag{5.5}$$

The choice of the time constants δ and δ' is tailored to maximize the identification of in-trace pile-ups, and to avoid the misidentification of multi-site events [202]. The application of the algorithm to the trace of Fig. 5.7 results in the waveform shown in Fig. 5.9. At this point, the energy depositions are identified via the search of the waveform region exceeding 4 times the baseline RMS for at least 1 µs. In the analysis of $0\nu\beta\beta$ decay, the events with more than one energy deposition in the same trace are certainly background induced, hence they are rejected. In the case of calibration data, the removal of such events also yields smaller low-energy tails in the peaks, as depicted in Fig. 5.10.

The last cut applied to the data is the rejection of pre-trace pile-ups. In this case the baseline is systematically overestimated and the reconstructed energy is smaller than the real one. Even if some filtering algorithms allow to correct for this effect, this is not done in the analysis of GERDA data. Namely, as for the in-trace pile-ups, the pre-trace pile-ups cannot be induced by a $\beta\beta$ decay event, hence they are rejected.

A GELATIO module performs a fit of the same time range with a decaying exponential of the form $a + ce^{t/\tau}$, where τ is set to 150 µs for all the channels. If the first half of the trace is flat, c will be zero and a (denoted in GELATIO as "fitExpOffset") will be equal to the baseline b. On the contrary, if the first half of the trace is exponentially decaying, a and b will have different values. In the

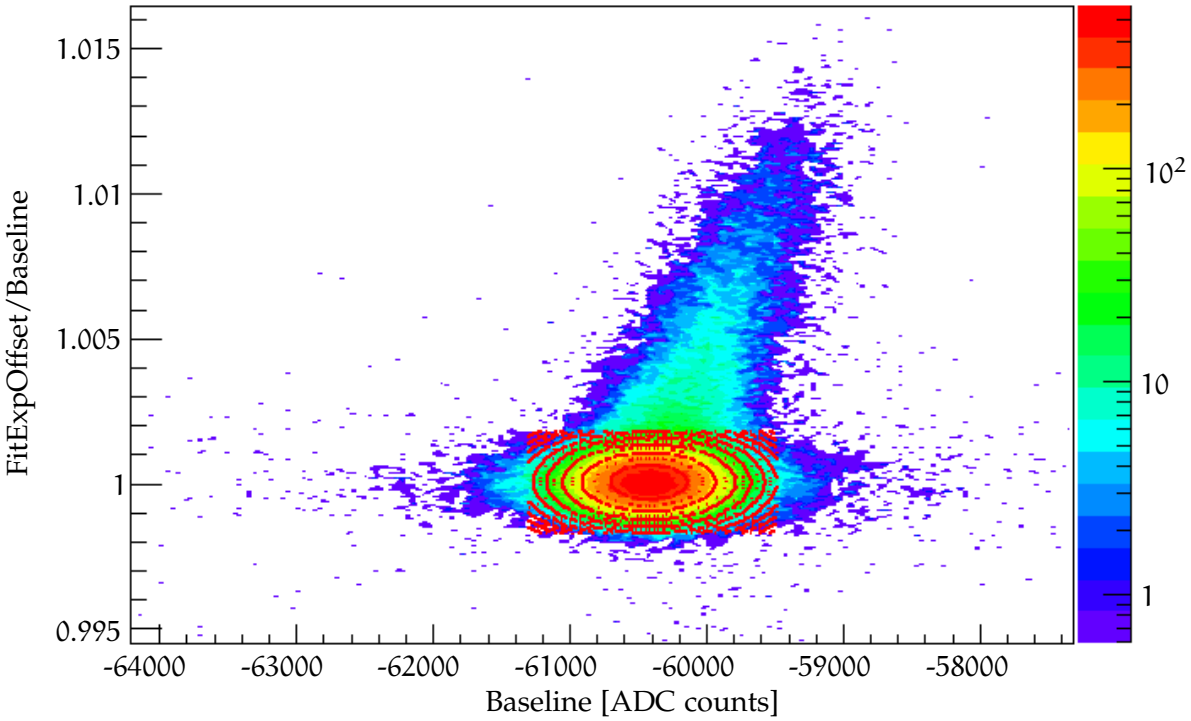

Figure 5.11.: FitExpOffset as a function of baseline for ANG2.

scatter plot of a against b, we expect to have a cluster of events centered around the average value of a and b, plus some tail given by the pre-trace pile-ups. One could then fit this distribution with a 2-dimensional Gaussian and reject the events outside some pre-defined range. From the numerical point of view, it is easier to fit a 2-dimensional Gaussian with the axes corresponding to those of the reference frame. The solution is given by plotting the ratio a/b against b, as depicted in Figure 5.11. The fit is performed only in the Gaussian part of the distribution (red box in the scatter plot), which is estimated based on the distributions of b and a/b only, and the cut consists of rejecting the events outside the 3 σ region obtained from the 2-dimensional fit. The effect of this cut is shown in Figures 5.12: the systematic underestimation of energy for pre-trace pile-up events yields to the presence of low-energy tails in the spectral peaks. These are removed with high efficiency by the pre-trace pile-up cut, leading to peaks with a Gaussian distribution. For Phase I calibration data, the cut of pre-trace pile-ups affects 4 to 10% of the total number of events, depending on the detector and on the source position and activity.

A summary of all quality cuts together with the cut implementation and the survival probabilities is given in Tab. 5.4.

5.4 PEAK SEARCH AND IDENTIFICATION

Given the high number of calibration data sets available, an algorithm for an automatic peak search and identification is required. This is based on the "TSpectrum" [203] class of ROOT [195]. TSpectrum allows to search for an arbitrary number of (Gaussian) peaks: firstly the highest peak is found, and subsequently all the other peaks are searched in order of decreasing amplitude. The algorithm

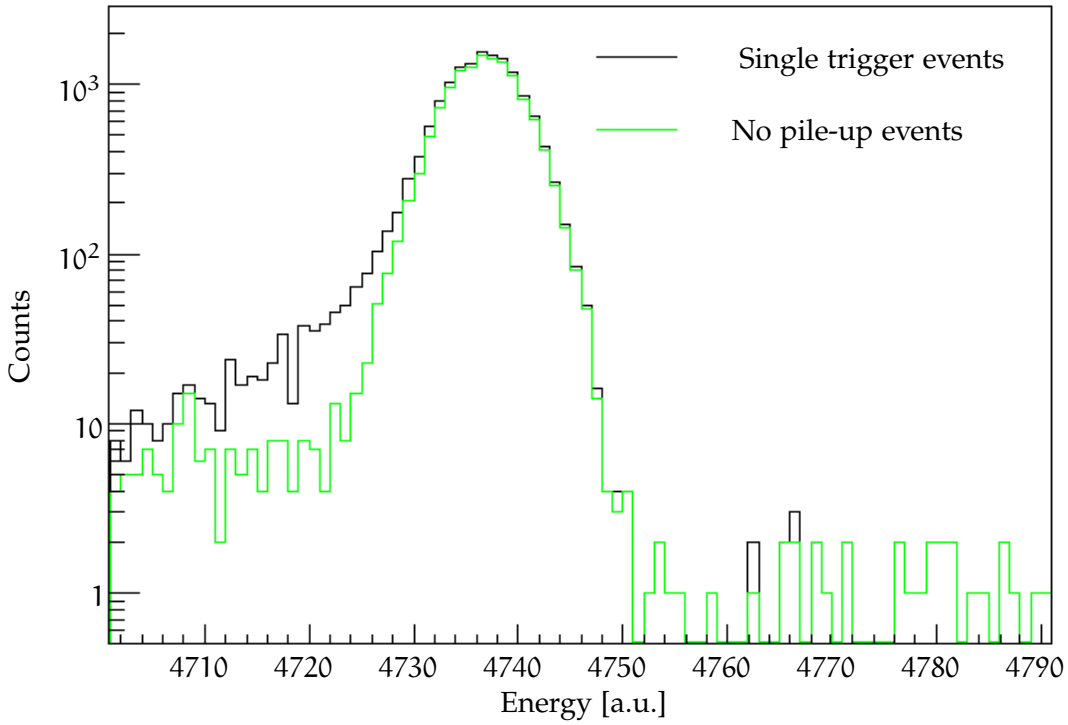

Figure 5.12.: ANG2 spectrum before (black) and after (green) the rejection of pre-trace pile-up events.

Table 5.4.: List of quality cuts applied to calibration data in GERDA Phase I. The survival probability for the cut of pulser events depends on the pulser setting and is not reported here. The loss due to events mis-classification is $< 0.1\%$ [101].

Cut	Cut implementation	Survival probabilities
Pulser	Reject pulser events	O(1%)
Coincidences	Reject events with $E > 0$ in > 1 detector	4–13%
Failing Reconstruction	Reject non well-reconstructed events	0.1–0.2%
Trigger	Reject events with $t \notin [79.5; 82]$ µs	0.1–0.2%
In-trace pile-ups	Reject events with > 1 charge deposits	1–5%
Pre-trace pile-ups	Reject events with exponential baseline	4–10%

allows the user to define a threshold on the minimum required peak amplitude (defined as a percentage of the highest peak amplitude), on the minimum distance between neighbor peaks, on the typical peak width and on the maximum number of peaks to be searched.

In the analysis of the calibration spectra and for peak search only, a spectrum with bins of ~ 1.5 keV is created. In this way, the peaks have a width of a few bins, and random fluctuations of the counts on the continuum are reduced. The threshold on the amplitude is set to 0.5%, the minimum distance between adjacent peaks to ~ 6 keV, the peak width (σ) to ~ 2 keV, and the total number of peaks to 20. This allows to efficiently find all the γ lines with a net peak counts number of $\gtrsim 50$. For a typical ^{228}Th calibration spectrum containing $O(10^5)$ events, at least 10 peaks from Tab. 5.2 are found. In most cases, several spurious peaks are found, too, due to the low threshold on the peak amplitude. A higher threshold would avoid this effect, but would also not allow to find the low intensity peaks, which could be used for the extraction of the calibration curve in case of high statistics data sets.

The peak identification proceeds as follows. Firstly, the ^{208}Tl line at 2614.5 keV is identified as the peak with highest energy. Secondly, for each peak i in the uncalibrated spectrum the ratio $R_i(a.u.)$ between its position and the position of the 2614.5 keV line is computed. This is then compared with the ratio between the energy of each literature value j of Tab. 5.2 and 2614.5 keV, $R_j(keV)$. If a literature value j is found for which:

$$\left| \frac{R_i(a.u.)}{R_j(keV)} - 1 \right| < 0.01 \quad , \tag{5.6}$$

the peak i is identified with the literature value j, otherwise it is classified as spurious and removed from the peak list. This algorithm assumes that the energy calibration curve is linear at level of 1%, which is true for all Phase I data.

5.5 FITTING OF THE SPECTRAL LINES

The peak fitting is a crucial point for the extraction of the calibration curves. In GERDA, the use of detectors with different geometries and charge collection properties is reflected in a variability of the peak shapes, which has to be accounted for. Moreover, the presence of data sets with different statistic has to be considered in the development of the fitting algorithm. These two obstacles have been faced by a routine which automatically adjusts the fitting function to the peak characteristics.

The peaks are fitted with a different functions, according to the considered peaks. The γ lines of Tab 5.2 with intensity higher than 5% and the annihilation peak at 511 keV are parametrized with the Hypermet function [204]:

$$f(E) = A \exp\left(-\frac{(E-\mu)^2}{2\sigma^2}\right) + B + \frac{C}{2}\operatorname{erfc}\left(\frac{E-\mu}{\sqrt{2}\sigma}\right) + \frac{D}{2}\exp\left(\frac{E-\mu}{\delta}\right)\operatorname{erfc}\left(\frac{E-\mu}{\sqrt{2}\sigma} + \frac{\sigma}{\sqrt{2}\delta}\right) + F\cdot(E-\mu) \quad , \tag{5.7}$$

which is the sum of a Gaussian distribution with mean μ and width σ over a linear continuum $B + F \cdot (E - \mu)$, a low-energy step (third term) and a low-energy tail (fourth term). This is parametrized as the product of a rising exponential with decay constant δ and an inverse error function. The presence of a low-energy tail is due to the events affected by an underestimation of energy as a consequence of incomplete charge collection (see Ch. 6) or of the residual presence of pile-up events in the spectrum.

The γ lines of Tab 5.2 with intensities below 5%, as well as the DEP and SEP, are fitted with the sum of a Gaussian distribution, a low-energy step and a linear background:

$$f(E) = A \exp\left(-\frac{(E-\mu)^2}{2\sigma^2}\right) + B + \frac{C}{2}\operatorname{erfc}\left(\frac{E-\mu}{\sqrt{2}\sigma}\right) + F \cdot (E - \mu) \quad . \tag{5.8}$$

For each peak, the fit range is defined a priori: if the continuum around the peak is linear and no other peak is present in its vicinity, a ~ 80 keV range is used, otherwise the range is reduced according to the properties of the spectrum.

In case of low statistic, the fit of the low-energy step and the tail is not always successful. Namely, the amplitude assigned to them by the fit routine might be smaller than the corresponding statistical uncertainty. For this reason, a minimal function is defined for all peaks as the sum of a Gaussian distribution over a linear continuum. In case the parameters of the low-energy step and/or tail are not well constrained, the fit is repeated without their contribution. The fitting method is the same for each peak, differing just by the starting and the minimal fit function used. The complete fit procedure is the following:

- the minimum and maximum of the fit range are computed according to some predefined values;
- the absolute maximum of the histogram in the fit region is searched;
- a preliminary fit with a Gaussian distribution over a flat background is performed in a very narrow region around the maximum;
- a preliminary fit with a first order polynomial $B + F \cdot (E - \mu)$ is performed on the sides of the peak, fixing μ to the mean of the Gaussian. For the 2614.5 keV peak only a flat background is considered;
- a fit with the starting function is performed (Eqs. 5.7 and 5.8), setting the initial values and the boundaries of all the parameters according to the results of the preliminary fits. The boundaries are then restricted according to the values of each parameter found so far, and the fit is repeated;
- if a tail is considered, the number of counts attributed to it and to the Gaussian peak are computed;
- if the tail parameters are smaller than twice their errors or if the tail integral is smaller than the 1% of the Gaussian integral, the fit is repeated without considering the tail;
- if the step height is smaller than twice its error, the fit is repeated without it;
- The FWHM is computed as $2.355 \cdot \sigma$ if only the Gaussian peak is considered. If also the tail is present, the FWHM is extracted numerically on the sum of the Gaussian distribution and the low-energy tail.

All the fits are performed using Minuit2 [205], which is characterized by a lower failure probability than Minuit [206]. A likelihood fit is done in order to deal with

both high and low statistic. A χ^2 fit is also done for comparison, yielding different results only in the case where the number of events both in the peak and in the continuum is very small. The reason why some fits are repeated with different boundaries is strictly related to the minimization algorithm. The extraction of the minimum χ^2 or maximum likelihood involves a high number of iterations when functions with strongly correlated parameters are used. This is the case of the Gaussian and the low-energy tail (Eq. 5.7). It is therefore necessary to set an allowed range to some or all the parameters. By doing so, Minuit2 (and Minuit) transform the function defined by the user into a new function, changing the original parameter P_1 into a new parameter P_2 in the following way [206]:

$$P_2 = \arcsin\left(2\frac{P_1 - P_{min}}{P_{max} - P_{min}} - 1\right) \quad , \tag{5.9}$$

where P_{min} and P_{max} are the lower and the upper limits, respectively. Given this non-linear transformation, if the best-fit parameter is close to the boundaries the result might not be reliable. The fit has then to be repeated either releasing the parameters or changing the boundaries such that the parameter stays roughly in the middle of the allowed range. After several attempts, the methods presented above appeared to be the most effective, both for the convergence of the fit and for the stability of the result, which was studied by changing the boundaries and/or the initial values.

A final check is performed on the effectiveness of the fit, rejecting the peak if one of the following conditions is true:

- the amplitude of the Gaussian is smaller than 5 counts (too few events in the peak);
- $\sigma_\mu > \mu/1000$ (bad evaluated peak position);
- $FWHM > \mu/100$ (too broad peak);
- $FWHM < \mu/5000$ (too narrow peak);
- $|F| > 0.2$ (too big slope in the linear background).

These are very weak requirements, which are not satisfied only in the case of a clear fit failure. The fraction of failing fits over all Phase I calibration data is at the 0.2% level.

The fits of the ^{208}Tl line at 2614.5 keV for ANG2 and GTF112 are shown in Figs. 5.13 and 5.14, respectively. While in the first case the low-energy tail is small and its amplitude is set to zero, in the second case it strongly affects the peak shape and its parameters are well constrained by the fit. The fits of most of other peaks reported in Tab. 5.2 are shown in Figs. A.1 and A.2.

5.6 CALIBRATION AND RESOLUTION CURVES

The position of the peaks is then exploited for the extraction of the calibration curve. For all spectra, two calibration curves are fitted to the data:

$$E_{keV} = a + b \cdot E_{a.u.} \quad , \tag{5.10}$$

$$E_{keV} = a + b \cdot E_{a.u.} + c \cdot E_{a.u.}^2 \quad , \tag{5.11}$$

$$\tag{5.12}$$

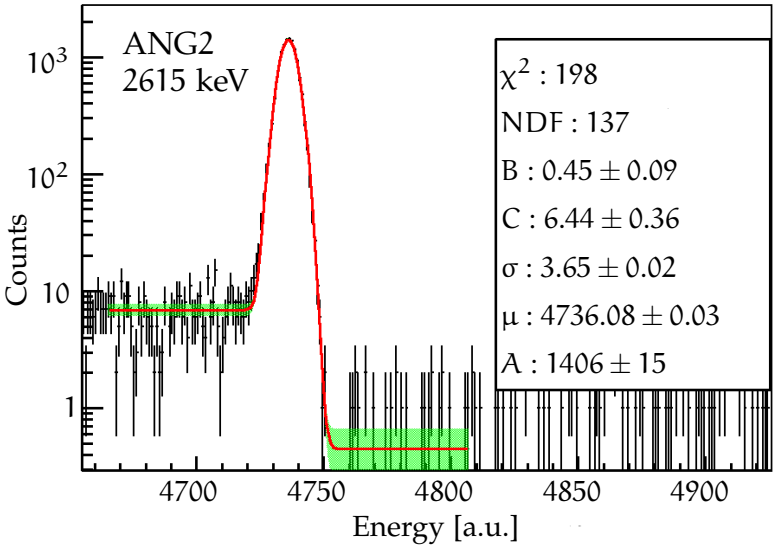

Figure 5.13.: Fit of 2614.5 keV line in the calibration spectrum for ANG2. The best fit values are reported in the inset.

where E_{keV} is the calibrated energy (in keV) and $E_{a.u.}$ is the uncalibrated one. The plot of literature values versus peak positions is fitted via a χ^2 minimization, using Minos [206] for a better determination of the parameters uncertainties. The residuals from the calibration curves are then calculated and plotted as function of energy:

$$\Delta E = E_{keV}(E_{a.u.}|\hat{a},\hat{b},...) - E_{lit} \quad , \tag{5.13}$$

where $E_{keV}(E_{a.u.}|\hat{a},\hat{b},...)$ is the value of the fitted calibration curve in correspondence of the peak position $E_{a.u.}$, and E_{lit} is the corresponding literature value. The errors on the calibrated energies are calculated taking into account the covariance matrix of the fit parameters:

$$\sigma^2_{E_{keV}} = \left(\frac{\partial E_{keV}}{\partial E_{a.u.}}\right)^2 \sigma^2_{E_{a.u.}} + \sum_{p=a,b,..} \left(\frac{\partial E_{keV}}{\partial p}\right)^2 \sigma^2_p + \sum_{p\neq q} \frac{\partial E_{keV}}{\partial p}\frac{\partial E_{keV}}{\partial q} Cov(p,q) \quad , \tag{5.14}$$

where p and q are generic parameters of the calibration curve. The error on the residuals is then be found as:

$$\sigma^2_{\Delta E} = \sigma^2_{E_{keV}} + \sigma^2_{E_{lit}} \quad . \tag{5.15}$$

In most cases Eq. 5.11 gives the best results, while for some detectors equation 5.10 gives already a good description of the data.

Two tests are performed to quantify the goodness of fit. Firstly, the χ^2/NDF and the corresponding probability are calculated using the routine provided by ROOT. Secondly, a Wald-Wolfowitz Run-Test [207] is performed to check if the considered curve is enough to describe the data. This non parametric test computes a probability for the fit according to how the residuals are grouped in clusters of the same sign. If, for example, the first half of the residuals has a sign and the second

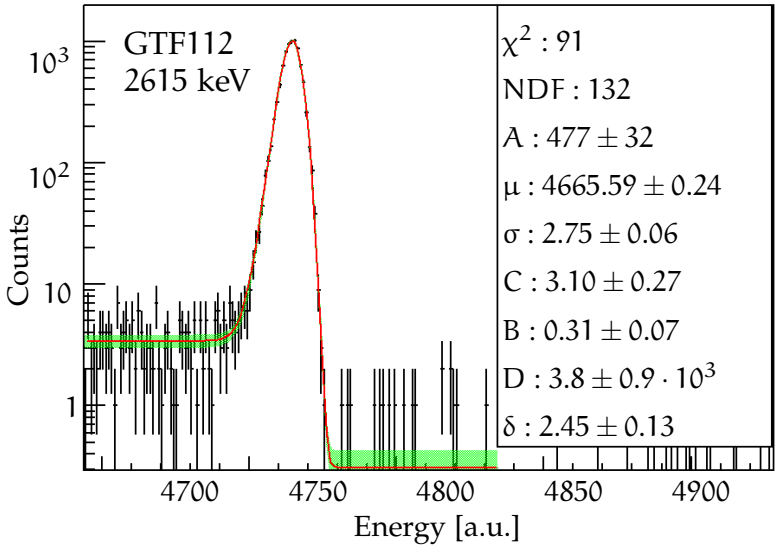

Figure 5.14.: Fit of 2614.5 keV line in the calibration spectrum for GTF112. The best fit values are reported in the inset.

half the opposite, the probability that this is given just by a statistical effect is very low. In the present case, probabilities smaller than 0.1 are considered as a hint for a bad description of the data.

The study of resolution is useful for comparing the performance of different reconstruction algorithms and for the smearing of the MC spectra. The plot of FWHM as function of energy is fitted using the formula of Eq. 3.23:

$$\begin{aligned} FWHM(E) &= 2.355\sqrt{\frac{\eta^2}{\varepsilon^2}ENC^2 + \eta F \cdot E + c^2 \cdot E^2} = \\ &= \sqrt{a^2 + b^2 \cdot E + c^2 \cdot E^2} \quad . \end{aligned} \tag{5.16}$$

An alternative fit is also performed using the formula [167]:

$$FWHM(E) = a + b\sqrt{E} \quad . \tag{5.17}$$

The curve obtained in this case is not used for the smearing of the MC spectra, but only to compute the systematic uncertainty of the FWHM at $Q_{\beta\beta}$ related to the choice of the fitting function.

The peak at 511 keV and the SEP are wider than the other gamma lines due to Doppler broadening, therefore they are not considered for the fit. An example of the resolution curve is reported in Figure 5.16.

5.7 EVALUATION OF SYSTEMATICS ON THE ENERGY SCALE

5.7.1 *Data Selection*

The detectors considered in this section are the six semi-coaxial and four BEGe detectors used for the $0\nu\beta\beta$ decay search (see Tab. 4.4). All the analyses were performed on the golden, silver and BEGe data sets, as reported in Tab. 5.5. The selection of the calibration data was done according to two criteria. Firstly, the calibrations taken in periods which are not considered for the $0\nu2\beta$ analysis are

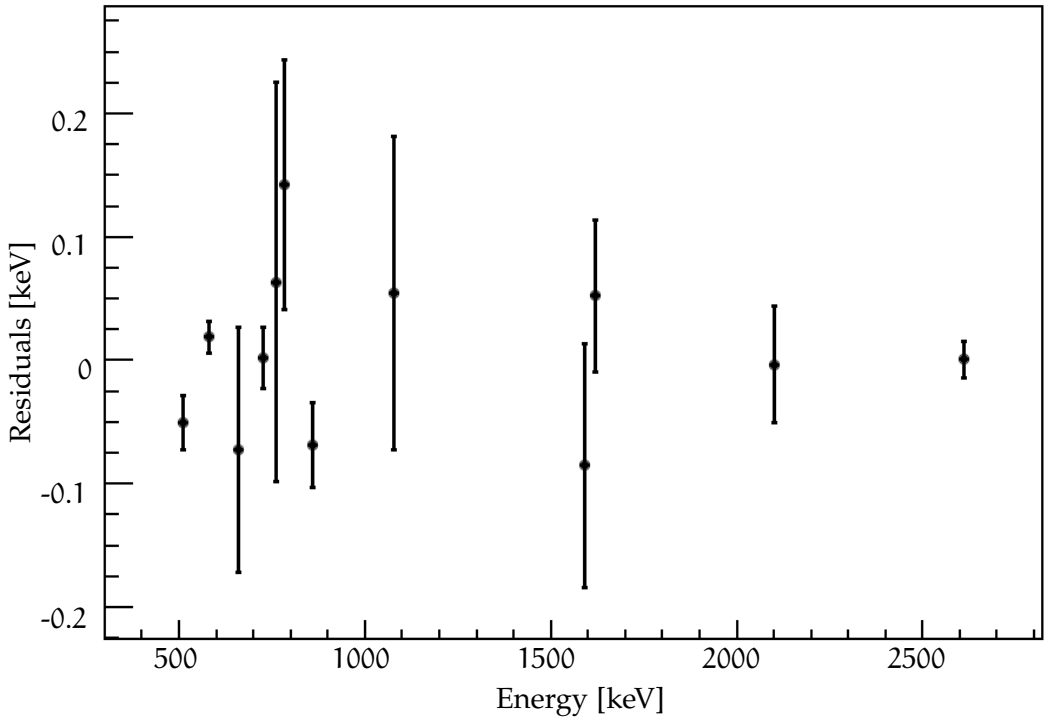

Figure 5.15.: Residuals of the peaks positions in the uncalibrated spectrum from the quadratic calibration curve for ANG2.

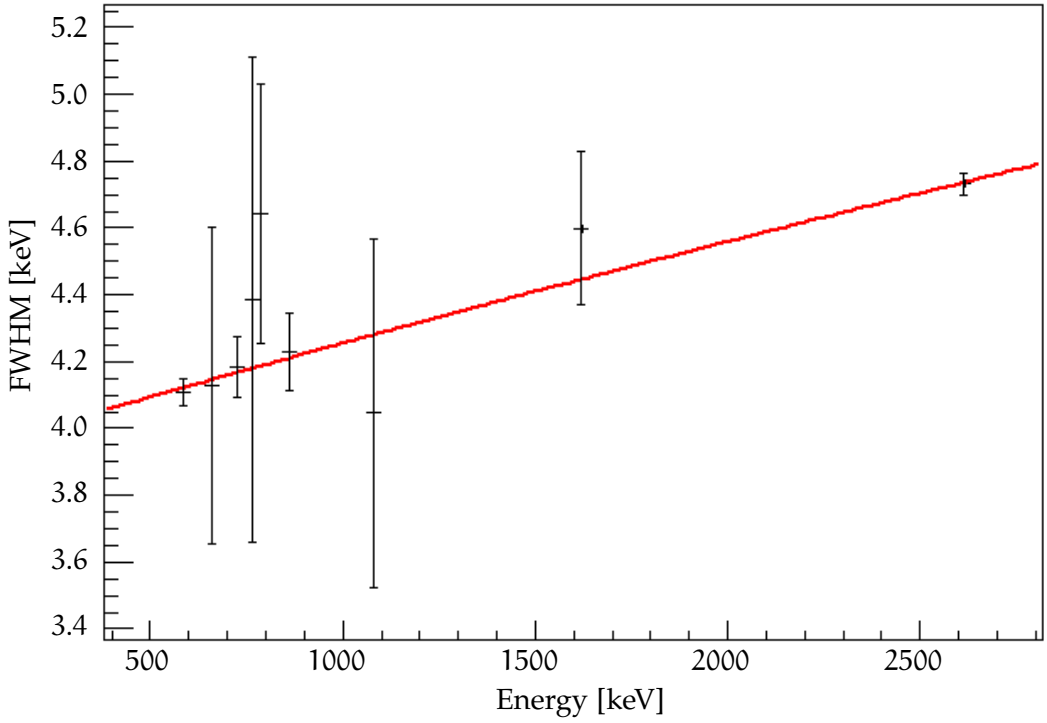

Figure 5.16.: FWHM as a function of energy for ANG2.

Table 5.5.: Data sets for analysis of systematic uncertainties related to the calibration procedure.

Data set	Detectors	Run number and data taking period
Golden	ANG1–5, RG1–2	24–32, 36–45 06.11.11–15.06.12, 27.07.12–02.05.13
Silver	ANG1–5, RG1–2	34–35 15.06.12–27.07.12
BEGe	GD32B, GD32C, GD32D, GD35B	35–45 08.07.12–02.05.13

discarded. For example, the calibrations taken during run 33 are not included in this analysis. Secondly, only the calibrations effectively applied to the background data are considered.

Each quantity (FWHM, systematic deviations and energy uncertainty) was determined in two different ways:

- on a "super-tier3", consisting of the sum of all calibrated spectra considered for each data set;
- on the single calibration tier2 data sets and then averaging on the period of validity of each calibration and on the error.

5.7.2 *Deviation from Literature Values for the Super-Tier3 Data Set*

A calculation of the systematic uncertainty on the energy reconstruction of each single event is obtained by comparing the position of the peaks in the super-tier3 with the literature values. The fit of the peaks in the super-tier3 spectra is performed with exactly the same procedure applied to the uncalibrated spectra (tier2) for the extraction of the calibration curves. The differences between the fitted peaks positions in the calibrated spectra super-tier3 spectra and the literature values for the peaks at 1620 keV, 2103 keV and 2615 keV are reported in Tab. 5.6.

The errors are the combination in quadrature of the uncertainty on the peaks positions and that on the literature values. For some detectors and data sets a systematic shift of the peaks in the super-tier3 spectra of up to 0.3 keV is present. This is due to the fit applied to the peaks (see Sec. 5.5): in the case of a single calibration spectrum, i.e. in the case of the uncalibrated tier2 spectra of a single data set, the statistics is often not enough to constrain the low-energy tail of the function given in Eq. 5.7. Therefore, in many cases the tail and/or the step are not used in the final fit of the peaks. On the other hand, the super-tier3 spectra allow to perform a fit with the maximal functions for all of the peaks. The systematic deviation comes from the sub-optimal parametrization of the peak shapes in case of low statistics spectra. As a cross-check, the fit of the super-tier3 spectra is performed without the parametrization of the low-energy tail in the fitting function. As a result, the deviations from literature values are reduced, but the fit shows a worse χ^2/NDF ratio.

Table 5.6.: Deviation of several peaks positions from literature values for the coaxial detectors and all Phase I data (super-tier3).

	Detector	Deviation at 1620 keV [keV]	2103 keV [keV]	2615 keV [keV]
G	ANG2	-0.05 ± 0.02	$+0.10 \pm 0.04$	$+0.06 \pm 0.01$
O	ANG3	$+0.04 \pm 0.02$	$+0.11 \pm 0.06$	$+0.13 \pm 0.01$
L	ANG4	-0.01 ± 0.02	-0.09 ± 0.02	$+0.03 \pm 0.01$
D	ANG5	-0.30 ± 0.02	-0.10 ± 0.06	$+0.13 \pm 0.01$
E	RG1	-0.05 ± 0.03	$+0.20 \pm 0.10$	$+0.32 \pm 0.03$
N	RG2	-0.35 ± 0.03	$+0.27 \pm 0.04$	$+0.19 \pm 0.02$
S	ANG2	$+0.08 \pm 0.04$	-0.05 ± 0.04	-0.15 ± 0.02
I	ANG3	-0.10 ± 0.04	-0.15 ± 0.06	-0.12 ± 0.02
L	ANG4	-0.01 ± 0.05	$+0.03 \pm 0.02$	-0.15 ± 0.02
V	ANG5	-0.17 ± 0.03	-0.02 ± 0.02	-0.05 ± 0.02
E	RG1	$+0.09 \pm 0.05$	-0.04 ± 0.01	$+0.11 \pm 0.03$
R	RG2	-0.11 ± 0.06	$+0.18 \pm 0.06$	$+0.07 \pm 0.02$
B	GD32B	$+0.08 \pm 0.02$	-0.19 ± 0.06	-0.04 ± 0.01
E	GD32C	-0.24 ± 0.02	-0.28 ± 0.05	-0.01 ± 0.01
G	GD32D	-0.04 ± 0.03	-0.20 ± 0.06	-0.03 ± 0.01
e	GD35B	$+0.01 \pm 0.05$	$+0.02 \pm 0.09$	$+0.02 \pm 0.01$

5.7.3 *Average Single Calibration Residuals from Literature Values*

A different approach in the calculation of the systematic uncertainty on the energy reconstruction consists of calculating the average residuals of the literature values from the calibration curves. This quantity is reported in Tab. 5.7 for the peaks at 1620 keV, 2103 keV and 2615 keV. In this case the values are in general smaller than for the deviations calculated on the super-tier3, as expected.

For the $0\nu\beta\beta$ decay analysis, a systematic of ± 0.2 keV in the energy reconstruction of each single event was considered [102]. This is a conservative choice which accounts for the higher deviations and residuals obtained with ANG5, RG2 and GD32C.

5.8 EVALUATION OF ENERGY RESOLUTION AT $Q_{\beta\beta}$ ON PHASE I PHYSICS DATA

One of the most important parameters in the search of $0\nu\beta\beta$ decay is the energy resolution of the detectors. A reliable determination of the FWHM at $Q_{\beta\beta}$ is mandatory for a successful analysis of the collected data. If the energy scale is stable over all the data collection period, the FWHM at $Q_{\beta\beta}$ can be taken from the resolution curves obtained from the calibration data. In GERDA Phase I some gain instabilities were present during the physics runs. The amplitude and frequency of these instabilities depend on the detector. For this reason, the effective energy resolution at $Q_{\beta\beta}$ on the physics data is expected to be – at least for some detec-

Table 5.7.: Average residuals from the calibration curves in correspondence to high energy peaks for the coaxial detectors and all Phase I data.

			Residual at	
	Detector	1620 keV [keV]	2103 keV [keV]	2615 keV [keV]
G	ANG2	-0.01 ± 0.03	$+0.00 \pm 0.02$	$+0.00 \pm 0.01$
O	ANG3	-0.01 ± 0.02	$+0.02 \pm 0.02$	$+0.08 \pm 0.06$
L	ANG4	-0.04 ± 0.02	-0.12 ± 0.02	$+0.02 \pm 0.04$
D	ANG5	-0.31 ± 0.02	-0.26 ± 0.01	$+0.06 \pm 0.07$
E	RG1	-0.11 ± 0.03	$+0.06 \pm 0.02$	$+0.11 \pm 0.13$
N	RG2	-0.28 ± 0.03	$+0.24 \pm 0.02$	$+0.20 \pm 0.12$
S	ANG2	$+0.02 \pm 0.05$	-0.07 ± 0.04	$+0.08 \pm 0.05$
I	ANG3	-0.12 ± 0.04	-0.15 ± 0.03	$+0.13 \pm 0.08$
L	ANG4	-0.04 ± 0.05	-0.10 ± 0.04	-0.13 ± 0.10
V	ANG5	-0.17 ± 0.04	-0.16 ± 0.03	$+0.11 \pm 0.09$
E	RG1	$+0.05 \pm 0.06$	-0.09 ± 0.04	-0.05 ± 0.18
R	RG2	-0.11 ± 0.07	$+0.13 \pm 0.05$	$+0.07 \pm 0.04$
B	GD32B	$+0.06 \pm 0.02$	-0.21 ± 0.02	-0.01 ± 0.05
E	GD32C	-0.26 ± 0.02	-0.32 ± 0.02	$+0.01 \pm 0.09$
G	GD32D	-0.02 ± 0.03	-0.20 ± 0.02	-0.01 ± 0.05
e	GD35B	$+0.00 \pm 0.05$	-0.03 ± 0.03	-0.01 ± 0.09

tors – worse than that obtained on the basis of calibration data only. To quantify this effect, the energy resolution of the background peaks present in the physics spectra has to be compared with the value expected at the same energy from the calibration data. In Phase I, the only background peak with sufficient statistic for the extraction of the FWHM is the ^{42}K peak at 1524.6 keV [197].

For each of the data sets reported in Tab. 5.5, the FWHM at $Q_{\beta\beta}$ is computed as follows for each detector separately:

- the FWHM at 1524.6 keV and its uncertainty are extracted from the resolution curves obtained from the calibration data. The exposure averaged values from the single calibration tier2 data are used. This quantities are referred as $FWHM_{1525,cal}$ and $\sigma_{1525,cal}$ from here on;
- the ^{42}K peak on the physical spectra is fitted, and the FWHM extracted, together with its uncertainty; This quantities are refered as $FWHM_{1525,phys}$ and $\sigma_{1525,phys}$ from here on;
- the two values of the FWHM at 1524.6 keV are compared. If the two are not compatible within 1 σ, a correction term is computed. In particular, if

$$FWHM_{1525,phys} - FWHM_{1525,cal} > \sqrt{\sigma^2_{1525,phys} + \sigma^2_{1525,cal}} \quad , \tag{5.18}$$

  the correction term ΔFWHM is defined:

$$\Delta FWHM = FWHM_{1525,phys} - FWHM_{1525,cal} \quad . \tag{5.19}$$

- the FWHM at $Q_{\beta\beta}$ is extracted from the resolution curves obtained from the calibration data;

– if the condition of Eq. 5.18 is satisfied, the correction term $\Delta FWHM$ is added to the FWHM at $Q_{\beta\beta}$:

$$FWHM_{Q_{\beta\beta},phys} = FWHM_{Q_{\beta\beta},cal} + \Delta FWHM \quad , \tag{5.20}$$

Otherwise the FWHM at $Q_{\beta\beta}$ is simply that obtained from the calibration data:

$$FWHM_{Q_{\beta\beta},phys} = FWHM_{Q_{\beta\beta},cal} \quad . \tag{5.21}$$

The FWHM of the three considered data sets is then calculated as the exposure weighted average of the single detector values.

The error on $FWHM_{Q_{\beta\beta},phys}$ is computed combining in quadrature the following uncertainties:

– the statistical uncertainty σ_{stat} from the fits of all single tier2 calibration data sets;
– the difference $\sigma_{syst,fit}$ between the $FWHM_{Q_{\beta\beta},cal}$ obtained with the functions given in Eqs. 3.23 and 5.17;
– the difference $\sigma_{syst,dataset}$ between the $FWHM_{Q_{\beta\beta},cal}$ obtained from the single tier2 calibration data sets and from the super-tier3 spectra;
– the uncertainty on the correction term $\Delta FWHM$, if present.

The error on $FWHM_{Q_{\beta\beta},phys}$ for the three data sets is then weighted on the exposure of the single detectors.

5.8.1 *FWHM at 1524.6 keV*

As a first step, the FWHM at 1524.6 keV is extracted from the calibration and physics data. In the case of calibration data, the value is extrapolated from the resolution curve of each calibration run, and averaged over the time of validity of the same. In detail:

$$FWHM_{cal} = \frac{\sum_i \frac{FWHM_{cal,i}\Delta t_{cal,i}}{\sigma^2_{cal,i}\cdot T}}{\sum_i \frac{\Delta t_{cal,i}}{\sigma^2_{cal,i}\cdot T}} \quad , \tag{5.22}$$

$$\sigma^2_{cal} = \frac{1}{\sum_i \frac{\Delta t_{cal,i}}{\sigma^2_{cal,i}\cdot T}} \quad . \tag{5.23}$$

where $\Delta t_{cal,i}$ is the time of validity of the i^{th} calibration, T is the total exposure, and $\sigma_{cal,i}$ is the error on the FWHM of the i^{th} calibration. The systematic uncertainty is computed as the sum in quadrature of two terms. The first is the difference between the FWHM obtained with Eqs. 3.23 and 5.17. The second is the difference between the average FWHM obtained from all single tier2 spectra and the FWHM obtained from the corresponding super-tier3.

In the case of physics data, a fit of the ^{42}K peak is done using a Gaussian distribution over a flat background. Given the small statistic, it was not possible to perform the fit separately for the Golden and the Silver data sets. Therefore a unique fit was performed on all the Phase I data for the semi-coaxial detectors.

The uncertainty on the FWHM of the ^{42}K peak is of about 0.3 keV for the semi-coaxial detectors, and up to 0.7 keV for the BEGe detectors, due to the much lower

Table 5.8.: FWHM at 1524.6 keV for all the detectors and all the three considered data sets. The first column shows the data set, the second the detector, the third the FWHM of the ^{42}K peak (computed on all Phase I physics data), the fourth is the FWHM at 1524.6 keV from the calibration data of the considered data set (the first error is statistical, the second systematic), and the fifth is the correction term, where used. The two errors on the offset are statistical and systematic and are propagated from those in the previous two columns.

	Detector	FWHM [keV] Physics	FWHM [keV] Calibration	Offset
G	ANG2	5.17 ± 0.29	$3.92 \pm 0.01 \pm 0.03$	$1.32 \pm 0.29 \pm 0.03$
O	ANG3	4.35 ± 0.26	$4.37 \pm 0.05 \pm 0.08$	
L	ANG4	4.48 ± 0.31	$3.98 \pm 0.03 \pm 0.05$	$0.50 \pm 0.31 \pm 0.05$
D	ANG5	4.04 ± 0.22	$3.97 \pm 0.04 \pm 0.06$	
E	RG1	4.12 ± 0.32	$4.22 \pm 0.06 \pm 0.18$	
N	RG2	4.43 ± 0.31	$4.67 \pm 0.06 \pm 0.18$	
S	ANG2	5.17 ± 0.29	$4.73 \pm 0.04 \pm 0.16$	$0.44 \pm 0.29 \pm 0.16$
I	ANG3	4.35 ± 0.26	$4.40 \pm 0.03 \pm 0.16$	
L	ANG4	4.48 ± 0.31	$4.23 \pm 0.04 \pm 0.09$	
V	ANG5	4.04 ± 0.22	$4.02 \pm 0.03 \pm 0.15$	
E	RG1	4.12 ± 0.32	$4.27 \pm 0.05 \pm 0.20$	
R	RG2	4.43 ± 0.31	$4.63 \pm 0.05 \pm 0.25$	
B	GD32B	2.25 ± 0.35	$2.41 \pm 0.04 \pm 0.03$	
E	GD32C	2.68 ± 0.55	$2.40 \pm 0.04 \pm 0.03$	
G	GD32C	3.45 ± 0.47	$2.51 \pm 0.05 \pm 0.03$	$0.94 \pm 0.47 \pm 0.05$
e	GD35B	4.24 ± 0.69	$3.85 \pm 0.09 \pm 0.05$	

statistic. The fit is performed several times changing the fit range to highlight eventual systematic effects. All fit parameters are always stable within the statistics uncertainties.

The values of the FWHM at the ^{42}K peak, with the corresponding values given by the calibration data and the correction terms are reported in Tab. 5.8.

5.8.2 *Average Single-Calibration* FWHM *at* $Q_{\beta\beta}$

The FWHM at $Q_{\beta\beta}$ is computed on the calibration data as described in Sec. 5.8.1. The values for all detectors and the three considered data sets are given in Tab. 5.9. Where present, the correction terms of Tab. 5.8 are added to the FWHM at $Q_{\beta\beta}$.

5.8.3 *Official FWHM at* $Q_{\beta\beta}$

The FWHM for the considered data sets is then obtained by weighting the FWHM for each detector with the corresponding exposure, which is reported in Tab. 6.11. The final FWHM value for the considered data sets is given in Tab. 5.10.

Table 5.9.: FWHM at $Q_{\beta\beta}$ for all the detectors and all the three considered data sets. The first column shows the data set, the second the detector, the third the FWHM at $Q_{\beta\beta}$ from the calibration data (the first error is statistical, the second systematic), the fourth the eventual correction term, and the fifth the FWHM at $Q_{\beta\beta}$ after adding the correction term, where used.

		FWHM [keV]		FWHM [keV]
	Detector	Calibration	Offset	Physics
G	ANG2	$4.52 \pm 0.01 \pm 0.00$	$1.32 \pm 0.29 \pm 0.03$	$5.84 \pm 0.29 \pm 0.08$
O	ANG3	$4.53 \pm 0.05 \pm 0.03$		$4.53 \pm 0.05 \pm 0.12$
L	ANG4	$4.44 \pm 0.03 \pm 0.02$	$0.50 \pm 0.31 \pm 0.05$	$4.94 \pm 0.31 \pm 0.07$
D	ANG5	$4.16 \pm 0.04 \pm 0.03$		$4.16 \pm 0.04 \pm 0.07$
E	RG1	$4.46 \pm 0.07 \pm 0.04$		$4.46 \pm 0.07 \pm 0.27$
N	RG2	$4.91 \pm 0.07 \pm 0.04$		$4.91 \pm 0.07 \pm 0.25$
S	ANG2	$4.85 \pm 0.04 \pm 0.03$	$0.44 \pm 0.29 \pm 0.16$	$5.29 \pm 0.29 \pm 0.25$
I	ANG3	$4.57 \pm 0.04 \pm 0.03$		$4.57 \pm 0.04 \pm 0.20$
L	ANG4	$4.36 \pm 0.04 \pm 0.02$		$4.36 \pm 0.04 \pm 0.10$
V	ANG5	$4.21 \pm 0.03 \pm 0.03$		$4.21 \pm 0.03 \pm 0.18$
E	RG1	$4.49 \pm 0.06 \pm 0.02$		$4.49 \pm 0.06 \pm 0.27$
R	RG2	$4.83 \pm 0.06 \pm 0.03$		$4.83 \pm 0.06 \pm 0.32$
B	GD32B	$2.62 \pm 0.05 \pm 0.02$		$2.62 \pm 0.05 \pm 0.07$
E	GD32C	$2.63 \pm 0.04 \pm 0.02$		$2.63 \pm 0.04 \pm 0.04$
G	GD32C	$2.74 \pm 0.06 \pm 0.02$	$0.94 \pm 0.47 \pm 0.05$	$3.68 \pm 0.47 \pm 0.06$
e	GD35B	$3.96 \pm 0.10 \pm 0.07$		$3.96 \pm 0.10 \pm 0.07$

Table 5.10.: Official FWHM at $Q_{\beta\beta}$ for the Golden, Silver and BEGe data sets. The FWHM of each detector is weighted with the corresponding exposure. The first error is statistic, the second systematic.

Data Set	FWHM [keV]
Golden	$4.83 \pm 0.15 \pm 0.13$
Silver	$4.63 \pm 0.09 \pm 0.22$
BEGe	$3.24 \pm 0.16 \pm 0.06$

5.9 EVALUATION OF THE SYSTEMATICS ON THE ENERGY SCALE WITH ^{56}CO DATA

After the end of Phase I, several dedicated measurements were taken in GERDA with the aim of better understanding the experiment's performances. Among these, a three weeks long calibration run was acquired with a ^{56}Co source with $\sim$ 5 kBq activity. This was custom-produced via proton irradiation on a pure ^{56}Fe target by the GERDA group of the Technische Universtität München.

The choice of ^{56}Co is motivated by the presence of 4 DEPs in vicinity of $Q_{\beta\beta}$. These can be used to cross-check the survival probabilities of SSE and MSE, which are determined with ^{228}Th measurements and MC simulations [208]. Moreover, the ^{56}Co spectrum is characterized by the presence of a about 25 gamma lines with at least 0.1% emission probability, evenly distributed between 800 and 3500 keV. Most of these γ's are emitted in cascade, thus several summation peaks are visible up to 4.2 MeV. Finally, up to 9 SEP and 5 DEP could be identified, provided that a high statistics spectrum is available. It is therefore possible to perform a high precision energy calibration using a total of about 40 peaks. which are listed in Tab. 5.11. A ^{56}Co spectrum collected with ANG4 is shown in Fig. 5.17.

At the moment of the measurement, only the 3-string arm was deployed (see Tab. 4.4). Three calibration runs were performed, with the ^{56}Co source at different heights in order to collect enough statistics with all detectors. Due to some concurrent maintenance operations, strong gain drifts affected some detectors. Thus, only part of the data can be exploited for the analysis.

The data are analyzed using a modified version of the calibration program. The only difference with respect to the standard one is the list of peaks to be fitted. The residuals from a quadratic calibration curve for ANG2 and ANG4 are shown in Fig. 5.18. In both cases, most of the residuals are distributed within $\pm$0.2 keV. Higher values are only found for the summation peaks above 4 MeV, for which a reliable spectral fit is not possible due to the limited statistics. The distribution of all residuals for all the available detectors is centered at zero, and has a RMS of 0.15 keV. This is in agreement with the 0.2 keV systematic uncertainty of the energy scale assumed for the Phase I $0\nu\beta\beta$ decay analysis. Moreover, no hint is found for a possible $>$ 0.2 keV shift of the DEPs, as claimed in [209].

Type	Energy [keV]	Intensity [%]
Annihilation	511	
γ	787.743(5)	0.311(3)
γ	846.770(2)	99.9399
γ	977.372(5)	1.421(6)
γ	1037.843(4)	14.05(4)
γ	1175.101(4)	2.252(6)
γ	1238.288(3)	66.46(12)
SEP	1260.357(4)	
γ	1335.40(3)	0.1224(12)
γ	1360.212(4)	4.283(12)
γ	1442.746(6)	0.180(4)
γ	1462.322(6)	0.074(4)
SEP	1504.215(5)	
SEP	1523.791(5)	
DEP	1576.500(4)	
γ	1771.357(4)	15.41(6)
γ	1810.757(4)	0.640(3)
γ	1963.741(8)	0.707(4)
γ	2015.215(5)	3.016(12)
γ	2034.791(5)	7.77(3)
SEP	2087.500(4)	
γ	2113.135(5)	0.377(3)
DEP	2180.029(8)	
γ	2113.135(5)	0.377(3)
DEP	2231.503(4)	
DEP	3273.079(4)	
γ	2276.131(4)	0.118(4)
SEP	2498.645(4)	
γ	2523.09(11)	0.059(4)
γ	2598.500(4)	16.97(4)
SEP	2691.029(8)	
SEP	2742.503(4)	
SEP	2762.079(4)	
SEP	2940.232(4)	
γ	3009.645(4)	1.036(13)
γ	3202.029(8)	3.209(12)
γ	3253.503(4)	7.923(21)
γ	3273.079(4)	1.8759(20)
γ	3451.232(4)	0.949(5)
γ	3548.05(6)	0.1955(15)
SUM	4048.799(8)	
SUM	4100.273(5)	
SUM	4119.849(5)	

Table 5.11.: ^{56}Co gamma lines $>$ 500 keV relevant for the energy calibration of GERDA. Values from [197].

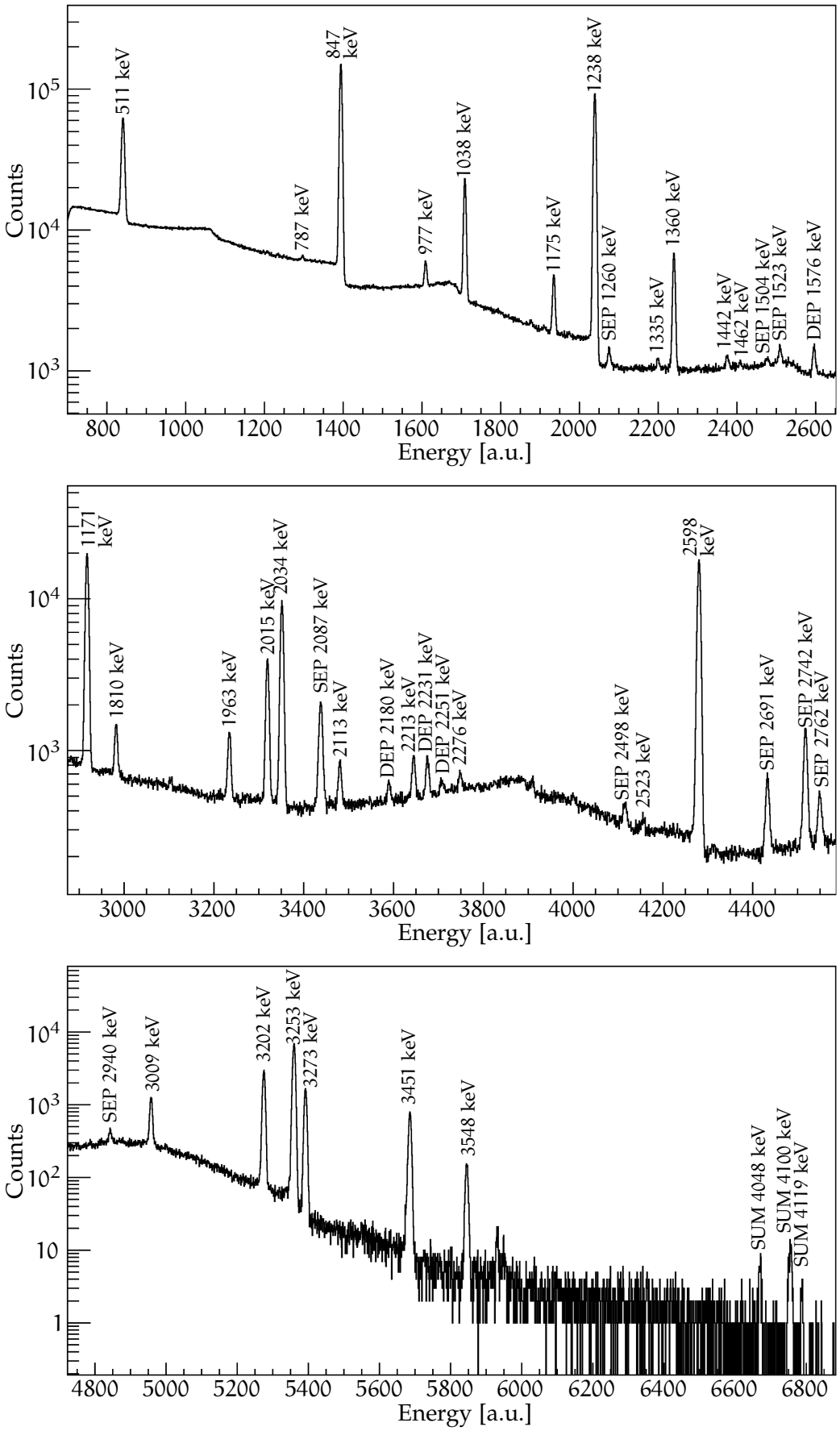

Figure 5.17.: ^{56}Co spectrum measured with ANG4 in the [0; ~ 4200] keV range.

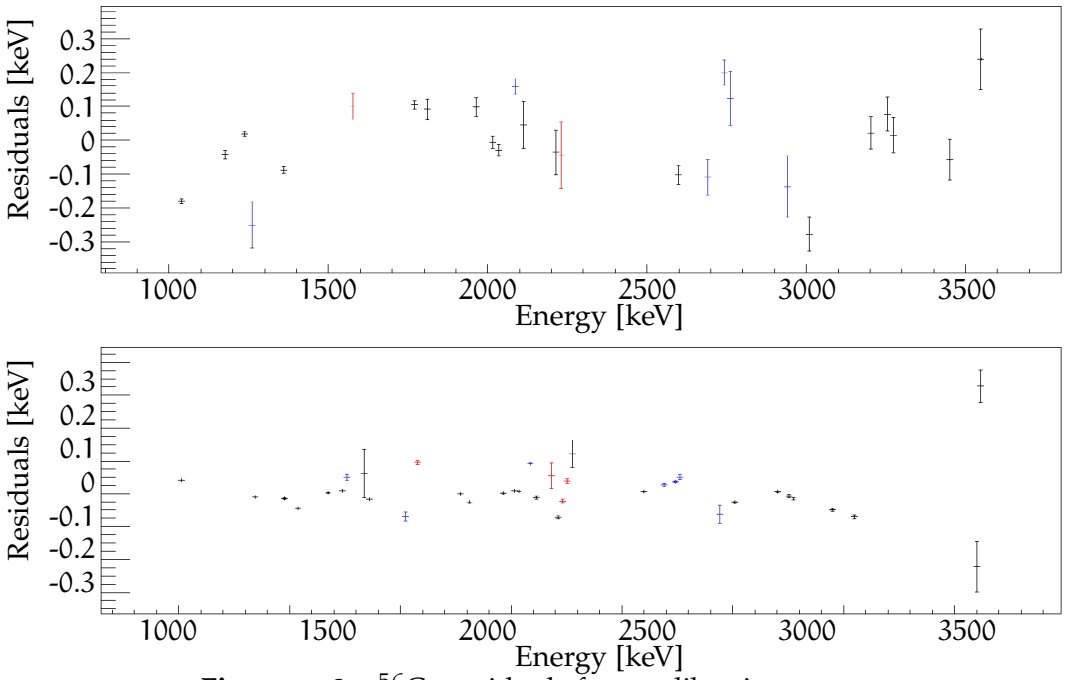

Figure 5.18.: ^{56}Co residuals from calibration curve.

6

REPROCESSING OF GERDA PHASE I DATA WITH THE ZAC FILTER

In this chapter, the development of a new shaping filter for the energy reconstruction is described. This filter was used for a full reprocessing of GERDA Phase I data. In Sec. 6.1 a short review on signal shaping is given. Secs. 6.2 and 6.3 are dedicated to the development and the optimization of the new filter. The results of the reprocessing are reported in Sec. 6.4. Finally, a re-analysis of $0\nu\beta\beta$ decay is presented in 6.5, while the prediction for the Phase II sensitivity on $T^{0\nu}_{1/2}$ on the basis of the obtained improvement in energy resolution is given in Sec. 6.6. Part of the chapter content was published as a GERDA collaboration paper [3].

6.1 SIGNAL SHAPING

The goal of a spectroscopy measurement is the determination of one or more physical parameters which characterize each single event. To maximize the precision of the measurement, the shape of the signal has to be modified in a dedicated way. This operation is referred to as "signal shaping" and can be performed either through a filtering circuit, or with the convolution of the digitized signal trace with a filtering algorithm. The advantages of digital shaping are that an infinite number of filters are available, and that the filter itself can be improved in a later stage and applied to the recorded data.

In the case of energy reconstruction, we are interested in measuring the total charge deposited in the detector.

6.1.1 *Digital Shaping in* GERDA

In GERDA Phase I the waveforms were digitized with 14 bits precision and 100 MHz sampling frequency [172], with 16384 samples for each pulse. For energy reconstruction only, the traces are rebinned summing up 4 consecutive bins. In this way, the waveforms contain 4096 bins of 40 ns width. A typical waveform is shown in Fig. 6.1: when the voltage overcomes the trigger threshold, a $\sim$ 164 µs trace is recorded. After a $\sim$ 80 µs long baseline the charge signal rises up with a $\sim$ 1 µs rise time followed by an exponential decay due to the discharge of the feedback capacitor. The exponential tail has a time constant $\tau = R_f C_f$. For GERDA, $\tau \simeq 150$ µs.

The standard energy reconstruction used in GERDA Phase I is a pseudo-Gaussian filter, implemented as:

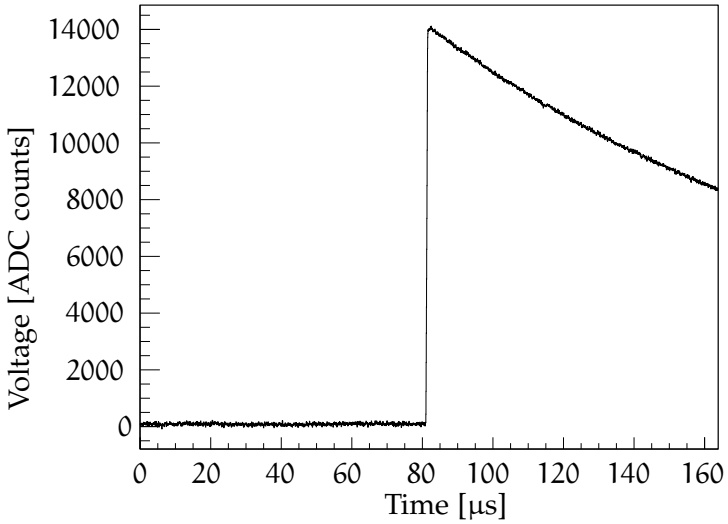

Figure 6.1.: Typical waveform recorded in GERDA Phase I. A ~ 80 μs long baseline is recorded before each signal rise. The exponential decay tail corresponds to the discharge of the feedback capacitor.

– a delayed differentiation of the signal trace:

$$y_0[i] \rightarrow y_1[i] = y_0[i] - y_0\left[i - \frac{\Delta x}{\delta}\right] \quad , \tag{6.1}$$

where $y_0[i]$ amplitude of the trace in the i^{th} bin, Δx is the bin width, and $\delta = 5\mu s$;

– a series of 25 moving average (MA) operations:

$$y_k[i] \rightarrow y_{k+1}[i] = \frac{\Delta x}{\delta} \sum_{j=i-\frac{\delta}{\Delta x}}^{i} y_k[j] \qquad k = 1, \ldots, 25 \quad . \tag{6.2}$$

The output signal has a quasi-Gaussian shape, and its height is proportional to the energy deposited in the detector. The main steps of the pseudo-Gaussian filter algorithm are graphically visualized in Fig. 6.2. The choice of a 5 μs shaping time and of 25 iterations for the MA ensures a good filtering of the high-frequency noise and avoids the maximum of the shaped signal to move out of the time window.

The pseudo-Gaussian filter is proven to be a very fast and robust algorithm leading to a quasi-optimal energy resolution if the $1/f$ noise component is negligible [173]. In GERDA Phase I, the preamplifiers were placed at 30-60 cm distance from the diodes in order to minimize the background. Moreover, the cables connecting the detector to the front-end electronics were simple unshielded OFHC copper strips with a soft PTFE insulation. For this reason, a strong low-frequency noise was present for some of the Phase I detectors, which makes the use of a dedicated shaping filter preferable.

As described in Sec. 3.4, the ENC depends on the properties of the detector, of the preamplifier and of the connection between them. In GERDA, detectors with different geometries and impurity concentrations are used, leading to different values of C_D and I_L. In addition, the non-standard connection between the diodes and the preamplifiers results in different input capacitances C_i. An improvement in energy resolution can therefore be obtained by tuning the parameters of the shaping filter individually for each detector.

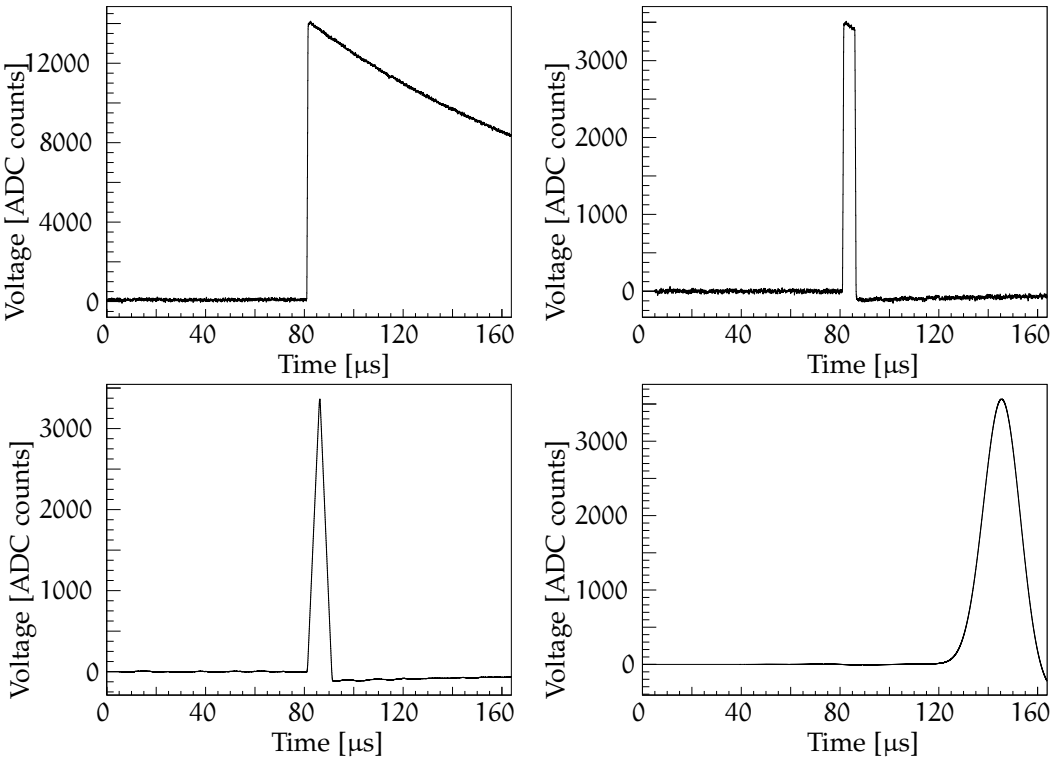

Figure 6.2.: Top left: typical waveform recorded in GERDA Phase I. Top right: the waveform after the differentiation operation described in Eq. 7.2. Bottom: the signal after one (left) and 25 (right) moving average operations (see Eq. 6.2).

Finally, the noise features are strongly dependent on the presence of non-coaxial cables for the connections of the diodes to the front-end electronics, yielding to low-frequency disturbance. For this reason, the shaping filter parameters leading to an optimal energy resolution are expected to be different for different detector arrangements.

6.2 THE ZAC FILTER

A new shaping filter has been developed with the aim of improving the energy resolution of GERDA Phase I data. Several factors are considered in the filter design and optimization. First, the filter ENC is minimized, with special attention to low-frequency noise. Second, the charge integration is maximized. Finally, the filter parameters are optimized separately for each detector and Phase I data are divided in data-sets, corresponding to different detector configurations in GERDA.

Assuming an infinite drift velocity of the charge carriers in the crystal, the current signal induced at the detector anode is delta-like:

$$s_0(t) = Q \cdot \delta(t) \quad . \tag{6.3}$$

In presence of noise, the recorded signal is transformed into:

$$s_1(t) = s_0(t) + n(t) = Q \cdot \delta(t) + n(t) \quad , \tag{6.4}$$

where $n(t)$ is the instantaneous value of the noise. In the ideal case of an infinitely long signal trace, the most precise energy determination is obtained by performing the convolution of the signal with a cusp-like filter of the form $f(t) = \exp(-|t|/\tau_s)$ [173, 174, 210]:

$$E = \max\left[\int_{-\infty}^{+\infty} s_1(t)\exp\left(-t/\tau_s\right)\,dt\right] \quad , \tag{6.5}$$

where τ_s is the reciprocal of the corner frequency, *i.e.* the frequency at which the ENC contributions of the series and parallel noise are equal.

In the real case, the recorded trace has a finite length 2L and the optimal filter is of the form [211, 210]:

$$f(t) = \begin{cases} \sinh\left(\frac{t}{\tau_s}\right) & 0 < t < L \\ \sinh\left(\frac{2L-t}{\tau_s}\right) & L < t < 2L \end{cases} . \tag{6.6}$$

If strong low-frequency noise or disturbances are present, the best energy resolution is obtained using a shaping filter with total zero area [212]. Moreover, the low-frequency baseline fluctuations, *e.g.* due to microphonics, are well suppressed by filters with parabolic shape [213]. This can obtained by subtracting two parabolas from the sides of the cusp filter keeping the area under the parabolas equal to that underlying the cusp.

In the real case, the charge collection process is not instantaneous and lies in the $[0.2; 1.5]$ µs range, depending on the location of energy deposition within the crystal and on the detector electric field configuration. Hence, the charge collection cannot be approximated with a δ-function. If a cusp filter is used, the charge is not fully integrated. This leads to an underestimation of the deposited energy and to the presence of low-energy tails in the spectral peaks, as anticipated in Sec. 3.5. This effect is called "ballistic deficit" and can be minimized using two approaches.

A first possibility is to modify the cusp filter by inserting a central flat part, denoted as "flat top", of the duration of almost the maximum length of the charge collection. The first implementation of the method was the gated-integrator analog circuit [214]. The use of a filter with flat top allows to fully integrate the charge, but has the disadvantage of not filtering the noise for the time window FT in which the flat filter is applied. It is therefore necessary to use the minimum FT which provides a full charge integration.

Other possible methods for the correction of ballistic deficit rely on the dependence of the reconstructed energy on the pulse rise time [215, 216, 217]. The advantage of these techniques is that they are not sensitive to low-frequency noise, but a fine tuning of the algorithm parameters is needed. In GERDA Phase I, the presence of up to 14 detectors made the applicability of such methods too complicated if compared with the achievable improvement in energy resolution, which was below the percent level.

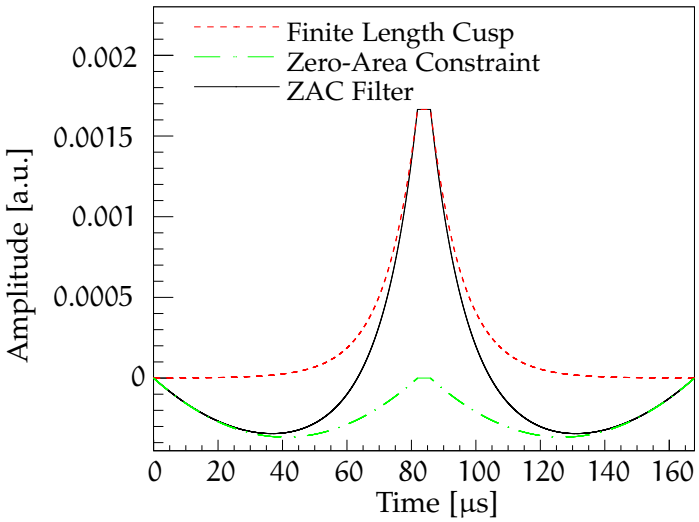

Figure 6.3.: Amplitude versus time for the ZAC filter (black full line). It is composed of the finite-length cusp (red dashed) from which two parabolas are subtracted on the cusp sides (green dash-dotted).

The final choice was a Zero-Area finite-length Cusp filter with central flat top that will be referred as ZAC from here on. It is implemented as:

$$ZAC(t) = \begin{cases} \sinh\left(\frac{t}{\tau_s}\right) + A \cdot \left[\left(t - \frac{L}{2}\right)^2 - \left(\frac{L}{2}\right)^2\right] & 0 < t < L \\ \sinh\left(\frac{L}{\tau_s}\right) & L < t < L + FT \\ \sinh\left(\frac{2L+FT-t}{\tau_s}\right) + A \cdot \left[\left(\frac{3}{2}L + FT - t\right)^2 - \left(\frac{L}{2}\right)^2\right] & \\ & L + FT < t < 2L + FT \end{cases} , \tag{6.7}$$

where FT is the length of the flat top, while A is a constant chosen such that the total integral is zero. Dealing with digitized signal traces, a discrete numerical expression has to be adopted for the shaping filter. This is obtained with the substitution $t \to \Delta t \cdot i$, where Δt is the sampling time and i the sample index. The total number of samples for the ZAC filter is n_{ZAC}, which satisfies the relation $2L + FT = \Delta t \cdot n_{ZAC}$. The construction of the ZAC filter is depicted in Fig. 6.3.

In order to perform the signal shaping, the original current pulse has to be reconstructed from the digitized trace, corresponding to the preamplifier output signal (Fig. 6.1). This is performed with a deconvolution of the preamplifier response function, an exponential decay with time constant $\tau = R_f C_f$. Specifically, it is implemented as the convolution with the two-samples filter:

$$f_\tau = \left[1, -\exp\left(-\frac{\Delta t}{\tau}\right)\right] \quad . \tag{6.8}$$

No correction for the finite band-width of the electronics was applied. Since the convolution operation is commutative, the convolution between the ZAC filter and the inverse preamplifier response function f_τ can be performed:

$$FF[i] = ZAC[i] \cdot \left(-\exp\left(-\frac{\Delta t}{\tau}\right)\right) + ZAC[i+1] \cdot 1 \qquad i = 1, \ldots, n_{ZAC} - 1 \quad . \tag{6.9}$$

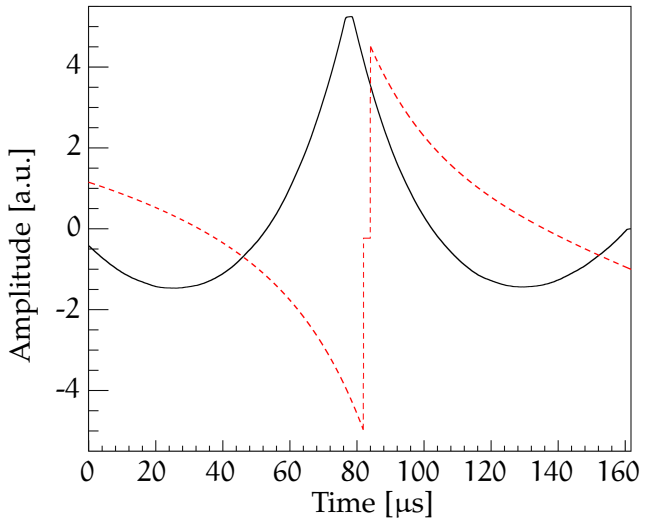

Figure 6.4.: The ZAC filter after the convolution with the inverse preamplifier response function (red dashed), and the waveform of Fig. 6.1 after the convolution with it (black).

The final filter FF is shown in red dashed in Fig. 6.4. The convolution of each signal waveform y with FF is then performed, leading to the shaped signal z:

$$z[i] = \sum_{k=i}^{i+n_{ZAC}-2} y[k] \cdot FF[i + n_{ZAC} - 1 - k] \quad , \qquad i = 1, \ldots, n_y - n_{ZAC} + 2 \quad , \quad (6.10)$$

where n_y is the number of samples in the digitized trace (4096 for GERDA Phase I). The shaped signal z for the trace of Fig. 6.1 is shown as blue full line in Fig. 6.4. The energy E is taken as the maximum height of z. The parameters to be optimized are the filter length $2L$, the flat-top FT, the shaping time τ_s, and the preamplifier decay constant τ.

6.3 THE OPTIMIZATION OF THE ZAC FILTER

The data considered for the optimization of the ZAC filter are the calibration runs taken during the entire Phase I, corresponding to the November 2011 – May 2013 period. The detectors considered are ANG2–5 from the HdM experiment, RG1–2 from IGEX and four of the five BEGes (with names starting with GD). These are the same detectors used for the $0\nu\beta\beta$ decay analysis [102]. The data were divided in the four data sets listed in Tab. 6.1, corresponding to different detector configurations in GERDA. In total, 72(45) calibration runs are available for the coaxial (BEGe) detectors.

For each of the data sets of Tab. 6.1, the first and the last calibration run were considered. Given their longer duration, one more calibration run taken in the middle of periods A and D was used, too. It is expected that the charge collection properties of all detectors remain constant within all Phase I duration, while the electronic noise and disturbances can change between different periods, but should be stationary within the same data set. If this is the case, the parameters of the ZAC filter giving the best energy resolution should be constant for each data set.

The choice of the shaping filter affects the electronic and charge collection terms of Eq. 3.23. While the ENC is not energy dependent, the optimal flat-top varies

Table 6.1.: Data sets definition for the optimization of the ZAC filter. The division of the period from 02.06.12 to 02.07.12 into two data sets is due to their very different noise conditions, mostly related to microphonics induced by maintenance operation performed in the first half of June 2012.

Data set	Duration	Detector configuration
A	09.11.11-22.05.12	ANGs + RGs + GTFs
B	02.06.12-15.06.12	ANGs + RGs + GTF112
C	15.06.12-02.07.12	ANGs + RGs + GTF112
D	08.07.12-21.05.13	ANGs + RGs + GTF112 + BEGes

at different energies. In order to quantify the improvement in energy resolution provided by an energy dependent flat-top tuning, the ZAC filter was optimized on the 583.2 keV and on the 2614.5 keV peaks of ^{208}Tl for one detector and one calibration run only. It turned out that the optimal flat-top is almost constant at all energies, and that the obtainable improvement at low energy ($\sim$ 500 keV) is below 1%, while it is negligible at $Q_{\beta\beta}$. Based on this, the optimization of the ZAC filter was performed only on the 2614.5 keV ^{208}Tl line, with a major reduction of computing time.

The standard quality cuts used for the analysis of calibration runs were applied to the data. These include the rejection of muon events, events with trigger outside the 80-82 µs range, coincidences and pile-up events (see Sec. 5.3). The energy reconstruction was then performed only on the surviving events.

The energy spectrum was reconstructed with different values of the four filter parameters L, FT, τ_s and τ. In particular:

- the total filter length $2L + FT$ was varied for only one calibration run between 120 and 163 µs. As expected [210], the best energy resolution was obtained for the longest possible filter, because all the available information contained in the signal trace is exploited for energy reconstruction. Given the variability of the trigger time within a 2 µs range, the maximum of the shaped signal can be at one of its extremes when the maximum filter length of 163 µs is used, leading to an energy underestimation. This effect completely disappears if the filter is shortened by 2 µs. Hence, the optimization was performed with $2L = 160$ µs, and a total filter length $2L + FT$ of $\sim$ 161 µs, depending on the FT choice;
- the optimal length of FT is related to the charge collection time in the detector. For coaxial detectors this is typically between 0.6 and 1 µs, depending on the electric field configuration and on the location of the energy deposition. For BEGes it is slightly longer due to the slower charge drift. The value of FT was therefore varied between 0.5 and 1.5 µs in 120 ns steps;
- the value of τ can in principle be calculated knowing the feedback resistance and capacitance. In reality τ is modified by the presence of parasitic capacitance in the front-end electronics. Moreover, given the presence of long cables a signal deformation can arise. Therefore, τ is normally obtained by fitting the pulse decay tail. This was not possible due to the presence of more

than one exponential, so τ was varied between 100 and 300 µs with 5 µs step size.

The peak at 2614.5 keV peak was fitted with the Hypermet function [204] described in Sec. 5.5:

$$f(E) = A\exp\left(-\frac{(E-\mu)^2}{2\sigma^2}\right) + B + \frac{C}{2}\operatorname{erfc}\left(\frac{E-\mu}{\sqrt{2}\sigma}\right) + \frac{D}{2}\exp\left(\frac{E-\mu}{\delta}\right)\operatorname{erfc}\left(\frac{E-\mu}{\sqrt{2}\sigma} + \frac{\sigma}{\sqrt{2}\delta}\right) \quad . \quad (6.11)$$

The FWHM was obtained numerically from the fitting function after the subtraction of the flat and step-like background components. The energy resolutions resulting from different parameters of the ZAC filter were compared, and the parameters leading to a minimal FWHM were chosen for the full reprocessing of the data. The optimal parameters of the ZAC filter for period D are reported in Table 6.2 as an example. For all the four data sets, the parameters leading to the best energy resolution remain constant within the same period. Moreover, the optimal value for FT is also constant for entire Phase I. On the other side, variations are present in the optimal values of τ_s and τ if different data sets are compared. With reference to Tab. 6.3, the optimal τ_s varies by 2 to 4 µs for all the coaxial detectors, with the exception of RG2, while τ changes by up to 60 µs. The application of the filter parameters to different data sets with respect to that used for the optimization leads to FWHM variations of up to 3%. The stability of the optimal parameters within the same data set and their variability between data sets confirms the dependence of the microphonic disturbances on the cable routing.

Table 6.2.: Optimized parameters of the ZAC filter for period D. While the filter length 2L is equal for all the detectors, the FT varies between 0.5 and 1.2 µs, according to the charge collection properties of each diode. As expected, the BEGes need a slightly longer FT due to their longer charge drift time.

Detector	2L [µs]	FT [ns]	τ_s [µs]	τ [µs]
ANG2	160	600	9	190
ANG3	160	840	16	220
ANG4	160	720	13	250
ANG5	160	960	17	170
RG1	160	720	12	210
RG2	160	680	8	240
GD32B	160	1080	13	220
GD32C	160	960	16	170
GD32C	160	840	15.5	170
GD35B	160	1200	17	135

Table 6.3.: Optimized shaping time τ_s and of the effective preamplifier time constant τ for the four periods. The values for the BEGe detectors are not shown because they were present only in period D.

	τ_s [μs]				τ [μs]			
Detector	A	B	C	D	A	B	C	D
ANG2	8	7	7.5	9	200	150	210	190
ANG3	15	11	13	16	200	180	230	220
ANG4	13	10	11	13	200	250	250	250
ANG5	17	15	15	17	180	190	190	170
RG1	13	10	11	12	180	180	200	210
RG2	8	8	8	8	260	250	250	240

6.4 RESULTS ON PHASE I CALIBRATION AND PHYSICS DATA

Once the optimization of the ZAC filter was completed, all Phase I calibration and physics data were reprocessed with the optimized ZAC filter. While the filter optimization was performed with a dedicated software tool tailored to the minimization of computing time, the final reprocessing was done using GELATIO. A copy of the "official" tier2 and tier3 was produced, with an additional variable given by the energy calculated with the ZAC filter.

Given the need to be as unbiased as possible, the following procedure has been followed, in which each step is performed only after the previous has been successfully completed with no indication for any possible failure or problem:

- the tier2 files, containing the uncalibrated spectra, of all calibration runs are created;
- the calibration curves are extracted using the standard calibration routine described in chapter 5;
- the stability of FWHM, peak positions and calibration curve parameters is checked;
- the tier3 files, containing the calibrated spectra, are produced for all calibration runs;
- the deviations of the peak positions in the calibrated spectra from the literature values are computed and plotted over time;
- all the calibration spectra of each detector are summed. These high-statistics spectra, denoted from here on as super-tier3, are then used to further check the peak positions, to study the energy dependence of the FWHM, and to determine the FWHM at $Q_{\beta\beta}$;
- the difference between the energy reconstructed with the ZAC and the pseudo-Gaussian filter for each event is computed for a random subset of all calibration data, and possible systematic deviations from zero are searched;
- the tier2 and tier3 files of the physics data are created;
- the difference between the energy reconstructed with the ZAC and the pseudo-Gaussian filter for each event of all physics data is computed, and the possible existence of systematic deviations from zero is searched;
- the effective FWHM at $Q_{\beta\beta}$ for physics data is calculated.

The results of each of the mentioned step were discussed within a restricted group of collaborators before undertaking the following one. The whole work was then presented to the GERDA collaboration, but the energy distribution of the events in the 10 keV region around $Q_{\beta\beta}$ was not shown. This was done only after all the points quoted above had been discussed, and after a general agreement was achieved on the eventual re-publication of the $0\nu\beta\beta$ decay analysis on the reprocessed data.

In order to provide a clearer picture to the reader, the results will not be presented here in the chronological order described above. First, the improvement in energy resolution for the calibration data will be presented. In a second part, the effective energy resolution at $Q_{\beta\beta}$ for physics data will be provided. Finally, the systematic effects of the reprocessing will be described.

6.4.1 *Energy Resolution for Calibration Data*

A first remarkable result of this work is the improvement of the energy resolution between 5 and 23% for the ^{208}Tl FEP at 2614.5 keV for all the Phase I calibration data. Fig. 6.5 shows the summed spectrum (super-tier3) of all Phase I calibrations around the 2614.5 keV line for ANG2. The same plots for all the semi-coaxial and BEGe detectors are reported in Figs. B.1 and B.2, respectively. In all cases, the amplitude of the Gaussian component is larger for the spectrum obtained with the optimized ZAC filter and its width is correspondingly reduced. The parameters B and C describing the continuum below the peak are compatible for the two shaping filters. While for the coaxial detectors a low-energy tail has to be accounted for in the fit, the amplitude of the tail in the BEGe detectors is negligible. The tail it therefore automatically removed from the fit. This is attributed to the smaller dimensions of the BEGe detector and its reduced charge collection inefficiency. For the coaxial detectors the tail amplitude D is strongly reduced when the ZAC shaping is used thanks to the presence of the flat-top that yields an improved integration of the collected charge.

A deeper understanding of the result is provided by studying the evolution of the FWHM as function of energy, which is fitted according to Eq. 3.23. Fig. 6.6 shows the resolution curve obtained from the super-tier3 spectra for ANG2. The same is shown for all detectors in Figs. B.3 and B.3. As expected, the major improvement regards the ENC, which reduces $FWHM^2$ at all energies by a constant. For all channels and for both the pseudo-Gaussian and the ZAC filter the charge production term $w_p^2 = 2.355\,\eta F$ is comparable with the theoretical value of $1.64 \cdot 10^{-3}$ keV. Finally, the charge collection term w_c^2 for the ZAC filter is in most cases compatible within the uncertainty with the value obtained for the pseudo-Gaussian filter. An exception is represented by ANG3 and RG2, for which a longer flat-top could further reduce the charge collection inefficiency. In any case, the large uncertainty of this parameter is due to the lack of peaks above 3 MeV which makes the fit imprecise. This term is the smallest of the three and accounts for maximally 15% of the width at 2614.5 keV.

One of the original motivations for the application of the ZAC filter to the Gerda Phase I data was the observation of temporary deterioration of the energy resolution in some detectors interpreted as due to time-evolving microphonic distur-

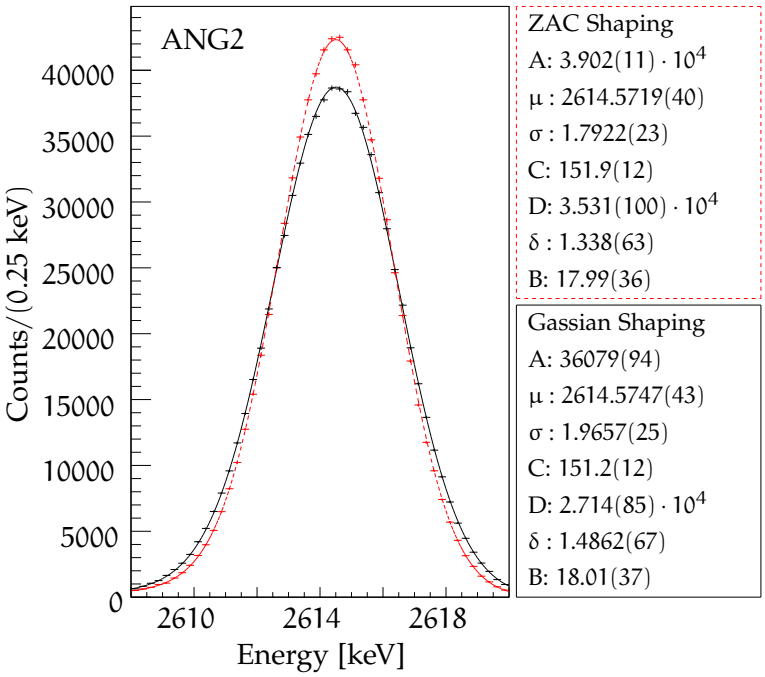

Figure 6.5.: ^{208}Tl line for ANG2. All Phase I calibration runs are merged together. The best fit values are reported in the plot.

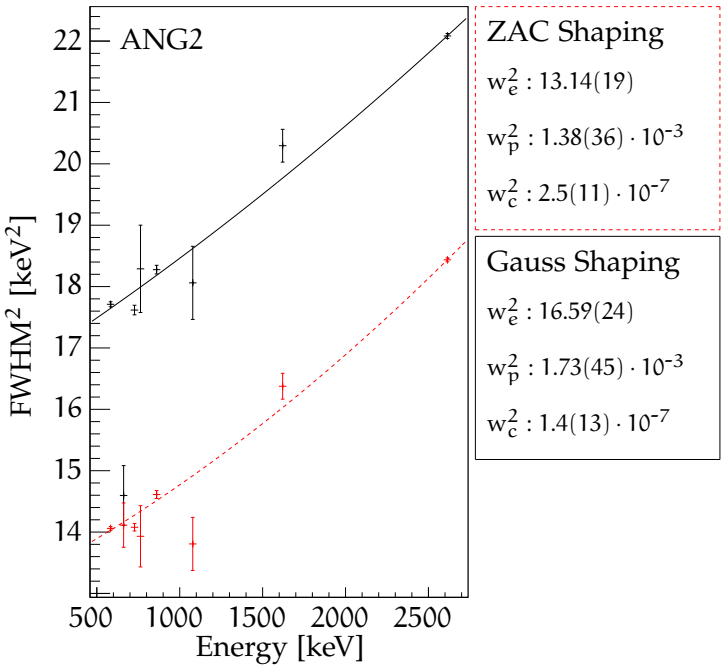

Figure 6.6.: FWHM^2 as a function of energy for the super-tier3 of ANG2 The best fit values are reported.

bance not being properly treated by the pseudo-Gaussian filter. This is confirmed by the comparison of the FWHM over time for both filters. Fig. 6.7 shows the FWHM of the ^{208}Tl 2614.5keV line for three detectors and for all Phase I calibration runs. In case of ANG2 the FWHM obtained with the pseudo-Gaussian shaping fluctuates between 4.5 and 4.4 keV. In June 2012 stronger microphonic disturbances caused a FWHM increase up to about 5.1 keV. When the ZAC filter is used the effect is significantly reduced and the FWHM obtained for the affected calibrations is brought back to a value consistent with the average. Stronger fluctuations were present for GD35B: a very poor energy resolution was observed during the first month of operation together with a continuous worsening of the spectroscopic performances in the last 4 months of Phase I. Also in this case the ZAC filter energy reconstruction is unaffected by the low-frequency baseline fluctuations induced by microphonics and allows to stabilize the FWHM over time to about 2.8 keV. The time development of the FWHM for all detectors is given in Figs. B.5, B.6 and B.7

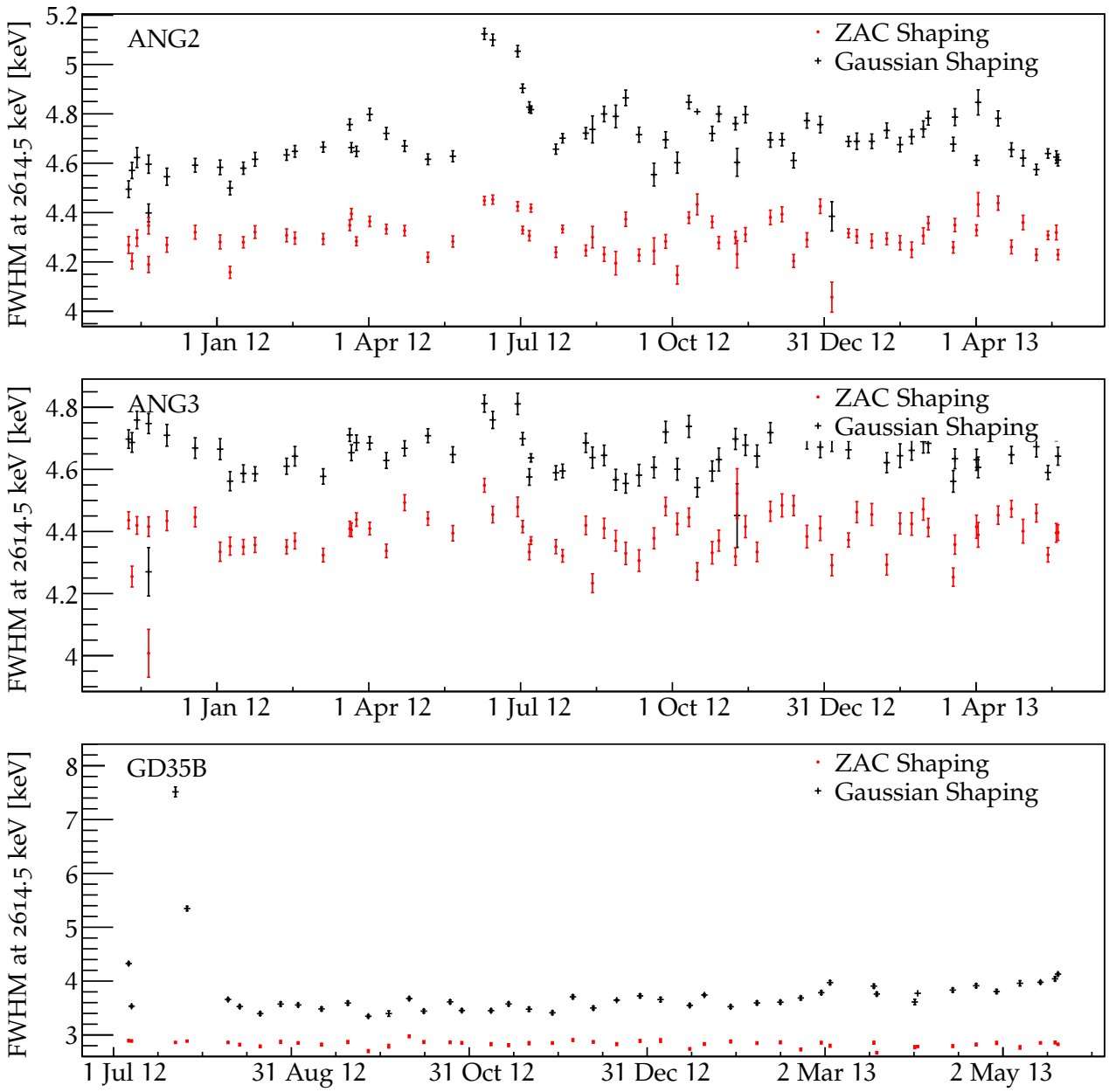

Figure 6.7.: Time evolution of FWHM for the ^{208}Tl line at 2614.5 keV over all Phase I.

Table 6.4.: Average FWHM over all Phase I. The improvement is computed as the difference between the FWHM for the pseudo-Gaussian and that for the ZAC filter. Only the statistical uncertainty due to the peak fit is quoted.

Detector	FWHM at ^{208}Tl FEP [keV] pseudo-Gaussian	ZAC	Improvement [keV]
ANG2	4.712(3)	4.314(3)	0.398(4)
ANG3	4.658(3)	4.390(3)	0.268(4)
ANG4	4.458(3)	4.151(3)	0.307(4)
ANG5	4.323(3)	4.022(3)	0.301(4)
RG1	4.595(4)	4.365(4)	0.230(6)
RG2	5.036(5)	4.707(4)	0.329(6)
GD32B	2.816(4)	2.699(3)	0.117(5)
GD32C	2.833(3)	2.702(3)	0.131(4)
GD32D	2.959(4)	2.807(3)	0.152(5)
GD35B	3.700(5)	2.836(3)	0.864(6)

The Phase I average FWHM for the ^{208}Tl line at 2614.5 keV for each detector, obtained from the graphs of Figs. B.5, B.6 and B.7, relative to the pseudo-Gaussian and the ZAC filter are reported in Tab. 6.4. The average improvement was calculated as the difference between the two values. This is about 0.31 keV for the coaxial and 0.13keV for the BEGe detectors, apart from GD35B for which a much larger improvement is obtained, as described above.

6.4.2 *Energy Resolution for Physics Data*

The effective energy resolution at $Q_{\beta\beta}$ for the physics data is computed as described in Sec. 5.8. As a first check, the summed energy spectra in the 1515-1535 keV range for all Phase I data for the six coaxial and the four BEGe detectors used for the $0\nu\beta\beta$ decay analysis are shown in Figs. 6.8 and 6.9, respectively. The FWHM obtained with the pseudo-Gaussian shaping for the coaxial detectors is 4.49 ± 0.11 keV, while it is 4.09 ± 0.11 keV if the ZAC filter is used. In the case of BEGes, the ZAC filter provides a 2.75 ± 0.21 keV FWHM compared to the 3.05 ± 0.30 keV obtained with the pseudo-Gaussian. The comparison in this case is harder due to the limited number of events.

Tab. 6.5 reports the FWHM at 1524.6 keV of each detector and data set as obtained from the ^{42}K peak fit and from calibration data. The first is determined with an unbinned likelihood fit using a Gaussian peak over a constant continuum in the [1515; 1535] keV range. The measured values both for the peak position and width remain consistent within their uncertainties if the fit range is changed by ± 5 keV. The energy resolution at 1524.6 keV from calibration data has been extrapolated from the resolution curves. The difference between the FWHM calculated on the super-tier3 and the corresponding value calculated on each single tier2 and averaged over all the calibration runs is given as systematic uncertainty. The fact that the systematic uncertainties always lie below 0.04 keV is an indication of the good performance of the ZAC filter when many data sets taken in

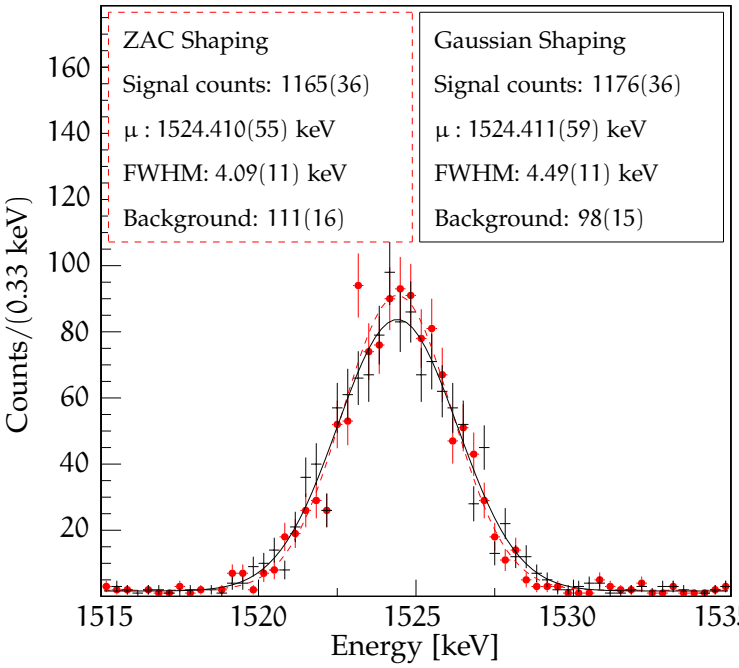

Figure 6.8.: ^{42}K peak obtained from all coaxial detector spectra merged together.

different times and conditions are merged together. This was not the case for the semi-Gaussian shaping (see Tab. 5.8), where the systematic uncertainties are one order of magnitude higher. Also in this case a correction term is computed, where needed. Finally, the exposure-weighted average is calculated for the golden, silver and BEGe data sets, leading to the final values of the FWHM at $Q_{\beta\beta}$ reported in Tab. 6.7. The overall improvement is 0.48 ± 0.24 keV for the golden data set, 0.36 ± 0.27 keV for the silver data set, and 0.50 ± 0.26 keV for the silver data set.

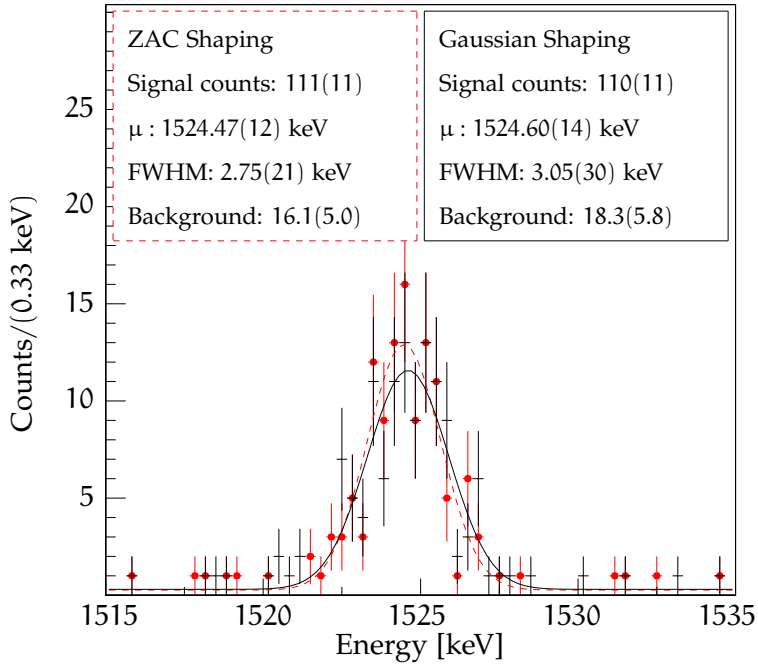

Figure 6.9.: ^{42}K peak obtained from all BEGes spectra merged together.

Table 6.5.: FWHM at 1524.6 keV for all Phase I detectors and all three data sets. The first column shows the data set, the second the detector, the third the FWHM of the ^{42}K peak (computed on all Phase I physics data), the fourth is the FWHM at 1524.6 keV from the calibration data of the considered data set (the first error is statistical, the second systematic), and the fifth is the correction term, where used. The two errors on the offset are statistical and systematic and are propagated from those in the previous two columns.

	Detector	FWHM [keV] Physics	FWHM [keV] Calibration	Offset
G	ANG2	4.75 ± 0.27	$4.006 \pm 0.003 \pm 0.007$	0.74 ± 0.27
O	ANG3	3.88 ± 0.22	$4.078 \pm 0.003 \pm 0.038$	
L	ANG4	4.10 ± 0.30	$3.846 \pm 0.003 \pm 0.016$	
D	ANG5	3.61 ± 0.20	$3.627 \pm 0.003 \pm 0.017$	
E	RG1	3.84 ± 0.28	$3.874 \pm 0.004 \pm 0.016$	
N	RG2	4.31 ± 0.31	$4.286 \pm 0.004 \pm 0.036$	
S	ANG2	4.75 ± 0.27	$4.056 \pm 0.005 \pm 0.004$	0.69 ± 0.27
I	ANG3	3.88 ± 0.22	$4.099 \pm 0.005 \pm 0.033$	
L	ANG4	4.10 ± 0.30	$3.896 \pm 0.005 \pm 0.014$	
V	ANG5	3.61 ± 0.20	$3.673 \pm 0.005 \pm 0.018$	
E	RG1	3.84 ± 0.28	$3.898 \pm 0.006 \pm 0.001$	
R	RG2	4.31 ± 0.31	$4.237 \pm 0.008 \pm 0.034$	
B	GD32B	2.32 ± 0.30	$2.263 \pm 0.004 \pm 0.006$	
E	GD32C	2.64 ± 0.44	$2.256 \pm 0.003 \pm 0.003$	
G	GD32D	3.18 ± 0.43	$2.366 \pm 0.005 \pm 0.025$	0.81 ± 0.43
e	GD35B	2.42 ± 0.47	$2.439 \pm 0.004 \pm 0.011$	

Table 6.6.: FWHM at $Q_{\beta\beta}$ obtained from the calibration data obtained with the ZAC shaping: the values are taken from the resolution curve fitted to the super-tier3. The first error is statistical, the second is the difference from the FWHM at $Q_{\beta\beta}$ averaged on each single calibration tier3 and considered here as systematic uncertainty. In case a correction term has to be applied, its value is reported in the right column. In this case, the reported error is the combination in quadrature of all the statistical and systematic uncertainties involved.

	Detector	FWHM [keV] Physics	FWHM [keV] Calibration	Offset
G	ANG2	$4.143 \pm 0.003 \pm 0.003$	0.74 ± 0.27	4.88 ± 0.27
O	ANG3	$4.234 \pm 0.004 \pm 0.029$		
L	ANG4	$3.986 \pm 0.003 \pm 0.013$		
D	ANG5	$3.813 \pm 0.004 \pm 0.007$		
E	RG1	$4.069 \pm 0.005 \pm 0.040$		
N	RG2	$4.486 \pm 0.005 \pm 0.039$		
S	ANG2	$4.199 \pm 0.006 \pm 0.001$	0.69 ± 0.27	4.89 ± 0.28
I	ANG3	$4.252 \pm 0.006 \pm 0.032$		
L	ANG4	$4.020 \pm 0.007 \pm 0.012$		
V	ANG5	$3.857 \pm 0.006 \pm 0.031$		
E	RG1	$4.091 \pm 0.008 \pm 0.007$		
R	RG2	$4.435 \pm 0.009 \pm 0.028$		
B	GD32B	$2.478 \pm 0.006 \pm 0.008$		
E	GD32C	$2.480 \pm 0.004 \pm 0.002$		
G	GD32D	$2.604 \pm 0.006 \pm 0.033$	0.81 ± 0.43	3.41 ± 0.43
e	GD35B	$2.641 \pm 0.066 \pm 0.014$		

Table 6.7.: FWHM at $Q_{\beta\beta}$ for the Golden, Silver and BEGe data sets. The values from Table 6.6 are averaged according to the corresponding exposure. The corrected FWHM is used for ANG2 and Anubis. The FWHM for the spectra reconstructed with the Gaussian shaping are reported for reference.

Data set	ZAC FWHM [keV]	Pseudo-Gaussian FWHM [keV]
Golden	4.25 ± 0.13	4.83 ± 0.20
Silver	4.27 ± 0.13	4.63 ± 0.24
BEGe	2.74 ± 0.20	3.24 ± 0.17

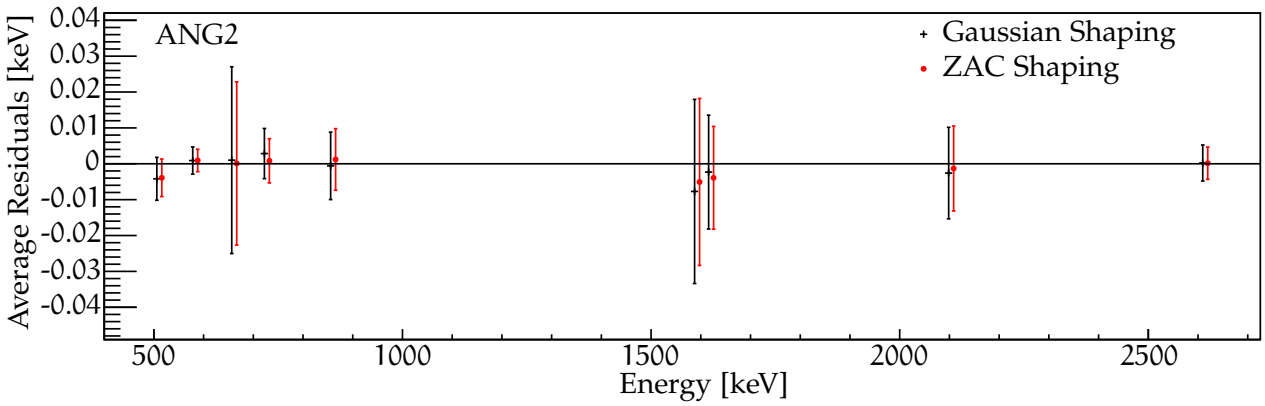

Figure 6.10.: Average deviations of the peak position on the tier3 spectra from literature values for ANG2.

6.4.3 *Systematics*

A further comparison between the performances of the pseudo-Gaussian and the ZAC filter is provided by the study of the systematic effects related to the signal shaping and the energy calibration. The improvement in energy resolution given by the ZAC filter is also reflected in a more precise determination of the energy scale for the single calibration runs. Fig. 6.10 shows the residuals of the ^{208}Tl peak position from the quadratic calibration curve averaged over all Phase I calibration runs for ANG2. Both for the pseudo-Gaussian and the ZAC shaping, the average residuals are of order of 10^{-2} keV. Hence, they are much smaller than the peak widths and do not give a significant contribution to the systematic uncertainty of the energy calibration.

A second check is the comparison of the deviations of the peaks positions in the calibrated spectra from the literature values. The deviations obtained with the two filters in the super-tier3 and the average deviations calculated on each single tier3 spectrum for the ^{208}Tl line at 2614.5 keV are given in Tab. 6.8. In the majority of the cases, the deviations and residuals obtained with the ZAC shaping are smaller than those of the semi-Gaussian shaping. This further confirms the improvement in energy reconstruction yielded by the ZAC filter.

A more informative evaluation of the energy calibration precision is obtained by calculating the uncertainty δ_E of the calibration curve at a given energy, e.g. at $Q_{\beta\beta}$. For each calibration run the quantity $\delta_E(E = 2039\ \text{keV})$ is calculated by error propagation on the calibration curve parameters. Using Monte Carlo (MC) simulations 10^5 events were randomly generated according to a Gaussian distribution with zero mean and sigma equal to $\delta_E(E = 2039\ \text{keV})$. The distributions from all Phase I calibration runs are then summed up and the systematic uncertainty of the energy scale at 2039 keV is given by the half-width of the 68% central interval. This results to be between 0.03 and 0.06 keV and is up to 16% smaller for ZAC with respect to the pseudo-Gaussian filter, depending on the detector. The systematic uncertainty on the energy reconstruction at $Q_{\beta\beta}$ for GD35B is shown in Fig. 6.11 as an example. The values of $\delta_E(E = 2039\ \text{keV})$ for all the detectors are reported in Tab. 6.9.

Table 6.8.: Deviations of the 2614.511 keV ^{208}Tl line from the literature values [197]. Both the value from the super-tier3 and the average value for the single calibration runs are reported. The values for the semi-Gaussian shaping are the same as in Tabs. 5.6 and 5.7.

		ZAC Shaping		Pseudo-Gaussian Shaping	
	Detector	Super-tier3 Deviation [keV]	Average Cal. Residuals [keV]	Super-tier3 Deviation [keV]	Average Cal. Residuals [keV]
G	ANG2	0.06 ± 0.01	0.00 ± 0.01	0.06 ± 0.01	0.00 ± 0.01
O	ANG3	0.05 ± 0.01	0.01 ± 0.08	0.13 ± 0.01	0.08 ± 0.06
L	ANG4	0.05 ± 0.01	0.01 ± 0.03	0.03 ± 0.01	0.02 ± 0.04
D	ANG5	0.08 ± 0.01	0.04 ± 0.07	0.13 ± 0.01	0.06 ± 0.07
E	RG1	0.23 ± 0.02	0.04 ± 0.15	0.32 ± 0.03	0.12 ± 0.13
N	RG2	0.05 ± 0.01	0.03 ± 0.11	0.19 ± 0.02	0.20 ± 0.12
S	ANG2	0.05 ± 0.01	0.01 ± 0.01	-0.15 ± 0.02	0.08 ± 0.05
I	ANG3	0.03 ± 0.01	0.00 ± 0.07	-0.12 ± 0.02	0.13 ± 0.08
L	ANG4	0.04 ± 0.01	0.01 ± 0.02	-0.15 ± 0.02	-0.13 ± 0.10
V	ANG5	0.04 ± 0.01	0.05 ± 0.02	-0.05 ± 0.02	0.11 ± 0.09
E	RG1	0.19 ± 0.04	0.00 ± 0.26	0.11 ± 0.03	-0.05 ± 0.18
R	RG2	0.04 ± 0.03	-0.01 ± 0.02	0.07 ± 0.02	0.07 ± 0.04
B	GD32B	0.00 ± 0.01	0.01 ± 0.02	-0.04 ± 0.01	-0.01 ± 0.05
E	GD32C	0.02 ± 0.01	0.02 ± 0.01	-0.01 ± 0.01	0.01 ± 0.09
G	GD32C	0.01 ± 0.01	0.02 ± 0.02	-0.03 ± 0.01	-0.01 ± 0.05
e	GD35B	0.00 ± 0.01	0.00 ± 0.01	0.02 ± 0.01	-0.01 ± 0.09

	$\delta_E(E = 2039$ keV$)$ [keV]	
Detector	Pseudo-Gaussian	ZAC
ANG2	0.041	0.035
ANG3	0.048	0.042
ANG4	0.045	0.042
ANG5	0.036	0.037
RG1	0.057	0.053
RG2	0.056	0.053
GD32B	0.035	0.035
GD32C	0.032	0.029
GD32D	0.042	0.041
GD35B	0.062	0.052

Table 6.9.: Systematic on the energy scale at $Q_{\beta\beta}$ for golden coax and BEGe detectors. For the coaxial detectors, the values refer to the golden data set only.

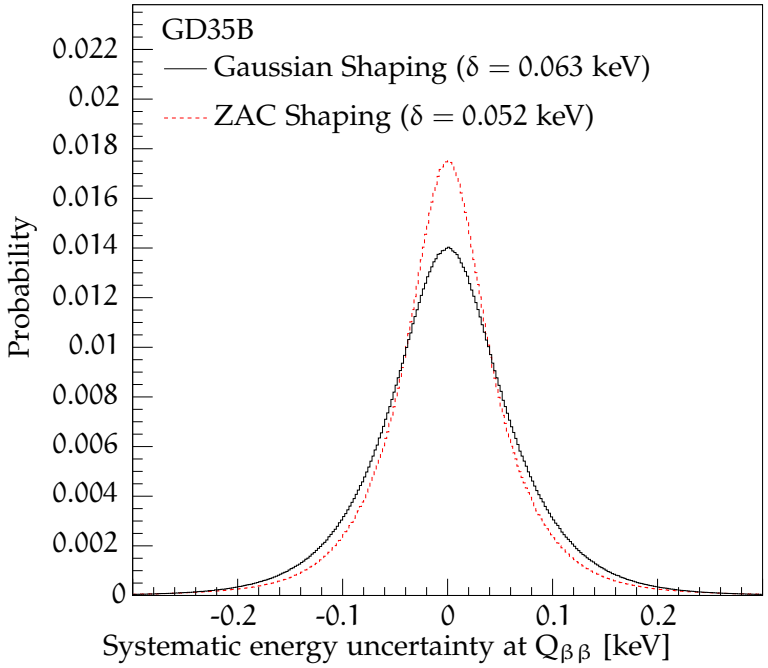

Figure 6.11.: Systematic of the energy scale for GD35B

A fundamental cross-check of the reprocessed data is given by the event-by-event comparison of the energy obtained with the ZAC and the pseudo-Gaussian filter. This is performed by calculating the energy difference of the events in the 2614.5 keV peak as shown in Fig. 6.12 for ANG2 and a typical calibration run. For all the detectors this distribution is a Gaussian with a mean value compatible with zero and a width $\sigma \sim 0.8$ keV. The same behavior is observed at all energies for both calibration and physics data.

6.5 RE-ANALYSIS OF $0\nu\beta\beta$ DECAY WITH GERDA PHASE I DATA

This section describes the re-analysis of $0\nu\beta\beta$ decay search using the Phase I data reprocessed with the ZAC filter. Before releasing the reprocessed data to the collaboration, the decision was taken not to publish a new result on $0\nu\beta\beta$ decay search on a stand-alone paper, but to combine the reprocessed data with the first data of GERDA Phase II. For this reason, the results reported here are not in any case to be considered official, but rather a case study for the future GERDA analyses. The author and the GERDA collaboration kindly require to refer to [102] until a new collaboration paper on $0\nu\beta\beta$ decay analysis is released.

6.5.1 *Comparison of Physics Spectra Obtained with the Pseudo-Gaussian and the ZAC Filters*

Before proceeding with the analysis, the Phase I physics spectra for the golden, silver and BEGe data sets obtained with the pseudo-Gaussian and the ZAC filter were compared. They are shown in Fig. 6.13: the spectra are well superimposed also in the region where the calibration curves are extrapolated, *i.e.* below 511 keV and above 2615 keV. In particular, the α events around 5 MeV are reconstructed at the same energy by both the shaping filters, and the spectra thresholds ($\sim$ 50 keV)

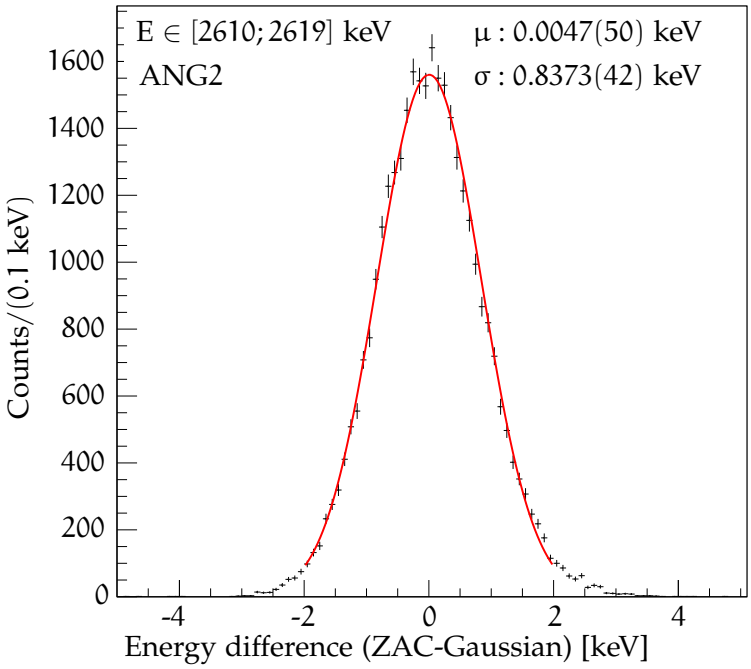

Figure 6.12.: Event by event energy difference for ANG2. The events in the 2615 ± 5 keV range are used.

differ by less than 1 keV. Also the background induced γ lines are reconstructed at the same energy and agree with the literature values for both filters.

More interesting is the comparison of the spectra around $Q_{\beta\beta}$. Fig. 6.14 shows the 40 keV region around $Q_{\beta\beta}$ for the golden, silver and BEGe data sets and the two filters. The events shown are those surviving the quality cuts, but before the application of pulse shape discrimination (PSD). The energy of each single event varies by up to 2 keV, in agreement with the distribution reported in Fig. 6.12.

The events which mostly affect the $0\nu\beta\beta$ decay analysis are those in the 10 keV region of interest (ROI) around $Q_{\beta\beta}$. The energy reconstructed with the pseudo-Gaussian and the ZAC filter, together with the data set, the date and the time are given in Tab. 6.10. Out of the 7 events in the ROI, only 3 survive the PSD cut. When the ZAC filter is used, all these 3 events move slightly apart from $Q_{\beta\beta}$. Hence, the limit on $0\nu\beta\beta$ decay half-life is expected to be higher if the ZAC reconstructed energy is exploited.

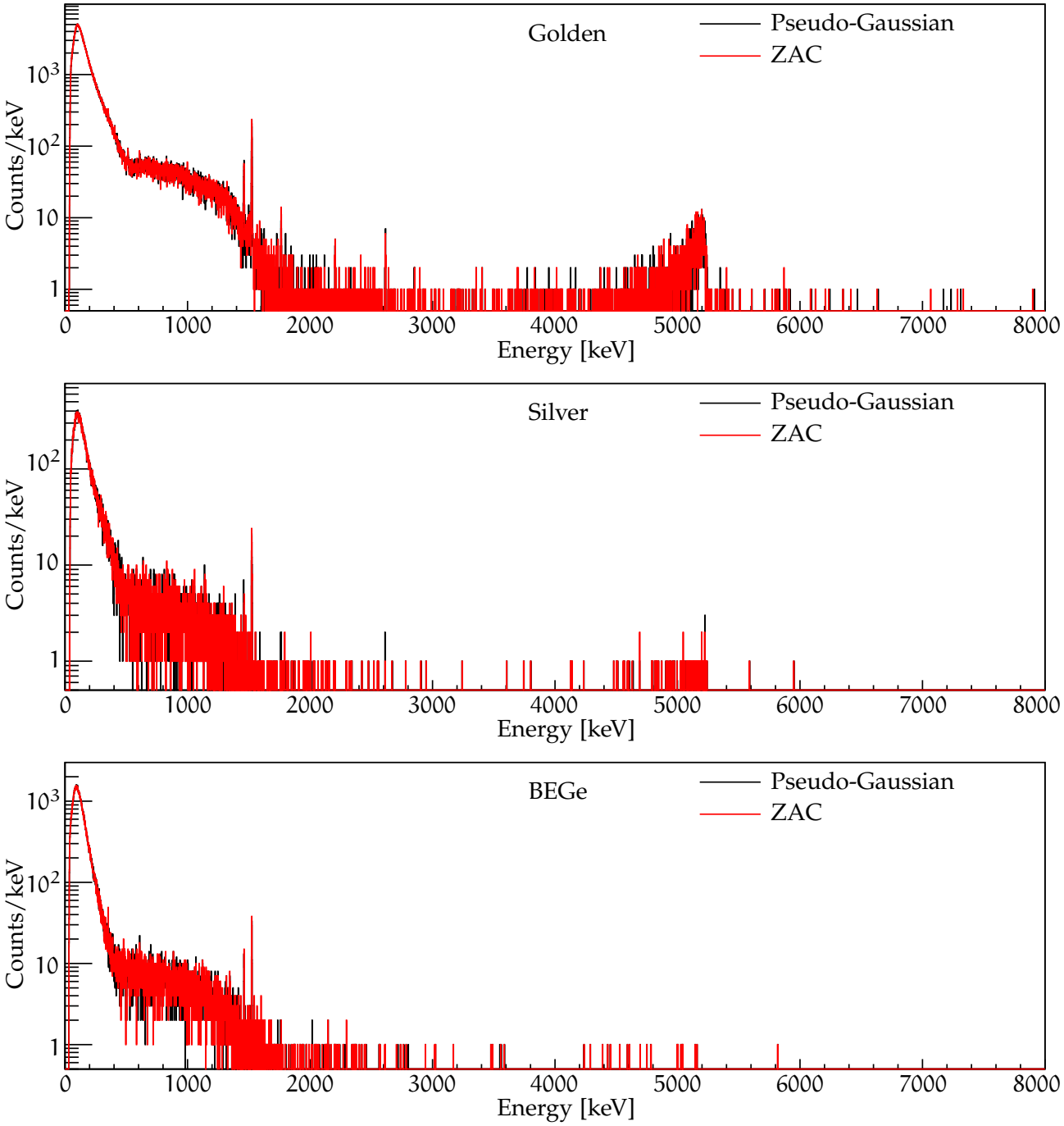

Figure 6.13.: Physics spectrum for golden, silver and BEGe data sets obtained with the pseudo-Gaussian (black) and the ZAC filter (red).

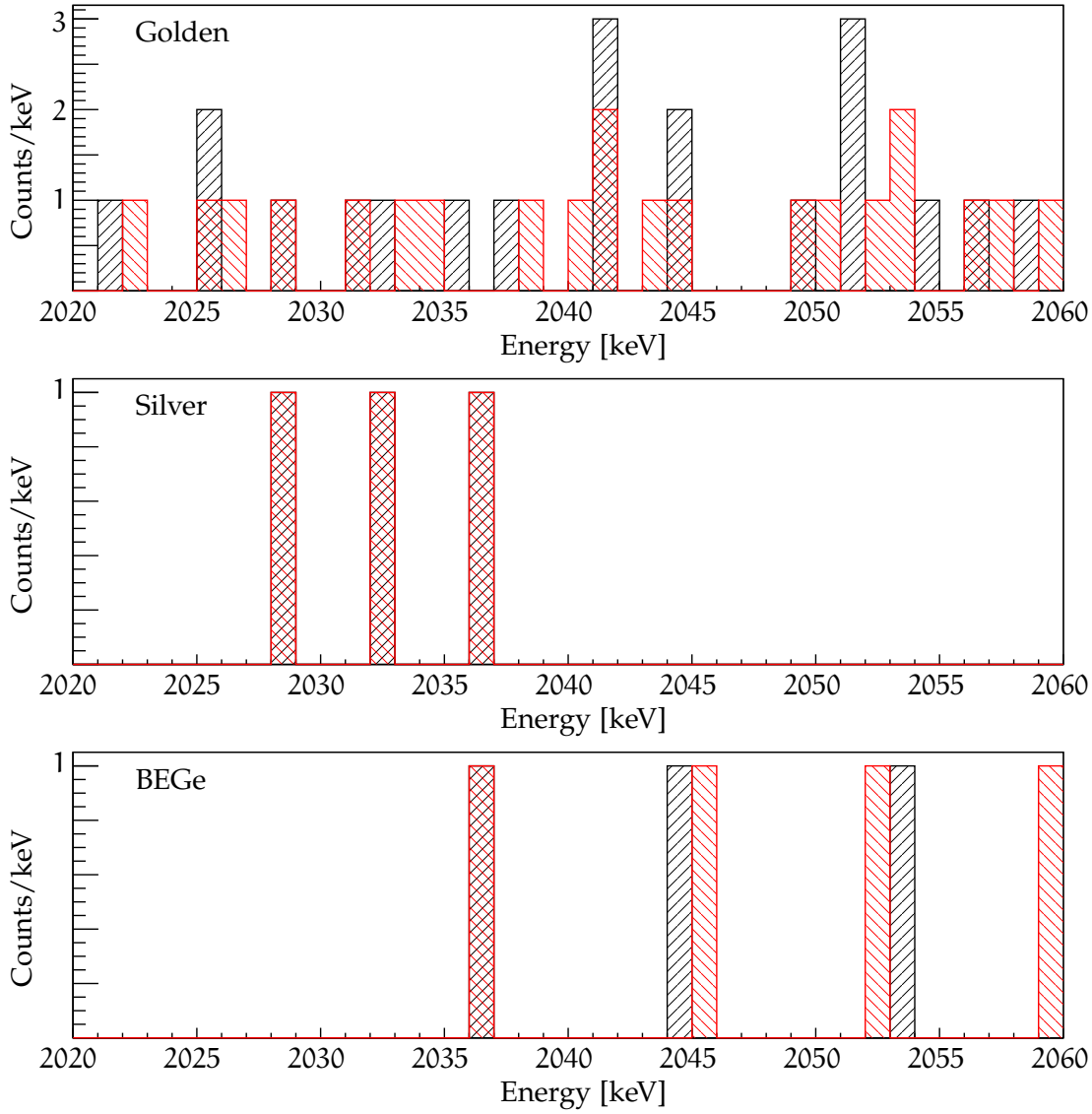

Figure 6.14.: Energy spectra relative to the golden, silver and BEGe data sets before the application of PSD for the pseudo-Gaussian (black) and ZAC filter (red).

Table 6.10.: Events in the 10 keV region around $Q_{\beta\beta}$. For each event the energy obtained with the pseudo-Gaussian and the ZAC shaping are reported.

		Energy [keV]				PSD
Data set	Detector	Gaussian	ZAC	Date	Time	Passed
Golden	ANG5	2041.8	2040.7	18-Nov-2011	22 : 52	no
Silver	ANG5	2036.9	2036.8	23-Jun-2012	23 : 02	yes
Golden	RG2	2041.3	2041.5	16-Dec-2012	00 : 09	yes
BEGe	GD32B	2036.6	2036.6	28-Dec-2012	09 : 50	no
Golden	RG1	2035.5	2034.3	29-Jan-2013	03 : 35	yes
Golden	ANG3	2037.4	2038.4	02-Mar-2013	08 : 08	no
Golden	RG1	2041.7	2041.3	27-Apr-2013	22 : 21	no

Table 6.11.: Detector parameters for $0\nu\beta\beta$ decay analysis.

	Detector	Exposure [kg·y]	f_{enr}	f_{76}	ε_{PSD}	ε_{γ}	FWHM at $Q_{\beta\beta}$ [keV] Gaussian	ZAC
G	ANG2	3.55610	0.871(51)	0.866(25)	0.918(18)	0.9	5.84(30)	4.88(27)
O	ANG3	3.00128	0.866(57)	0.883(26)	0.916(18)	0.9	4.53(13)	4.234(29)
L	ANG4	2.97743	0.901(57)	0.863(13)	0.916(18)	0.9	4.94(32)	3.986(13)
D	ANG5	3.44689	0.831(48)	0.856(13)	0.918(18)	0.9	4.16(8)	3.813(8)
E	RG1	2.64856	0.904(59)	0.855(15)	0.915(18)	0.9	4.46(28)	4.069(40)
N	RG2	2.28174	0.831(53)	0.855(15)	0.912(18)	0.9	4.91(26)	4.486(40)
S	ANG2	0.25278	0.871(51)	0.866(25)	0.918(18)	0.9	5.29(38)	4.94(27)
I	ANG3	0.21334	0.866(57)	0.883(26)	0.916(18)	0.9	4.57(20)	4.252(6)
L	ANG4	0.21165	0.901(57)	0.863(13)	0.916(18)	0.9	4.36(11)	4.020(14)
V	ANG5	0.24502	0.831(48)	0.856(13)	0.918(18)	0.9	4.21(18)	3.857(32)
E	RG1	0.18827	0.904(59)	0.855(15)	0.915(18)	0.9	4.49(28)	4.091(11)
R	RG2	0.19327	0.831(53)	0.855(15)	0.912(18)	0.9	4.83(33)	4.435(29)
B	GD32B	0.54988	0.890(27)	0.877(13)	0.899(18)	0.92	2.62(9)	2.478(10)
E	GD32C	0.61754	0.911(30)	0.877(13)	0.901(18)	0.92	2.63(6)	2.480(5)
G	GD32D	0.56234	0.923(26)	0.877(13)	0.899(18)	0.92	3.68(47)	3.41(43)
e	GD35B	0.67489	0.914(29)	0.877(13)	0.901(18)	0.92	3.96(12)	2.641(15)

6.5.2 $0\nu\beta\beta$ *Decay Analysis: Procedure and Parameters*

The analysis of $0\nu\beta\beta$ decay is performed following a Bayesian approach. Similar studies have been performed using the profile likelihood method by other members of the GERDA collaboration, hence they are not reported here.

Suppose we have a set of energy measurements $\vec{E} = E_1, \ldots, E_n$ for a total of n events, and that we need a set of parameters $\vec{\theta}$ to properly describe the energy distribution of the events. The energy of each event follows a distribution $f(E|\vec{\theta})$, while the total number of events will follow a Poisson distribution. The extended likelihood can be formulated as:

$$\begin{aligned} \mathcal{L}(\vec{E}|\vec{\theta}) &= \frac{\nu^n}{n!} e^{-\nu} \prod_{i=1}^{n} f(E_i|\vec{\theta}) \\ &= \frac{e^{-\nu}}{n!} \prod_{i=1}^{n} \left[\nu \cdot f(E_i|\vec{\theta})\right] \quad , \end{aligned} \tag{6.12}$$

where ν is the expectation value for the total number of events n. We can express ν as the sum between the total number of signal events s and background events b, and we can split the energy distribution of the single events into a signal and a background components. In particular, we assume the signal to be distributed

according to a Gaussian centered at $Q_{\beta\beta}$, and the background to be flat in all the fit region of width ΔE:

$$\begin{aligned} f\left(E|\vec{\theta}\right) &= f_s\left(E|\vec{\theta}\right) + f_b\left(E|\vec{\theta}\right) \\ &= \frac{s}{s+b}\frac{1}{\sigma\sqrt{2\pi}}\exp\left(-\frac{(E-Q_{\beta\beta})^2}{2\sigma^2}\right) + \frac{b}{s+b}\frac{1}{\Delta E} \quad . \end{aligned} \tag{6.13}$$

Notice that f is normalized to unity. We can then expand Eq. 6.12 into:

$$\begin{aligned} \mathcal{L}\left(\vec{E}|\vec{\theta}\right) &= \frac{e^{-(s+b)}}{n!}\prod_{i=1}^{n}\left[(s+b)\left(\frac{s}{s+b}G(E_i|Q_{\beta\beta},\sigma) + \frac{b}{s+b}\frac{1}{\Delta E}\right)\right] \\ &= \frac{e^{-(s+b)}}{n!}\prod_{i=1}^{n}\left[\left(s\cdot G(E_i|Q_{\beta\beta},\sigma) + \frac{b}{\Delta E}\right)\right] \quad , \end{aligned} \tag{6.14}$$

where we summarized the Gaussian into $G(E_i|Q_{\beta\beta},\sigma)$ for convenience. The log-likelihood is then given by:

$$\ln\mathcal{L}\left(\vec{E}|\vec{\theta}\right) = -s - b + \sum_{i=1}^{n}\ln\left(s\cdot G(E_i|Q_{\beta\beta},\sigma) + \frac{b}{\Delta E}\right) \quad , \tag{6.15}$$

where the term $\ln(n!)$ has been dropped because it does not influence the result.

Following the Bayesian approach, the maximization is performed on the log-likelihood for the parameters given the data:

$$\ln\mathcal{L}\left(\vec{\theta}|\vec{E}\right) = \ln\mathcal{L}\left(\vec{E}|\vec{\theta}\right) + \sum_{k=1}^{m}\ln\pi(\theta_k) + C \quad , \tag{6.16}$$

where $\pi(\theta_k)$ is the prior probability for the parameter θ_k, for a total of m parameters, and C is a constant coming from the normalization of the probability and which can be set to zero.

The posterior probability for the parameter of interest $\bar{\theta}$ is extracted via marginalization [218]: the log-likelihood $\ln\mathcal{L}\left(\vec{\theta}|\vec{E}\right)$ is integrated over all the parameters, but $\bar{\theta}$, and normalized to unity. At this point, a criterion has to be chosen for the interpretation of the result. The standard choice is to compute the distance between the mode of the marginalized distribution and the value corresponding to the background-only hypothesis. In our case the parameter of interest is the inverse of the $0\nu\beta\beta$ decay half-life, $\bar{\theta} = 1/T^{0\nu}_{1/2}$, and distance of the mode in the marginalized $1/T^{0\nu}_{1/2}$ distribution from zero is computed. If this distance has a significance of at least 99.73% (corresponding to 3σ for a Gaussian distribution), a claim for evidence is made and the result is reported as the mode, together with the 68.3% central interval. On the contrary, if the mode is at zero or close to it, the limit at 90% credibility interval (CI) is quoted.

So far, no detail about the expectation values s and b was given. For the $0\nu\beta\beta$ decay analysis we can recall Eq. 2.38:

$$\begin{aligned} s &= \frac{1}{T^{0\nu}_{1/2}}\frac{\ln 2\cdot N_A}{m_A}\cdot f_{enr}\cdot f_{AV}\cdot\varepsilon_\gamma\cdot\varepsilon^{SSE}_{psd}\cdot mt \\ b &= BI\cdot\Delta E\cdot mt \quad . \end{aligned} \tag{6.17}$$

The parameter of interest is $1/T_{1/2}^{0\nu}$, while the active volume fraction f_{enr}, the enrichment fraction f_{enr}, the efficiency for $0\nu\beta\beta$ decay detection ε_γ, the PSD efficiency ε_{PSD}^{SSE} and the background index BI are nuisance parameters, and the Avogadro number N_A, the atomic mass m_A, the exposure mt and the fit range width ΔE are constant.

If in the case of one single detector, we just have to plug the expressions of Eq. 6.17 into Eq. 6.15. For the analysis of GERDA Phase I data a broad variety of choices is possible. Namely, it must be considered that:

- f_{enr}, f_{enr}, ε_γ, ε_{PSD}^{SSE} and mt are detector dependent. In particular, the exposure values of the single detectors differ by up to 35%;
- the BI and the width of the Gaussian distribution for the signal parametrization, $\sigma = FWHM/2.355$, depend both on the detector and on the data set (golden, silver).

For the official $0\nu\beta\beta$ decay analysis of Phase I data [102], a common fit was performed on the three data sets (golden, silver and BEGe), and the energy spectra of all detectors belonging to the data set were merged together. In this analysis, the log-likelihood is expressed as:

$$\ln \mathcal{L}\left(\vec{E}|\vec{\theta}\right) = \sum_{d=1}^{3}\left[-s_d - b_d + \sum_{i=1}^{n_d} \ln\left(s_d \cdot G(E_i|Q_{\beta\beta},\sigma_d) + \frac{b_d}{\Delta E}\right)\right] \quad , \tag{6.18}$$

where the index d runs over the three data sets, and n_d is the number of events for each data set. Given the small uncertainty affecting f_{enr}, f_{enr}, ε_γ, ε_{PSD}^{SSE} and $Q_{\beta\beta}$, these parameters were considered constant. Their errors were considered as systematic. The propagation was performed by repeating the analysis a number of times, each time sampling the value of these four parameters from a Gaussian distribution with mean and sigma corresponding to those reported in Tab. 6.11. On the other side, BI_d and $FWHM_d = 2.355 \cdot \sigma_d$ were considered as nuisance parameters, and their prior probability was inserted in Eq. 6.16.

As an alternative approach the spectra of all detectors are kept separated, and f_{enr}, f_{AV}, ε_γ, $Q_{\beta\beta}$are considered as nuisance parameters, to which a prior probability is assigned according to the values of Tab. 6.11. For $Q_{\beta\beta}$ the value 2039.006(50) keV is used [100]. The log-likelihood is in this case:

$$\ln \mathcal{L}\left(\vec{E}|\vec{\theta}\right) = \sum_{d=1}^{3}\sum_{c=1}^{m_c}\left[-s_c - b_c + \sum_{i=1}^{n_c} \ln\left(s_c \cdot G(E_i|Q_{\beta\beta},\sigma_c) + \frac{b_c}{\Delta E}\right)\right] \quad , \tag{6.19}$$

where the index d runs over the data sets (golden, silver, BEGe), and the index c over the detectors of a given data set. Considering all data sets and detectors, a total of 64 parameters is used, against the 7 of the standard analysis.

6.5.3 *Results*

The analysis is performed for the spectra reconstructed with the pseudo-Gaussian and the ZAC filter, using both the official method with merged spectra and the alternative approach with separate spectra for each detector. In order to understand the origin of possible differences, the fit is run also on the golden, silver and BEGe

Table 6.12.: Results of $0\nu\beta\beta$ decay analysis for the pseudo-Gaussian and the ZAC energy reconstructed spectra using the official analysis method, and keeping each detector spectrum separate.

	$T^{0\nu}_{1/2}$ 90% CI Lower Limit [yr]			
	pseudo-Gaussian		ZAC	
Data set	Official	Separate	Official	Separate
Golden	$1.71 \cdot 10^{25}$	$1.72 \cdot 10^{25}$	$1.89 \cdot 10^{25}$	$2.00 \cdot 10^{25}$
Silver	$1.24 \cdot 10^{24}$	$1.19 \cdot 10^{24}$	$1.24 \cdot 10^{24}$	$1.20 \cdot 10^{24}$
BEGe	$3.79 \cdot 10^{24}$	$3.79 \cdot 10^{24}$	$3.80 \cdot 10^{24}$	$3.79 \cdot 10^{24}$
All	$1.92 \cdot 10^{25}$	$2.06 \cdot 10^{25}$	$2.09 \cdot 10^{25}$	$2.36 \cdot 10^{25}$

data sets only. All the results are reported in Tab. 6.12. For the official analysis, the use of the ZAC filter yields a $\sim 0.17 \cdot 10^{25}$ yr higher limit on $T^{0\nu}_{1/2}$. This difference comes from both the improved energy resolution and the outwards shifting of the three events in the 10 keV region around $Q_{\beta\beta}$.

The alternative analysis approach gives a further $0.25 \cdot 10^{25}$ yr increase in the $0\nu\beta\beta$ decay half-life limit when all data sets are exploited. The two analyses yield the same result for the BEGe data set due to the absence of events around $Q_{\beta\beta}$ (see Tab. 6.10). For the silver data set no difference is introduced by the improved energy resolution, while a $\sim 0.05 \cdot 10^{24}$ yr worse limit is obtained with the application of the alternative analysis. This is probably due to the propagation of the uncertainty on the nuisance parameters. A $0.21 \cdot 10^{25}$ yr difference on the $T^{0\nu}_{1/2}$ limit is obtained on the golden data set, again due to the better energy resolution and the event shifts. On the contrary, the BI is compatible within its uncertainty for all data sets, shaping filter and statistical analysis.

To further understand the capability of the alternative analysis, we can compare the $T^{0\nu}_{1/2}$ limits obtained on the single data sets with that obtained using all three. Both for the pseudo-Gaussian and the ZAC case, the standard analysis on all data sets yields a limit which is just $\sim 0.20 \cdot 10^{25}$ yr higher than for the golden data set only, although the limit obtained with the silver and BEGe data sets are $\sim 0.12 \cdot 10^{25}$ yr and $\sim 0.38 \cdot 10^{25}$ yr, respectively. Using the alternative analysis, the $T^{0\nu}_{1/2}$ limit with all data sets is $\sim 0.35 \cdot 10^{25}$ yr higher than that obtained with the golden data set only. This means that the alternative analysis exploits to a higher extend the information contained in the energy spectra of each single detector.

On the basis of the results presented here it is clear that the alternative analysis yields a higher sensitivity especially with the use of a high number of detectors with different energy resolution and BI. This is of particular interest for the analysis of $0\nu\beta\beta$ decay with GERDA Phase II data, in which ~ 40 detectors are going to be operated.

6.6 SENSITIVITY TO $0\nu\beta\beta$ DECAY IN GERDA PHASE II

The influence of an improved energy resolution on the physics reach of GERDA Phase II can be quantified by studying the sensitivity curve for a 90% CI limit on $T^{0\nu}_{1/2}$. This is done using toy MC simulations.

The Phase II detectors will consist in 17.6 kg of coaxial, and 20.0 kg of BEGes. Given their different resolutions and PSD properties (and, hence, background levels), the analysis has to be performed on two separate data sets. Since the actual BI and energy resolution of each detector is not available yet, the study is performed only using the official analysis described in Sec. 6.5.2. The sensitivity as function of the exposure mt can be obtained by generating N virtual experiments for fixed values of mt, with events sampled only from the background distribution. The $0\nu\beta\beta$ decay analysis is then performed on each of the spectra and the 90% CI limit on $T^{0\nu}_{1/2}$ is extracted. For each value of the exposure, 10^4 experiments have been simulated. Exposures in the range from 1 to 200 kg·yr, with 1 kg·yr steps, have been considered. The number of events in the spectra was generated according to a Poisson distribution, with an expectation value given by the BI. This is assumed to be 0.005 and 0.001 counts/(keV·kg·yr) for coaxial and BEGe detectors, respectively. The nuisance parameters $\sigma = FWHM/2.355$ and the total efficiency ε are sampled from Gaussian distributions centered around the detector-averaged values taken from Phase I (Tab. 6.11). For each exposure, the median sensitivity is extracted, as well as the 1σ and 3σ equivalent coverage regions. The study is performed twice:

- assuming the same FWHM at $Q_{\beta\beta}$ obtained in Phase I. This is 4.8(2) keV for the coaxial, and 3.2(2) keV for the BEGe detectors (Tab. 6.7);
- using the values obtained with the Phase I reprocessed calibration data, and averaging over the detectors. In this case the FWHM is 4.2 and 2.6 keV for the coaxial and the BEGes, respectively. These values are slightly better than those reported in Tab. 6.7, the difference coming from the fact that the worsening in energy resolution due to the merging of the physics runs is neglected. This can be assumed thanks to the deployment in GERDA Phase II of improved front-end electronics, which should lead to a higher energy resolution on the single calibration run and, consequently, also on the physics data. We assume in any case an uncertainty of 0.2 keV on the FWHM, as for Phase I.

The results are shown in Fig. 6.15 for the two cases. An improvement of 4.5% on the median sensitivity (bold line) is obtained with the use of the ZAC filter for all the exposures. On the contrary, the 3σ region is not affected in the same way by the improved resolution. The reason comes from the deep Poisson regime characterizing the analysis. If no event is present in the region of interest (ROI), the same limit is set with both the energy resolutions, corresponding to ~ 2.3 signal counts. This is the case of the highest dotted lines in Fig. 6.15. Similarly, if one event is present exactly at $Q_{\beta\beta}$, the result is again very similar in the two cases. This case is reflected on the bottom dotted lines. Once the energy resolution and BI of each channel are available, the study can be repeated with the alternative approach described in Sec. 6.5, with an even larger improvement in sensitivity.

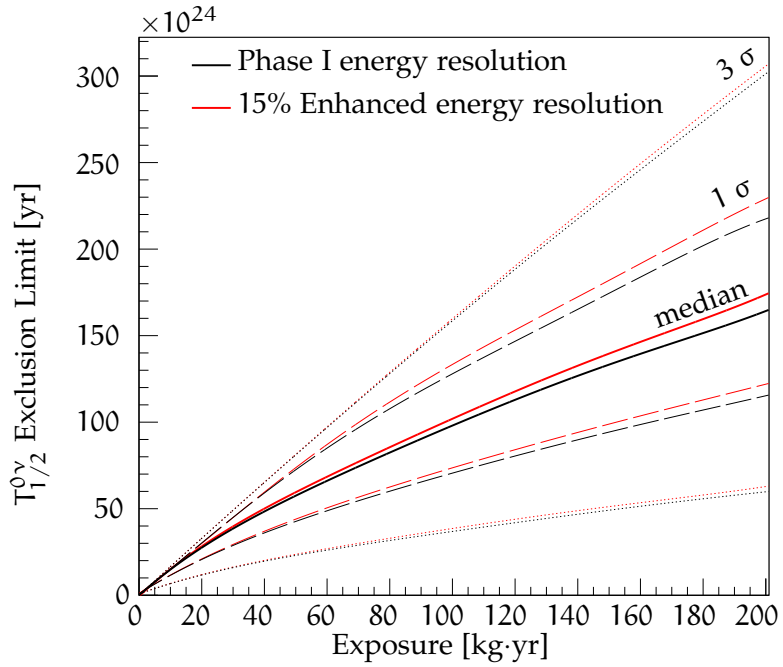

Figure 6.15.: Projected sensitivity for GERDA Phase II assuming the average Phase I energy resolution, and a 15% improved energy resolution.

The importance of an improved energy resolution is not only given by the enhanced sensitivity discussed so far. The main advantage is that narrower peaks allow to perform a more precise modeling of the experimental background. Consequently, the determination of the BI at $Q_{\beta\beta}$ is more precise and the result on the $0\nu\beta\beta$ decay is more robust. Last but not least, all the other possible analysis results obtained with GERDA Phase II will profit from an improved energy resolution, as well.

7

OPTIMIZATION OF DIGITAL FILTERS FOR PULSE SHAPE DISCRIMINATION OF BEGE DETECTORS

In GERDA Phase II, ~ 20 kg of enriched BEGe detectors are going to be operated in addition to the ~ 18 kg of coaxial detectors used in Phase I. The GERDA Phase II sensitivity to a possible $0\nu\beta\beta$ decay signal strongly depends to the pulse shape discrimination (PSD) performance of BEGe detectors. If the current PSD method is already proven to be highly effective in the distinction between signal-like and background-like events [208], a further improvement can be provided by an optimized digital shaping filter for the extraction of the current pulse. For this reason, a set of digital shaping filters has been tested and optimized on a single calibration run of GERDA Phase I, with the aim of scrutinizing the achievable performance and improving the Phase II sensitivity.

In Sec. 7.1 a short review of the current PSD method for BEGe detectors is given. Sec. 7.2 describes the optimization of new digital shaping filters, while the results obtained with Phase I calibration data and the perspectives for Phase I are reported in Sec. 7.3.

7.1 PULSE SHAPE DISCRIMINATION OF BEGE DETECTORS

The reasons why BEGe detectors have been selected for GERDA Phase II are their superior energy resolution and PSD performance, as described in Sec. 4.1.1. The reduced dependence of the peak shape on the position of the energy deposition, can be exploited in the discrimination between different event topologies. The possible signal types are:

- single site events (SSE) induced by $2\nu\beta\beta$ or $0\nu\beta\beta$ decay, with the total electrons energy absorbed in a small fraction ($O(mm^3)$) of the detector volume;
- SSE induced by a γ undergoing a photoelectric absorption (if $E_\gamma \lesssim 1$ MeV), or a Compton scattering plus a photoelectric absorption in a small region of the detector;
- SSE induced by a γ with $E_\gamma > 1022$ keV undergoing a pair production: the electron releases its energy within a few mm, while the positron slows down to the eV level before annihilating with an electron of the crystal lattice, inducing two 511 keV γ's which escape the detector volume. This is the case of events in the ^{208}Tl DEP at 1592.5 keV;
- multi site events (MSE) induced by a γ undergoing multiple Compton scattering, or a Compton scattering plus a photoelectric absorption in two separate regions of the detector;

- MSE induced by a γ with $E_\gamma > 1022$ keV undergoing a pair production, with the absorption of one of the 511 keV γ's in a different detector region. This is the case of events in the SEP;
- slow pulse induced by β's being emitted on the n^+ surface. Given the small electric field at the n^+ electrode, the charge collection is slower than for bulk events and the signal will present a longer rise time;
- fast pulse induced by energy release close to the p^+ electrode. In this case the high electric field yields yields a fast charge collection, with a signal characterized by a short rise time. During physics runs, these events are mostly given by α contamination of the p^+ contact.

The current signal readout at the p^+ contact has different shapes, depending on the interaction type [219, 168]. While for a SSE the current pulse shows a single maximum, for a MSE it is characterized by more than one local maximum. For a fixed energy, the amplitude of a SSE current pulse is therefore larger than a MSE. Given that the charge collection time is energy dependent in first approximation, similar current pulse shapes are expected for SSE at different energies, the difference being only their amplitude. Based on this, the ratio A/E between the current pulse amplitude A and the deposited energy E can be exploited for the distinction between SSE and MSE. Following the same reasoning, a slow n^+ contact pulse will be characterized by a smaller A/E value than a SSE, while a fast p^+ contact pulse will have a larger A/E.

The plot of A/E vs E for a test measurement performed with a BEGe detector is reported in Fig. 7.1, where the A/E has been normalized such that the SSE are have $A/E \sim 1$. A broad low A/E tail given by MSE and slow pulses is present at all energies, with values of A/E down to ~ 0.2, while the sparsely populated region above $A/E = 1$ is induced by events taking place in the vicinity of the p^+ contact.

7.1.1 *Shaping of Current Signal in* GERDA *Phase I*

The first step for the PSD is the calculation of the current pulse from the preamplifier output charge pulse recorded by the FADC. In absence of electronic noise, this could be done with a differentiation of the charge trace. In reality, the noise in the range of few MHz has to be filtered out in order to obtain a good signal-to-noise ratio on the current pulse.

In GERDA Phase I a different philosophy has been followed for calibration and physics runs. During these, a 160 µs long trace with 10 ns sampling time is recorded for each pulse. The higher number of events involved would involve a significant use of disk space if the same was done in calibration runs. Hence, a "high frequency" (HF) waveform with 4 µs length and 10 ns sampling time is recorded in addition to the 160 µs long trace with 40 ns sampling time used for energy reconstruction.

The current pulse reconstruction was performed during GERDA Phase I with the following algorithm, applied to the HF trace.

- Three moving average (MA) operations with $\delta = 50$ ns width are applied:

$$x_i[t] \to x_{i+1}[t] = \frac{1}{\delta} \sum_{t'=t-\delta}^{t} x_i[t'] \qquad i = 0, \ldots, 2 \tag{7.1}$$

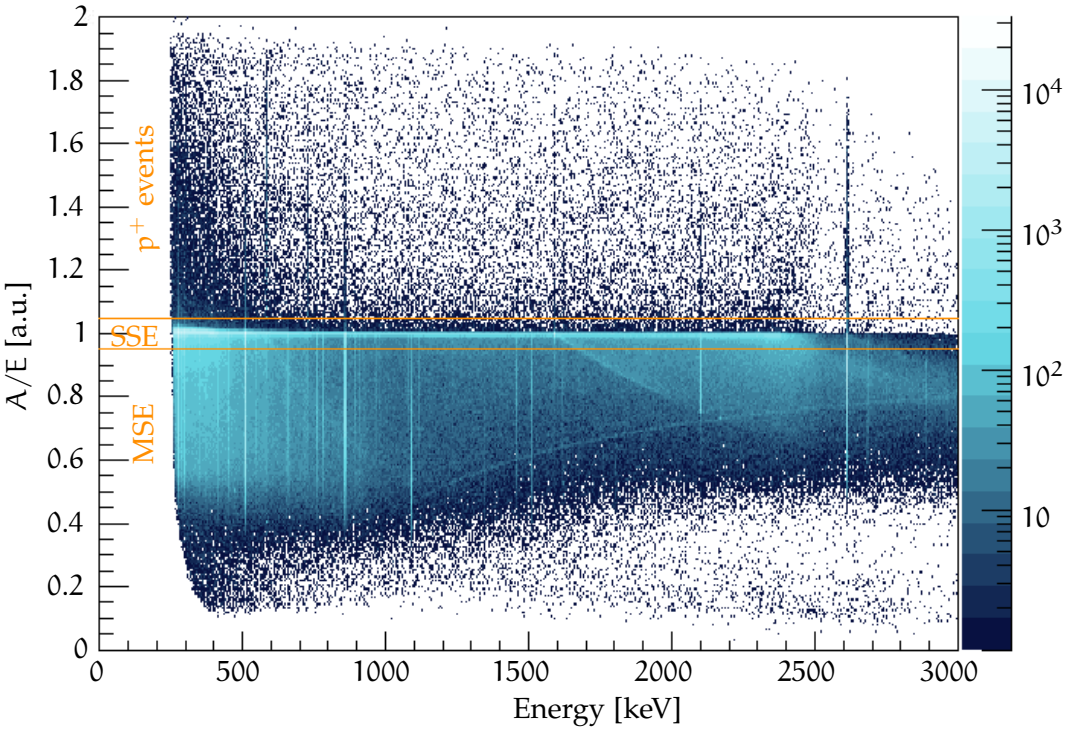

Figure 7.1.: A/E vs E for the DD BEGe detector. The data refer to a measurement performed with a test stand as part of GERDA Phase II preparation.

where x_0 is the original trace. This operation allows to filter out the noise with frequency higher than ~ 20 MHz.

– The trace is differentiated, leading to the current pulse x_3:

$$x_2[t] \rightarrow x_3[t] = x_2[t] - x_2[t - \Delta t] \tag{7.2}$$

where $\Delta t = 10$ ns is the sampling time.

– A $\times 10$ subsampling of the current pulse is done, followed by three MA with 10 ns width. This last step is performed with the aim of improving the precision in the A determination.

The value of A/E is then calculated as the ratio between the maximum of the shaped current trace and the calibrated energy.

This shaping of the current pulse proved to be robust and reliable over all Phase I data taking [208]. Nevertheless, some improvements are possible, which might lead to a higher sensitivity to $0\nu\beta\beta$ decay. As for energy reconstruction, the only reason for using the same filter for all detectors is the ease of data processing. On the other hand, an extensive test of different shaping filters for the current pulse can be performed. Moreover, the filter parameters can be optimized separately for each detector. Finally, faster and more reliable subsampling techniques are available and should be scrutinized, too.

7.2 OPTIMIZATION OF DIGITAL SHAPING FILTERS FOR PSD

Based on the above mentioned considerations, several digital shaping filters have been tested, and their PSD performances compared. The study has been per-

formed on a single Phase I calibration run for the four BEGe detectors used for $0\nu\beta\beta$ analysis. The aim of the work is to prove the feasibility of the filter optimization for current pulse reconstruction in view of Phase II data collection.

The first modification to the standard pulse processing regards the subsampling. The use of 3×10 ns MA on the subsampled trace works as a low-pass filter and involves the application of 3 operations on each trace. The separation between the subsampling and noise filtering allows to disentangle the contributions of the two on the PSD performances and to perform a separate optimization of them.

Several subsampling algorithms are available in many software packages. In our case, the cubic-spline interpolation provided by ALGLIB [220] was chosen for its speed, efficiency and stability. The only parameter into play in the process is the subsampling factor, k. In order to fully exploit the information available in the trace, the subsampling was applied to the original digitized trace and not after the filtering.

Following the philosophy used for the development of the ZAC filter (see Ch. 6), a set of digital filters has been applied via convolution to the subsampled trace. Each HF trace is subject to the following operations:

- subsampling by factor k, with the sampling time transformation $\Delta t \to \Delta t' = \Delta t/k$
- Convolution with the inverse of the preamplifier response function (see Sec. 6.2):

$$f_\tau = \left[1, -\exp\left(-\frac{\Delta t'}{\tau}\right)\right]$$
$$x[i] \to y[i] = x[i] \cdot \left(-\exp\left(-\frac{\Delta t'}{\tau}\right)\right) + x[i+1] \cdot 1$$
$$i = i, \ldots, n-1 \qquad (7.3)$$

  where τ is the preamplifier decay constant, $\tau = R_f C_f$, and n is the number of bins in the resampled trace.
- Convolution with the shaping filter F of length n_F:

$$y[i] \to z[i] = \sum_{k=i}^{i+n_F-1} y[k] \cdot F[i + n_F - k]$$
$$i = 1, \ldots, n - n_F + 1 \qquad (7.4)$$

In reality, the convolution of filter F with the inverse preamplifier response function f_τ is performed once for all, such that only one operation is applied to the resampled trace x. The amplitude A is given by the maximum of the shaped pulse z.

The main difference with respect to the development and optimization of filters for energy reconstruction is that no optimal filter can be computed from the theory because no ideal pulse is available. Namely, even if the time evolution of charge collection for a SSE does not strongly depend on the location of energy deposit inside the detector, some variability does exist, making the calculation of the ideal filter impossible. Recalling the argumentation given in Sec. 6.2, the proof that the sinh -like cusp filter provides the best energy resolution is based on the assumption of a δ-like current pulse. Since the charge collection is not instantaneous, the

flat top is introduced to ensure the full integration of the deposited charge. The effectiveness of the cusp filter with non-zero flat top is ensured by the fact that the charge collection has a much shorter duration than that of the shaping filter. In other words, for energy reconstruction the shape of the current signal can be completely ignored as long as the flat top is as long as the charge collection time. The task is completely different when A is to be computed. In this case we are interested in extracting the maximum of the current pulse, whose shape depends on the event type and location in the detector volume. It is therefore clear that the computation of an ideal shaping filter is in this case impossible.

A set of filters F for the reconstruction of the current pulse has been tested. Given the need not to integrate the charge, no flat top is used. Moreover, given that the duration of charge collection if of $O(1)$ µs, the noise on the MHz frequency range has to be filtered out, making the employment of zero area filters not necessary. Finally, the length of the filter should be of the order of the charge collection time. In general, the filter will be characterized by two parameters, i.e. length $2L$ and shaping time τ_s. The list of tested filters is given below.

– Gaussian:

$$F(t) = \frac{1}{\tau_2\sqrt{2\pi}} \cdot \exp\left(-\frac{(t-2L)^2}{2\tau_s^2}\right) \tag{7.5}$$

– Lorentzian:

$$F(t) = \frac{1}{\pi\tau_s} \cdot \frac{1}{1+\left(\frac{t-L}{\tau_s}\right)^2} \tag{7.6}$$

– Sinh-cusp:

$$F(t) = \frac{1}{2\tau_s\left(\cosh\left(\frac{L}{\tau_s}\right)-1\right)} \begin{cases} \sinh\left(\frac{t}{\tau_s}\right) & 0 < t < L \\ \sinh\left(\frac{2L-t}{\tau_s}\right) & L < t < 2L \end{cases} \tag{7.7}$$

– Exponential cusp:

$$F(t) = \frac{1}{2\tau_s\left(\exp\left(\frac{L}{\tau_s}\right)-1\right)} \begin{cases} \exp\left(\frac{t}{\tau_s}\right) & 0 < t < L \\ \exp\left(\frac{2L-t}{\tau_s}\right) & L < t < 2L \end{cases} \tag{7.8}$$

– Mexican hat:

$$F(t) = \left(1-\frac{(t-L)^2}{\tau_s^2}\right) \cdot \exp\left(-\frac{(t-L)^2}{2\tau_s^2}\right) \tag{7.9}$$

– Delayed differentiation, for which no convolution was used, but the following numerical algorithm on the trace y given in Eq. 7.3:

$$y[i] \to z[i] = y[i] - \frac{1}{m} \cdot \sum_{k=i-m}^{i-1} y[k] \qquad \text{with } m = \frac{2L}{\Delta t'} \tag{7.10}$$

All the filters presented here have a total area equal to one, except from the last two, for which the total area is zero.

7.2.1 *Comparison of Filter Performances*

In order to compare the performances obtained with the different filters, we need to define a criterion for the optimization of the PSD algorithm. This is more complex than for the case of energy reconstruction described in Ch. 6, due to the large variety of possible signal topologies listed in Sec. 7.1. As shown in Fig. 7.1, the SSE events band is superimposed to a broad low A/E tail given by MSE and n^+-contact events. Additionally, p^+-contact events induce a high A/E tail. In the physics data of GERDA these events are mainly α decays from the p^+-contact surface, and represented only about 10% of the total background at $Q_{\beta\beta}$ [198]. The largest background component is given by ^{42}K β decays on the n^+-contact with a low A/E value [208]. For this reason, we can tune the PSD on the separation between the SSE band and the low A/E tail, neglecting the presence of the high A/E tail.

The final goal of PSD is the maximization of sensitivity to a possible $0\nu\beta\beta$ decay signal. Recalling Eqs. 2.37 and 2.38, and noting that the limit on $T^{0\nu}_{1/2}$goes as:

$$\hat{T}^{0\nu}_{1/2} \propto \frac{n_s}{\sqrt{n_b}} \tag{7.11}$$

we can define a figure of merit (FOM) as:

$$\mathrm{FOM} = \frac{\varepsilon^{SSE}_{psd}}{\sqrt{\varepsilon^{MSE}_{psd}}} \tag{7.12}$$

where ε^{SSE}_{psd} and ε^{SSE}_{psd} are the PSD survival probabilities for SSE and MSE at $Q_{\beta\beta}$. Since only calibration data are involved in this work, for which no clear SSE peak is available at $Q_{\beta\beta}$, we will assume that the survival probabilities for the net counts of the ^{208}Tl DEP at 1592.5 keV and the ^{212}Bi full energy peak (FEP) at 1620.5 keV are equal to ε^{SSE}_{psd} and ε^{SSE}_{psd} at $Q_{\beta\beta}$, respectively. Hence, the FOM becomes:

$$\mathrm{FOM} = \frac{\varepsilon_{DEP}}{\sqrt{\varepsilon_{1620}}} \tag{7.13}$$

where the psd subscript is dropped due to the laziness of the author. This approximation is justified by the fact that 1620.5 keV is mostly composed by MSE due to the high Compton cross section for γ's of that energy, while the DEP is mostly made of SSE. Moreover, the SSE and MSE efficiencies can in first approximation be considered equal at $\sim$ 1.5 MeV and $Q_{\beta\beta}$ [208].

The evaluation of the filter performances and the filter optimization will be tailored on the FOM maximization. In order to determine the FOM, a cut on A/E and a procedure for the evaluation of ε_{DEP} and ε_{1620} need to be defined. These definitions are arbitrary, in the sense that the cut definition and the analysis procedure for the calculation of the survival probabilities are not unique. Different choices can lead to different FOM and to different sensitivities to $0\nu\beta\beta$ decay. The purpose of this work is just to test if the use and optimization of different filters for the reconstruction of the current pulse can provide a substantial improvement in sensitivity. Hence, it is only limited to the improvement of the current signal processing, and a unique definition of the A/E cut and FOM calculation is used.

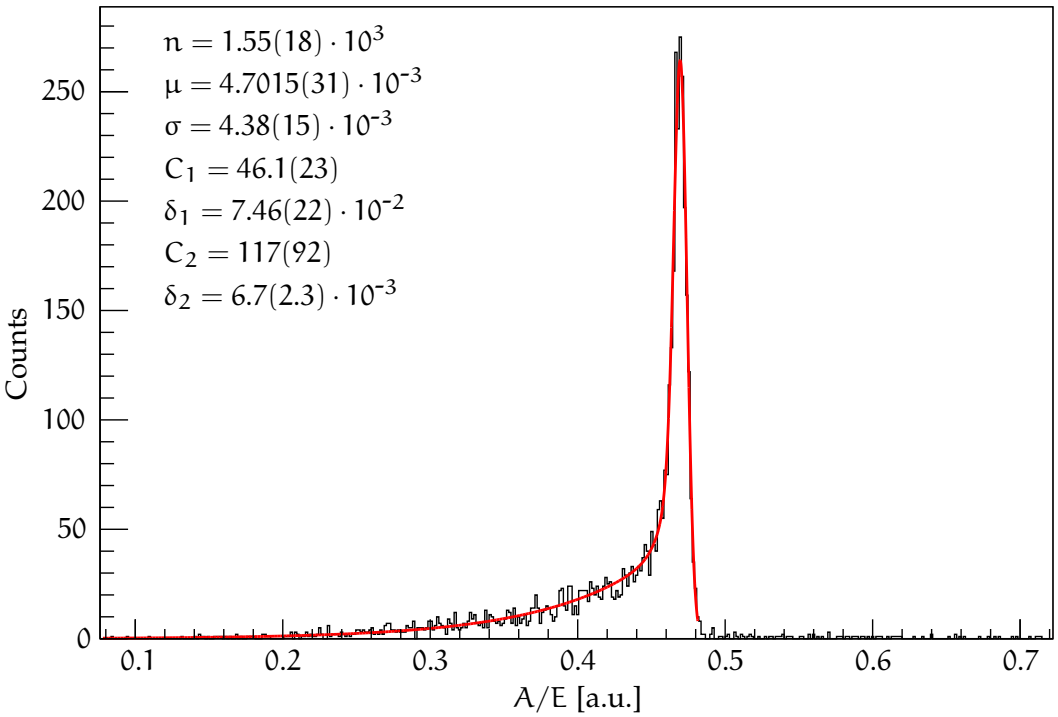

Figure 7.2.: A/E fit for Compton continuum in the 1520–1700 keV range relative to the GD32B data. The best-fit parameters are reported.

The comparison of different cut procedures and FOM calculations is planned for Phase II, where the BEGe detectors are expected to provide the strongest contribution to the sensitivity to $0\nu\beta\beta$ decay.

For the definition of the A/E cut, the events in the Compton region between 1520 and 1700 keV are exploited, excluding two 10 keV region around the DEP and the 1620.5 keV peak. The distribution of A/E for these events obtained with GD32B is shown in Fig. 7.2. It is composed by a SSE peak around 0.47 a.u., with a broad tail on its left given by MSE and n^+-contact events, and a few p^+ contact events on its right. The SSE peak and the left-side tail are fitted with the function:

$$\begin{aligned} f(A/E) = {} & \frac{n}{\sqrt{2\pi}\sigma} \exp\left(\frac{(A/E-\mu)^2}{2\sigma^2}\right) \\ & + \frac{C_1}{2} \exp\left(\frac{A/E-\mu}{\delta_1}\right) \operatorname{erfc}\left(\frac{A/E-\mu}{\sqrt{2}\sigma} + \frac{\sigma}{\sqrt{2}\delta_1}\right) \\ & + \frac{C_2}{2} \exp\left(\frac{A/E-\mu}{\delta_2}\right) \operatorname{erfc}\left(\frac{A/E-\mu}{\sqrt{2}\sigma} + \frac{\sigma}{\sqrt{2}\delta_2}\right) \end{aligned} \tag{7.14}$$

where the tail is parametrized through a large component with decay constant δ_1 and a narrow component with decay constant δ_2. The parameters are extracted with a binned likelihood fit in ROOT. The PSD cut is defined by keeping the events in the $[\mu - 2\sigma, \mu + 2\sigma]$ range, and rejecting those outside.

In order to extract the survival probabilities and the FOM, a spectral fit is performed on the original energy spectrum in the [1520, 1700] keV range, and in the

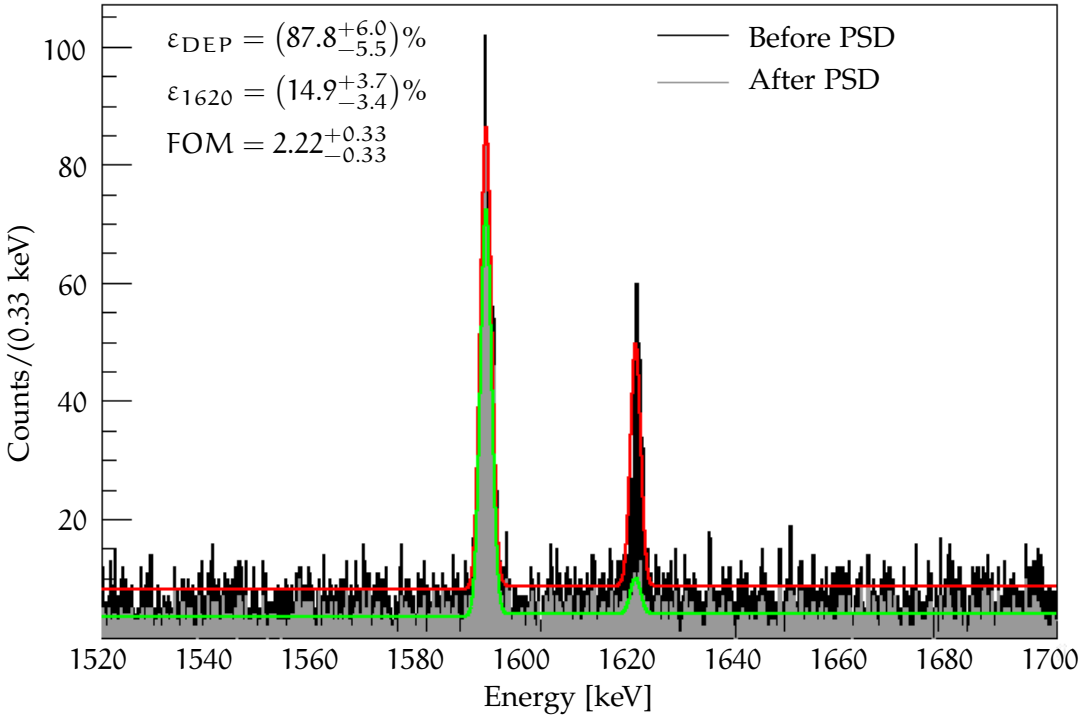

Figure 7.3.: Energy spectrum before and after PSD relative to the GD32B data.

the energy spectrum containing the accepted events only. The fitting function is in this case:

$$f(E) = \frac{n_{DEP} \cdot \Delta E}{\sqrt{2\sigma}} \exp\left(-\frac{(E-1592.5)^2}{2\sigma^2_{DEP}}\right) + \frac{C \cdot \Delta E}{2} \mathrm{erf}\left(\frac{E-1592.5}{\sqrt{2}\sigma_{DEP}}\right) + \frac{n_{1620} \cdot \Delta E}{\sqrt{2\sigma}} \exp\left(-\frac{(E-1620.5)^2}{2\sigma^2_{1620}}\right) + n_{Compton} \cdot \Delta E \quad (7.15)$$

where ΔE is the bin width. The function is the sum of a flat background for the Compton continuum, plus two Gaussian distributions for the DEP and 1620.5 keV line, and a high-energy step for the DEP. The binned likelihood fit is performed using BAT [221], and the posterior probability density functions (PDF) for n_{DEP} and n_{1620} are saved to disk. The PDF of ε_{DEP}, ε_{1620} and FOM are extracted via random sampling of n_{DEP} and n_{1620} PDFs obtained from the original spectrum, and of those surviving the PSD cut. For each of these parameters, the mode and the 68.3% central interval are saved to disk.

Fig. 7.3 shows an example of the original energy spectrum, and that with the events accepted by the PSD for GD32D. The best fit curves are shown, and the values of ε_{DEP}, ε_{1620} and FOM are reported on the figure.

7.2.2 *Filter Optimization*

The optimization was run for all the six filters mentioned above. The first five involve the convolution of the HF trace with the shaping filter. First, the optimal filter length was extracted using a fixed subsampling factor and shaping time. As a

result, the FOM reaches a plateau for $2L \gtrsim 1.5$ µs. Hence, a filter length $2L = 2$ µs was chosen. A scan of the subsampling factor k in the $[1, 30]$ range and of the shaping time τ_s in the $[1 : 100]$ ns range with 1 ns step was performed.

For the delayed differentiation, the scan was run on the subsampling factor ($k = 1, \ldots, 30$) and on the filter length 2L in the $[5, 500]$ ns range with 5 ns step.

7.3 RESULTS AND PERSPECTIVES

Among the six tested filters, the best FOM was obtained with the Gaussian filter and the delayed differentiation, with similar values in both cases for all four detectors. Hence, only the results obtained with these two filters are reported.

Fig. 7.4 shows ε_{DEP}, ε_{1620} and the FOM as function of the shaping time for the Gaussian filter, and as function of the filter length for the delayed differentiation for GD32B with subsampling factor 20. The uncertainty on ε_{DEP} is about 6%, while it is between 30% and 40% for ε_{1620}, due to the very small number of counts in the 1620.5 keV peak after the application of PSD. As a result, the lower uncertainty on the FOM is at the 15% level, while the upper one is about 20%.

Looking at the central values of the acceptance scatter plots, it is clear that while ε_{DEP} is always around 85%, with variations of about 2-6% over all the considered range, ε_{DEP} varies by up to a factor two. This results in a variation of the FOM by about 30%. Even if the best and worst FOM are still compatible within 2σ, a clear trend is present. The highest FOM is around 2.6 for $\tau_s \sim 60$ ns with the Gaussian filter, and for $2L \sim 300$ ns with the delayed differentiation. The reference value for the FOM obtained with the standard reconstruction of A/E described in Sec. 7.1.1 is $2.20^{+0.32}_{-0.27}$. More details on the comparison are given below.

The dependence of the FOM on the subsampling factor k is shown in Fig. 7.5 for BD32B and the delayed differentiation filter. A rise for small values of k is expected, but this is not visible in the data. Namely, the FOM seems to be independent from k, with an average value of 2.66 ± 0.16, where the uncertainty is the RMS. This behavior is opposite to what found with the standard shaping [222], and can be explained either by the limited statistics of the considered data set, or by a null improvement yielded by the subsampling of the trace. In order to disentangle the two possible causes, a data set with much higher statistics is needed.

The comparison between the performances of the Gaussian and delayed differentiation filters with the standard Phase I shaping is given in Tab. 7.1 for all four BEGe detectors. For the new filters, the best FOM is reported. Given the unclear effect of the subsampling, the reported results are relative to the optimization of the filters with no subsampling applied. A correct determination of the FOM statistical uncertainty should take into account the statistical uncertainty on the single FOM evaluation, and the variability of the FOM with respect to the shaping time or filter length. As stated above, the lower uncertainty is about 15%, and the upper about 20%, with slightly higher values for GD35B due to the smaller number of events surviving the PSD. A quantification of the FOM improvement is not possible on the base of the current statistics. The values obtained with both Gaussian and the delayed differentiation filter are between 10 and 25% higher than those obtained with the standard shaping.

To summarize, no clear statement can be made on the real improvement in sensitivity at this stage, although an indication for a $\sim$ 10–25% enhancement is found. Given the FOM improvement obtained with the Gaussian and delayed differentiation filter, the same filter optimization technique is going to be applied extensively throughout GERDA Phase II. Long dedicated calibration runs are going to be performed with the aim of precisely determining the achievable improvement. These runs will also allow the comparison the two selected filters, and and the quantification of the effect yielded by the subsampling.

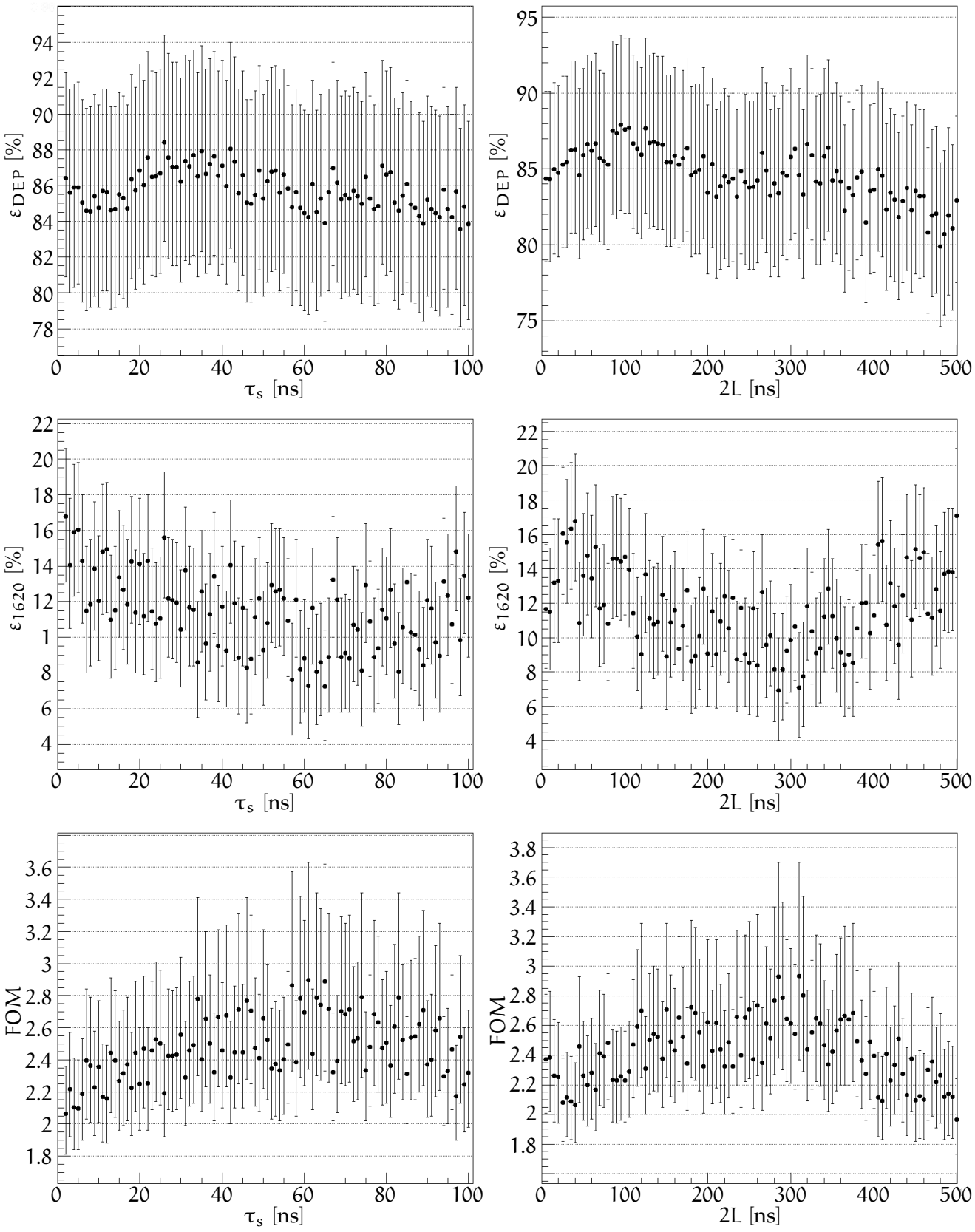

Figure 7.4.: Acceptances and FOM for GD32B for the Gaussian filter (left) and the delayed differentiation (right) with resampling factor 20

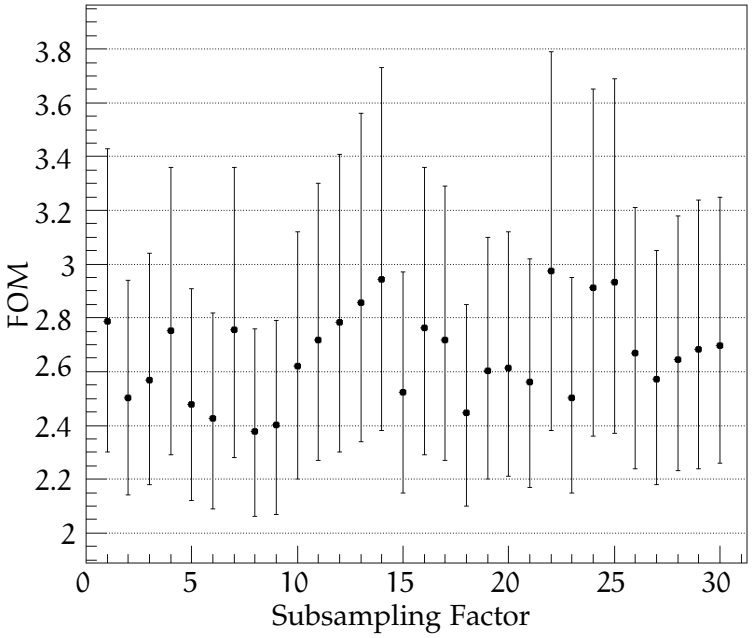

Figure 7.5.: FOM as function of the subsamling factor for GD32B and the delayed differentiation.

Table 7.1.: Best FOM for Gaussian and delayed differentiation filters.

	Best FOM		Reference FOM
Detector	Gaussian	Differentiation	3×50 ns MA
GD32B	2.6	2.6	$2.20^{+0.32}_{-0.27}$
GD32C	2.2	2.2	$2.05^{+0.27}_{-0.24}$
GD32D	2.8	2.8	$2.52^{+0.45}_{-0.36}$
GD35B	4.0	4.2	$3.19^{+0.85}_{-0.61}$

8

PRODUCTION AND CHARACTERIZATION OF ^{228}TH CALIBRATION SOURCES FOR GERDA PHASE II

This chapter describes the production and characterization of ^{228}Th calibration sources for GERDA Phase II. In Section 8.1 the production of low-neutron emission ^{228}Th sources is revised. Sections 8.2 and 8.3 describe the measurements of the sources activity and neutron strength. In Section 8.4 the results of leak test after use in cryogenic environment are reported. The content of this chapter is also available in [2].

As reported in Sec. 5.1, the optimal source for the energy calibration in GERDA is ^{228}Th. The main drawback of using ^{228}Th sources is that, starting from a ^{228}Th nucleus, 5 α particles with energies between 5.2 and 8.8 MeV are emitted before a stable nucleus (^{208}Pb) is reached [197] (see Fig. 5.1). If the radioactive substance is embedded in materials with low threshold for (α, n) reactions, a parasitic neutron flux is obtained. This is the case for standard commercial sources, for which ceramic components, e.g. $NaAlSiO_2$, are used for practical reasons. In GERDA, neutrons could generate ^{77}Ge and ^{77m}Ge via ^{76}Ge activation, both of which undergo beta decay with > 2 MeV Q-value, or they could be captured in the materials surrounding the detectors and produce high energy gamma rays. The background contribution at $Q_{\beta\beta}$ prior to the application of PSD and liquid argon veto cuts induced by such neutrons would be $3 \cdot 10^{-5}$ counts/(keV·kg·yr·kBq) [181]. With a total activity of ~ 70 kBq, this would not fulfill the background requirements of GERDA Phase II [190]. The reduction of the neutron source strength by about one order of magnitude can be achieved by embedding ^{228}Th in a metallic material with cross section for (α, n) reactions higher than 8.8 MeV. As described in [181, 223], gold is the best candidate due to its 9.94 MeV threshold, its < 20 μm range for ^{228}Th alphas, its ductility and ease of procurement.

Given the ultra-low background requirements of the GERDA experiment and the need to deploy the sources at cryogenic temperatures, it is crucial to avoid any leakage of the source active material. Thus, a new leak test procedure with a sensitivity to leaks of $\lesssim 10$ mBq activity was developed at the ENEA-INMRI, Italy, and tested for the first time on the GERDA Phase II sources.

8.1 PRODUCTION OF ^{228}TH SOURCES WITH LOW NEUTRON EMISSION

The production technique of ^{228}Th sources with reduced neutron emission was originally developed by the University of Zurich (UZH) and the Paul Scherrer Institute (PSI). Several prototype sources were produced during GERDA Phase I [181].

The technique was later used and improved [223] to produce a strong calibration source of several MBq activity for Borexino. A brief summary of the technique is given below for completeness.

The radioactive substance was provided in form of $ThCl_4$ dissolved in 1 M HCl by Eckert und Ziegler Isotope Products Int., Valencia (CA), USA, with a total ^{228}Th activity of 150 ± 23 kBq (Fig. 8.1a). Chlorine has two stable isotopes, ^{35}Cl and ^{37}Cl, both of which have (α, n) thresholds below 8.8 MeV. It is therefore mandatory to completely separate chlorine from thorium prior before its deposition on gold. The thorium tetrachloride solution was evaporated in a PTFE crucible almost to dryness; it was subsequently worked-up two times with 1 ml concentrated nitric acid and dried by evaporation (Fig. 8.1b). Thus the $ThCl_4$ was converted in $Th(NO_3)_4$ using surplus concentrated HNO_3 through the reaction:

$$3ThCl_4 + 16HNO_3 \xrightarrow{\sim 115\,^{\circ}C} [3Th(NO_3)_4]_s + [4NOCl + 8H_2O + 4Cl_2]_g \quad , \tag{8.1}$$

where the subscripts s and g stand for solid and gaseous, respectively. Subsequently, the solid $Th(NO_3)_4$ was diluted in two molar HNO_3 and transferred into a gold crucible prepared out of a 2×2 cm gold foil of 20 µm thickness. The gold has a $\geqslant$ 99.99% purity and was produced by mechanical means, lamination and hammering, with no alteration of the original purity level [224]. The HNO_3 was evaporated by heating the solution to $\sim$ 120°C (Fig. 8.1c). Subsequently, the gold crucible was folded and heated to $\sim$ 700°C to form ThO_2 on the gold surface (Fig. 8.1d). The evaporation of the remaining nitrogen and oxygen was done through the reaction:

$$3Th(NO_3)_4 \xrightarrow{\sim 700\,^{\circ}C} [3ThO_2]_s + [12NO_2 + 3O_2]_g \quad . \tag{8.2}$$

Finally, the gold crucible was further folded (Fig. 8.1e) and wrapped in a second gold foil of the same dimension in order to prevent any loss of radioactive material (Fig. 8.1f). The procedure was performed separately for each of the four sources. The production of the GERDA Phase II sources was performed at the Institute for Nuclear Chemistry of the University of Mainz, Germany.

The sources were then encapsulated by Eckert und Ziegler Nuclitec GmbH, Braunschweig, Germany, with a double-sealed stainless steel VZ-3474 capsule (Fig. 8.2), and certified according to ISO-2919 requirements.

8.2 MEASUREMENT OF THE SOURCE ACTIVITY

A precise measurement of the sources activity is required for several reasons. First, a correct $0\nu\beta\beta$ decay analysis can be performed only if a proper understanding of all the background components is available. This is possible thanks to the development of a background model via MC approach and the fit of the model to the physics data. The correctness of the MC geometry and physics implementation can be assessed by simulating the calibration measurements and comparing the simulated with the experimental spectra recorded by the germanium detectors. In GERDA Phase I, the activity of the calibration sources was known within a 15% uncertainty [181], hence the quality of the MC model could only be inferred by comparing the spectral shape of simulated and measured spectra, and not by the

(a) Solution of $ThCl_4$ in 1 M HCl.

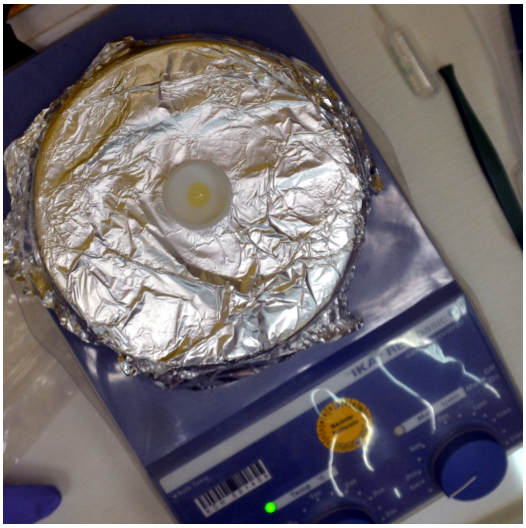

(b) Evaporation of clorine.

(c) HNO_3 evaporation.

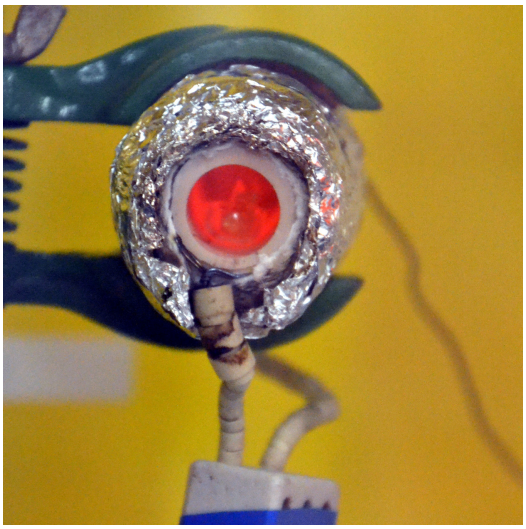

(d) Conversion of $Th(NO_3)$ to $Ch)_2$

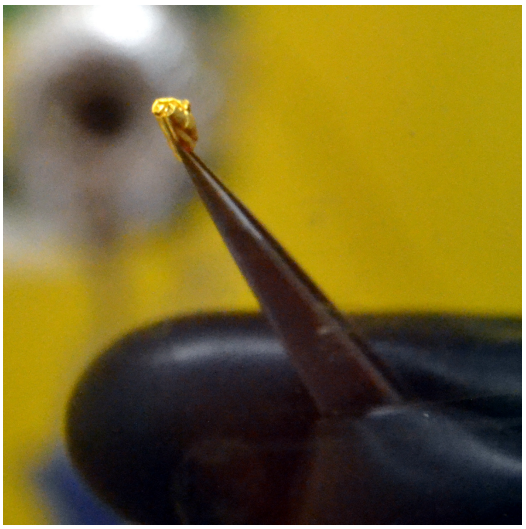

(e) Folding of the inner gold foil, containing the ThO_2.

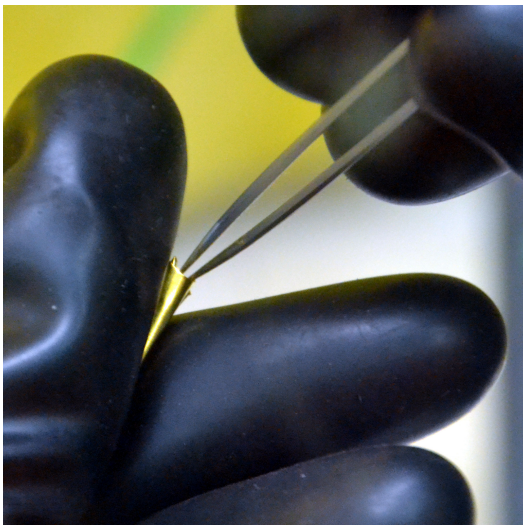

(f) Outer gold foil.

Figure 8.1.: Source production.

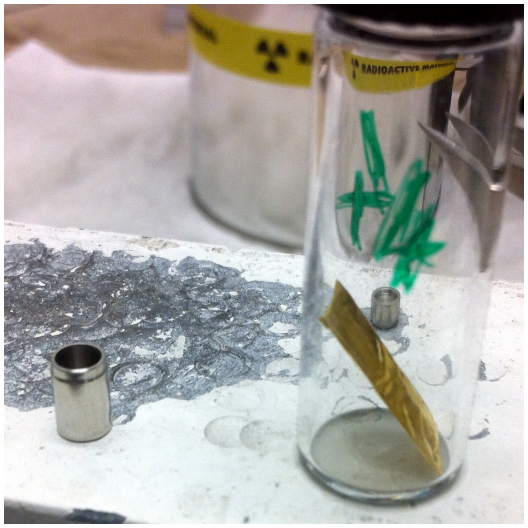

(a) Inner source capsule (left) with the ^{228}Th in the gold envelope (right).

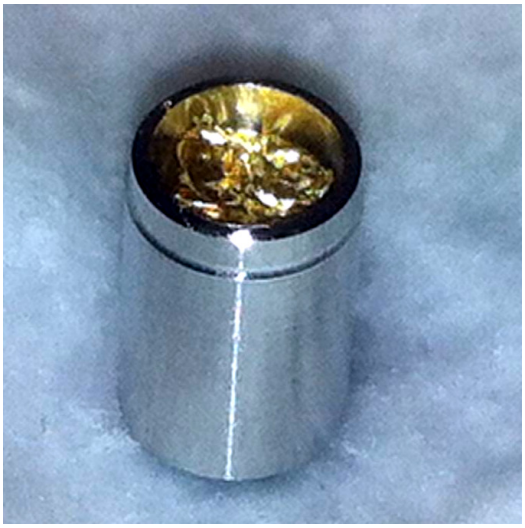

(b) Gold envelope pressed in the inner capsule.

(c) Outer capsule, inner capsule and outer capsule lid.

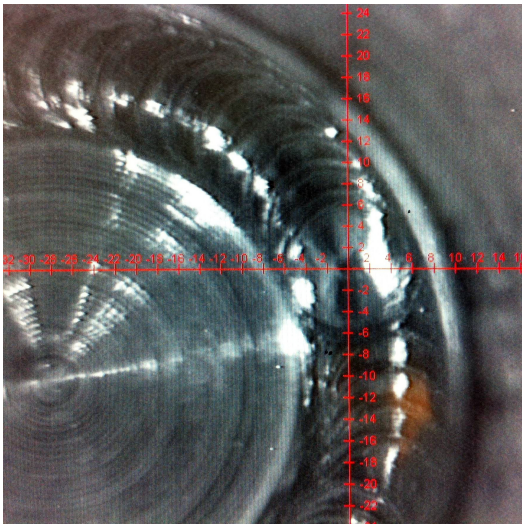

(d) Detail picture of the TIG welded inner capsule lid.

Figure 8.2.: Source encapsulation.

absolute number of events. Second, the simulation of the calibration measurement is required for the evaluation of the PSD efficiency on the DEP, the Compton continuum and the full energy peaks [208]. Finally, a measurement of the LAr veto efficiency for different background source locations can be addressed by lowering the ^{228}Th sources to different positions and comparing the measured with the simulated suppression factors.

The measurement of the Phase II ^{228}Th source activities was performed in the Gator facility [225] at LNGS. Gator consists of a high-purity p-type coaxial germanium crystal encased in an ultra-low activity copper cryostat. The detector is placed in a $25 \times 25 \times 33$ cm^3 cavity where the material samples can be inserted. The integrated background of Gator is ~ 0.16 events/min in the 100-2700 keV range. The $\sim$ 30 kBq activity of Phase II sources induces a count rate which is 4 orders of magnitude higher, hence the measurements described here can be considered background free.

A 20 min long measurement was performed for each of the four sources, placed on a PTFE holder at $\sim$ 120 mm distance from the top of the detector to reduce the pile-up rate. The dead time was between 16 and 25%, depending on the source activity. The spectrum is recorded in the 10-2770 keV range, thus covering the entire ^{228}Th spectrum, with the highest energy line at 2614.5 keV.

In order to determine the activity, a GEANT4 based simulation was performed [226]. The implementation of Gator geometry in the simulation is shown in Fig. 8.3. The measured spectrum for one of the four sources is shown in Fig. 8.4. A negligible fraction of events are present in the experimental spectrum above the 2614.54 keV peak. These are pile-up events and are not accounted for in the MC. Similarly, a $\sim$ 25% discrepancy between data and MC is visible below $\sim$ 70 keV. This is attributed to a sub-optimal implementation of the ^{228}Th decay chain in GEANT4. To avoid any bias due to the two effects explained above, the analysis is performed in the 100-2617 keV range.

For the comparison of measured and simulated data the finite experimental energy resolution is applied to the simulated spectrum via energy smearing on a single event basis. This is obtained with the substitution of the original event energy E with

$$E \rightarrow E + \Delta E \quad , \tag{8.3}$$

where ΔE is a random number generated from a Gaussian distribution centered at zero and with a FWHM given by the resolution curve (see Sec. 5.6).

The activity is determined with a maximum likelihood analysis performed with BAT [221]. The log-likelihood is written as:

$$\ln \mathcal{L} = \sum_{\text{bin } i} \ln \left(\frac{\lambda_i^{k_i} \ e^{-\lambda_i}}{k_i!} \right) \quad , \tag{8.4}$$

where k_i is the measured number of events and λ_i the expectation value in the bin i, defined as:

$$\lambda_i = \frac{A \cdot \Delta t \cdot R_i}{N_{MC}} \quad , \tag{8.5}$$

where A is the source activity, Δt is the live time of the measurement, R_i is the number of events in the i-th bin of the simulated spectrum, and N_{MC} is the total

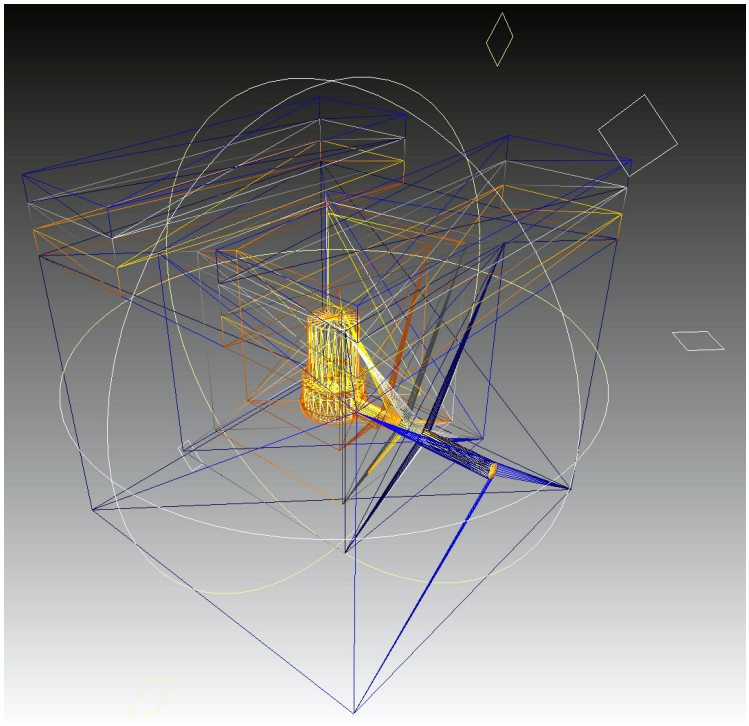

Figure 8.3.: Gator MC geometry

Table 8.1.: Measured activity of the four GERDA Phase II ^{228}Th calibration sources. The first error is to the statistical uncertainty of the fit, while the second is the total systematic uncertainty.

Source	Activity [kBq]
AD9854	24.2 ± 0.1 (stat) $^{+1.1}_{-0.9}$ (syst)
AD9855	34.2 ± 0.1 (stat) $^{+1.5}_{-1.3}$ (syst)
AD9856	30.8 ± 0.1 (stat) $^{+1.4}_{-1.2}$ (syst)
AD9857	41.3 ± 0.1 (stat) $^{+1.8}_{-1.6}$ (syst)

number of simulated events. The only free parameter is A, its best value is given by the maximum of $\ln \mathcal{L}$, and its uncertainty is obtained from the central 68.3% interval.

The experimental spectrum, along with the simulated one scaled according to the best-fit result, is shown in Fig. 8.4 for one of the sources. The good agreement between data and MC at all energies in the considered range together with the high statistics of the measurement are reflected in a statistical uncertainty on the activity of $\sim 2‰$. The activity of the four Phase II sources is reported in Tab. 8.1.

The major source of uncertainty for this measurement is of systematic origin. It is due to the limited knowledge of the experiment's geometry, to an imprecise knowledge of the cross sections for the physics processes involved, and to the fitting procedure itself.

Regarding the implementation of the geometry in the MC simulation, the major uncertainty is induced by the distance between the source and the germanium crystal, known with ± 2 mm precision. All other uncertainties connected to the geometry and thickness of the materials in between can be considered negligible.

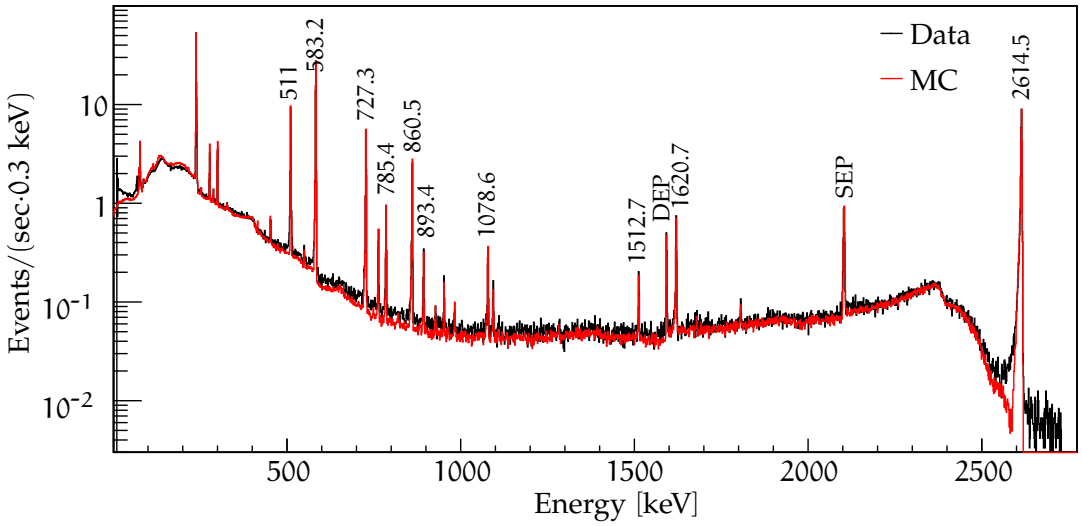

Figure 8.4.: ^{228}Th spectrum recorded by the Gator spectrometer with the AD9857 source (black), together with the simulated spectrum (red) scaled according to the best fit. The gamma lines used for the energy calibration in GERDA are labeled.

A difference of ± 2 mm distance has negligible effect on the spectral shape but results in a different covered solid angle and, therefore, a different activity. The simulations and the analysis have been repeated after changing the source height by ± 2 mm. This results in a $^{+2.5}_{-2.1}$% systematic error on the activity.

The uncertainty due to the limited accuracy of the physics models implemented in GEANT4 is almost exclusively related to that of the cross sections for the photoelectric, Compton and pair production processes. The accuracy of these was estimated to be at a 5% level, as described in [227]. As for the previous case, the simulations have been repeated after separately changing the cross sections of each of the three processes by ± 5%. The possible energy dependence of the cross section for the three processes is below the 5% level, hence it is not considered. Given the considered energy range, the largest effect on the activity is induced by the cross section for Compton scattering and is $^{-2.0}_{+2.5}$%. The systematic error related to the photoelectric effect is $^{-0.4}_{+0.2}$%, while the one related to the pair production is below 1‰.

Finally, the uncertainty given by the choice of the energy range used for the analysis has to be considered. To quantify this effect, the analysis has been repeated by increasing the minimum of the energy range from 100 to 2600 keV with 20 keV steps. The root mean square (RMS) of the resulting activities distribution has been taken as systematic error. This results at 2.5% level.

The three sources of systematic uncertainties considered so far originate from independent causes. Therefore, the errors are summed in quadrature, resulting in a $^{+4.4}_{-3.9}$% uncertainty in the activity. As a comparison, the activity of the GERDA Phase I sources was only known with a ± 15% uncertainty [181]. Given the high precision obtained in the measurement, a more precise validation of the GERDA Phase II MC simulation is possible. In addition, the measurement of ^{56}Co and ^{226}Ra radioactive sources for GERDA Phase II will be performed using the same procedure.

8.3 NEUTRON STRENGTH MEASUREMENT

The measurement of the neutron source strength of the four GERDA Phase II sources was performed with a LiI(Eu) detector and a ^{3}He counter underground at LNGS in a low background environment. As both detectors are suitable for the detection of thermal neutrons, a moderator had to be used in order to thermalize the neutrons emitted by the ^{228}Th sources. Namely, the neutrons are characterized by a continuum energy spectrum with a maximum at ~ 2.5 MeV [181]. Three measurements were performed: first, the total detection efficiency was determined using an AmBe neutron source of known neutron strength, keeping the same geometrical configuration as for the ^{228}Th sources screening. In a second step, the background spectrum was acquired for a period long enough to make its influence on the neutron source strength uncertainty smaller than the systematic error. Finally, the four GERDA Phase II sources were measured.

8.3.1 *Measurement with LiI(Eu) Detector*

The first measurement of the neutron source strength was performed with a LiI(Eu) detector. The physical process exploited for the detection of thermal neutrons is:

$$ {}^{6}_{3}\mathrm{Li} + \mathrm{n} \quad \rightarrow \quad {}^{7}_{3}\mathrm{Li}^{*} \quad \rightarrow \quad {}^{3}_{1}\mathrm{H} + {}^{4}_{2}\mathrm{He} + 4.78\ \mathrm{MeV} \quad . \tag{8.6} $$

The experimental signature is a peak at the Q-value of the reaction, i.e. 4.78 MeV. Given the different light yield induced by electrons with respect to alphas and tritons [228], the thermal neutron peak is recorded at ~ 4.1 MeV in electron-equivalent energy scale [229]. Since no environmental γ-ray is commonly present with an energy higher than 2615 keV (full energy peak of ^{208}Tl), this assures a very good γ-n discrimination. A major concern for the detection of small thermal neutron fluxes is the presence of environmental thermal neutrons, as well as radioactive contaminants of the LiI(Eu) crystal bulk or its surface, emitting α or β particles in the 3.5-4.5 MeV range.

The employed experimental setup consists of a LiI(Eu) cylindrical crystal with 25.4 mm diameter and 3 mm height enriched to 96% in ^{6}Li provided by Scionix, Bunnik. The crystal is coupled to a 1" square R8250 low-background photomultiplier tube (PMT) from Hamamatsu Photonics. In order to minimize the background, the system is encased in a custom made copper holder (Fig. 8.5a). The detector is surrounded by 20 cm thick borated polyethylene (PE) panels acting as a shielding for external neutrons. A 2 cm thick lead brick and a 5 cm thick PE moderator were present in front of the detector during all measurements (Fig. 8.5b). The detector was designed in the past to measure the neutron fluxes of the ^{228}Th prototype sources produced during Gerda Phase I. A detailed description can be found in [181].

The determination of the total efficiency ε was performed using an AmBe source with a neutron strength of 160 ± 4 n/s [230]. For this measurement only, the setup was installed at the surface laboratory at LNGS. The AmBe source was measured for 12.56 h, and a 5 days long background run was performed under the same conditions. The collected spectra are shown in Fig. 8.6. The analysis was

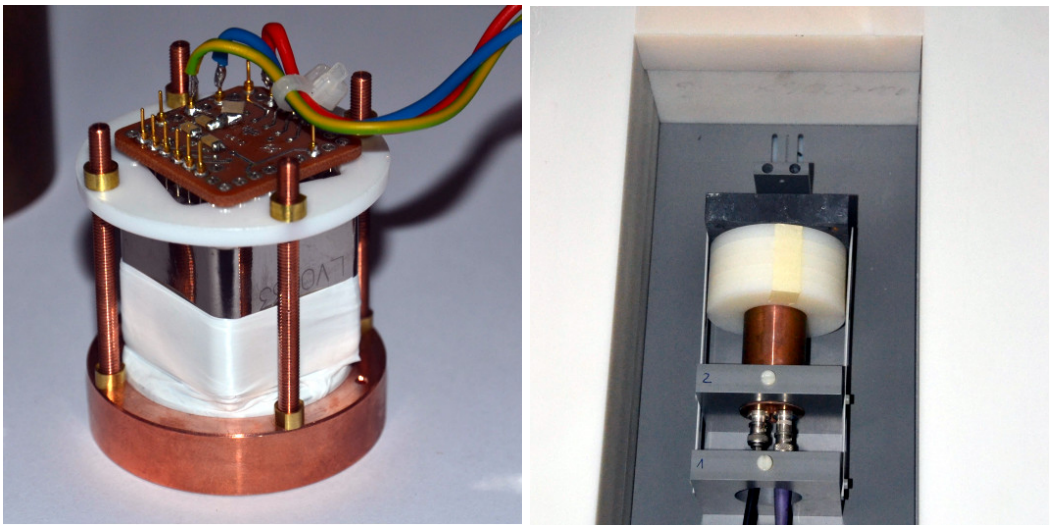

(a) The LiI(Eu) crystal coupled to the 1″ PMT and mounted on the copper holder.

(b) The detector (in the copper case) in the borated PE shielding, together with the 5 cm thick PE moderator and the 2 cm thick Pb absorber. The sources were mounted on the holder in front of the Pb brick.

Figure 8.5.: LiI detector.

performed via a maximum likelihood analysis in the 7000-9500 bin range, with ε as the parameter of interest:

$$\ln \mathcal{L} = \ln\left(\frac{\lambda_s^{k_s}\ e^{-\lambda_s}}{k_s!}\right) + \ln\left(\frac{\lambda_b^{k_b}\ e^{-\lambda_b}}{k_b!}\right) - \frac{(S-\mu_S)^2}{2\cdot\sigma_S^2} \quad , \tag{8.7}$$

where k_s and k_b are the measured number of counts in the fit range for the AmBe and the background measurement, respectively, while λ_s and λ_b are the corresponding expectation values, and S is the known AmBe neutron flux. A Gaussian prior is assigned to S, with $\mu_S = 160$ n/s and $\sigma_S = 4$ n/s. The expectation values are defined as:

$$\lambda_s = \Delta t_s \cdot (\varepsilon \cdot S + B) \quad , \tag{8.8}$$

$$\lambda_b = \Delta t_b \cdot B \quad , \tag{8.9}$$

where B is the background index in events/s in the fit range and Δt_s (Δt_b) is the live time of the AmBe (background) measurement. The measured efficiency is:

$$\varepsilon = \left(5.32^{+0.18}_{-0.15} \pm 0.27\right) \cdot 10^{-4} \quad , \tag{8.10}$$

where the first error is the statistical uncertainty of the fit and the second is the systematic related to the choice of the energy range for the fit.

The four GERDA Phase II sources were measured together underground for 11 days, and a background measurement was carried out for 142 days. Fig. 8.7 shows the two recorded spectra. The determination of the neutron source strength was performed using the same method as for the efficiency. The log-likelihood contains

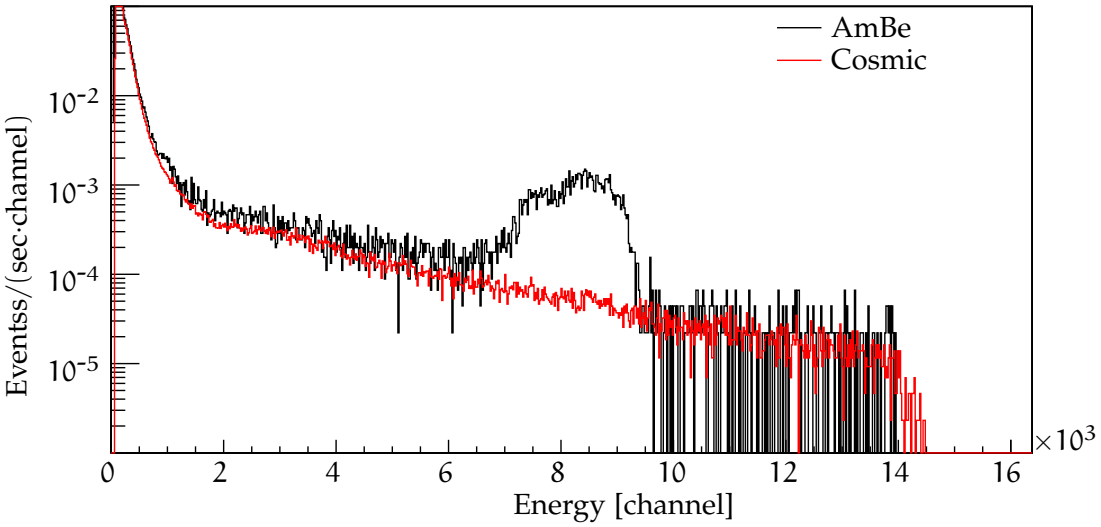

Figure 8.6.: LiI spectra recorded with and without the AmBe source. The peak due to thermal neutrons is clearly visible around channel 8000, corresponding to about 4.1 MeV in electron-equivalent energy scale. For these measurements only, the LiI(Eu) detector was operated at the surface laboratory at LNGS.

a Gaussian prior for the total efficiency and the total activity $A = 130.4 \pm 5.5$ kBq of the four sources:

$$\ln \mathcal{L} = \ln\left(\frac{\lambda_s^{k_s}\ e^{-\lambda_s}}{k_s!}\right) + \ln\left(\frac{\lambda_b^{k_b}\ e^{-\lambda_b}}{k_b!}\right) - \frac{(\varepsilon-\mu_\varepsilon)^2}{2\cdot\sigma_\varepsilon^2} - \frac{(A-\mu_A)^2}{2\cdot\sigma_A^2} \quad , \tag{8.11}$$

where the subscripts s and b refer to the measurement with the sources and the background, respectively. The expectation values are given by:

$$\lambda_s = \Delta t_s \cdot (\varepsilon \cdot A \cdot S + B) \quad , \tag{8.12}$$

$$\lambda_b = \Delta t_b \cdot B \quad . \tag{8.13}$$

The resulting neutron source strength is:

$$S = \left(8.2^{+1.7}_{-1.2} \pm 1.1\right) \cdot 10^{-7} n/(\text{sec} \cdot \text{Bq}) \quad . \tag{8.14}$$

The first uncertainty is the statistical error from the fit, while the second is the systematic uncertainty related to the choice of the energy range. This in particular includes the effect of the background peak present around channel 7000 (see Fig. 8.7).

The measured neutron source strength is based on the assumption that the AmBe and ^{228}Th emitted neutron spectra are the same. As mentioned in [181, 223], while the first has a mean energy at $\sim$ 4 MeV, gold-encapsulated ^{228}Th yields a mean neutron energy of 2.58 MeV. The use of the same total efficiency for the AmBe and ^{228}Th measurements thus induces a systematic error, which was computed to be 12% in [223]. As a result, the neutron source strength for the GERDA Phase II calibration sources is:

$$S = \left(8.2^{+1.7}_{-1.2}(\text{stat}) \pm 1.1(\text{fit range}) \pm 1.0(\text{eff})\right) \cdot 10^{-7} n/(\text{sec} \cdot \text{Bq}) \quad . \tag{8.15}$$

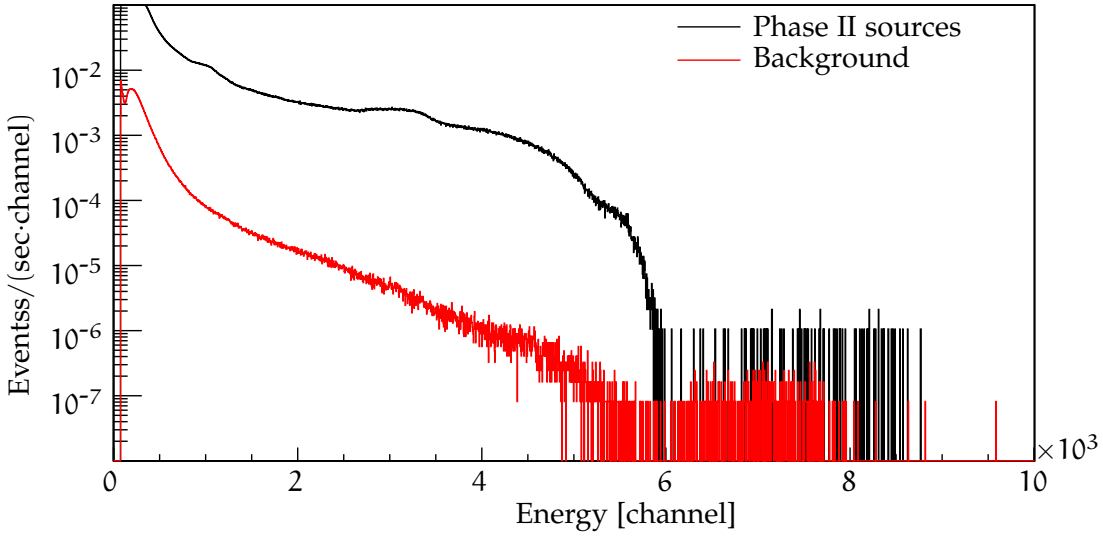

Figure 8.7.: Background of the LiI(Eu) detector operated underground at LNGS (red) and spectrum recorded with the four GERDA Phase II ^{228}Th sources (black). While the γ contribution is only present up to channel $\sim$ 6000, a thermal neutron signal is present around channel 8000. The faint peak in the background spectrum around channel 7000 is likely due to an internal α contamination of the crystal.

For comparison, the same measurement and analysis were performed for a commercial ^{228}Th source (i.e., with ceramic substrate) with 19.5 ± 2.9 kBq activity. The neutron source strength in this case is $7.5^{+2.5}_{-1.3} \cdot 10^{-6}$ n/(sec·Bq). Thus, the use of gold as a support material for ^{228}Th yields a reduction in the emitted neutron flux by one order of magnitude.

8.3.2 *Measurement with ^{3}He Detector*

A second measurement of the neutron source strength was performed with a ^{3}He counter. The exploited reaction is:

$$^3_2\mathrm{He} + \mathrm{n} \rightarrow ^3_1\mathrm{H} + \mathrm{p} + 746\ \mathrm{keV} \quad . \tag{8.16}$$

Ero un bambino e già me n'ero accorto – raccontò Qfwfq – Gli atomi d'idrogeno li conoscevo uno per uno, e quando ne saltava fuori uno nuovo lo capivo subito. I. Calvino, *Le Cosmicomiche*

The expected signal induced by thermal neutrons is therefore a peak at 746 keV. In spite of this low Q-value, γ radiation does not represent a background for the measurement because of the gaseous state of the detector, with a mean energy deposit for electrons of about 2 keV/cm. The discrimination between neutrons and gammas or electrons is thus performed based on the deposited energy alone.

The ^{3}He counter is a LND-2531 produced by LND inc., New York. The tube has an effective diameter of 47.75 mm and a height of 203.2 mm. It is filled with ^{3}He at a pressure of 6078 mbar and is operated at 1950 V. The counter is inserted in a 6.5 cm thick 4π PE moderator, on which a borehole is present for source insertion. The distance between the tube and the bottom of the borehole is 1.1 cm. The system is shielded by a ^{113}Cd foil and a 4π castle of borated paraffin with 10 cm thickness for the absorption of environmental neutrons.

The four sources were screened for 17.5 hours, while the background spectrum was acquired for 10 days. The total detection efficiency, determined using an

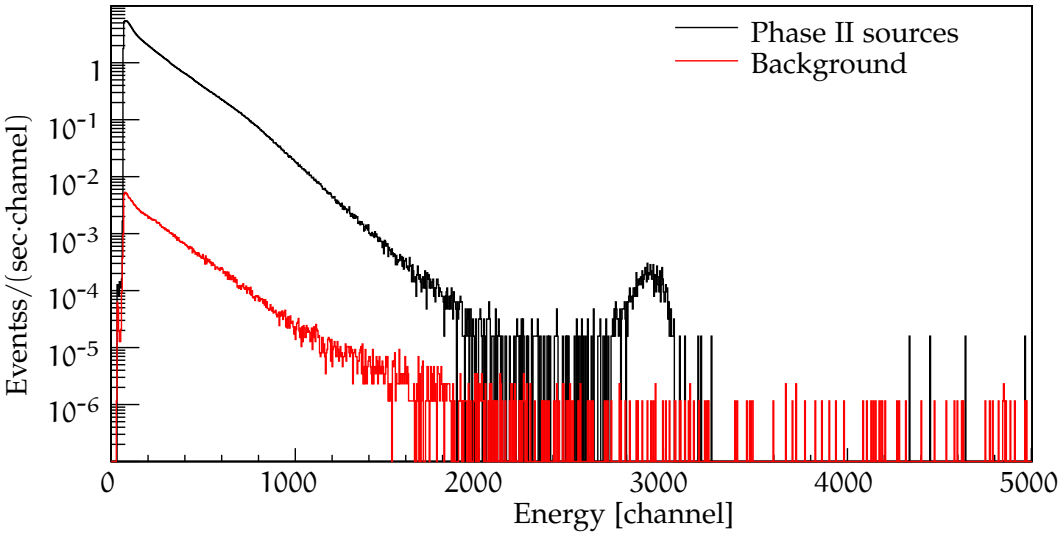

Figure 8.8.: Background of the ^{3}He counter operated underground at LNGS (red) and spectrum recorded with the four GERDA Phase II ^{228}Th sources (black). The thermal neutron peak is visible around channel 2900, while the broad continuum below channel 2000 is due to γ background.

AmBe source in a previous measurement, is $(7.13 \pm 0.85) \cdot 10^{-2}$ [231]. Following the same analysis procedure used for the LiI(Eu) measurements, the neutron source strength of the GERDA Phase II sources is:

$$S = \left(9.4^{+2.0}_{-0.8}(\text{stat}) \pm 0.4(\text{fit range}) \pm 1.1(\text{eff})\right) \cdot 10^{-7} \text{n}/(\text{sec} \cdot \text{Bq}) \quad , \tag{8.17}$$

where the first uncertainty is statistical, the second is the systematic due to the choice of the energy range, and the third is the efficiency related systematic.

8.3.3 *Interpretation of the Results*

The neutron source strengths measured with the LiI(Eu) and the ^{3}He detectors agree within the errors. This demonstrates the reliability of the LiI(Eu) as a low-flux neutron detector. For both measurements, the total uncertainty of $\sim$ 20% is mostly due to the limited statistics. A higher precision could be obtained with a longer screening, but this was not possible due to time constraints related to the preparation of GERDA Phase II.

Previous measurements performed with two custom ^{228}Th sources for GERDA Phase I lead to similar results [181]. The measured neutron source strengths vary between $7.59 \cdot 10^{-7}$ n/(sec·Bq) and $1.50 \cdot 10^{-6}$ n/(sec·Bq), depending on the source and detector. In this case the uncertainties were $\sim$ 30%, which might explain the spread of the values by up to a factor two. A more precise measurement was performed in [223] on a ^{228}Th source with gold substrate and the same encapsulation of the GERDA sources. The measured neutron source strength of $(1.22 \pm 0.17) \cdot 10^{-6}$ n/(sec·Bq) is also in good agreement with the results presented here.

The agreement of independent measurements on the gold-encapsulated ^{228}Th sources confirms the reliability of the production technique. The reproducibility

Table 8.2.: Experimental conditions and results for the leak test performed at ENEA-INMRI.

Number of BB readings	108
Number of A1, LN, A2 readings for each source	6
Counting time [s]	6000
Mean BB count rate $\left[s^{-1}\right]$	0.00250
Experimental standard deviation of BB count rate $\left[s^{-1}\right]$	0.00087
Expected Poisson standard deviation $\left[s^{-1}\right]$	0.00064
Decision threshold for the net indivitual count rate $\left[s^{-1}\right]$	0.00202

of ^{228}Th sources with neutron emission at the level of 10^{-6} n/(sec·Bq) can thus be guaranteed to present and future low background experiments. In the case of GERDA Phase II, the neutrons emitted by the calibration sources induce a background index at $Q_{\beta\beta}$ of $\sim 2 \cdot 10^{-4}$ counts/(keV·kg·yr) prior to the application of PSD and LAr veto. This is a factor 5 lower than the total expected background and is sufficient to fulfill the Phase II requirements.

8.4 LEAK TEST OF RADIOACTIVE SOURCES FOR CRYOGENIC SYSTEMS

A new set of leakage tests intended to check the tightness of ^{228}Th radioactive sources after deployment at cryogenic temperatures has been developed at the Istituto Nazionale di Metrologia delle Radiazioni Ionizzanti of ENEA (ENEA-INMRI). It consists of a series of source insertions in acetone and liquid nitrogen, each one followed by a search for possible leaks. A blank capsule, identical to the GERDA ^{228}Th sources but with no radioactive material, was used for a cross-check. Each of the four radioactive sources and the blank capsule was enveloped in circular aluminium foil of 24 cm^2 surface, and dipped in acetone (A1) for 1 hour. After acetone evaporation, the α contamination of the aluminium foil was measured with a Berthold LB 770 α-β low level counter. The operation was repeated using liquid nitrogen (LN) and then one more time with acetone (A2). The same procedure, without the second immersion in acetone, was applied without using any radioactive source or blank capsule for background determination. While the background measurement is needed to assess the intrinsic contamination of aluminium, the comparison between the α count rates obtained with the real and blank capsules allow to disentangle between real ^{228}Th leaks and possible removable surface contaminations. Since the blank and the background count rates are not distinguishable, they have been considered as belonging to the same population (BB).

The distribution of A1, LN and A2 count rates for each of the four sources was compared with that of BB. The test conditions and the results of the analysis are reported in Tab. 8.2. Following [232], the decision threshold at 95% confidence level was calculated based on the standard deviation of the BB readings. The experimental standard deviation of the BB includes components of variability due to counting statistics, long term system stability and homogeneity of used materials.

Table 8.3.: Activity found after each source treatment, with reported 2 σ uncertainties.

Source	A1 [mBq]	LN [mBq]	A2 [mBq]
AD9854	7.5 ± 3.5	1.0 ± 6.3	4.4 ± 3.8
AD9855	4.2 ± 4.6	1.0 ± 6.1	4.0 ± 3.0
AD9856	1.0 ± 2.9	-0.8 ± 2.7	-0.2 ± 3.6
AD9857	3.2 ± 3.8	2.6 ± 6.4	0.8 ± 3.9

If the sample reading of the sources exceeds the decision threshold, a ^{228}Th leak has been detected.

Out of all the 24 LN readings only 2 (8.3%) exceed the decision threshold, while they are in average lower than the A1 and A2 readings. In addition, the A1 counting rates are always slightly higher than those of A2. This means that the higher LN counting rates are not induced by a ^{228}Th leak, but from a surface contamination of the source capsules, which is removed by the two insertions in acetone.

The activity removed from each of the sources after the A1, LN and A2 immersions is reported in Tab. 8.3. The efficiency of the counter was measured with a standard ^{241}Am source with known activity (555.64 Bq) and is 0.3968. A more precise measurement of the counting efficiency would be possible with an open ^{228}Th source, which was not available at the moment of the measurement. In any case, no large energy dependence is expected in the efficiency of the counter in the 5-10 MeV range, inside which the α particles of both ^{214}Am and ^{228}Th are contained. For all sources, no leak is detected after the insertion in LN and the second insertion in acetone. Hence the sources are suited to be used in GERDA Phase II.

9

CONCLUSIONS AND OUTLOOK

The GERDA experiment is searching for $0\nu\beta\beta$ decay in ^{76}Ge. Isotopically modified germanium crystals with $\sim$ 86% enrichment in ^{76}Ge are used as source and detectors for the process. With a BI of 10^{-2} counts/(keV·kg·yr) and a 21.6 kg·yr exposure, GERDA Phase I set the strongest limit on the half-life of the reaction, $T^{0\nu}_{1/2} > 2.1 \cdot 10^{21}$ yr (90% C.L.). In Phase II, GERDA aims at a sensitivity $> 10^{26}$ yr on $T^{0\nu}_{1/2}$ with 100 kg·yr exposure. The experimental sensitivity is enhanced with a larger active mass, a lower BI, and an better energy resolution. The optimization of energy resolution and the BI minimization are the main topics of this thesis. Alongside with these, the calibration of the energy spectrum and the determination of the systematic uncertainty on the single event energy induced by the calibration procedure are a important ingredients for a successful $0\nu\beta\beta$ decay search, and are part of this work.

The precision of the calibration procedure is a mandatory requirement for a reliable analysis of GERDA data. The calibration of the energy scale in GERDA is performed weekly with the insertion of three ^{228}Th sources in the vicinity of the detectors. The calibration frequency and the presence of a dozen detectors make the use of an automatic procedure for the analysis of calibration data necessary. A dedicated software was developed for the automatic search, identification and fit of the peaks in the calibration spectrum. This represented the official tool for energy calibration of GERDA Phase I. The information from the calibration data is also used to extract the systematic uncertainty of the energy determination for each single event, which is 0.2 keV for Phase I data. The resolution curves obtained from the calibration data and the comparison of these with the energy resolution of the ^{42}K peak in the physics spectrum are exploited for the extraction of the FWHM at $Q_{\beta\beta}$. In addition to this, the precision of the energy reconstruction is cross-checked with a dedicated ^{56}Co calibration run performed at the end of Phase I. The calibration software is then further extended and improved for the analysis of Phase II data, and is already in use by the GERDA collaboration.

A better energy resolution can be obtained tuning the shaping filter on the detector and noise properties. In Phase I, for some detectors the signal quality was strongly deteriorated by low-frequency baseline fluctuations due to the long non-coaxial cables connecting the diodes to the front-end electronics. The ZAC filter was developed and its parameters optimized on Phase I calibration data. The reprocessing of all Phase I data with the optimized ZAC filter yields a 0.3 keV lower FWHM at the ^{208}Tl 2514.5 keV line, and a $\sim$ 0.5 keV improvement on the FWHM at $Q_{\beta\beta}$ for the physics data. The larger improvement obtained on the physics data

is due to the higher precision of the energy calibration achievable with the ZAC-reconstructed energy spectra, and to the reduced sensitivity of the ZAC filter to microphonic noise. Thanks to this, the application of the calibration curves to the physics data and the merging of data sets affect less severely the energy resolution than for the spectra reconstructed with the pseudo-Gaussian shaping filter.

The reprocessed Phase I physics data are used to test the performance of alternative methods for $0\nu\beta\beta$ decay analysis. Firstly, the Bayesian method used in GERDA is applied to the reprocessed spectra, and a new limit on the process half-life is obtained, $T^{0\nu}_{1/2} > 2.09 \cdot 10^{25}$ yr (90% C.I.), which is 9% higher than that achieved with the semi-Gaussian shaping. In a second step, the fit is performed on the individual detector spectra, and all involved parameters are inserted in the fit with a proper prior based on previous independent measurements. The spectra separation allows to fully exploit the available information, and yields a limit of $T^{0\nu}_{1/2} > 2.36 \cdot 10^{25}$ yr (90% C.I.), 23% higher than the one obtained with the standard analysis and the semi-Gaussian shaping. This clearly demonstrates the advantage given by the separation of the individual detector spectra. Furthermore, the impact of the improved energy resolution on Phase II sensitivity is computed with the generation of toy MC spectra using the predicted BI of 10^{-3} counts/(keV·kg·yr) and a 15% better resolution with respect to the one obtained with the semi-Gaussian shaping in Phase I. As a result, a $\sim$ 5% higher median sensitivity is obtained with the Bayesian method applied on two data sets, corresponding to the merged spectra of semi-coaxial and BEGe detectors. Once the BI and energy resolution of individual channels are available, the sensitivity can be extracted keeping the individual detector spectra separate. In this case, the improvement is expected to be higher than 5%, as it is for the limit resulting from Phase I data.

The optimization of digital filters is also applied to the reconstruction of current pulses for PSD with BEGe detectors. A set of 6 filters was tested and optimized for 4 BEGe detectors on a single calibration data set from GERDA Phase I. The filter optimization was tailored on the maximization of a FOM defined as $\mathrm{FOM} = \varepsilon_{\mathrm{DEP}}/\sqrt{\varepsilon_{1620}}$, where $\varepsilon_{\mathrm{DEP}}$ and ε_{1620} are the survival probabilities for the ^{208}Tl DEP at 1592.5 keV and the ^{214}Bi line at 1620.5 keV, respectively. For all detectors, the best performances are obtained with a Gaussian shaping and a delayed differentiation filter, which yield comparable results. A precise determination of the FOM improvement is not possible due to the limited statistics of the considered data set, but a positive indication for a 10–25% higher FOM is found. Based on this result, the filter optimization technique for PSD is planned to be extensively applied to GERDA Phase II data in the near future.

Alongside with the analysis of Phase I data, part of my effort was dedicated to the production and characterization of 4 ^{228}Th calibration sources for GERDA Phase II. The γ activity is determined with a $\pm$4% total uncertainty thanks to a background-free measurement performed underground at LNGS with the Gator spectrometer. The neutron source strength was measured with a ^{3}He and a low-background LiI(Eu) detector. Also in this case, the measurements were performed underground at LNGS. The two measurements yield results in agreement within the uncertainties. The neutron source strength of the GERDA Phase II sources is $\sim 10^{6}$ n/(sec·Bq), and is one order of magnitude lower than that of a commercially

available ^{228}Th source. This reduced source neutron activity fulfills the background requirement for GERDA Phase II. Additionally, the tightness of Phase II calibration sources after the deployment in cryogenic environment was investigated with a dedicated leak test. As a result, the presence of leaks is excluded at the 10 mBq level.

Furthermore, a study of the perspectives for the $0\nu\beta\beta$ decay search was performed as a byproduct of the thesis writing. The probability distribution for the effective Majorana mass as a function of the lightest neutrino mass in the standard three neutrino scheme is computed via a random sampling from the distributions of the involved mixing angles and squared mass differences. If a flat distribution in the $[0; 2\pi]$ range for the Majorana phases is assumed, the probability of obtaining $|m_{\beta\beta}| < 10^{-3}$ eV in the NH regime is below 7%. If the cosmological bound on the sum of the neutrino masses is inserted in the calculation, a $3.32 \cdot 10^{-3}$ eV ($2.14 \cdot 10^{-2}$ eV) discovery sensitivity on $|m_{\beta\beta}|$ would yield a 90% probability to detect $0\nu\beta\beta$ decay in case of NH (IH). Finally, the probability distribution for $T^{0\nu}_{1/2}$ as function of the lightest neutrino mass is given for different values of the NME.

In summary, important contributions in terms of data reconstruction and analysis were made to the improvement of the GERDA sensitivity. A digital shaping filter for energy reconstruction was developed and optimized, yielding a $\gtrsim$ 5% improvement on the $T^{0\nu}_{1/2}$ sensitivity of GERDA Phase II. If a similar approach is applied to the reconstruction of the current pulse for the PSD of BEGe detectors, a $\gtrsim$ 10% improvement in sensitivity is achievable. Additionally, the calibration of all GERDA Phase I data was performed with a dedicated program developed in the context of this PhD work. 4 ^{228}Th calibration sources with reduced neutron strength for GERDA Phase II were produced and characterized, and fulfill the Phase II background requirements. Finally, a phenomenological study of $|m_{\beta\beta}|$ was performed, which lead to the probability distribution of $|m_{\beta\beta}|$ and $T^{0\nu}_{1/2}$ on the basis of the current knowledge of the involved parameters.

A

PEAK FITS ON CALIBRATION SPECTRA

This appendix gives the fit of all ^{228}Th peaks used for the extraction of the calibration curve of ANG2 for the February 15, 2013 calibration run. The spectra are reconstructed using the semi-Gaussian filter. The best fit values are reported in the inset.

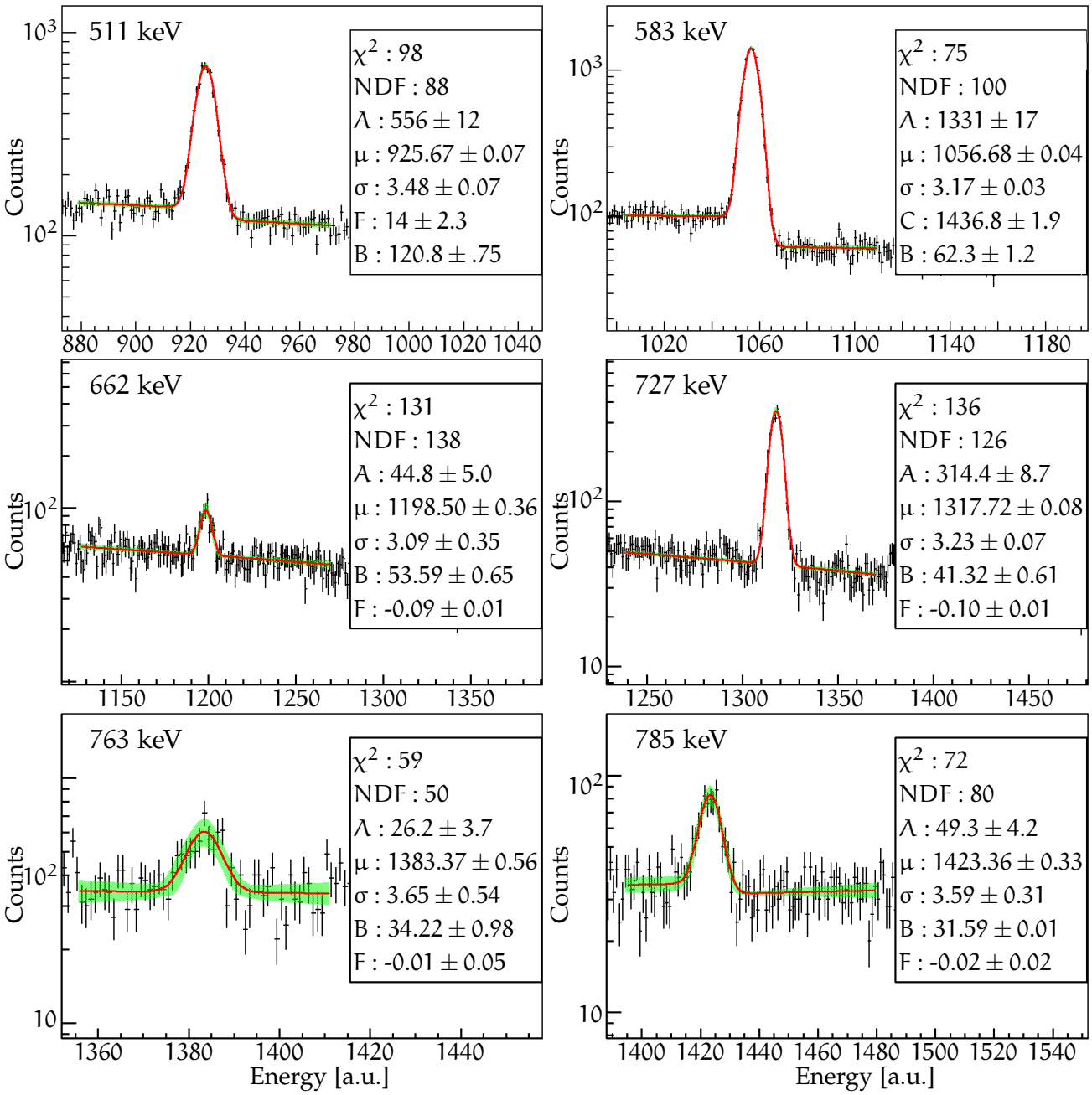

Figure A.1.: Fit of peaks in calibration spectrum for ANG2.

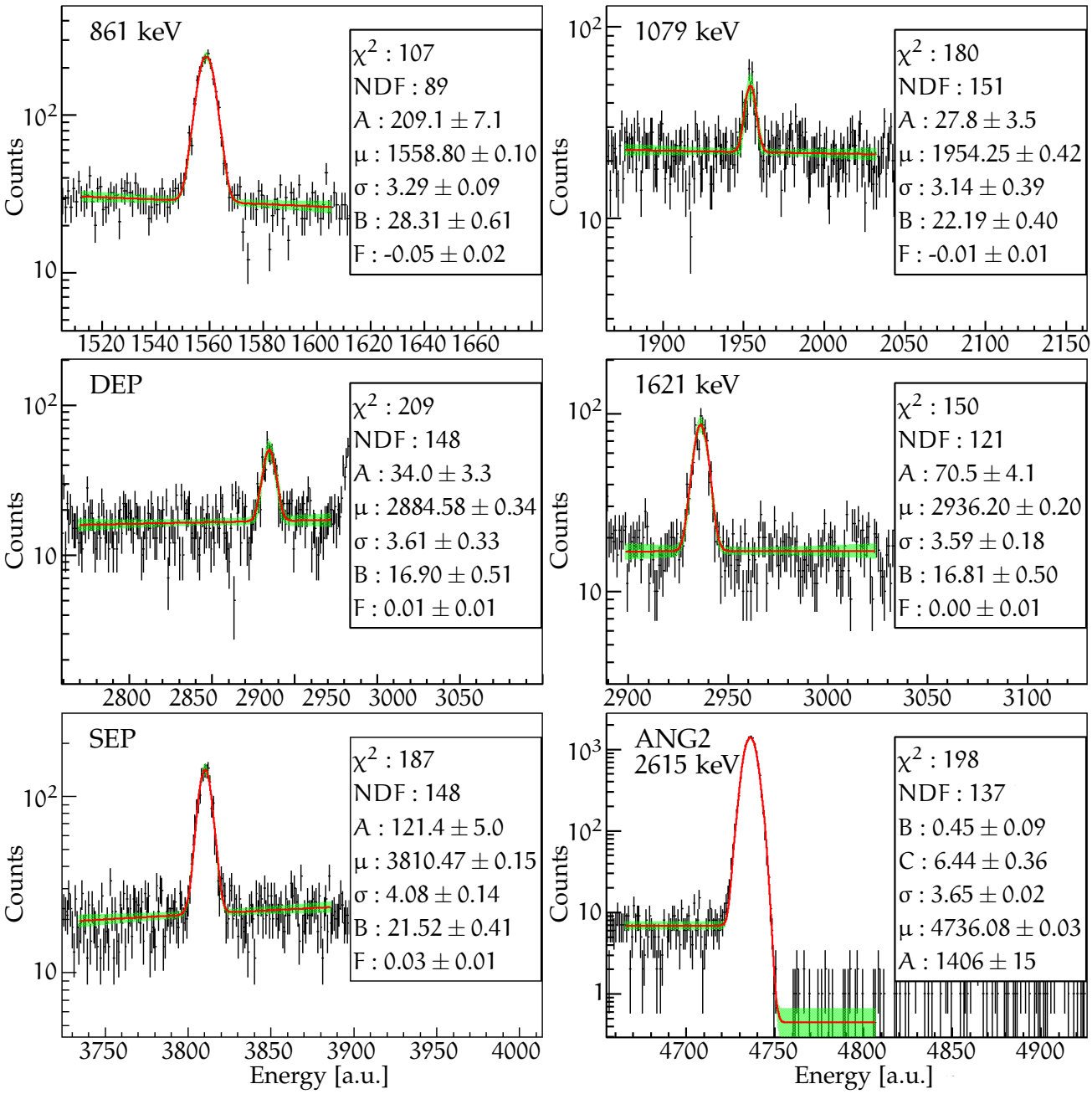

Figure A.2.: Fit of peaks in calibration spectrum for ANG2.

B

PEAK FITS AND STABILITY PLOTS FOR THE ZAC SHAPING FILTER

This appendix reports the following plots for all detectors used for the Phase I $0\nu\beta\beta$ decay analysis.

- fit of the ^{208}Tl peak on the super-tier3 of semi-coaxial and BEGe detectors (Figs. B.1 and B.2). For the semi-coaxial detectors, only the calibration runs acquired during the period corresponding to the golden data set are used;
- $FWHM^2$ as a function of energy for the super-tier3 of semi-coaxial and BEGe detectors (Figs. B.3 and B.4). For the semi-coaxial detectors, only the calibration runs acquired during the period corresponding to the golden data set are used;
- $FWHM$ as a function of time for all calibration runs of GERDA Phase I (Figs. B.5, B.6 and B.7).

In all cases, the results obtained with both the pseudo-Gaussian and ZAC filter are reported.

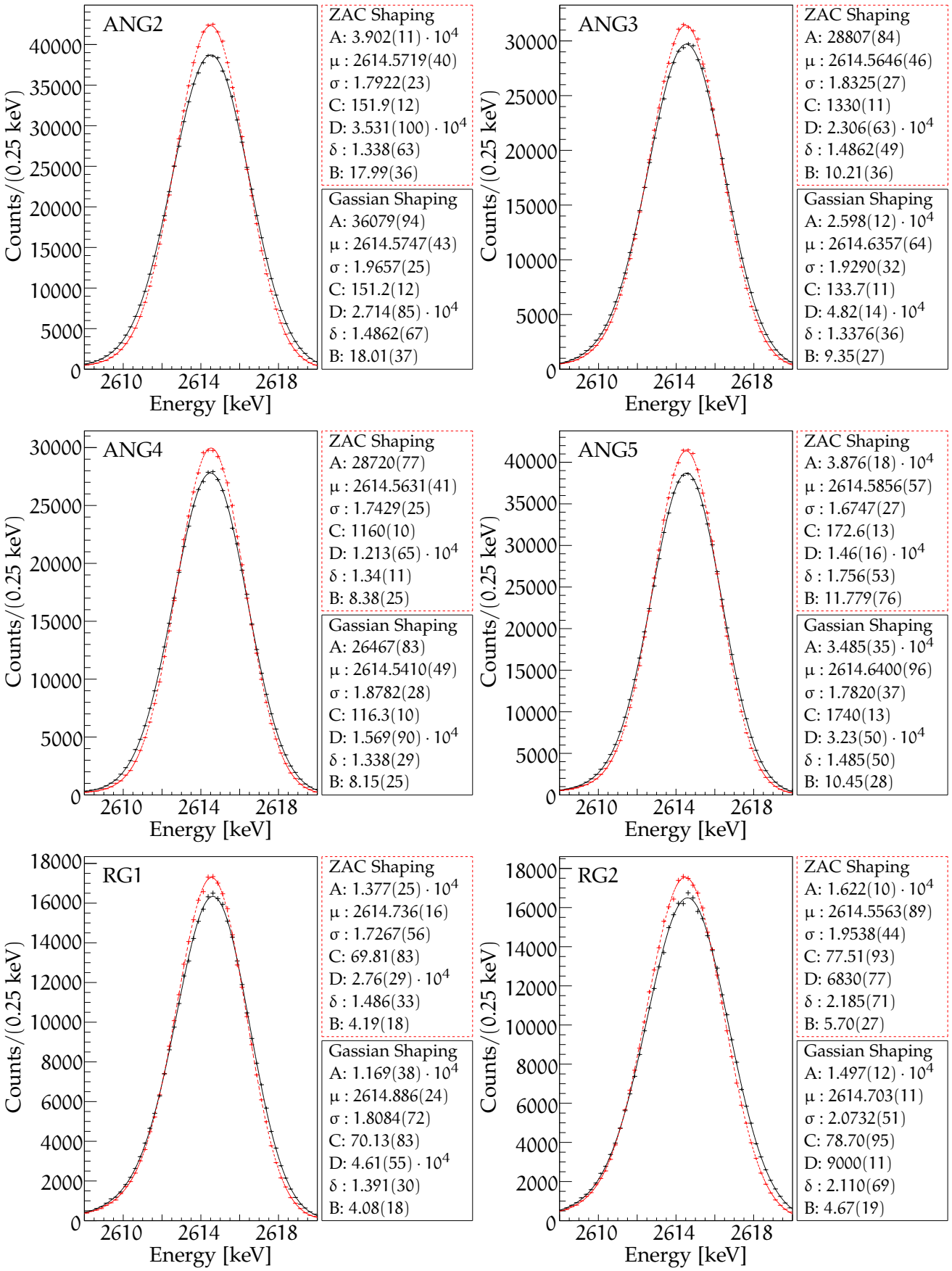

Figure B.1.: ^{208}Tl line for the super-tier3 of the calibration runs taken in the period corresponding to the golden data set. All calibration runs are merged together. The best fit values are reported in the plot.

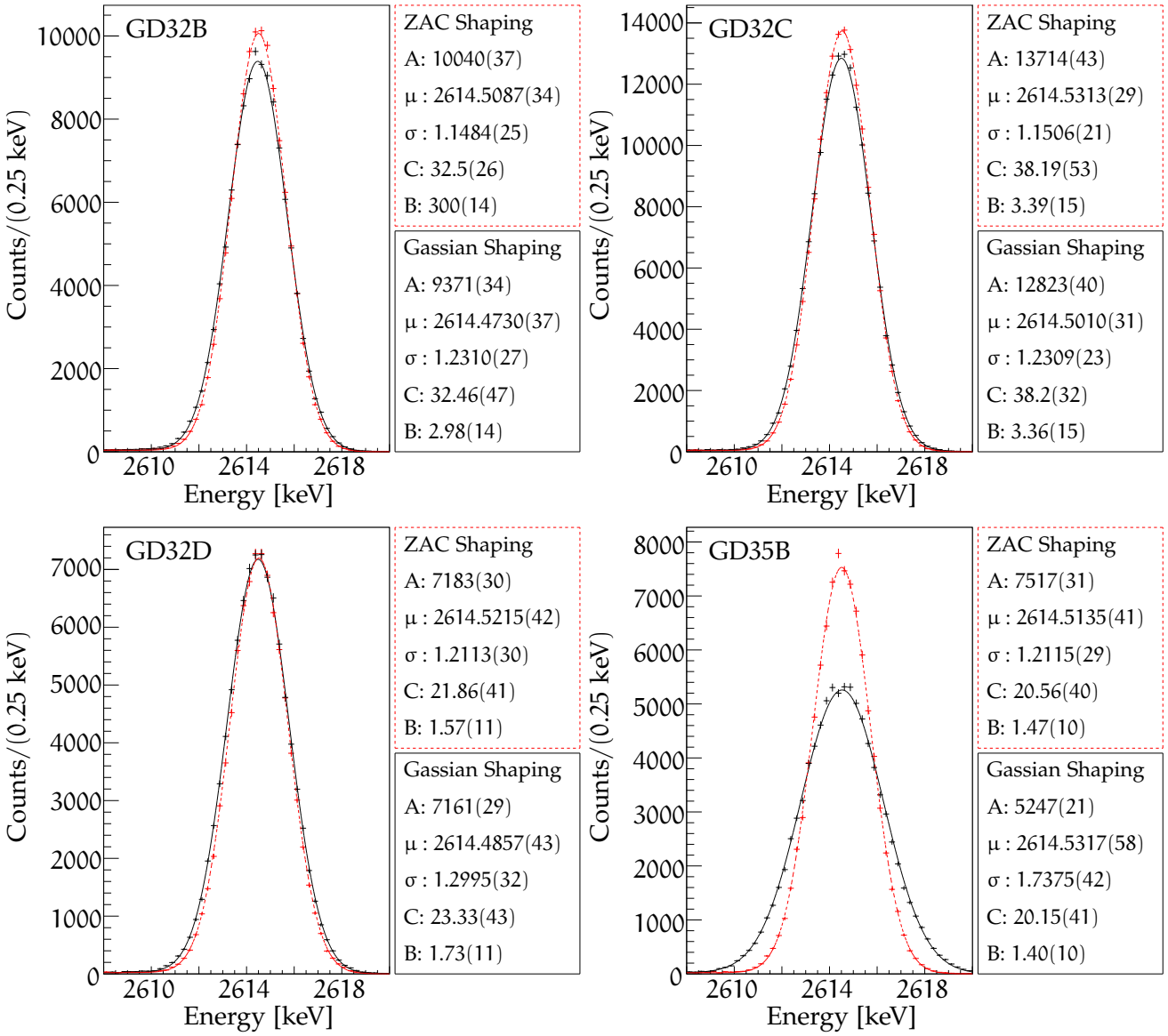

Figure B.2.: ^{208}Tl line for the BEGe detectors. All Phase I calibration runs are merged together. The best fit values are reported in the plot.

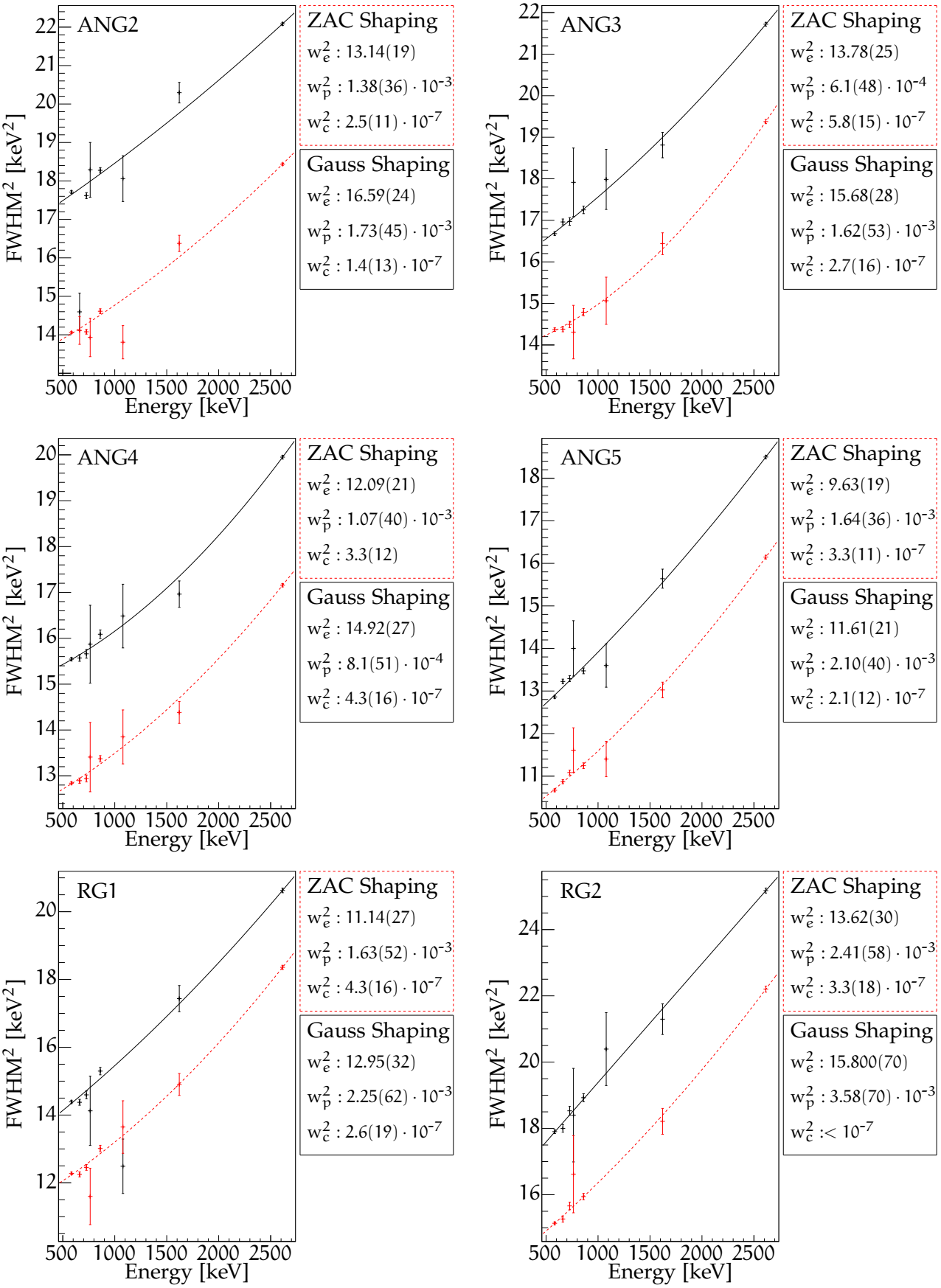

Figure B.3.: FWHM^2 as a function of energy for the super-tier3 of semi-coaxial detectors. The calibration runs taken in the period corresponding to the golden data set are used. The best fit values are reported.

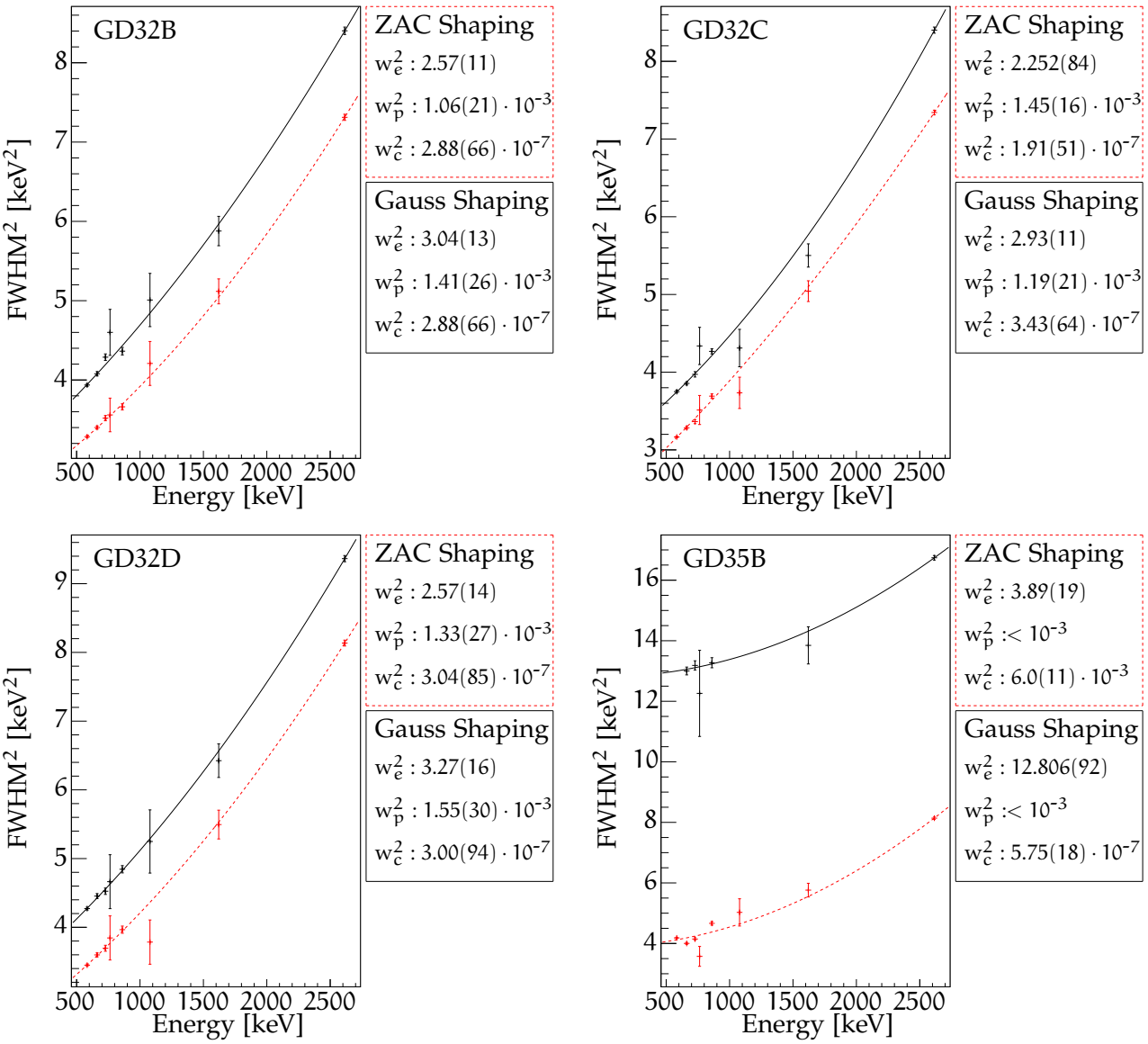

Figure B.4.: FWHM^2 as a function of energy for the super-tier3 of BEGe detectors. The best fit values are reported.

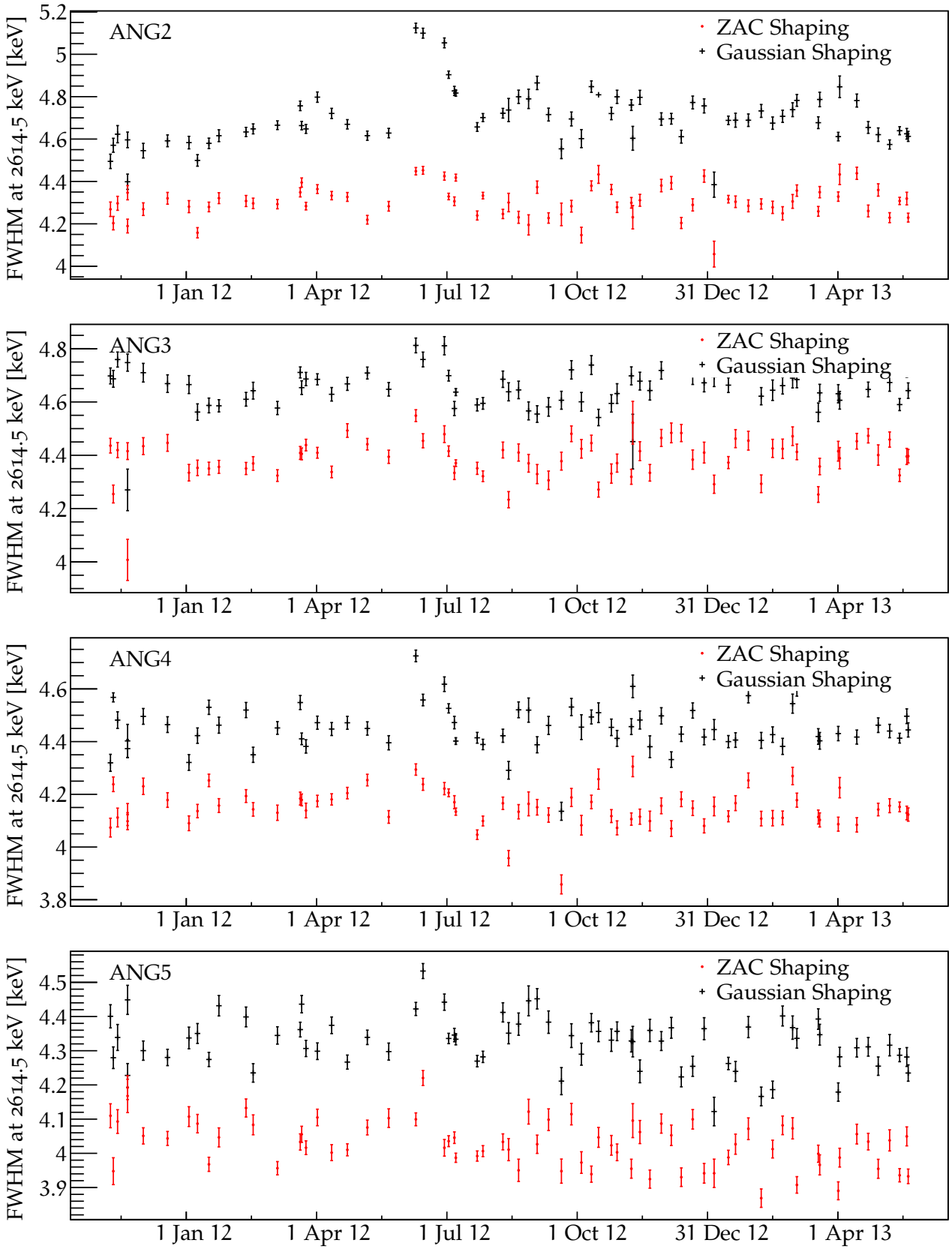

Figure B.5.: Time evolution of FWHM for the ^{208}Tl line at 2614.5 keV over all Phase I.

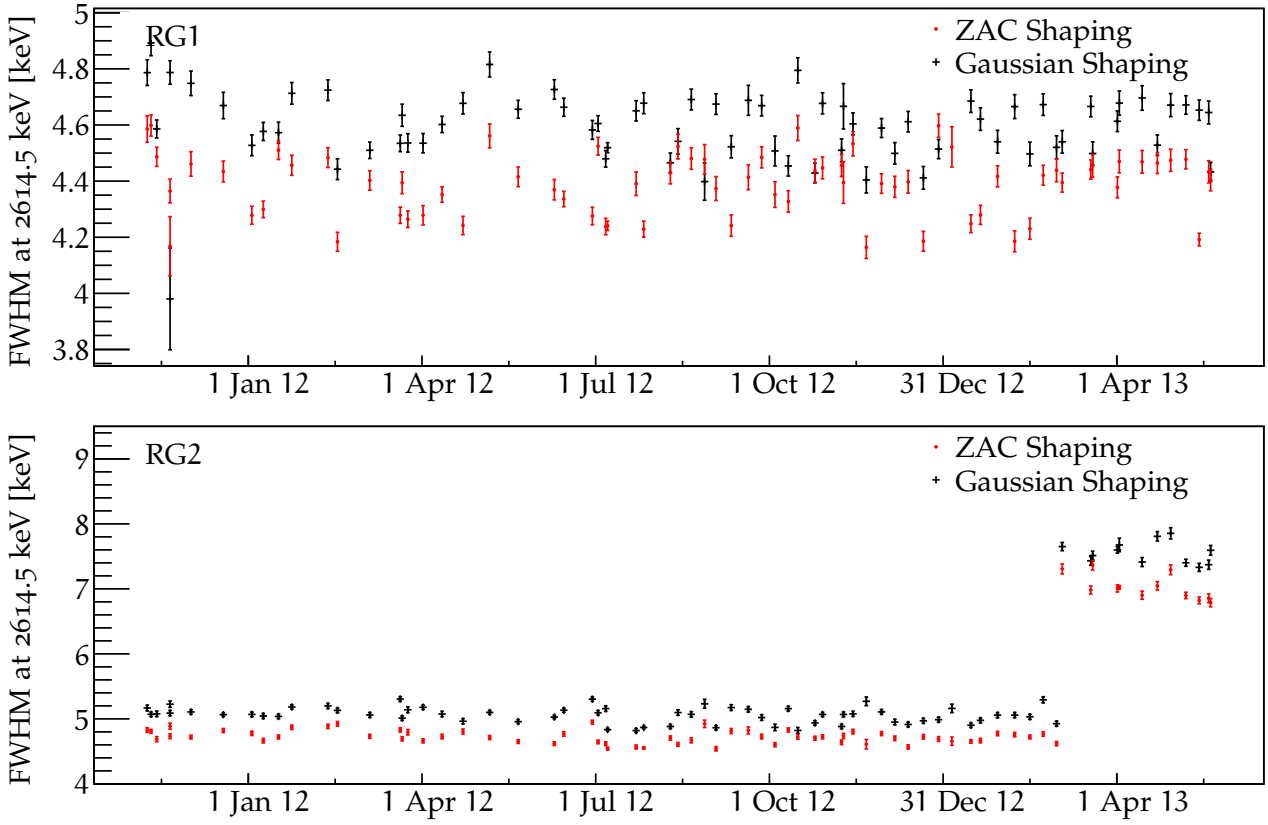

Figure B.6.: Time evolution of FWHM for the ^{208}Tl line at 2614.5 keV over all Phase I.

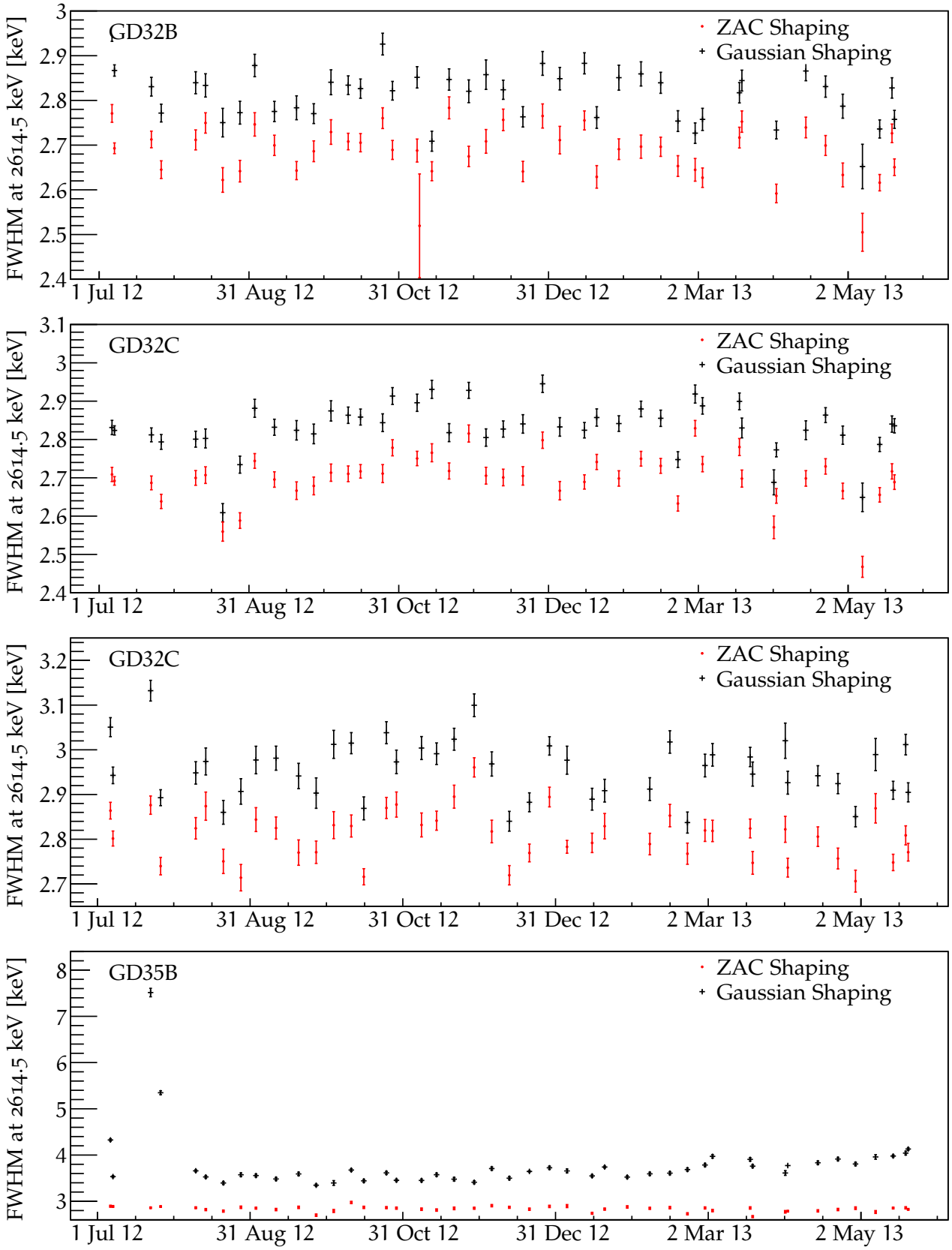

Figure B.7.: Time evolution of FWHM for the ^{208}Tl line at 2614.5 keV over all Phase I.

C

GERDA-ADA AND ENERGY CALIBRATION ALGORITHMS FOR GERDA PHASE II

In view of GERDA Phase II, a new software package called GERDA-Advanced-Gerda-Analysis (GERDA-ADA is being developed by the collaboration. It is designed to comprehend all the tools for the analysis of tier2 data and provide the final data files for the analysis of the physics data. The tasks of GERDA-ADA are the following:

- analysis of calibration data from germanium detectors, PMTs and SiPM;
- calibration of the energy scale for germanium detectors, PMTs and SiPM;
- extraction of PSD cut parameters for BEGe and semi-coaxial detectors;
- extraction of LAr veto cut parameters;
- optimization of signal filtering for energy reconstruction and PSD of germanium signals;
- event selection for $0\nu\beta\beta$ decay search and other analyses of the physics data;
- creation of tier3 files.

GERDA-ADA is coded in C++11 and is based on ROOT6, which is guaranteed to be maintained for all the duration of GERDA Phase II. It additionally depends on CLHEP [193], MGDO [191], GELATIO [192] and the newly developed framework for modular data analysis DatABriCxx [233]. Being a project in fast development, additional dependencies on other packages are being added or planned. A complete documentation of the framework is currently not possible, and will be given once the software package reaches a stable version. All the input and output parameters of the various routines are of JSON format [234]. The parsing of the JSON files is performed by DatABriCxx.

The source code of GERDA-ADA is available to all the GERDA collaboration. It can be compiled and installed on any system with GNU-C++. So far, the installation has been successfully completed on several Linux and MacOS distributions.

The core of GERDA-ADA has been designed by the author, M. Agostini, L. Pandola and O. Schulz. In addition to this, the author developed and implemented the tool for the analysis of calibration data, denoted "CalibGPII" (Calibration GERDA Phase II). Specific analysis tools are currently being integrated by several other members of GERDA.

In the following sections, a review of the procedure for the analysis of Phase II calibration data is given. In Sec. C.1 the main steps of the calibration routine are reported, in Sec. C.2 the algorithm for the fit of the spectral peaks is described, and in Sec. C.3 the additional designed developments of the Phase II calibration program are described.

C.1 CALIBRATION OF PHASE II DATA

The analysis scheme of the calibration data is very similar to the one used in Phase I and reported in Ch. 5. Therefore only the general procedure is given here, together with the main differences introduced for Phase II. The analysis flow consists of the following steps:

- the JSON files with the detector parameters (name, mass, dimensions, ...) and detector configuration (detector-channel mapping, high voltage) are read;
- the JSON files with the source parameters (name, activity, ...) and source configuration (position, deployment, ...) are read;
- the tier2 ROOT files are opened;
- the event selection is applied. Differently from Phase I, the list of quality cuts can be modified by the user;
- the peak search and identification is performed;
- the fit of the spectral lines is performed;
- the calibration and resolution curves are extracted;
- the best-fit functions for all the considered peaks, calibration curves and resolution curves are saved to ROOT files and as png images, too. The calibration curves are saved in JSON format, too.

The main differences with respect to the software used in Phase I regard the interface to the input/output parameter files and the peak fitting routine. The first modification is justified by the need of a common format of the parameter files for all the GERDA analysis tools, while the improvement of the fit procedure is justified by both computational and physical reasons, as explained below.

C.2 ALGORITHM FOR AUTOMATIC PEAK FITTING

In GERDA-ADA, several modifications have been applied to the algorithm for peak fitting. In Phase II, a total of about $2 \cdot 10 \cdot 10^5$ fits have to be performed, to be compared with the $\sim 2 \cdot 10 \cdot 10^4$ of Phase I. For this reason, the fitting routine needs to be further improved and the identification of failing fits automatized.

The parametrization of the spectral peaks is slightly different than in Phase I, as described below. In the following, the uncalibrated energy is referred as x.

- For the high-statistics peaks a corrected Hypermet function [235] is used:

$$f(x) = \frac{A}{\sigma\sqrt{2\pi}} \exp\left(-\frac{(x-\mu)^2}{2\sigma^2}\right) + B + \frac{C}{2}\operatorname{erfc}\left(\frac{x-\mu}{\sqrt{2}\sigma}\right) + \frac{D}{2}\exp\left(\frac{\sigma^2}{2\delta^2}\right)\exp\left(\frac{x-\mu}{\delta}\right)\operatorname{erfc}\left(\frac{x-\mu}{\sqrt{2}\sigma} + \frac{\sigma}{\sqrt{2}\delta}\right) + F\cdot(x-\mu) \quad \text{(C.1)}$$

  which is the same as Eq. 5.7, with a different low-energy tail normalization. In this way, the correlation between σ and δ is correctly taken into account, and the fit convergence time reduced [235].
- The low-statistics peaks are described with a Gaussian distribution over a linear continuum:

$$f(x) = \frac{A}{\sigma\sqrt{2\pi}} \exp\left(-\frac{(x-\mu)^2}{2\sigma^2}\right) + B + F\cdot(x-\mu) \quad \text{(C.2)}$$

In Phase I, the low-energy step was never used for these peak, hence it is removed from the fitting function.

– The SEP and DEP are parametrized with a Gaussian distribution over a linear continuum and a high-energy step:

$$f(x) = \frac{A}{\sigma\sqrt{2\pi}} \exp\left(-\frac{(x-\mu)^2}{2\sigma^2}\right) + B + \frac{C}{2}\operatorname{erf}\left(\frac{x-\mu}{\sqrt{2}\sigma}\right) + F\cdot(x-\mu) \quad \text{(C.3)}$$

The presence of the high-energy step accounts for events in which one of the two 511 keV γ's undergoes a Compton scattering in the detector before escaping from it (see Sec. 3.1.4).

– For ^{228}Th spectra, the 511 keV line is the sum of the annihilation peak and a γ line at 510.77 keV (see Tab. 5.2). The ratio between the amplitude of the two depends on the detector size and on the position of the calibration source with respect to the detector. In general it is $\lesssim 3:1$. In Phase I, this fact was not considered. The presence of this weaker γ peak at 0.2 keV distance from the annihilation peak does not strongly affect the measurement of the peak position because of the Doppler broadening acting on the annihilation peak. Thus, the systematic introduced by this non-optimal parametrization of the peak is well below 0.1 keV. A $> 3\sigma$ deviation of this peak position from the calibration curve is visible only for spectra with good resolution (BEGe's) and $> 10^6$ events. To remove this bias, an additional Gaussian term is added to the corrected Hypermet function:

$$\begin{aligned} f(x) = \frac{A_1}{\sigma_1\sqrt{2\pi}} \exp\left(-\frac{(x-\mu_1)^2}{2\sigma_1^2}\right) + \frac{A_2}{\sigma_2\sqrt{2\pi}} \exp\left(-\frac{(x-\mu_2)^2}{2\sigma_2^2}\right) + \\ B + \frac{C}{2}\operatorname{erfc}\left(\frac{x-\mu}{\sqrt{2}\sigma}\right) + F\cdot(x-\mu) + \\ \frac{D}{2}\exp\left(\frac{\sigma^2}{2\delta^2}\right)\exp\left(\frac{x-\mu}{\delta}\right)\operatorname{erfc}\left(\frac{x-\mu}{\sqrt{2}\sigma} + \frac{\sigma}{\sqrt{2}\delta}\right) \end{aligned} \quad \text{(C.4)}$$

in which the ratio μ_1/μ_2 is fixed to 511/510.77 keV.

The automatization of the peak fitting routine relies on two ingredients. Firstly, a preliminary estimation of all function's parameters is performed, leading to the assignment of initial values and allowed ranges. Secondly, the peak fit is performed iteratively with different algorithms and fitting functions, following the same philosophy used in Phase I (see Sec. 5.5) All the steps of the fitting procedure are described below.

In the following, the central value of a bin with index i is denoted as $x[i]$, and its amplitude $y[i]$. In the first step, the fit region $[x[a]; x[d]]$ is divided in three parts for the study of the central peak and of the continuum on its sides. With reference to Fig. C.1, the boundaries of the central peak region b and c are searched. The average on the left of the peak is calculated:

$$\bar{y}[m] = \frac{1}{m-a+1}\sum_{i=a}^{m} y[m] \quad \text{(C.5)}$$

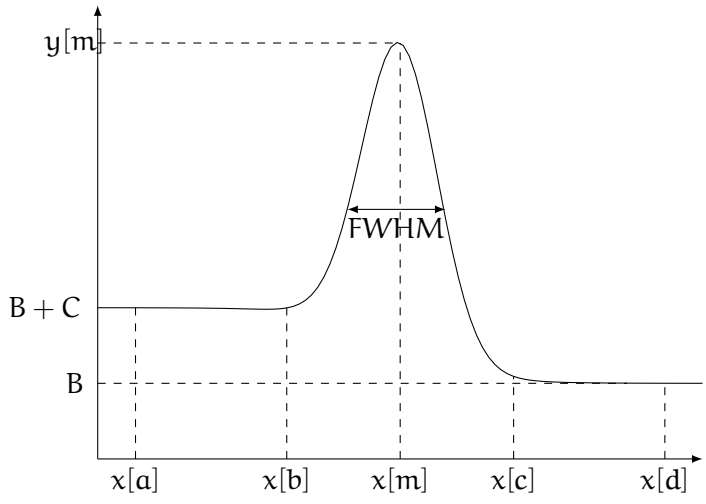

Figure C.1.: Schematic of a typical spectral peak. The ranges for the peak fit and main parameters involved in the fitting algorithm are reported.

where $x[m]$ is the x coordinate of the total maximum. The corresponding RMS is:

$$RMS[m] = \sqrt{\frac{\sum_{i=a}^{m} (y[i] - \bar{y}[m])^2}{m - a + 1}} \tag{C.6}$$

The maximum index is then iteratively lowered by one unit ($m \to m-1 \to m-2 \to \dots$) until the following condition is reached:

$$y[b] \leqslant \bar{y}[b] + RMS[b] + 1 \qquad b \in [a; m] \tag{C.7}$$

The bin b indicates the position at the right of which the peak starts to rise. The approximation of the continuum on the left side of the peak with a flat distribution is not affected by the presence of possible slopes, which are typically small enough not to invalidate the algorithm described above. The same routine is applied to the right side of the peak, and the two coordinates $x[b]$ and $x[c]$ are found.

In a second stage a simultaneous fit of the regions $[x[a]; x[b]]$ and $[x[c], x[d]]$ is performed. For high statistics peaks the fitting function is:

$$f(x) = \begin{cases} B + F \cdot (x - \mu) + C & x \in [x[a]; x[b]] \\ B + F \cdot (x - \mu) & x \in [x[c]; x[d]] \end{cases} \tag{C.8}$$

For low statistics peaks:

$$y = B + F \cdot (x - \mu) \tag{C.9}$$

And for the SEP and DEP:

$$f(x) = \begin{cases} B + F \cdot (x - \mu) & x \in [x[a]; x[b]] \\ B + F \cdot (x - \mu) + C & x \in [x[c]; x[d]] \end{cases} \tag{C.10}$$

The parameters B, F and C used here correspond to the same in Eqs. C.1, C.2, C.3 and C.4. The initial values B_{ini}, F_{ini} and C_{ini} as well as the parameter ranges for the final fit of the whole peak region are set to:

$$\begin{aligned} B_{ini} &= \hat{B} \\ B_{min} &= \hat{B} - 3 \cdot \sigma_B \\ B_{max} &= \hat{B} + 3 \cdot \sigma_B \end{aligned} \tag{C.11}$$

where $\hat{B}$ is the best fit value of B just found, and σ_B the corresponding uncertainty. The same is done for F and C.

At this point, the mean of the Gaussian distribution is computed:

$$\hat{\mu} = \frac{\sum_{i=b}^{c} x[i] \cdot y[i]}{\sum_{i=b}^{c} y[i]} \tag{C.12}$$

The initial value and range for μ are set to:

$$\begin{aligned} \mu_{ini} &= \hat{\mu} \\ \mu_{min} &= \hat{\mu} - 15 \cdot \Delta x \\ \mu_{max} &= \hat{\mu} + 15 \cdot \Delta x \end{aligned} \tag{C.13}$$

$$\tag{C.14}$$

where Δx is the bin width.

In the next step, σ is estimated. The two bins l and r are searched on the left and right of the peak, respectively, for which:

$$y[l](r) = B + \frac{y[m] - B}{2} \tag{C.15}$$

The initial value and the range for σ are then given by:

$$\begin{aligned} \sigma_{ini} &= \frac{x[r] - x[L]}{2.355} \\ \sigma_{min} &= 0 \\ \sigma_{max} &= x[r] - x[L] \end{aligned} \tag{C.16}$$

Additionally, the initial value for the area A of the Gaussian peak is computed as the total area in the $[x[b]; x[c]]$ range, minus the contribution of the flat continuum and that of the low-energy step, if present. The sloping component of the continuum is neglected, being symmetric on the two sides of the peak. Thus:

$$\begin{aligned} A_{ini} &= \sum_{i=b}^{c} y[i] - \frac{(x[c] - x[b]) \cdot B}{\Delta x} - \frac{(x[c] - x[b]) \cdot C}{2\Delta x} \\ A_{min} &= 0 \\ A_{max} &= 5 \cdot A_{ini} \end{aligned} \tag{C.17}$$

Finally, the initial values for the parameters of the low-energy tail are chosen arbitrarily according to the typical values obtained in Phase I. The amplitude D is set as function of the peak amplitude:

$$\begin{aligned} D_{ini} &= \frac{y[m]}{20} \\ D_{min} &= 0 \\ D_{max} &= 100 \cdot y[m] \end{aligned} \tag{C.18}$$

$$\tag{C.19}$$

While the value of the decay constant of the exponential is initialized as function of σ:

$$\begin{aligned} \delta_{ini} &= 6 \cdot \sigma_{ini} \\ \delta_{min} &= \sigma_{ini} \\ \delta_{max} &= 20 \cdot \sigma_{ini} \end{aligned} \tag{C.20}$$

The final peak fit is then performed using Minuit2 according to the following procedure:

- a first χ^2 is performed to get a first estimate of the best-fit parameters;
- a maximum likelihood fit (ROOT option "L") is run, leading to the final estimate of the parameters;
- the maximum likelihood fit is repeated with the use of Minos for the correct handling of asymmetric uncertainties;
- the fit of the low-energy tail is checked. If its amplitude is not large enough, or not well enough constrained, the fit is repeated without the tail. In particular, the requirement for a reliable fit are:

$$\hat{D} < 2 \cdot \sigma_D \tag{C.21}$$

and:

$$\int_{x[a]}^{x[d]} \frac{D}{2} \exp\left(\frac{\sigma^2}{2\delta^2}\right) \exp\left(\frac{x-\mu}{\delta}\right) \operatorname{erfc}\left(\frac{x-\mu}{\sqrt{2}\sigma} + \frac{\sigma}{\sqrt{2}\delta}\right) < 0.1 \cdot A \tag{C.22}$$

- the fit of the low- or high-energy step is checked. If its amplitude is not well constrained, the fit is repeated without the step. The applied condition is:

$$C < \sigma_C \tag{C.23}$$

Once the final fit is available, the FWHM is computed in two ways. Firstly, the FWHM of the Gaussian distribution is taken:

$$FWHM = 2.355 \cdot \sigma \tag{C.24}$$

Secondly, if the low-energy tail is present, the FWHM is computed numerically also on the Gaussian and tail components. This is done searching the zeroes of the function:

$$\begin{aligned} g(x) = &\frac{A}{\sigma\sqrt{2\pi}} \exp\left(-\frac{(x-\mu)^2}{2\sigma^2}\right) \\ &+ \frac{D}{2} \exp\left(\frac{\sigma^2}{2\delta^2}\right) \exp\left(\frac{x-\mu}{\delta}\right) \operatorname{erfc}\left(\frac{x-\mu}{\sqrt{2}\sigma} + \frac{\sigma}{\sqrt{2}\delta}\right) - \frac{\max(g(x))}{2} \end{aligned} \tag{C.25}$$

where $\max(g(x))$ is the maximum of the peak in the $[x[a]; x[d]]$ range. The function $g(x)$ is zero for two values $x[l]$ and $x[r]$ at the left and right side of the peak, respectively. The FWHM is given as:

$$FWHM = x[r] - r[l] \tag{C.26}$$

In order to compute the uncertainty on the FWHM, the 68% coverage band for the function $g(x)$ is extracted, and the calculation is repeated after having substituted the best-fit parameters with the ones describing the $\pm 1\sigma$ band.

During the Phase II integration tests some detectors suffered strong gain instabilities within the duration of a calibration run. Hence, the shape of the peaks in the energy spectra were not as expected and could not be fitted properly. As an example, if the a sudden gain jump of few keV takes place during the data collection, the peaks show a double component. The FWHM of the fitted function will be larger than it would be for data taken in stable conditions, and the χ^2/NDF of the fit will be $\gg 1$. A list of checks is therefore necessary to make sure that the peak fits are reliable. For the moment, the following conditions are required:

$$\begin{aligned} FWHM &< 20 \text{ keV} \\ \frac{\sigma_{FWHM}}{\mu} &< 5 \cdot 10^4 \end{aligned} \tag{C.27}$$

If they are not satisfied, the peak is not exploited for the extraction of the calibration and resolution curves. A further cut based on the χ^2/NDF ratio is under development and is expected to be applied for the analysis of Phase II calibration data. Further checks might be included in the future, depending on the quality of the data.

Finally, the residuals and pulls, i.e. the residuals normalized to their uncertainty, for the peak fit are extracted. These are useful for a visual check of the performance of all peak fits. For each bin i in the considered range, the residual $r[i]$ of the spectrum from the best-fit function $\hat{f}(x[i])$ in the same bin is given by:

$$\begin{aligned} r[i] &= y[i] - f(x[i]) \\ \sigma^{+(-)}_{r[i]} &= \sigma^{+(-)}_{y[i]} \end{aligned} \tag{C.28}$$

where $\sigma^{+(-)}_{r[i]}$ is the upper (lower) uncertainty of the residual $r[i]$, and $\sigma^{+(-)}_{y[i]}$ is the same for $y[i]$. The pulls $p[i]$ and their upper (lower) uncertainties $\sigma^{+(-)}_{p[i]}$ are given by:

$$\begin{aligned} n[i] &= \begin{cases} \sigma^{+}_{y[i]} & y[i] > 0 \\ \sigma^{-}_{y[i]} & y[i] < 0 \end{cases} \\ p[i] &= \frac{y[i]}{n[i]} \\ \sigma^{+(-)}_{p[i]} &= \frac{\sigma^{+(-)}_{y[i]}}{n[i]} \end{aligned} \tag{C.29}$$

For the analysis of the Phase II integration tests data, the residual and pull graphs have only be used for a visual check of the fit performance. As for the χ^2/NDF check, an algorithm to quantify the reliability of the fit is being developed and is expected to be ready by the start of Phase II.

The Phase II calibration software presented here has been successfully tested in $\sim 2 \cdot 10^2$ spectra so far, with a total of $\sim 2 \cdot 10^3$ peak fits. The percentage of failures in the peak fitting is $O(10^{-3})$. This is enough to ensure a reliable determination

of the energy scale for all considered spectra, provided that they are not affected by strong deficiencies. If $2 \cdot 10^5$ are collected, a maximum of $O(10^2)$ failures is expected. Additional improvements of the peak fitting routine can be developed based on the failing cases.

C.3 FURTHER DEVELOPMENTS

A list of further developments to the calibration program for GERDA Phase II are planned to be implemented in the near future. Two main features are going to be added to the peak fitting routine, as described below.

- The initial values of the low-energy tail amplitude and decay constant can be extracted fitting the left side of the Gaussian peak. In particular, the logarithm of the spectral amplitude $\ln y[i]$ can be computed and fitted with a linear function:

$$\ln y[i] = p_0 + p_1 \cdot (x[i] - \mu) \qquad x[i] \in [x[b]; x[m]] \tag{C.30}$$

  and the parameters D and δ can be initialized solving the system of equations:

$$\begin{aligned} p_0 &= \ln\left[\frac{D}{2}\exp\left(\frac{\sigma^2}{2\delta^2}\right)\right] \\ p_1 &= \frac{1}{\delta} \end{aligned} \tag{C.31}$$

  where the two terms on the right side correspond to the factors of the low-energy tail. The erfc factor has been dropped because its amplitude is 1 for $x < \mu$, hence its logarithm vanishes.
  In Eq. C.30 the fit is performed on the left half of the Gaussian peak. If the tail is not very pronounced, the upper bound of the fit range should be reduced so that only the very first part of the peak is considered. Preliminary studies show that using $[x[b], x_k]$ with $x_k = (x[b] + x[m])/2$ as a fit range provide a good estimation;
- The linear continuum and the eventual step can be described in an alternative way using one right-handed and one left-handed steps:

$$\frac{C_1}{2}\mathrm{erfc}\left(\frac{F_1 \cdot (x-\mu)}{\sqrt{2}\sigma}\right) + \frac{C_2}{2}\mathrm{erf}\left(\frac{F_2 \cdot (x-\mu)}{\sqrt{2}\sigma}\right) \tag{C.32}$$

  Due to the lack of a physical explanation for the use of this parametrization, this is planned to be employed only to extract the systematic on the energy scale coming from the choice of the fitting function.
- The design of a check of the fit quality based on the χ^2/NDF and on the study of the residuals and pulls is ongoing, too.

Moreover, additional features regarding the extraction of the calibration and resolution curves are on the development pipeline, as listed here.

- The calibration curve is currently extracted through a χ^2 fit with Minuit2. This can be substituted rather easily by an analytic fit. While the best fit parameters are expected to remain the same for the two cases, their uncertainties might be affected by the employed method.

- The resolution curve can be computed fixing the charge production term w_p (see Eq. 3.21). Also in this case, the alternative fit can be exploited for the study of systematics.
- As for the calibration curve, an analytic fit can be used for the resolution curve, too. In particular, this can be applied to the squared of Eq. 3.23.

All these tasks are currently under design or implementation, and are expected to be available in the beginning of Phase II.

D

MEASUREMENT OF THE ^{56}CO SOURCE ACTIVITY

In view of other ^{56}Co calibration runs during Phase II it is necessary to precisely quantify the activity of the source used in Phase I, in order to better estimate the required irradiation time for the source production. A dedicated measurement was performed with the Gator facility [225] at LNGS. As for the measurement of the Phase II ^{228}Th sources (see Sec. 8.2), the count rate induced by the ^{56}Co activity is 3 orders of magnitude higher than the background rate of Gator, hence the measurement described here can be considered background free. The source was placed on the top of the detector cryostat, and the energy spectrum was acquired for 30 min. Since Gator is normally used for material screening, where the gamma peak with highest energy is the ^{208}Tl line at 2614.5 keV, the spectrum is recorded in the $[0; 2700]$ keV region. This was not changed in order to prevent any instability of the setup, with the consequence that the high-energy part of ^{56}Co spectrum is not available. Nevertheless a good precision in the activity determination was achieved.

The measurement of the source activity follows the same procedure used for the Phase II ^{228}Thsources (see Sec. 8.2). Thanks to the available statistics and to the good agreement between data and MC, an accurate evaluation of the activity is possible, with a statistical error of 0.6‰ (see Fig. D.1).

The systematic uncertainty is computed taking into consideration the geometrical effects and the cross sections used in the MC. While the measurements of the ^{228}Th source activities were taken with the sources at a $\sim$ 120 mm distance from the detector top, the lower activity of the ^{56}Co source allowed to place it directly on the detector cryostat. Hence, the distance between the source and the crystal is known with a sub-millimeter precision and the systematic uncertainty induced by it on the activity is negligible. On the contrary, the limited precision on the cross section of the photoelectric, Compton and pair production processes are considered, yielding a $\pm 2\%$ effect, which is comparable to what obtained with the Phase II ^{228}Th sources. Additionally, the systematic related to the limited knowledge of the n^+ dead layer thickness is determined. The simulations are repeated by changing the DL by ± 0.1 mm, resulting in a $\sim 0.7\%$ systematic uncertainty on the activity.

The final value for the ^{56}Co source activity about 10 days after the production is:

$$A = 5.122 \pm 0.003\,(\text{stat})\,^{+0.04}_{-0.03}\,(\text{DL}) \pm 0.10\,(\text{cross section})\ \text{kBq} \quad . \tag{D.1}$$

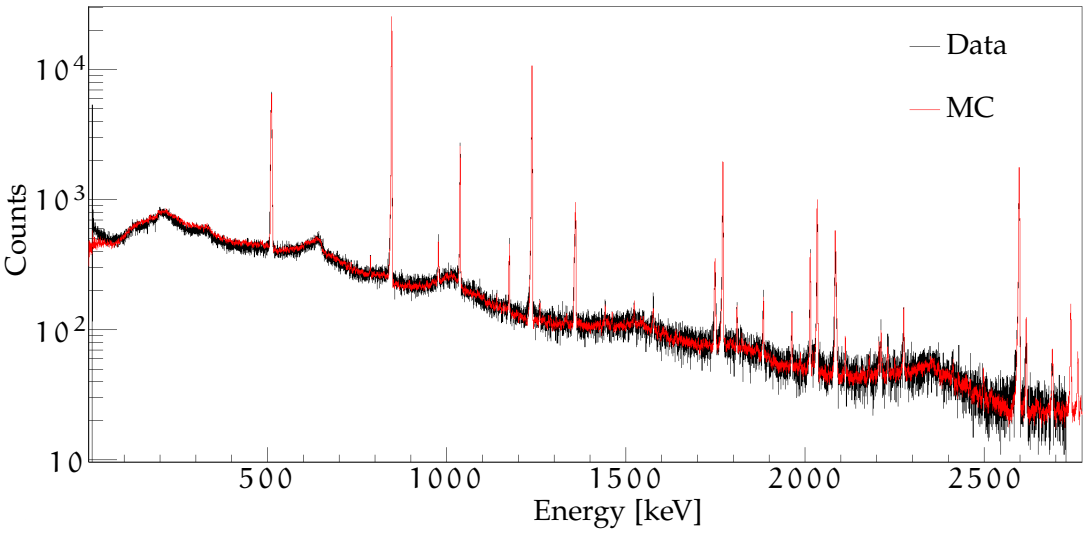

Figure D.1.: Measured and simulated ^{56}Co spectra, scaled according to the best fit value for the source activity.

BIBLIOGRAPHY

[1] G. Benato, (2015), arXiv:1510.01089.

[2] L. Baudis *et al.*, (2015), arXiv:1508.05731.

[3] GERDA, M. Agostini *et al.*, Eur. Phys. J. **C**75, 255 (2015), arXiv:1502.04392.

[4] C. Giunti and C. W. Kim, *Fundamentals of Neutrino Physics and Astrophysics* (Oxford University Press, Oxford, UK, 2007), ISBN 978-0-19-850871-7.

[5] E. Rutherford, Phylos. Mag. 47, 109 (1899).

[6] J. Chadwick, Verhandlungen der Deutschen Physikalischen Gesellschaft 16, 303 (1914).

[7] W. Pauli, Cambridge Monogr. Part. Phys. Nucl. Phys. Cosmol. 14, 1 (2000).

[8] W. Heisenberg, Zeitschrift fr Physik A Hadrons and Nuclei 78, 156 (1932).

[9] E. Fermi, Nuovo Cimento 11, 1 (1934).

[10] M. Goeppert-Mayer, Physical Review (Series I) 48 (1935).

[11] E. Majorana, Il Nuovo Cimento Series 10 14 (1937).

[12] W. H. Furry, Phys. Rev. 56, 1184 (1939).

[13] E. J. Konopinski and H. M. Mahmoud, Physical Review 92, 1045 (1953).

[14] B. Pontecorvo, Zhur. Eksptl. i Teoret. Fiz. 34, 172 (1958).

[15] F. Reines and C. L. Cowan, Phys. Rev. 92, 830 (1953).

[16] M. Goldhaber, L. Grodzins, and A. W. Sunyar, Phys. Rev. 109, 1015 (1958).

[17] M. Bardon, P. Franzini, and J. Lee, Phys. Rev. Lett. 7, 23 (1961).

[18] A. Possoz *et al.*, Phys. Lett. **B**70, 265 (1977), [Erratum: Phys. Lett.B73, 504(1978)].

[19] ARGUS, H. Albrecht *et al.*, Phys. Lett. **B**250, 164 (1990).

[20] ALEPH, D. Buskulic *et al.*, Phys. Lett. **B**346, 379 (1995), [Erratum: Phys. Lett.B363,265(1995)].

[21] SLD, K. Abe *et al.*, Phys. Rev. Lett. 78, 4691 (1997), arXiv:hep-ex/9701020.

[22] G. Danby *et al.*, Physical Review Letters 9 (1962).

[23] S. Weinberg, Phys. Rev. Lett. 19, 1264 (1967).

[24] A. Salam, Weak and electromagnetic interactions, in *Elementary particle theory*, edited by N. Svartholm, pp. 367–377, Almquist & Wiksell, 1968.

[25] B. Pontecorvo, Sov. Phys. JETP 6, 429 (1957), [Zh. Eksp. Teor. Fiz.33, 549(1957)].

[26] B. Pontecorvo, Sov. Phys. JETP 7, 172 (1958), [Zh. Eksp. Teor. Fiz.34, 247(1957)].

[27] B. Pontecorvo, Sov. Phys. JETP 26, 984 (1968), [Zh. Eksp. Teor. Fiz.53, 1717(1967)].

[28] V. N. Gribov and B. Pontecorvo, Phys. Lett. **B**28, 493 (1969).

[29] H. Fritzsch and P. Minkowski, Phys. Lett. **B62**, 72 (1976).

[30] R. Davis, D. S. Harmer, and K. C. Hoffman, Physical Review Letters 20 (1968).

[31] B. T. Cleveland *et al.*, Astrophys. J. 496, 505 (1998).

[32] Kamiokande-II, K. S. Hirata *et al.*, Phys. Rev. Lett. 63, 16 (1989).

[33] Kamiokande, Y. Fukuda *et al.*, Phys. Rev. Lett. 77, 1683 (1996).

[34] A. I. Abazov *et al.*, Phys. Rev. Lett. 67, 3332 (1991).

[35] SAGE, J. N. Abdurashitov *et al.*, J. Exp. Theor. Phys. 95, 181 (2002), arXiv:astro-ph/0204245, [Zh. Eksp. Teor. Fiz.122, 211(2002)].

[36] GALLEX, P. Anselmann *et al.*, Phys. Lett. **B**357, 237 (1995), [Erratum: Phys. Lett.B361, 235(1996)].

[37] GNO, M. Altmann *et al.*, Phys. Lett. **B**616, 174 (2005), arXiv:hep-ex/0504037.

[38] Super-Kamiokande, Y. Fukuda *et al.*, Phys. Rev. Lett. 81, 1158 (1998), arXiv:hep-ex/9805021, [Erratum: Phys. Rev. Lett.81, 4279(1998)].

[39] Super-Kamiokande, K. Abe *et al.*, Phys. Rev. **D**83, 052010 (2011), arXiv:1010.0118.

[40] SNO, Q. R. Ahmad *et al.*, Phys. Rev. Lett. 87, 071301 (2001), arXiv:nucl-ex/0106015.

[41] SNO, B. Aharmim *et al.*, Phys. Rev. **C**88, 025501 (2013), arXiv:1109.0763.

[42] Borexino, C. Arpesella *et al.*, Phys. Lett. **B**658, 101 (2008), arXiv:0708.2251.

[43] G. Bellini *et al.*, Phys. Rev. Lett. 107, 141302 (2011), arXiv:1104.1816.

[44] KamLAND, S. Abe *et al.*, Phys. Rev. **C**84, 035804 (2011), arXiv:1106.0861.

[45] R. Becker-Szendy *et al.*, Phys. Rev. **D**46, 3720 (1992).

[46] Kamiokande-II, K. S. Hirata *et al.*, Phys. Lett. **B**280, 146 (1992).

[47] Kamiokande, Y. Fukuda *et al.*, Phys. Lett. **B**335, 237 (1994).

[48] MACRO, M. Ambrosio *et al.*, Phys. Lett. **B**434, 451 (1998), arXiv:hep-ex/9807005.

[49] MACRO, M. Ambrosio *et al.*, Phys. Lett. **B**566, 35 (2003), arXiv:hep-ex/0304037.

[50] MINOS, P. Adamson *et al.*, Phys. Rev. **D**75, 092003 (2007), arXiv:hep-ex/0701045.

[51] MINOS, P. Adamson *et al.*, Phys. Rev. **D**86, 052007 (2012), arXiv:1208.2915.

[52] W. W. M. Allison *et al.*, Phys. Lett. **B**391, 491 (1997), arXiv:hep-ex/9611007.

[53] Soudan 2, M. C. Sanchez *et al.*, Phys. Rev. **D**68, 113004 (2003), arXiv:hep-ex/0307069.

[54] Super-Kamiokande, Y. Fukuda *et al.*, Phys. Lett. **B**433, 9 (1998), arXiv:hep-ex/9803006.

[55] Super-Kamiokande, Y. Fukuda *et al.*, Phys. Rev. Lett. 81, 1562 (1998), arXiv:hep-ex/9807003.

[56] ANTARES, S. Adrian-Martinez *et al.*, Phys. Lett. **B**714, 224 (2012), arXiv:1206.0645.

[57] IceCube, M. G. Aartsen *et al.*, Phys. Rev. Lett. 111, 081801 (2013), arXiv:1305.3909.

[58] KamLAND, K. Eguchi *et al.*, Phys. Rev. Lett. 90, 021802 (2003), arXiv:hep-ex/0212021.

[59] KamLAND, S. Abe *et al.*, Phys. Rev. Lett. 100, 221803 (2008), arXiv:0801.4589.

[60] Daya Bay, F. P. An *et al.*, Phys. Rev. Lett. 108, 171803 (2012), arXiv:1203.1669.

[61] Daya Bay, F. P. An *et al.*, Phys. Rev. Lett. 115, 111802 (2015), arXiv:1505.03456.

[62] Double Chooz, Y. Abe *et al.*, Phys. Rev. Lett. 108, 131801 (2012), arXiv:1112.6353.

[63] Double Chooz, Y. Abe *et al.*, JHEP 10, 086 (2014), arXiv:1406.7763, [Erratum: JHEP02, 074(2015)].

[64] RENO, J. K. Ahn *et al.*, Phys. Rev. Lett. 108, 191802 (2012), arXiv:1204.0626.

[65] K2K, M. H. Ahn *et al.*, Phys. Rev. Lett. 90, 041801 (2003), arXiv:hep-ex/0212007.

[66] K2K, S. Yamamoto *et al.*, Phys. Rev. Lett. 96, 181801 (2006), arXiv:hep-ex/0603004.

[67] MINOS, D. G. Michael *et al.*, Phys. Rev. Lett. 97, 191801 (2006), arXiv:hep-ex/0607088.

[68] MINOS, P. Adamson *et al.*, Phys. Rev. Lett. 112, 191801 (2014), arXiv:1403.0867.

[69] T2K, K. Abe *et al.*, Phys. Rev. Lett. 107, 041801 (2011), arXiv:1106.2822.

[70] T2K, K. Abe *et al.*, Phys. Rev. **D**91, 072010 (2015), arXiv:1502.01550.

[71] OPERA, N. Agafonova *et al.*, Phys. Lett. **B**691, 138 (2010), arXiv:1006.1623.

[72] OPERA, N. Agafonova *et al.*, Phys. Rev. Lett. 115, 121802 (2015), arXiv:1507.01417.

[73] S. M. Bilenky and C. Giunti, Int. J. Mod. Phys. **A**30, 1530001 (2015), arXiv:1411.4791.

[74] S. M. Bilenky, in *Proceedings, 22nd International Baldin Seminar on High Energy Physics Problems, Relativistic Nuclear Physics and Quantum Chromodynamics, (ISHEPP* 2014*)*, 2014, arXiv:1408.2864.

[75] F. Capozzi *et al.*, Phys. Rev. **D**89, 093018 (2014), arXiv:1312.2878.

[76] P. Minkowski, Phys. Lett. **B**67, 421 (1977).

[77] T. Yanagida, Conf. Proc. **C**7902131, 95 (1979).

[78] R. N. Mohapatra and G. Senjanovic, Phys. Rev. Lett. 44, 912 (1980).

[79] R. N. Mohapatra and A. Y. Smirnov, Ann. Rev. Nucl. Part. Sci. 56, 569 (2006), arXiv:hep-ph/0603118.

[80] E. K. Akhmedov, M. Lindner, E. Schnapka, and J. W. F. Valle, Phys. Rev. **D**53, 2752 (1996), arXiv:hep-ph/9509255.

[81] S. M. Barr, Phys. Rev. Lett. 92, 101601 (2004), arXiv:hep-ph/0309152.

[82] W. C. Haxton and G. J. Stephenson Jr., Progress in Particle and Nuclear Physics 12 (1984).

[83] J. Kotila and F. Iachello, Phys. Rev. **C**85, 034316 (2012), arXiv:1209.5722.

[84] J. Schechter and J. W. F. Valle, Phys. Rev. **D**25, 2951 (1982).

[85] M. Duerr, M. Lindner, and A. Merle, JHEP 06, 091 (2011), arXiv:1105.0901.

[86] J. Barea, J. Kotila, and F. Iachello, Phys. Rev. **C**91, 034304 (2015), arXiv:1506.08530.

[87] J. Barea, J. Kotila, and F. Iachello, Phys. Rev. **C**87, 014315 (2013), arXiv:1301.4203.

[88] Planck, P. A. R. Ade *et al.*, (2015), arXiv:1502.01589.

[89] N. Palanque-Delabrouille *et al.*, JCAP 1502, 045 (2015), arXiv:1410.7244.

[90] S. Dell'Oro, S. Marcocci, M. Viel, and F. Vissani, (2015), arXiv:1505.02722.

[91] C. Giunti and E. M. Zavanin, JHEP 07, 171 (2015), arXiv:1505.00978.

[92] F. Vissani, JHEP 06, 022 (1999), arXiv:hep-ph/9906525.

[93] F. Vissani, M. Narayan, and V. Berezinsky, Phys. Lett. **B**571, 209 (2003), arXiv:hep-ph/0305233.

[94] F. Vissani, Phys. Lett. **B**508, 79 (2001), arXiv:hep-ph/0102236.

[95] EUCLID, R. Laureijs *et al.*, (2011), arXiv:1110.3193.

[96] J. Hamann, S. Hannestad, and Y. Y. Y. Wong, JCAP 1211, 052 (2012), arXiv:1209.1043.

[97] H. V. Klapdor-Kleingrothaus, I. V. Krivosheina, A. Dietz, and O. Chkvorets, Phys. Lett. **B**586, 198 (2004), arXiv:hep-ph/0404088.

[98] V. Tretyak and Y. Zdesenko, Atomic Data and Nuclear Data Tables 61, 43 (1995).

[99] M. Berglung and M. E. Wieser, Pure Appl. Chem. 83, 397 (2011).

[100] G. Douysset, T. Fritioff, C. Carlberg, I. Bergstrom, and M. Bjorkhage, Phys. Rev. Lett. 86, 4259 (2001).

[101] GERDA Collaboration, M. Agostini *et al.*, (2015), arXiv:1501.02345.

[102] GERDA Collaboration, M. Agostini *et al.*, Phys. Rev. Lett. 111, 122503 (2013), arXiv:1307.4720.

[103] A. Kwiatkowski *et al.*, Phys. Rev. **C**89, 045502 (2014), arXiv:1308.3815.

[104] NEMO, A. Barabash and V. Brudanin, Phys.Atom.Nucl. 74, 312 (2011), arXiv:1002.2862.

[105] D. L. Lincoln *et al.*, Phys.Rev.Lett. 110, 012501 (2013), arXiv:1211.5659.

[106] A. Barabash, Nucl.Phys. **A**935, 52 (2015), arXiv:1501.05133.

[107] K. Gulyuz *et al.*, Phys.Rev. **C**91, 055501 (2015).

[108] NEMO-3, J. Argyriades *et al.*, Nucl.Phys. **A**847, 168 (2010), arXiv:0906.2694.

[109] S. Rahaman *et al.*, Phys.Lett. **B**662, 111 (2008), arXiv:0712.3337.

[110] NEMO, R. Arnold *et al.*, Phys.Rev.Lett. 95, 182302 (2005), arXiv:hep-ex/0507083.

[111] L. Cardani *et al.*, J.Phys. **G**41, 075204 (2014), arXiv:1312.4680.

[112] NEMO-3, R. Arnold *et al.*, (2015), arXiv:1506.05825.

[113] S. Rahaman *et al.*, Phys.Lett. **B**703, 412 (2011).

[114] M. Redshaw, B. J. Mount, E. G. Myers, and I. Avignone, Frank T., Phys.Rev.Lett. 102, 212502 (2009), arXiv:0902.2139.

[115] NEMO-3, R. Arnold *et al.*, Phys.Rev.Lett. 107, 062504 (2011), arXiv:1104.3716.

[116] CUORE, K. Alfonso *et al.*, Phys. Rev. Lett. **115**, 102502 (2015), arXiv:1504.02454.

[117] N. Scielzo *et al.*, Phys.Rev. **C**80, 025501 (2009), arXiv:0902.2376.

[118] P. M. McCowan and R. C. Barber, Phys. Rev. C 82, 024603 (2010).

[119] KamLAND-Zen, A. Gando *et al.*, Phys.Rev. **C**86, 021601 (2012), arXiv:1205.6372.

[120] EXO-200, J. Albert *et al.*, Phys.Rev. **C**89, 015502 (2014), arXiv:1306.6106.

[121] KamLAND-Zen, A. Gando *et al.*, Phys.Rev.Lett. 110, 062502 (2013), arXiv:1211.3863.

[122] M. Redshaw, E. Wingfield, J. McDaniel, and E. Myers, Phys.Rev.Lett. 98, 053003 (2007).

[123] V. Kolhinen *et al.*, Phys.Rev. **C**82, 022501 (2010).

[124] E. E. Haller, W. L. Hansen, and F. S. Goulding, Advances in Physics 30, 93 (1981).

[125] E. Fiorini, A. Pullia, G. Bertolini, F. Cappellani, and G. Restelli, Lettere Al Nuovo Cimento Series 1 3, 149 (1970).

[126] A. A. Vasenko *et al.*, Mod. Phys. Lett. **A**5, 1299 (1990).

[127] H. V. Klapdor-Kleingrothaus *et al.*, Eur. Phys. J. **A**12, 147 (2001), arXiv:hep-ph/0103062.

[128] H. V. Klapdor-Kleingrothaus, A. Dietz, H. L. Harney, and I. V. Krivosheina, Mod. Phys. Lett. **A**16, 2409 (2001), arXiv:hep-ph/0201231.

[129] H. V. Klapdor-Kleingrothaus, Int. J. Mod. Phys. **D**13, 2107 (2004).

[130] H. V. Klapdor-Kleingrothaus, A. Dietz, I. V. Krivosheina, and O. Chkvorets, Nucl. Instrum. Meth. **A**522, 371 (2004), arXiv:hep-ph/0403018.

[131] H. V. Klapdor-Kleingrothaus and I. V. Krivosheina, Mod. Phys. Lett. **A**21, 1547 (2006).

[132] F. Feruglio, A. Strumia, and F. Vissani, Nucl. Phys. **B**637, 345 (2002), arXiv:hep-ph/0201291, [Addendum: Nucl. Phys.B659,359(2003)].

[133] B. Schwingenheuer, Annalen Phys. 525, 269 (2013), arXiv:1210.7432.

[134] E. Fiorini, A. Pullia, G. Bertolini, F. Cappellani, and G. Restelli, Phys. Lett. **B**25, 602 (1967).

[135] E. Fiorini, A. Pullia, G. Bertolini, F. Cappellani, and G. Restelli, Il Nuovo Cimento A 13, 747 (1973).

[136] F. T. Avignone *et al.*, Phys. Rev. Lett. 50, 721 (1983).

[137] A. Forster, H. Kwon, J. K. Markey, F. Boehm, and H. E. Henrikson, Physics Letters B 138, 301 (1984).

[138] J. J. Simpson, P. Jagam, J. L. Campbell, H. L. Malm, and B. C. Robertson, Phys. Rev. Lett. 53, 141 (1984).

[139] E. Bellotti *et al.*, AIP Conference Proceedings 114, 189 (1984).

[140] E. Bellotti *et al.*, Physics Letters B 146, 450 (1984).

[141] R. L. Brodzinski *et al.*, AIP Conf. Proc. 126, 50 (1985).

[142] (PNL-USC Collaboration), F. T. Avignone *et al.*, Phys. Rev. Lett. 54, 2309 (1985).

[143] A. Alessandrello *et al.*, Nucl. Instrum. Meth. **B**17, 411 (1986).

[144] P. Fisher *et al.*, Phys. Lett. **B**218, 257 (1989).

[145] D. Reusser *et al.*, Phys. Rev. **D**45, 2548 (1992).

[146] A. Balysh *et al.*, Phys. Lett. **B**283, 32 (1992).

[147] A. Balysh *et al.*, Physics Letters B 356, 450 (1995).

[148] C. E. Aalseth *et al.*, Nucl. Phys. Proc. Suppl. 48, 223 (1996).

[149] M. Gunther *et al.*, Phys. Rev. **D**55, 54 (1997).

[150] IGEX, C. E. Aalseth *et al.*, Phys. Rev. **C**59, 2108 (1999).

[151] D. Gonzalez *et al.*, Nucl. Phys. Proc. Suppl. 87, 278 (2000).

[152] A. Morales and J. Morales, Nuclear Physics B - Proceedings Supplements 114, 141 (2003), Proceedings of the {XXXth} International Meeting of Fundamentals Physics.

[153] A. M. Bakalyarov, A. Y. Balysh, S. T. Belyaev, V. I. Lebedev, and S. V. Zhukov, Phys. Part. Nucl. Lett. 2, 77 (2005), arXiv:hep-ex/0309016, [Pisma Fiz. Elem. Chast. Atom. Yadra2,21(2005)].

[154] H. S. Miley, R. L. Brodzinski, J. H. Reeves, F. T. Avignone, and J. I. Collar, Phys. Rev. Lett. 65, 3092 (1990).

[155] M. Agostini *et al.*, (2015), arXiv:1501.02345.

[156] F. T. Avignone *et al.*, Phys. Lett. **B**256, 559 (1991).

[157] F. T. Avignone, Prog. Part. Nucl. Phys. 32, 223 (1994).

[158] A. Balysh *et al.*, Phys. Lett. **B**322, 176 (1994).

[159] A. Morales, Nuclear Physics B - Proceedings Supplements 77, 335 (1999).

[160] C. Dorr and H. V. Klapdor-Kleingrothaus, Nucl. Instrum. Meth. **A**513, 596 (2003).

[161] GERDA, M. Agostini *et al.*, J. Phys. **G**40, 035110 (2013), arXiv:1212.3210.

[162] H. Bethe, Annalen der Physik 397 (1930).

[163] F. Bloch, Zeitschrift für Physik A Hadrons and Nuclei 81 (1933).

[164] M. J. Berger *et al.*, XCOM: Photon Cross Section Database (Version 3.1), http://www.nist.gov/pml/data/xcom/, 2010.

[165] F. E. Emery and T. A. Rabson, Physical Review 140 (1965).

[166] Y. P. Varshni, Physica 34 (1967).

[167] G. Gilmore, *Practical Gamma-ray Spectrometry* (Wiley, 2008), ISBN 978-0-470-86196-7.

[168] M. Agostini, *Signal and background studies for the search of neutrinoless double beta decay in* GERDA, PhD thesis, Technische Universität München, 2013.

[169] W. Shockley, Journal of Applied Physics 9 (1938).

[170] S. Ramo, Proceedings of the IRE 27 (1939).

[171] Z. He, Nucl. Instrum. Meth. **A**463 (2001).

[172] GERDA, K. Ackermann *et al.*, Eur.Phys.J. **C**73, 2330 (2013), arXiv:1212.4067.

[173] E. Gatti and P. Manfredi, La Rivista del Nuovo Cimento 9, 1 (1986).

[174] V. Radeka, Annual Review of Nuclear and Particle Science 38, 217 (1988).

[175] U. Fano, Phys. Rev. 72, 26 (1947).

[176] H. R. Bilger, Phys. Rev. 163, 238 (1967).

[177] N. Strokan, V. Ajdai, and B. Lalovi, Nuclear Instruments and Methods 94, 147 (1971).

[178] S. Croft and D. Bond, Int. J. Rad. Appl. Instrum. **A**42, 1009 (1991).

[179] B. Lowe, Nucl. Instrum. Meth. **A**399, 354 (1997).

[180] Borexino, G. Bellini *et al.*, JCAP 1205, 015 (2012), arXiv:1202.6403.

[181] M. Tarka, *Studies of Neutron Flux Suppression from a Gamma-ray Source and the* GERDA *Calibration System*, PhD thesis, University of Zurich, 2012.

[182] F. Froborg, *Calibration of Phase I of the* GERDA *Double Beta Decay Experiment*, PhD thesis, University of Zurich, 2012.

[183] M. Walter, *Background Reduction Techniques for the* GERDA *Experiment*, PhD thesis, University of Zurich, 2015.

[184] J. Hellmig and H. V. Klapdor-Kleingrothaus, Z. Phys. **A**359, 351 (1997), arXiv:nucl-ex/9801004.

[185] Canberra, www.canberra.com.

[186] GERDA, M. Agostini *et al.*, Eur.Phys.J. **C**75, 39 (2015), arXiv:1410.0853.

[187] E. Andreotti *et al.*, JINST 8, P06012 (2013), arXiv:1302.4277.

[188] J. R. De Laeter *et al.*, Pure Appl. Chem. 75, 683 (2003).

[189] S. Riboldi *et al.*, Proceedings, 2010 IEEE Nuclear Science Symposium and Medical Imaging Conference (NSS/MIC 2010) , 1386 (2010).

[190] GERDA, K. T. Knöpfle, PoS **TIPP**2014, 109 (2014).

[191] M. Agostini *et al.*, J. Phys. Conf. Ser. 375, 042027 (2012), arXiv:1111.7260.

[192] M. Agostini, L. Pandola, P. Zavarise, and O. Volynets, JINST 6, P08013 (2011), arXiv:1106.1780.

[193] L. Lonnblad, Comput. Phys. Commun. 84, 307 (1994).

[194] M. Frigo and S. G. Johnson, Proceedings of the IEEE 93, 216 (2005), Special issue on "Program Generation, Optimization, and Platform Adaptation".

[195] B. Rene and R. Fons, Nucl. Instrum. Meth. **A**389, 81 (1997), New Computing Techniques in Physics Research V.

[196] M. Ballintijn, C. Loizides, and C. Reed, Tree analysis modules, www.cmsaf.mit.edu/twiki/pub/Software/TAM/tamdoc.pdf.

[197] National Nuclear Data Center (NuDat 2.6), http://www.nndc.bnl.gov/nudat.

[198] GERDA, M. Agostini *et al.*, Eur. Phys. J. **C**74, 2764 (2014), arXiv:1306.5084.

[199] N. Becerici-Schmidt, *Results on Neutrinoless Double Beta Decay Search in* GERDA*: Background Modeling and Limit Setting*, PhD thesis, Technische Universität München and Max Planck Institut für Physik München, 2014.

[200] S. Hemmer, *Study of Lepton Number Conserving and Non-Conserving Processes Using* GERDA *Phase I Data*, PhD thesis, University of Padova, 2014.

[201] C. E. Aalseth *et al.*, Phys. Rev. **D**70, 078302 (2004), arXiv:nucl-ex/0404036.

[202] M. Agostini, L. Pandola, and P. Zavarise, J. Phys. Conf. Ser. 368, 012047 (2012), arXiv:1111.3582.

[203] M. Morháč, J. Kliman, V. Matoušek, M. Veselský, and I. Turzo, Nucl. Instrum. Meth. **A**443, 108 (2000).

[204] G. W. Phillips and K. W. Marlow, Nuclear Instruments and Methods 137, 525 (1976).

[205] Minuit2, https://seal.web.cern.ch/seal/MathLibs/Minuit2/html/.

[206] Minuit, http://seal.web.cern.ch/seal/work-packages/mathlibs/minuit/.

[207] A. Wald and J. Wolfowitz, The Annals of Mathematical Statistics 11 (1940).

[208] M. Agostini *et al.*, Eur. Phys. J. **C**73, 2583 (2013), arXiv:1307.2610.

[209] H. V. Klapdor-Kleingrothaus and I. V. Krivosheina, Phys. Part. Nucl. Lett. 10, 704 (2013), arXiv:1308.2524.

[210] M. O. Deighton, IEEE Transactions on Nuclear Science 16 (1969).

[211] F. T. Arecchi, G. Cavalleri, E. Gatti, and V. Svelto, Energia nucleare 7, 691.

[212] A. Geraci and E. Gatti, Nucl. Instrum. Meth. **A**361 (1995).

[213] A. Geraci, I. Rech, E. Gatti, and G. Ripamonti, Nucl. Instrum. Meth. **A**482, 441 (2002).

[214] V. Radeka, Nuclear Instruments and Methods 99 (1972).

[215] F. S. Goulding and D. A. Landis, IEEE Transactions on Nuclear Science 35 (1988).

[216] F. S. Goulding, D. A. Landis, and S. M. Hinshaw, IEEE Transactions on Nuclear Science 37 (1990).

[217] M. Salathe and T. Kihm, (2015), arXiv:1504.02039.

[218] A. Caldwell and K. Kroninger, Phys. Rev. **D**74, 092003 (2006), arXiv:physics/0608249.

[219] D. Budjas, M. Barnabe Heider, O. Chkvorets, N. Khanbekov, and S. Schonert, JINST 4, P10007 (2009), arXiv:0909.4044.

[220] S. Bochkanov and V. Bystritsky, Alglib, http://www.alglib.net/.

[221] A. Caldwell, D. Kollar, and K. Kroninger, Comput. Phys. Commun. 180, 2197 (2009), arXiv:0808.2552.

[222] M. Agostini, Private communication.

[223] W. Maneschg *et al.*, Nucl. Instrum. Meth. **A**680, 161 (2012), arXiv:1110.1217.

[224] Berta Battiloro, www.berta-battiloro.com.

[225] L. Baudis *et al.*, JINST 6, P08010 (2011), arXiv:1103.2125.

[226] GEANT4, S. Agostinelli *et al.*, Nucl. Instrum. Meth. **A**506, 250 (2003).

[227] G. A. P. Cirrone *et al.*, Nucl. Instrum. Meth. **A**618, 315 (2010).

[228] T. R. Ophel, Nuclear Instruments 3, 45 (1958).

[229] J. B. Birks, *The theory and practice of scintillation counting* (Pergamon Press, Oxford, 1967).

[230] XENON100, E. Aprile *et al.*, Phys. Rev. **D**88, 012006 (2013), arXiv:1304.1427.

[231] E. Bellotti, Private communication.

[232] ISO/CD 11929, Determination of the characteristic limits (decision threshold, decision limit, and limits of the confidence interval) for ionizing radiation measurements – fundamentals and applications.

[233] O. Schulz, Databricxx data analysis framework, https://github.com/databricxx/databricxx.

[234] Introducing JSON, http://json.org/.

[235] J. Campbell and J. Maxwell, Nucl. Instrum. Meth. **A**129 (1997).

ACKNOWLEDGMENTS

Four years of PhD can be a draining experience for a poor human being of good will. Surviving it strongly relies on the help and support of many colleagues and friends. Achieving some good results depends even more on their presence, in addition to a required dose of good luck. Whether the material presented here is of some significant quality will be only judged after its composition is completed. To be on the safe side, I'll take the full responsibility for the possible failure, and share the honor of an eventual success.

This section is structured as follows. Firstly, I thank my supervisors, then the notable members of the GERDA collaboration, followed by the colleagues of Zurich University. In a second part I thank the family, flatmates and friends. Eventual complaints about the content or the order of the acknowledgments are going to be shipped back to the sender.

First of all, I would like to thank Laura Baudis for supervising me with great expertise during these four years, for leaving me the freedom to test and develop new ideas, and for wisely advising me about my future. A great thank goes also to Alexander Kish for the fruitful discussions about work and life, and for carefully correcting my thesis.

I am particularly thankful to Bernhard Schwingenheuer and Peter Grabmayr for reading and correcting with extreme dedication and attention all the papers, proceedings and slides I prepared during these years, and for being always an open to discussion about my work.

Special thanks also to Carla Cattadori for guiding me in the development of the ZAC filter and the reprocessing of the Phase I data.

I thank Riccardo Brugnera and Alberto Garfagnini for being always available when I had some question, and for encouraging me in the moments of doubt.

Furthermore, I would like to thank Luciano Pandola and Matteo Agostini for their enthusiastic approach to the work and for having always enlightened me with fruitful suggestions.

I thank all the members of the GERDA collaboration for being great colleagues, with whom is always possible to work in a productive and friendly atmosphere. And, of course, I also thank all of them for the fun of the collaboration dinners, which magically smooth even the most heated discussions. Thanks in particular to "my wife" Sabine for the endless conversations ranging from Bayesian statistics to the dreams of life, and to Björn and the young Carla for making me enjoy the periods at LNGS.

I also thank the members of the Baudis group in Zurich, in particular Francesco, Gaudenz, Payam, and Rizalina for being cool friends in and outside of the office.

Now that the scientific acknowledgments are done, I'll take some more freedom with the personal ones.

I thank all my family for always encouraging me in the hard times and for constantly believing in me.

I thank my flatmates for bearing me over the time and for not having me left on a street. At least not yet. In addition to that, I definitely have to thank Robert for the amazing food, and Stefi for washing the dishes and for sharing the content of the corner.

A mandatory and grateful thanks goes also to the Italian gang for making me feel at home even after long periods of absence. A particular thank to Pera for having always asked the right questions and given the right provocations. Special thanks also to my sister Bisi for sharing her innocence no matter what, to Gabri for her inexhaustible and infectious smile, and to Eli for being always there in case of need.

A big thank goes also to Mara for her infinite patience, and, in spite of everything, to Julia for letting me see the world from a different perspective.

Thanks also to thank Marco for the countless relaxing evenings in front of a beer and for considering a dinner with friends more important then anything else.

Moreover, I want to acknowledge Deborah (with "h") for recursively addressing me in public with unrepeatable and colorful expressions, and for sustaining me in the moments of despair. Together with her, I also thank Ale and Marzia for the remarkable Friday's fun.

Finally, I'll keep the tradition alive and thank the Giants, the Speci and the Bianchi for always keeping me in balance on my way, no matter where it is from and where it goes.